A porphyrin and some phthalocyanines conjugated to graphitic carbon nitride and manganase ferrites nanoparticles and supported on electrospun nanofibers for photosono-degradation of organic pollutants

Thesis submitted in fulfilment of the requirement for the degree of

Doctor of Philosophy

In

CHEMISTRY

Of

Rhodes University

By

Siphumelele Thandokwazi Mkhondwane

Supervisor

Distinguished Professor Tebello Nyokong

March 2025

Dedications

This work is dedicated to my village that raised me, my firiends Philani and Zolile Machi and exclusively to my parents Khaladi and Thulani Mkhondwane.

Acknowledgements

The Proverb “It takes a village” cannot even begin to describe the collaborative effort it took to ensure the success of this study. First and foremost, I would like to express my deepest gratitude to my supervisor Distinguished Tebello Nyokong. The words cannot express how grateful I am for giving me an opportunity to work under your supervision. Thank you for being a great supervisor; for support, patience, suggestions throughout the study and great desire you have for the success of your students.

I would like to further extend my gratitude to Dr Britton, Prof. Mack, Mr Chindeka, Gail Cobus and Prof. F. Opoku. for their valuable support. I woul also like to thank Drs Refilwe Matshitse, Sithi Mgidlana, Yolande Openda, Lindokuhle Nene, Sixolile Centane, Aviwe Magadla and Mr Mbulelo Jokazi for their valuable assistance and support. I will also like to apprecieate all the members of the Tebello Nyokong-Institude of Nanotechnology Innovation (TN-INI) for a conjusive ambience research.

I would also like to duly acknowledge the full support I have received from Rhodes university research office particularly from Nwabisa Mkosana. Special thanks also go to National Research Foundation (NRF) and DSI-MINTEK for financial support.

I would like to also express my deepest gratitude to my friends Philani Machi and Zolile Machi for their moral support. Exclusively, I would like to thank my parents (Thulani Mkhondwane and Khaladi Sigwebela) for their unprecedented support and constant love. Without them it woul not be possible for me to be where I am.

Contents

Abstract

This thesis reports on the synthesis, characterization and application of the zinc phthalocyanines (Pcs) and porphyrin in degradation of organic pollutants using photo- (visible light), sono- (ultrasound) and photosono-catalytic processes (combined visible light and ultrasound). To enhance the physicochemical properties, the Pcs and porphyrin were conjugated with nanoparticles (g-C_3N_4 nanosheets, g-C_3N_4 quantum dots and $MnFe_2O_4$ nanoparticles) through covalent linkage. To enhance catalytic stability and usability, the Pcs porphyrin and conjugates were supported on electrospun nanofibers. The electrospun nanofibers that were used as supports were TiO_2 and ZnO nanofibers. The Pcs were supported on TiO_2 nanofibers using covalent linkage and physical adsorption. The effect of the symmetry of the Pcs, number of the oxygen species and the mode of support on electrospun nanofibers were investigated by comparing their catalytic efficiencies in degradation of organic pollutants. The pollutants that were studied were Rhodamine 6G and 2,4-dichlorophenol. The catalytic efficiencies of the conjugate of $MnFe_2O_4$ nanoparticles were also studied. The catalytic efficiencies of the conjugate of g-C_3N_4 nanosheets, g-C_3N_4 quantum dots could not be investigated because these conjugates were soluble in water. The results showed that the asymmetric Pcs were more catalytically active than their symmetrical analogous. The Pcs with higher number of oxygen species were more catalytically active than the Pcs with lesser number of oxygen species. The conjugates of the $MnFe_2O_4$ nanoparticles were more active than pristine Pcs and the conjugates of g-C_3N_4 nanosheets, g-C_3N_4 quantum dots had improved photophyiscal properties. The functionalized TiO_2 fibers through conjugate linkage with the Pcs were more catalytically active than functionalized TiO_2 fibers through physical adsorption. The functionalized TiO_2 fibers and ZnO fibers with the conjugates of Pcs and nanoparticles

were more active than the functionalized fibers with Pcs only. The photosono-catalytic process was more active than photo- and sono-catalytic processes alone. The investigation of the reactive species revealed that photocatalytic processes is driven by singlet oxygen while sono- and photosono-catalytic processes are driven by singlet oxygen and hydroxide radicals.

List of Symbols

Φ_{ADMA}	ADMA Quantum Yield
K_A	Adsorption coefficient
k	Apparent reaction rate constant
τ_F	Fluorescence Lifetime
Φ_F	Fluorescence Quantum Yield
$t_{1/2}$	Half-life
r_o	Initial photocatalytic degradation rate
Co	Initial concentration of pollutant
n	Refractive index of sample solvent
n_{std}	Refractive index of standard solvent
Φ_Δ	Singlet Oxygen Quantum Yield
τ_T	Triplet Lifetime
Φ_T	Triplet Quantum Yield
α	Absorption coefficient
h	Planck's constant,
ν	Photon's frequency
E_g	Band gap energy
k	Proportionality constant

List of Abbreviations

ADMA	Anthracene-9,10-bis-methylmalonate
APTES	(3-Aminopropyl)triethoxysilane
AIBN	Azo-bis-isobutyronitrile
BET	Brunauer–Emmett–Teller
BQ	4-benzoquinone
DBU	1,8-Diazabicyclo[5.4.0]undec-7ene
DCC	Dicyclohexylcarbodiimide
DCP	Dichlorophenol
DMA	9,10-dimethylanthracene
DMSO	Dimethyl sulfoxide
DMF	N,N-Dimethylformamide
DPBF	1,3- Diphenylisobenzofuran
EDC	N,N' -dicyclohexylcarbodiimide
EDX	Energy Dispersive X-ray
EPR	Electron paramagnetic resonance
FFA	Furfuryl alcohol
FT-IR	Fourier transform infrared
HA	Humic acid
1H NMR	Proton Nuclear Magnetic resonance
HOMO	Highest Occupied Molecular Orbital
ISC	Intersystem crossing

LUMO	Lowest Unoccupied Molecular Orbital
MALDI-TOF	Matrix- Assisted Laser Desorption Ionization- Time of Flight
Pc	Phthalocyanine
PMS	Peroxy monosulfate
PVP	Polyvinylpyrrolidone
ROS	Reactive Oxygen Species
SEM	Scanning Electron Microscopy
TBA	Tert-butyl alcohol
TBHP	Tert-butyl hydrogen peroxide
TCSPC	Time-Correlated Single Photon Counting
TGA	Thermogravimetric
TEM	Transmission Electron Microscopy
THF	Tetrahydrofuran
TEMPO	2,2,6,6-tetramethylpiperidone
XRD	X-ray Diffraction
XPS	X-ray Photoelectron Spectroscopy
ZnTPP	

Preamble

This thesis reports on the synthesis and characterisation of some new and previously reported phthalocyanines and porphyrins and their nanomaterial conjugates that have been supported on electrospun nanofibers. The composites are used as catalysts in degradation of organic water pollutants in the presence of light (photo-catalytic process), ultrasound (sono-catalytic process) and both light and ultrasound (photosono-catalytic process).

Chapter one

This chapter discusses the basis of the thesis. It provides background on the properties of phthalocyanines, porphyrin, nanomaterials and nanofibers and how their composites enhance degradation of organic pollutants in the presence of ultrasound and light.

1.1. Introduction

Organic pollutants discharged into wastewater from textile and pharmaceutical industries have a global threat to quality of drinking water [1]. These compounds are highly carcinogenic and detrimental to aquatic life, hence, their complete mineralization to less or non-toxic low molecular compounds is mandatory [2]. However, organic pollutants are highly refractory against conventional degradation processes such as flocculation [3], sedimentation [4], coagulation [5], chlorination [6] and chemical oxidation [7]. Therefore, designing new, highly effective and environmentally friendly contemporary processes that can be utilized to degrade these compounds is necessary. Advanced oxidation processes (AOPs) are a promising solution due to their high efficiency. AOPs encompass in-situ generation of the highly reactive oxygen species (ROS) such singlet oxygen ($^1O_2$), hydroxide radicals ($^{\bullet}OH$), superoxide ($O_2^{\bullet-}$) and sulphate radicals ($SO_4^{2\bullet-}$). The reactive oxidation species subsequently degrade organic pollutants to less toxic compounds [8].

Some of the well-established AOPs include ozonation [9], Fenton [10], sono-catalysis [11] and photo-catalysis [12]. These processes have also been combined in most studies in quest to enhance efficiency. In this thesis, photo-catalysis process is first used to degrade Rhodamine 6G and dichlorophenol. Subsequently, photocatalysis process is combined with sono-catalysis for photosono-catalytic process. The photosono-catalytic process was used for degradation of Rhodamine 6G. Rhodamine 6G and dichlorophenol (DCP) are water soluble, organic water pollutants. Rhodamines 6G is commonly used in plastic, textile and cosmetic industries [13], whereas DCP is used as herbicide, preservative, disinfectant and synthesis of pharmaceuticals [14]. For comparison purposes Rhodamine 6G was separately degraded using photo- and sono-catalytic processes.

The photo-catalytic process involves the excitation of the semiconductor catalyst from ground state to first excited state, a phenomenon that results in migration of the electrons from the valence band (VB) to the conduction band (CB) leaving the holes in the VB (generating electron-hole pairs). Some of the electrons in the CB recombine with the holes in the VB through fluorescence while others interact with oxygen and other substrates to generate reactive oxygen species (ROS) [15].

In general, sono-catalytic process involves the formation and collapse of the H_2O bubbles in the presence ultrasound. The process is known as pyrolysis. After collapsing, the bubbles generate high temperature and pressure conditions which produces •OH species from water pyrolysis and sonoluminescence in the form of hot light [16]. The photosono-catalytic process is the combination of these two processes. However, it is worth noting that the excitation of the catalyst from ground state to the first excited state transpires as a consequence of both visible light illumination and ultrasound. Depending on the catalysts utilized photo-, sono- and photosono-catalytic process often suffer from rapid recombination of electron-hole pairs, which compromises the efficiency [17].

In this study, for the first time, some nanoparticles were conjugated with phthalocyanines and porphyrins and used to functionalize electrospun nanofibers. The hybrids were subsequently used as photosono-catalysts for degradation of Rhodamine 6G. The nanoparticles that were used were graphitic carbon nitride nanosheets (g-C_3N_4 NS), graphitic carbon nitride quantum dots (g-C_3N_4 QDs) and spinel manganese ferrite ($MnFe_2O_4$). The electrospun fibers that were used were titanium dioxide (TiO_2) and zinc (ZnO) fibers.

1.1.1 Background: Porphyrins and Phthalocyanines

Porphyrins are naturally occurring compounds with tetrapyrrolic aromatic macrocycles composed of 18 π conjugated electronic system linked by methylene bridges [18]. The structure of the porphyrin has two main positions where functionalization can be performed. These positions are β and meso positions (**Fig. 1.1**) [19]. The free base porphyrin can accommodate various metal cations [20].

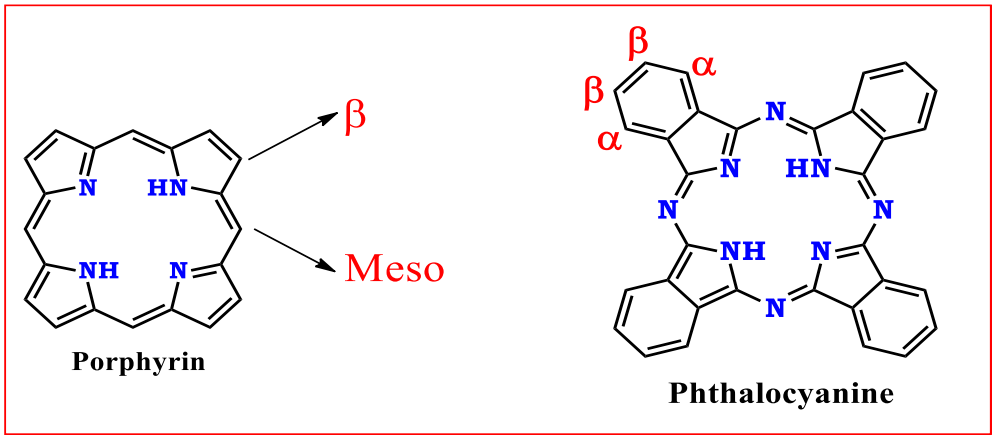

Fig.1.1. Typical structures of phthalocyanine and porphyrin

Phthalocyanines (Pcs) are a class of synthetic porphyrin derivative compounds composed of two-dimensional tetrapyrrolic macrocycles. Pcs were first discovered by chance in 1928 by Dandridge and co-workers [21]. The following year, fascinated by these compounds, Linstead and co-workers at Imperial College developed the synthetic route and studied their structure [22]. Like porphyrins, Pcs are composed 18 π-electrons system structure which is responsible for their excellent light absorption efficiency. There are two main points of substitutions in phthalocyanines, which are β and α positions shown in **Fig**.**1**.**1**.

Structurally, the differences between Pcs and porphyrins are four nitrogen atoms and four extended benzo subunits of phthalocyanines. Porphyrins and phthalocyanines are non-toxic, have high stability, are easy to modify to fine tune their physical and

chemical properties and can generate reactive oxygen species (such as singlet oxygen and radical species) under irradiation [23,24]. These properties make these complexes ideal photosensitizers for various applications such as nonlinear optics [25,26], photodynamic therapy [27,28], as pigments in paint industry [29,30], solar cells [31,32], electrocatalysis [33,34] and photocatalysis [35,36].

1.1.2. Synthesis of phthalocyanines and porphyrins

1.1.2.1. Synthesis of phthalocyanines

Generally, Pcs are synthesized by condensation method in the presence of precursors. Compared to direct substitution of the substituents to the macrocycle, condensation method is more environmentally friendly and easier to control. The most commonly utilized precursors are diiminoisoindoles, phthalic acid, phthalic anhydride, 1,2-dibromobenzene, phthalonitriles and etc (**Scheme 1.1**) [37].

Phthalonitriles are the most commonly utilized precursors at laboratory scale, in which they are refluxed at alleviated temperatures in high boiling solvents such as pentanol, N,N-dimethylaminoethanol (DMAE) or quinoline in the presence or absence of a metal salt. In the presence of the metal salt, the metalated Pc (MPc) is obtained. In the absence of the metal salt, H_2Pc is obtained. H_2Pc can be metalated by subsequent boiling in the presence of the metal salt [38,39]. At industrial scale, due to their low cost, the phthalic anhydrides are the most commonly utilized precursors. Pcs can be symmetrical or asymmetrical depending on the number of the substituents [40].

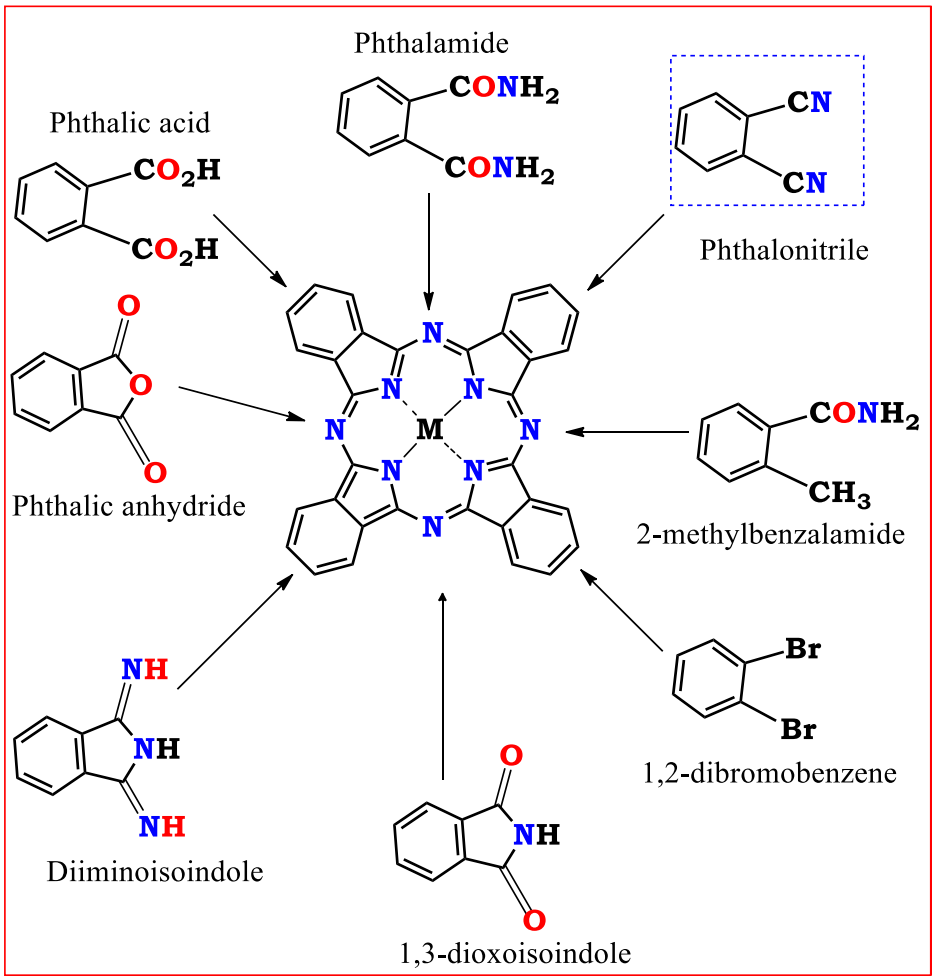

Scheme 1.1. The synthesis of tetrasubstituted Pcs from various precursors

Symmetrical phthalocyanines are synthesized from a single phthalonitrile by means of cyclotetramerization in the presence of a suitable solvent and a base such as 1,8-diazabicyclo[5.4.0]undec-7-ene (DBU). When they are prepared in the absence of the metal salt H_2Pc is obtained, however in the presence of the metal salt metalated Pc (MPc) is obtained [38,40].

Asymmetrical phthalocyanines or A_3B phthalocyanines can be synthesized by various methods such as statistical mixed condensation [41,42], ring expansion [43] and polymeric-support synthetic routes [44]. Among these methods, statistical condensation, owing to its simplicity and high yield of the A_3B and B_3A

phthalocyanines, is most utilized method for the synthesis of asymmetrical phthalocyanines. However, other compounds are also obtained (**Scheme. 1.2**) and extensive column chromatography is performed to separate A_3B phthalocyanines. The statistical mixed condensation method involves cyclization of two phthalonitrile (A and B) with different substituents in the presence of an appropriate solvent [45,46].

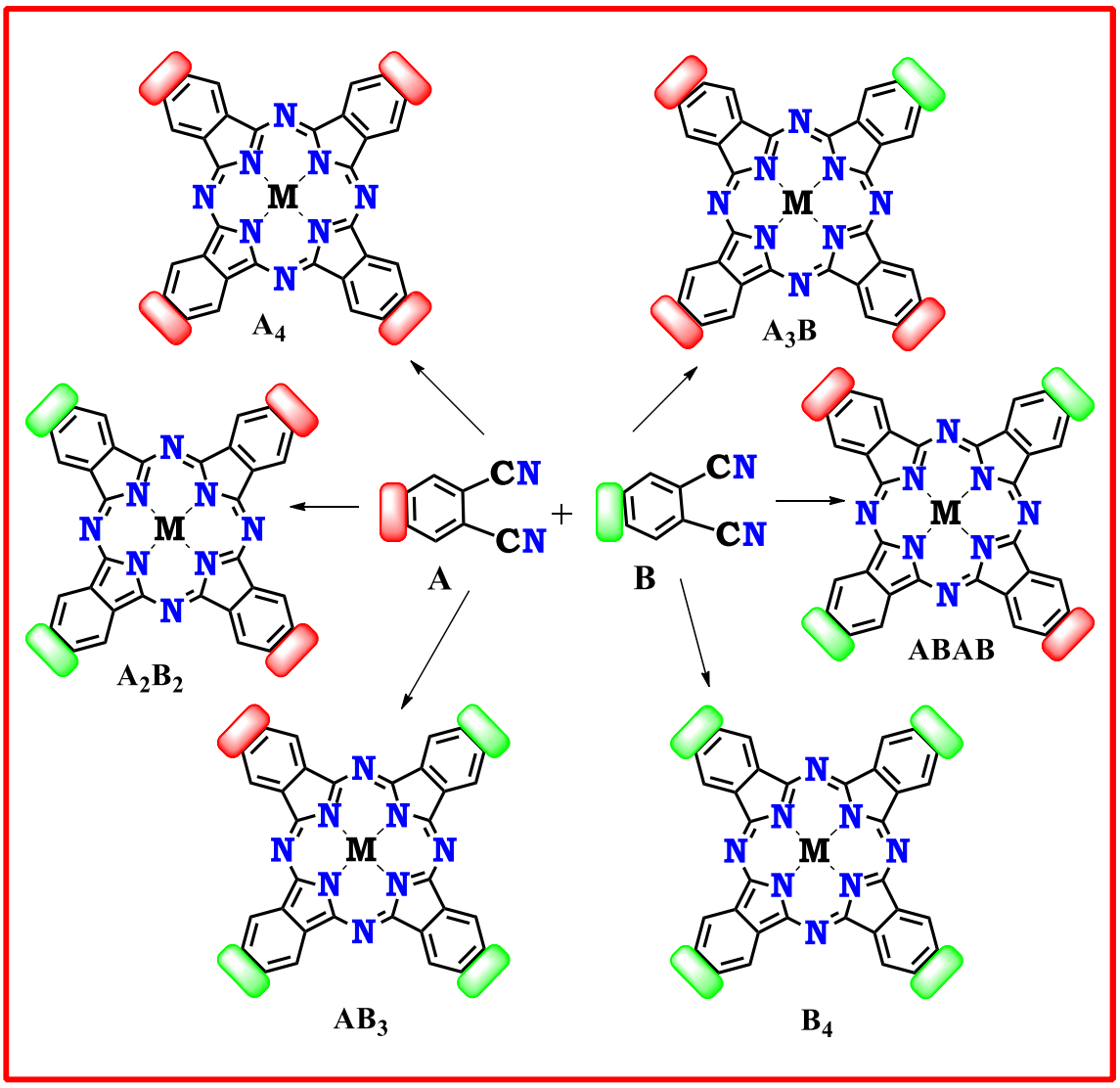

Scheme 1.2. The synthesis of monosubstituted Pcs.

1.1.2.2. Synthesis of porphyrins

Symmetrically and asymmetrically substituted porphyrins can be synthesized using various methods such as Rothemund and Menotti, Adler Longo and co-workers, Lindsey and co-workers, microwave-assisted methods and other methods using pyrrole and the desired benzaldehyde as precursors. Similar to phthalocyanines, the porphyrin core can be metalated or unmetalated. The unmetalated porphyrin is called free base porphyrin.

Rothemund and Menotti method involves the utilization of harsh conditions. In this method, the benzaldehyde and pyrrole are condensed in pyridine at 220 ^{o}C in an isolated system for 24 h. However, this method suffers from low yield (~10%) [47].

Lindsey and co-workers' method involves reacting an equal ratio of benzaldehyde and pyrrole in the presence of the catalyst such as trifluoroacetic acid (TFA) or boron trifluorideetherate ($BF_3.OEt_2$) under inert environment in dichloromethane (DCM) as solvent for 1 h. The 2,3-dichloro-5,6-dicyanobenzoquinone (DDQ) is then used to convert intermediates to porphyrin. The advantages of this method is that it can be utilized in the synthesis of the porphyrins involving acid-sensitive functional groups [48].

Microwave assisted (MW) method involves reacting pyrrole, benzaldehyde and DCM in 10% iodide in microwave irradiation. Subsequently, p-chloranaline is added. The advantages of microwave assisted method it can afford about 47% yield [49]. The synthesis time is also short [50,51].

Adler Longo method is on the most prominent methods for the synthesis of porphyrins due to the fact that it utilizes mild conditions [52]. This method encompasses refluxing

pyrrole in propionic acid which is followed by the addition of benzaldehyde (**Scheme 1.3**). Adler and Longo method can afford up to 20% yield. However, this method also has its shortcomings such as the formation of high quantity of tar, which requires extensive purification. In addition, due to the acidic conditions that are utilized in this method, acid sensitive functional groups such as thiol, amino and hydroxyl groups often do not form the desired products [53]. However, this method was used for the synthesis of the porphyrin utilized in this study due to improved yield compared to Rothemund and Menotti method.

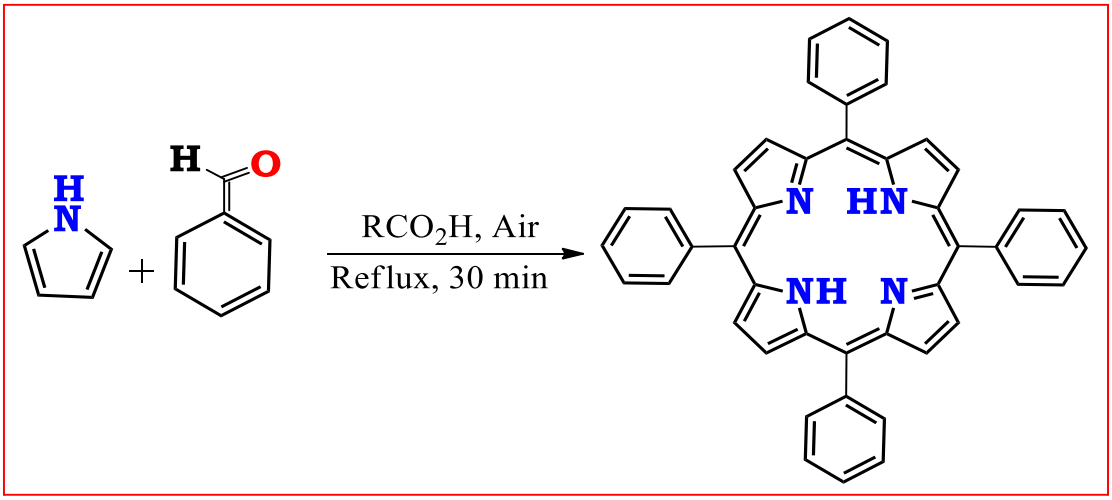

Scheme 1.3. Alder-Longo method for synthesis of porphyrins.

The differences in synthesis of the symmetrically and asymmetrically substituted porphyrins is that with the later, two different aldehydes and pyrrole are utilized. The molar ratio of the benzaldehyde depends on the reactivity of the utilized benzaldehyde, however 1:3 ratio is often utilized. With this ratio, the formation of the symmetrical porphyrins (A_4 and B_4) is minimized. During the synthesis of A_3B and B_3A porphyrins, six possible porphyrins analogous are formed (**Scheme 1.4**), suggesting that extensive column chromatography is required for obtaining pure A_3B porphyrin.

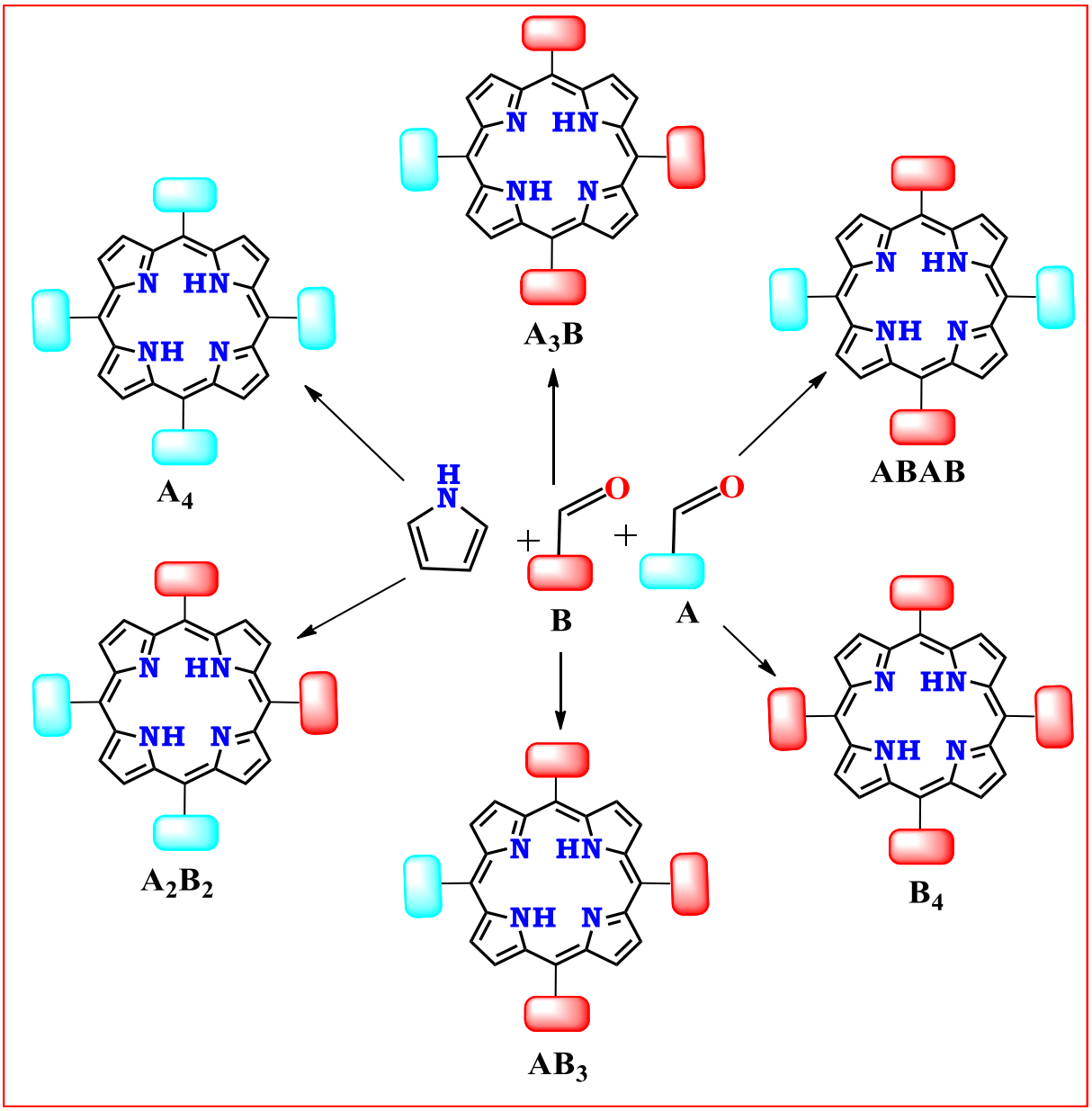

Scheme 1.4. Schematic illustration of possible asymmetric porphyrins and their symmetrical analogues resulting from the reaction mixture during synthesis of asymmetrical porphyrin.

1.1.3. The electronic absorption properties of Pcs and porphyrins

Pcs generally display an intense blue or green colour which is attributed to the 18 π-electrons system of the Pc core. The typical spectrum of the Pc is shown in **Figure 1.2A**. The ground state absorption spectra of the metalated Pc has a weak Soret band

(B-band) and an intense, lowest energy band (Q-band). The Q-band is due π-π transition from the highest occupied molecular orbital (HOMO) orbital to the lowest unoccupied molecular orbital (LUMO). The B-band is associated with the overlap of the B_1 and B_2 bands emanating from transition of a_{2u} and b_{2u} of the HOMO to the e_g of the LUMO (**Fig. 1.3**). Two transitions are the main course of the apparent broad B-band [54,55].

The absorption profile of the porphyrin displays (**Figure 1.2b**) one intense absorption around 400 nm (Soret band) and four or two weaker absorption bands between 450 nm to 700 nm range (Q-bands), depending on the presence or absence of the central metal. The free base porphyrin (unmetalated porphyrin) has four Q-bands, while the metalated porphyrin has two Q-bands. The four Q-bands in the free base porphyrin emanates from split of the symmetry by the N-H proton, which collapse upon the introduction of the central metal [56]. In addition, introduction of the central metal to the porphyrin core usually results in a shift in the absorption bands to shorter or longer wavelengths. The observed absorption bands in the porphyrin emanates from a_{1u} and a_{2u} orbitals to e_g orbitals [57], **Fig. 1.3**.

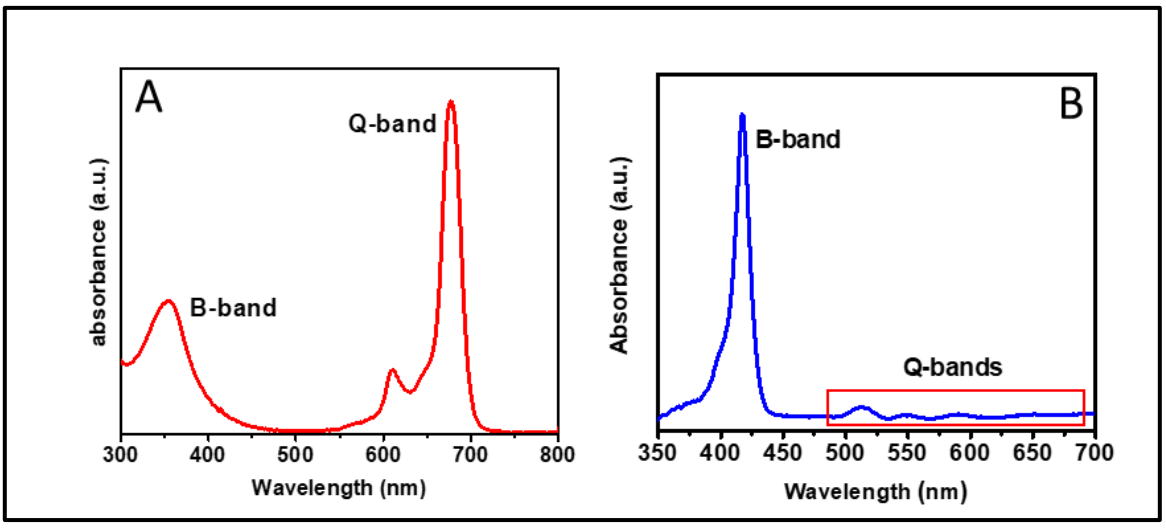

Fig.1.2. Example of the ground state UV-Vis absorption spectrum of porphyrins and phthalocyanines.

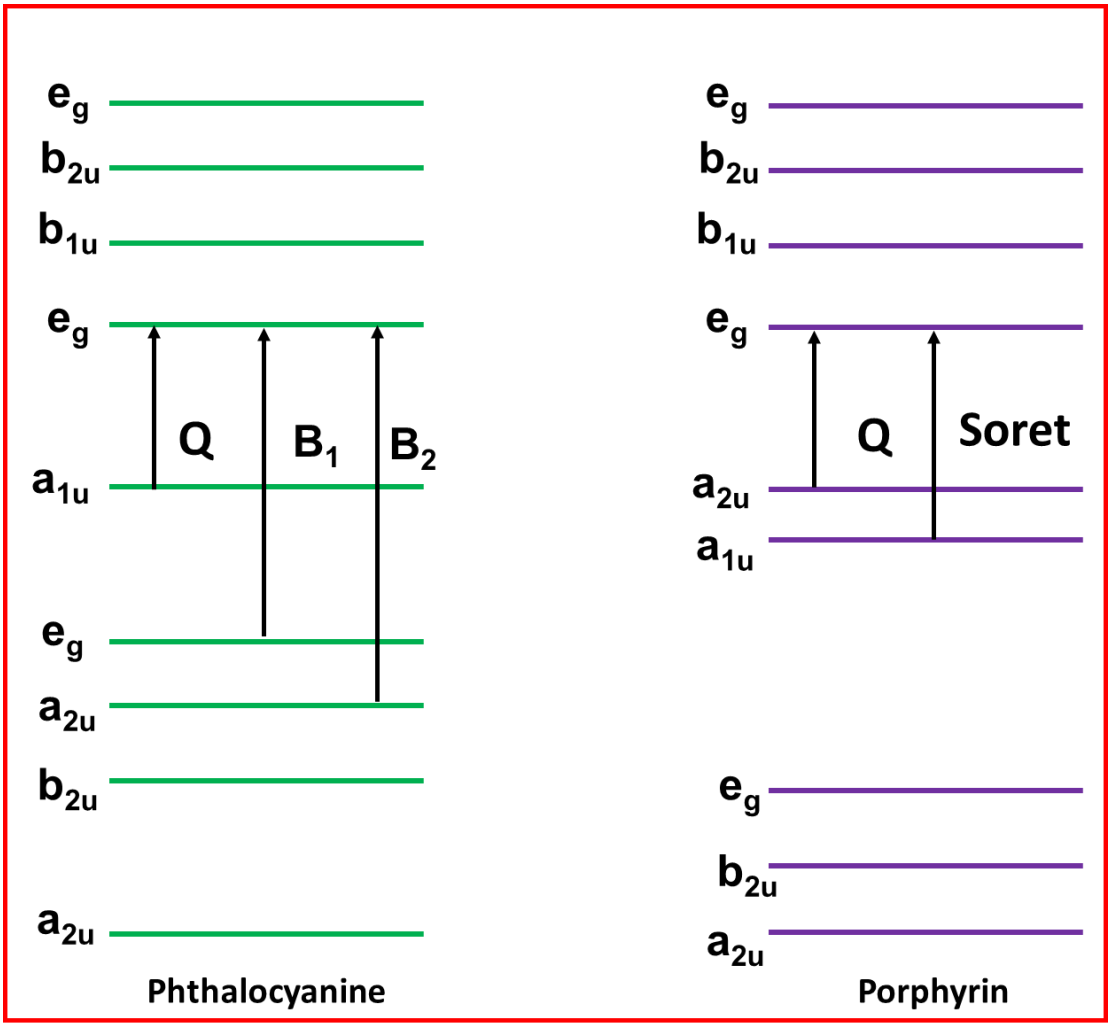

Fig. 1.3. Displays the electronic energy levels of the set of e_g orbitals showing the origin of Q and B bands in Pcs and porphyrins.

1.1.4. Photophysical properties of Pcs and porphyrins

The photophysical properties of the Pcs and porphyrins can be used to predict their catalytic efficacy under light illumination. The processes of the Pcs and porphyrins under light illumination can be elucidated using Jabloski diagram (**Figure 1.4**). Typically, in the presence of light, Pcs and porphyrins in their ground state (S_o)

becomes excited to first excited singlet state (S_1), generating the electron-hole pairs. Subsequently, the molecule can either undergo fluorescence, a phenomenon in which it returns to its ground state following recombination of the electron-hole pairs or undergo intersystem crossing (ISC) to forbidden triplet state (T_1). In the triplet state, the molecule can transfer electrons to molecular oxygen (O_2) and biological molecules to generate free radicals (Type 1 mechanism) or can transfer energy to molecular oxygen to generate singlet oxygen ($^1O_2$), Type 2 mechanism. The generated $^1O_2$ or radicals then initiate oxidation pathways. The $^1O_2$ quantum yield is influenced by numerous parameters such as fluorescence quantum yield (Φ_F) and lifetimes (τ_f) and triplet quantum yield (Φ_T) and lifetimes (τ_T) [58,59].

The Φ_F is the ratio of the photons absorbed to photons emitted through fluorescence. The τ_f measure the average time an excited molecule stays in the excited state before undergoing fluorescence [60,61].

The triplet quantum yield (Φ_T) measures the fraction of the species that undergoes intersystem crossing (ISC) to forbidden triplet state (T_1) [62]. The triplet lifetimes (τ_T) denote the time it takes for the excited triplet state to be depopulated by the generation of the reactive oxygen species (ROS) including singlet oxygen ($^1O_2$). Triplet lifetimes is measured in microseconds (μs) [63].

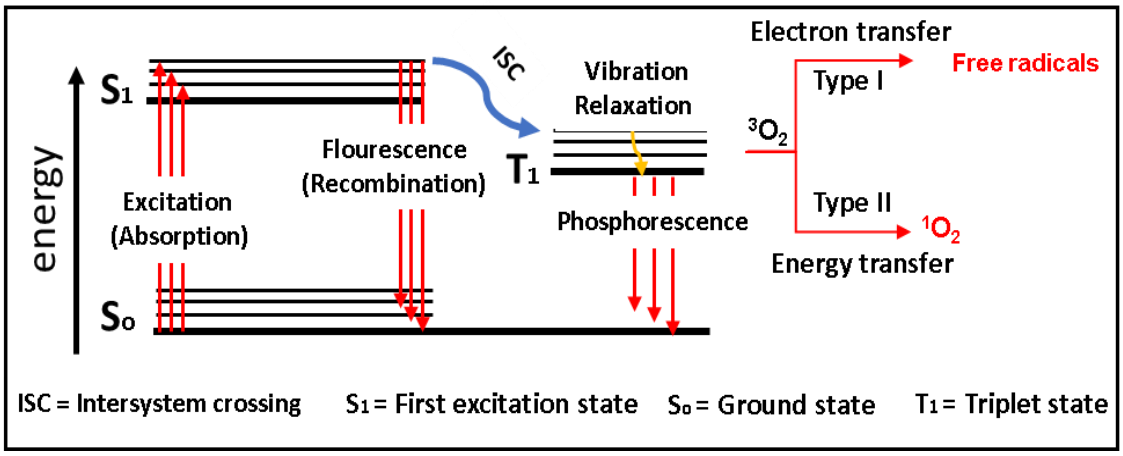

Fig.1.4. Jabloski diagram illustrating processes involved follows light illumination of the photosensitizer.

1.1.5. Factors affecting photophysical properties of Pcs and porphyrins

Porphyrins and Pcs have a tendency of aggregating. Aggregation is one of the factors that affects photophysical parameters of the porphyrins and Pcs. The effect of aggregation is often negative, for example, it can reduce singlet oxygen quantum yield of the Pcs and porphyrins [64]. The presence of the central metal such as zinc(II), gallium(III) and indium(III) affect the photophysical properties of the porphyrins and Pcs. The presence of the central metal containing axial ligand such as gallium(III) and indium(III) reduces aggregation [65]. The addition of the bulky substituents on the macrocycle can also affect the photophysical properties. Different substituents may have different effect on the photophysical properties of the porphyrins and Pcs. Therefore, the choice of the substituent also depends on the intended application [66].

The symmetry plays a significant role in photocatalytic activity of the porphyrins and Pcs. Low symmetry porphyrins and Pcs display enhanced ISC and subsequently high $^1O_2$ production [67]. Conjugation of the Pc with nanoparticles or physically adsorbing the porphyrins and Pcs to a highly stable, high surface area material such as electrospun fibers improves photophysical properties of the porphyrins and Pcs [68].

All these strategies were adopted in thesis. There are two prominent ways in which conjugation to nanoparticles can be achieved. These are; covalent bonding and π- π stacking [69]. Conjugation enhances stability of the porphyrins and Pcs.

1.1.6. Pcs and porphyrin used in this work

This work reports on the synthesis and application of novel metalated symmetrical and asymmetrical substituted phthalocyanines and porphyrin for degradation of the organic pollutants. The Zn was used as central metal because it is a diamagnetic-metals. Diamagnetic metals generally improve intersystem crossing (ISC) to forbidden triplet state (T_1). ISC is crucial for the generation of ROS which plays a massive role in the degradation of organic pollutants. The phthalocyanines and porphyrin complexes used in this work were conjugated with nanomaterials and supported on electrospun nanofibers as elucidated in **Table 1.1**.

Table 1.1. Phthalocyanines/porphyrins, nanoparticles and nanofibers hybrids used in the current work and their applications.

Tetra-substituted phthalocyanine			
Photosensitiser	**Photosensitiser-NPs (Type of bonding)**	**Photosensitiser or conjugates supported on nanofibers (Type of bonding)**	**Studies**
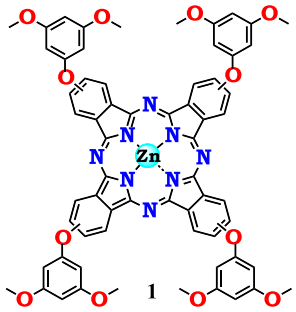 1 Zinc(II) *tetrakis*-(3,5-dimethoxyphenoxy) phthalocyanine **[not new] [70]**	No nanoparticles	Physically adsorbed to TiO_2 nanofibers (**1**-TiO_2 fibers)	Physicochemical Degradation of Rhodamine 6G
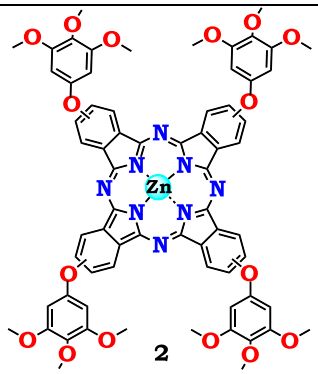 2 Zinc(II) *tetrakis*-(3,5-trimethoxyphenoxy) phthalocyanine **[Not new] [71]**	No nanoparticles	Physically adsorbed to TiO_2 nanofibers (**2**-TiO_2 fibers)	Physicochemical Degradation of Rhodamine 6G

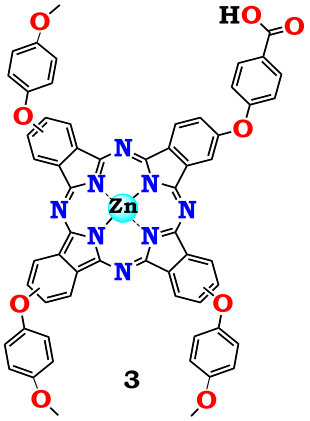 **3** *Zinc*(II)-4-(carboxylic acid phenoxy)-tris-(1,4-methoxyphenoxy) phthalocyanine **[New]**	Conjugation with g-C_3N_4 NS via covalent bonding (**3**@ g-C_3N_4 NS) Conjugation with g-C_3N_4 QDs via covalent bonding (**3**@g-C_3N_4 QDs)	Physically adsorbed to TiO_2 nanofibers (**3**-TiO_2 fibers) conjugated to TiO_2 nanofibers through via covalent bond (**3**@TiO_2 fibers) **3**@g-C_3N_4 NS physically adsorbed to TiO_2 nanofibers (**3**@g-C_3N_4 NS-TiO_2 fibers) **3**@g-C_3N_4 QDs physically adsorbed to TiO_2 nanofibers (**3**@g-C_3N_4 QDs-TiO_2 fibers)	Physicochemical Degradation of dichlorophenol Degradation of Rhodamine 6G
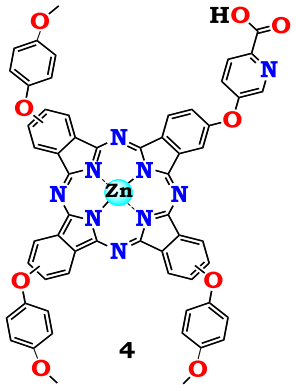 **4**	Conjugation with g-C_3N_4 NS via covalent bonding (**4**@g-C_3N_4 NS)	Physically adsorbed to TiO_2 nanofibers (**4**-TiO_2 fibers) conjugated to TiO_2 nanofibers through via covalent bond (**4**@TiO_2 fibers)	Physicochemical

Zinc*(II)*-4-picolinic acid phenoxy)-tris-(1,4-methoxyphenoxy) phthalocyanine **[New]**	Conjugation with g-C_3N_4 QDs via covalent bonding (**4**@g-C_3N_4 QDs)	**4**@g-C_3N_4 NS physically adsorbed to TiO_2 nanofibers (**4**@g-C_3N_4 NS -TiO_2 fibers)	Degradation of dichlorophenol
		4@g-C_3N_4 QDs physically adsorbed to TiO_2 nanofibers (**4**@g-C_3N_4 QDs -TiO_2 fibers)	Degradation of Rhodamine 6G
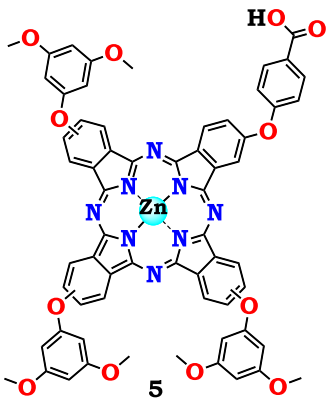 **5** *Zinc*(II)-4-carboxylic acid phenoxy)-tris-(1,3,5-dimethoxyphenoxy) phthalocyanine **[Not new]** [70]	Conjugation with $MnFe_2O_4$ NPs via covalent bonding (**5**@ $MnFe_2O_4$)	Physically adsorbed to TiO_2 nanofibers (**5**-TiO_2 fibers)	Physicochemical
		conjugated to TiO_2 nanofibers through via covalent bond (**5**@TiO_2 fibers)	
	Conjugation with g-C_3N_4 NS via covalent bonding (**5**@g-C_3N_4 NS)	5@g-C_3N_4 NS physically adsorbed to TiO_2 nanofibers (5@g-C_3N_4 NS-TiO_2 fibers)	Degradation of Rhodamine 6G

		5@$MnFe_2O_4$ physically adsorbed to TiO_2 nanofibers (**5**@ $MnFe_2O_4$-TiO_2 fibers)	
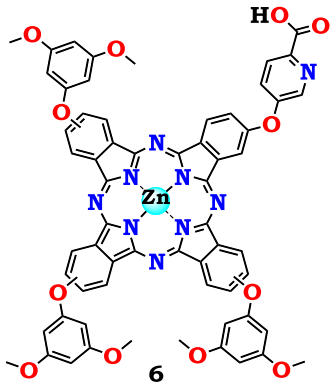 **6** *Zinc*(II)-4-picolinic acid phenoxy)-tris-(1,3,5-dimethoxyphenoxy) phthalocyanine **[New]**	Conjugation with g-C_3N_4 NS via covalent bonding (**6**@g-C_3N_4 NS)	Physically adsorbed to TiO_2 nanofibers (**6**-TiO_2 fibers)	Physicochemical
		Physically adsorbed to ZnO nanofibers (**6**-ZnO fibers)	
		conjugated to TiO_2 nanofibers through via covalent bond (**6**@TiO_2 fibers)	
		6@g-C_3N_4 NS physically adsorbed to TiO_2 nanofibers (**6**@g-C_3N_4 NS-TiO_2 fibers)	Degradation of Rhodamine 6G
		6@g-C_3N_4 NS physically adsorbed to ZnO nanofibers (**6**-g-	

		C_3N_4 NS-ZnO fibers)	

Porphyrin			
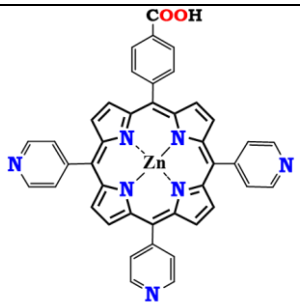 **7** Zinc-5-p-carboxyphenyl-10,15,20-(tris-4-pyridyl)-porphyrin **[New]**	Conjugation with g-C_3N_4 QDs via covalent bonding (**7**@g-C_3N_4 QDs)	Physically adsorbed to TiO_2 nanofibers (**7**-TiO_2 fibers) **7**@g-C_3N_4 QDs physically adsorbed to TiO_2 nanofibers (**7**@g-C_3N_4 QDs-TiO_2 fibers)	Physicochemical Degradation of dichlorophenol (DCP) Degradation of Rhodamine 6G

QDs = quantum dots NS = nanosheets

The complexes **1** [70], **2** [71] and **5** [70] have been reported before, whereas complexes **3**, **4**, **6** and **7** are novel. Complexes **1**, **2** and **7**, were physically adsorbed onto titanium dioxide (TiO_2) nanofibers. Complexes **3**, **4**, **5** and **6** were physically adsorbed onto TiO_2 nanofibers and were also covalently conjugated to TiO_2 nanofibers. Complex **5** was covalently conjugated to manganese ferrites ($MnFe_2O_4$) and complexes **3**, **4**, **5** and **6** were conjugated to graphitic carbon nitride nanosheets (g-C_3N_4 NS). complexes **3** and **4** were also conjugated to graphitic carbon nitride quantum dots (g-C_3N_4 QDs). Complex **7** was conjugated to graphitic carbon nitride quantum dots (g-C_3N_4 QDs). The conjugates of the Pc@g-C_3N_4 NS, Pc@g-C_3N_4 QDs, Pc@$MnFe_2O_4$ and Por@g-C_3N_4 QDs were further used to functionalize TiO_2 and ZnO nanofibers as illustrated in **Table 1.1**. Manganese ferrites nanoparticles ($MnFe_2O_4$), graphitic carbon nitride nanosheets (g-C_3N_4), titanium

dioxide nanofibers (TiO_2) and zinc oxide fibers (ZnO) were chosen in this study because of their tremendous photocatalytic properties. Various porphyrins and Pcs supported on electrospun fibers previously used for degradation of various organic pollutants are listed in **Table 1.2** [72-77].

Table 1.2. Various Pcs and porphyrins linked to nanoparticles and supported to electrospun nanofibers previously reported in degradation of organic pollutants.

Phthalocyanines				
Phthalocyanine	**NPs**	**Nanofibers**	**Degraded pollutant**	**Ref.**
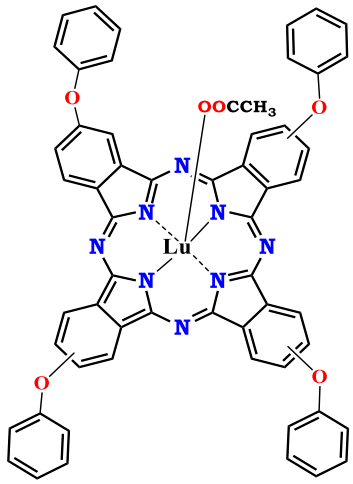	None	Polystyrene fibers	4-chlorophenol Photocatalysis	[72]
	Ag	Polystyrene fibers	Rhodamine 6G	[73]

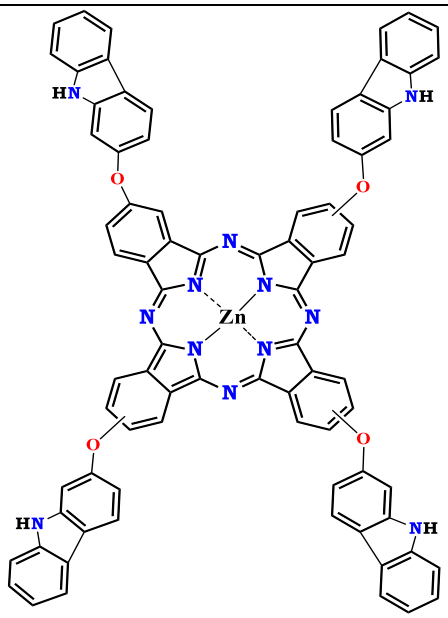			Photocatalysis	
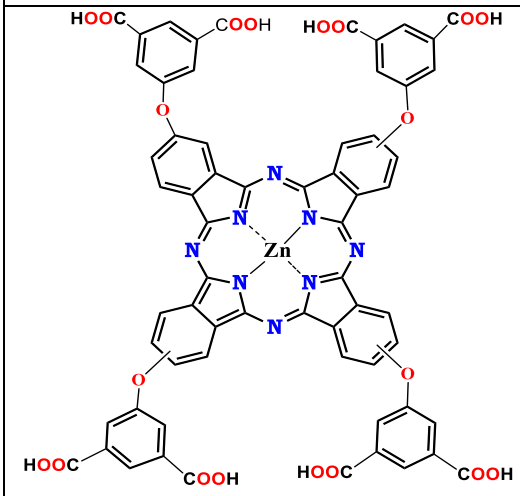	$CoFe_2O_4$	Polyamide-6	Methyl Orange and Orange G	[74]
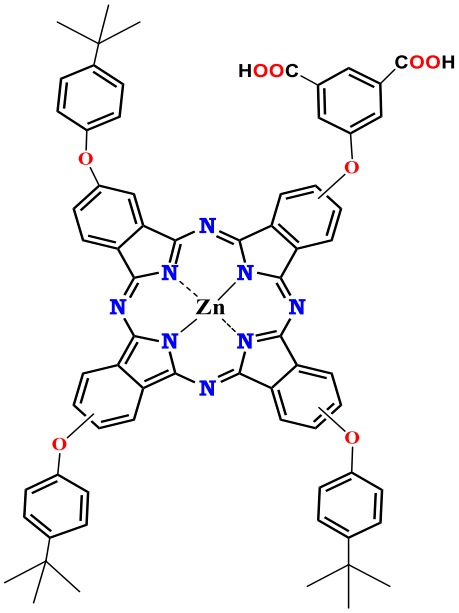	None	ZnO and TiO_2	Methyl Orange	[75]

Porphyrins				
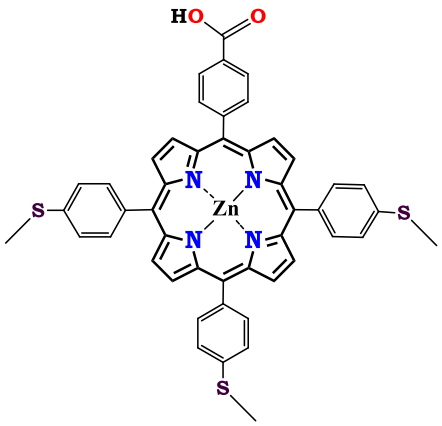	None	PAN polymer	Chlorophenol Photocatalysis	[76]
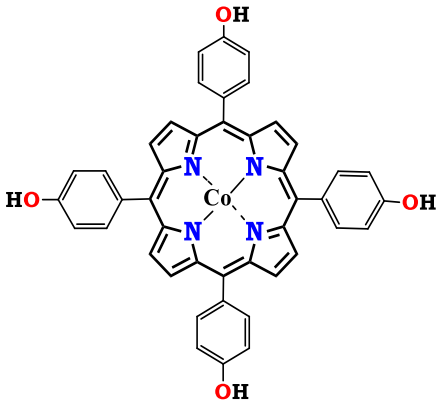	None	PAN polymer	Crystal Violet Photocatalysis	[77]

PAN = Polyacrylonitrile

1.1.7. Novelty of this work

As Table 1.2 shows:

- ❖ No phthalocyanine and porphyrin complexes have ever been reported for photosono-catalytic degradation dichlorophenol and Rhodamine 6G before.
- ❖ No phthalocyanine and porphyrin-TiO_2 and ZnO nanofibers have ever been reported for photosono-catalytic degradation of organic pollutants before.
- ❖ Complexes **1**, **2** and **5** (known) have never been reported for degradation of Rhodamine 6G and dichlorophenol before.
- ❖ Complexes **3**, **4**, **6** and **7** have never been synthesized before, hence they are novel.
- ❖ The conjugate synthesized in this work are new and the combinations of the conjugates and the fibers (TiO_2 and ZnO nanofibers) have never been synthesized before.

1.2. Nanoparticles

Nanoparticles are a class of materials with at least one of their dimensions falling in the range of 1 to 100 nm. These materials have emerged as the most important class of materials in science. Nanomaterials can be in any shape such as nanospheres, nanotubes and nanosheets etc [78]. They can also be organic or inorganic [79-82]. The discussion on nanoparticles in this thesis will be limited to ferrites nanoparticles and graphitic carbon nitrides, since only these were utilized in this study.

1.2.1. Ferrite nanoparticles

Magnetic nanoparticles with superparamagnetic properties have attracted interest in the recent years due to their unique properties particularly, transition metal oxides-based ferrites nanoparticles [83]. Ferrite nanoparticles, based on their magnetic properties and crystal structure, can be categorized as spinel, garnet, hexaferrites and orthoferrites. Spinel nanoparticles are represented as MFe_2O_4 (where M = Mn, Fe, Co, Ni, Co or Zn), garnet as $M_3Fe_5O_{12}$ crystal structure (where M = rare earth cations), hexaferrites as $BaFe_{12}O_{19}$ and $SrFe_{12}O_{19}$ and orthro ferrites as $MFeO_3$, (where M = rare earth cations) [84]. Among these, spinel nanoparticles have attracted particular interest by virtue of their tremendous magnetic properties and ease to maintain chemical composition [85]. Hence these have been utilized in wide range of applications such as catalysis [86], electronic devices [87] and medicine [86] and are used in this work.

1.2.1.1. Properties of spinel ferrite nanoparticles

Spinel ferrites nanoparticles have a general formula of AB_2O_4, where A is Mn, Fe, Co, Ni, Co or Zn metallic cations and B is Fe. Both A and B are positioned at two different crystallographic sites. Both coordinated to oxygen atom **(Fig. 1.5**) [88].

In MFe_2O_4 depending on the sites of M(II) and Fe(III), three types of spinel can be formed which are normal, inverse and mixed spinel nanoparticles [89]. The difference in these types of spinel nanoparticles is the location of the M(II) and Fe(III). Typically, in normal spinel nanoparticles, the M(II) and Fe(III) occupy the tetrahedral and the octahedral sites, respectively. However, in inverse spinel nanoparticles, the Fe(III) is equally distributed in both tetrahedral and octahedral sites, while M(II) occupies only octahedral sites. In mixed spinel nanoparticles, both M(II) and Fe(III) randomly occupies both tetrahedral and octahedral sites [90].

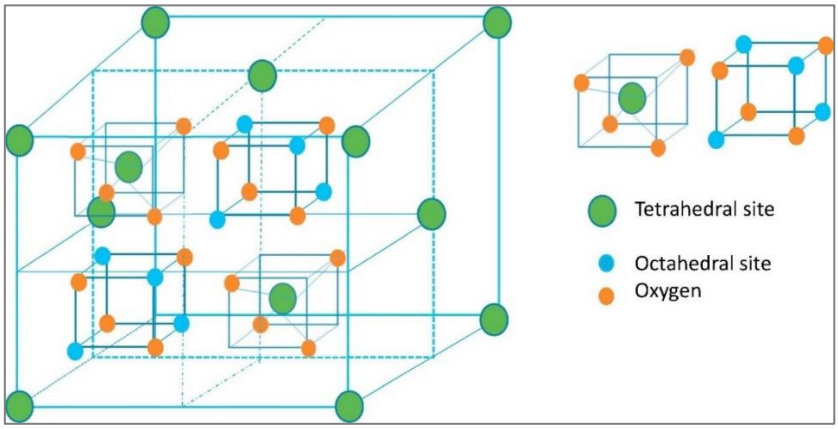

Fig. 1.5. Unit cell structure of spinel ferrite showing tetrahedral and octahedral sites [88].

1.2.1.2. Synthesis of spinel ferrite nanoparticles

The spinel nanoparticles can be synthesized using various methods. The most commonly used methods are solid state [89], co-precipitation [91-96], sol-gel [97-99], microemulsion [100,101], solvo(hydro)thermal method [102-104] and template method [105,106]. In this study, co-precipitation was used for the synthesis of $MnFe_2O_4$, hence it is discussed.

Co-precipitation method is highly a convenient, quick and economically viable method. Co-precipitation method generates particles of uniform size and it is easy to control the morphology of the particles using this method [92]. This method encompasses the mixing metal salts with the desired stoichiometric amounts followed by vigorous stirring in alkaline environment. During co-precipitation, the solution pH plays a crucial role. Spinel ferrites $MnFe_2O_4$ [93], $MgFe_2O_4$ [94], $CoFe_2O_4$ [95] and $CuFe_2O_4$ [96] have been synthesized by co-precipitation.

1.2.1.3. Spinel ferrites nanoparticles in photocatalytic processes

Spinel ferrites nanoparticles have been utilized in photocatalytic degradation of the organic pollutants owing to their catalytic activity, non-toxicity, chemical stability, facile recovery due to their magnetic property and re-usability without the loss of the catalytic activity [107]. However, the catalytic activity of these materials is far from the required merit. Various strategies have been employed over the past years to improve their catalytic activity [108].

These strategies involve dye sensitization with organic dyes to extend light absorption towards visible region of the spectrum [109], fabrication of the composites with other semiconductors and using two or more processes such as photo-Fenton catalytic process [107], photo-electro-catalytic process [110] etc.

To my best knowledge, there is no literature report on spinel nanoparticles based sono or photosono-catalytic processes reported so far. Hence, photosono-catalytic efficiency of these materials in degradation of Rhodamine 6G are studied in this thesis.

The spinel nanoparticles studied in this work are $MnFe_2O_4$. These materials were first conjugated with phthalocyanine to extend their absorption efficiency in the visible

region of the spectrum. The conjugates were then utilized to functionalize electrospun nanofibers. The Pcs and porphyrins together with their nanoparticles and nanofibers utilized in this work are listed in **Table 1.1**.

1.2.2. Graphitic carbon nitride (g-C_3N_4)

Graphitic carbon nitride (g-C_3N_4) has attracted tremendous interest in photocatalysis [111]. g-C_3N_4 can occur as either of the two main units which are tris-s-triazine and s-triazine (**Figure 1.6**) [112,113]. Using density functional theory (DFT) it has been shown that s-triazine is most thermodynamically stable form of g-C_3N_4. Due to its unprecedented degree of condensation and heptazine ring structure, g-C_3N_4 possess numerous advantages such as unique electronic structure, high physicochemical stability and medium band gap energy (2.7 eV) [111]. These properties make g-C_3N_4 a promising future catalyst for light driven catalytic processes. In addition, g-C_3N_4 can be easily prepared by polymeric condensation of a cheap precursor such as urea, melamine, cyanamide, thiourea and dicyanimide [112].

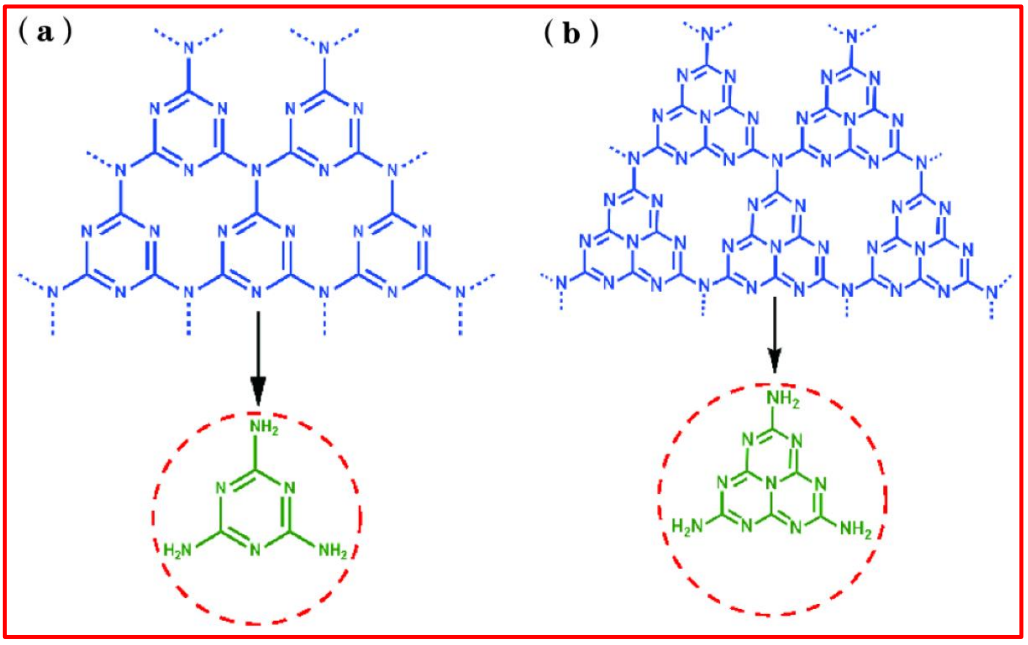

Fig.1.6. structures of (a) s-triazine and (b) tris-s-triazine [113]

1.2.2.1. Electronic structure of g-C_3N_4

g-C_3N_4 contains sp^2 hybridized nitrogen and carbon bonding forming a high density of π-conjugated system. It is the lone pair of the nitrogen that plays an important role in the electronic structure of g-C_3N_4 [114,115]. g-C_3N_4 is an n-type semiconductor. g-C_3N_4 can occur in various morphologies such as bulk [116,117], nanotubes [118,119], quantum dots [120,121] and nanosheets [117-122].

Bulk g-C_3N_4 possess a 0D structure. Due to stacking of the layer, bulk g-C_3N_4 has significantly low surface area, rapid recombination of the photo-generated electron-hole pairs and very poor quantum yield [123]. Various strategies have been adopted to combat these short-comings. These encompasses dye sensitization, fabrication of the nanotubes [118,119], quantum dots [120] and nanosheets [122]. Doping and forming hybrid nanocomposites with other semiconductors has also been adopted [116].

Nanotubes are 1D tubular/hollow structured g-C_3N_4. This material exhibits large surface area, enhanced visible light absorption efficiency, efficient separation of the electron-hole pairs and fast electron transport compared to bulk g-C_3N_4 [118]. The g-C_3N_4 nanotubes are often prepared using soft, hard and self-template methods. During hard template method, the g-C_3N_4 interact with an appropriate template of desired morphology under pyrolysis. Afterwards, template is removed and the g-C_3N_4 gains an opposite replica structure of the template. The surfactants are utilized in soft-template. The precursor is mixed with the surfactant under pyrolysis. The g-C_3N_4 with the desired morphology is achieved. In self-template method, there is no surfactant that is used. Instead, the desired morphology is achieved by changing the reaction conditions such as pH and temperature [119].

Quantum dots (g-C_3N_4 QDs) have 0D dimensional structure. These materials have gained significant attention in various processes because of their chemical stability, large surface area, high fluorescence and biocompatibility [120]. Various methods such as hydrothermal, sonication, microwave and chemical vapour deposition (CVD) have been used to synthesize g-C_3N_4 QDs. Among these, hydrothermal method has been widely used because it is straight forward [121] and is employed in this work.

Nanosheets (g-C_3N_4 NS) are unlike the bulk g-C_3N_4 in that they display high surface area and enhanced separation of the photo-generated electron-hole pairs. An enhanced electron-hole pair separation is attributed to their 2D structure due to high charge mobility. These materials can be fabricated by separating the layers of the bulk g-C_3N_4. This is achieved by breaking weak Van der Waals forces between carbon and nitrogen [122]. g-C_3N_4 NS and g-C_3N_4 QDs were used in this work.

1.2.2.2. Application of g-C_3N_4 in photosono-catalytic processes

Due to their physicochemical stability, appealing electronic properties and medium band gap, g-C_3N_4 nanoparticles have been used in photosono-catalytic process [123]. However, pristine g-C_3N_4 NPs suffer from drawbacks such as low visible harvesting efficiency and rapid recombination of photo-generated electron–hole pairs [124]. Dependable and facile strategies have been explored to fabricate modified g-C_3N_4 with enhanced properties. Such strategies include doping [125,126], dye sensitization [127] and hybridization with other semiconductors [128,129]. g-C_3N_4 have been sensitized with both porphyrin [130,131] and phthalocyanine [132] in photo-degradation of organic pollutants. However, there is not much studies on sono-catalysis. Doped g-C_3N_4 have also been reported in both photo and sono-catalytic studies [133,134]. The hybrids of g-C_3N_4 with other semiconductor materials have

been extensively studied in photo-, sono- and photosono-catalytic degradation of organic pollutants [123, 135,136].

In this work, g-C_3N_4 nanosheets were conjugated with complexes **3**, **4**, **5, 6** and **7** by means of an amide bond. The effect of conjugation is synergistic. The Pc and porphyrin complexes extend light absorption of the g-C_3N_4 towards visible light regions, on the other hand, g-C_3N_4 facilitate charge migration and separation in Pc and porphyrin complexes. All the conjugates synthesized were, for the first time used to functionalize electrospun nanofibers. Hence, following section discusses background, synthesis, functionalization and photocatalytic applications of the electrospun nanofibers.

1.3. Electrospun fibers

Electrospun nanofibers have been used as supports for photocatalysts in various applications. Electrospun nanofibers possess tremendous additional properties such as 3D open hierarchical structure, high surface area and large pores [137-139].

1.3.1. The principle of electrospinning

Electrospinning method is an electrodynamic process, which involves electrification of the liquid droplet by the high voltage to produce a jet [140]. The produced jet subsequently elongate and stretches to generate the fibers. The basic electrospinning setup is displayed in **Figure 1.7**. The setup has four major components which are: Syringe equipped with a needle, syringe pump, high voltage power supply and a metal collector (such as aluminum foil). During the electrospinning process, a small amount of viscous liquid is extruded from the syringe through the tip of the needle by syringe pump. Due to surface tension, the viscous liquid form pendant spherical droplets. When these droplets are subjected to large potential (voltage), they deform into conical

shape due to the electrostatic repulsion between charges of the same sign (+). This phenomenon results in the formation of a jet. The diameter of the jet continues to decrease due to electrostatic repulsion. Eventually, the jet starts to twist or curve, while simultaneously undergoing solidification resulting in deposition of the solid fiber(s) on the collector [141,142]. Electrospinning process most often utilizes polymer material such as poly(vinyl alcohol) (PVA), polyvinylpyrrolidone (PVP) and polyvinylidene fluoride (PVDF) to increase the viscosity of the solution. Upon deposition, the polymer can be sacrificed by thermal treatment at elevated temperatures [143,144].

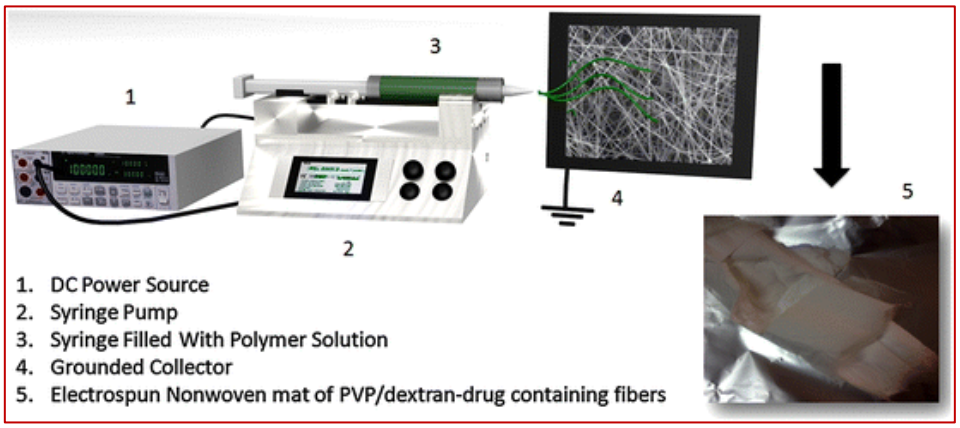

Fig. 1.7. Electrospinning set up [144].

1.3.2. Methods of enhancing efficiency of electrospun nanofibers

Even though semiconductor materials containing electrospun nanofibers have good photocatalytic properties, their photocatalytic efficiency is still not good enough due to low visible light quantum efficiency or ultrafast electron-hole recombination efficiency [145]. There are various ways in which the photo- and sono-catalytic efficiencies of the semiconductor containing electrospun nanofibers can be enhanced. These strategies include doping [146], dye sensitization [147] and hybridization (composites with a co-catalysts) to form heterostructures [148].

1.3.2.1. Doping

Doping is one of the most common strategies often utilized to fabricate heterostructures of the electrospun nanofibers. Heterostructures fabricated by doping often display high density of vacant sites and enhanced optoelectrical properties [149]. Doping results to the formation of the composite with enhanced charge separation, improved light absorption properties and charge trapping by vacant sites. The enhanced light harvesting properties of the doped semiconductor materials emanate from reduced band gap and a new energy level (induced energy state) from defect sites [150].

1.3.2.2. Sensitization of the fibers

Dye sensitization is one of the strategies often used to extend the absorption range of the semiconductor containing electrospun nanofibers to the visible light region of the spectrum. Dye sensitizers can efficiently absorb visible light and significantly enhance the activity by providing extended energy to the semiconductor. Typically, in a system that involves the combination of semiconductor and dyes, the semiconductor act as carriers of the charges generated by dye. The most commonly utilized dyes as sensitizers can be categorized as metal complexes [151] and organic dyes [152]. The metal complexes are known electron injectors, increasing the density of electrons in the conduction band of the semiconductors [153].

1.3.2.3. Hybridization of the semiconductor in fibers with other semiconductors

Electrospun nanofibers can be hybridized with other semiconductors as co-catalysts to form heterostructures with improved properties [154]. The role of the co-catalyst is usually to enhance visible light harvesting ability of the fibers, promoting charge

separation or both. Semiconductors such as, metal oxides, metal sulphides [137], graphitic materials, bimetallic metal oxides [155] have been used.

1.3.3. Applications of semiconductor containing electrospun nanofibers in photo-, sono-, photosono-catalytic degradation of organic pollutants

The degradation of organic pollutants using semiconductor containing electrospun nanofibers have been studied and some are listed in **Table 1.4** [156-164]. The photocatalytic degradation of Rhodamine 6G has been studied using polyacrylonitrile@titanium carbide@silver-silver sulphide (PAN/MXene@Ag–Ag_2S) nanofibers [156]. The study offers the possibility of eco-friendly and efficient methods for degradation of Rhodamine 6G in wastewater. To my best knowledge, there is only one study that has been reported on photo-catalytic degradation of Rhodamine 6G using semiconductor containing electrospun nanofibers [156] and there are no studies reported on sono- and photosono-catalytic degradation processes. There are no studies reported for photo-, sono- and photosono-catalytic degradation of dichlorophenol using semiconductor containing electrospun nanofibers. The degradation of other semiconductors such as tetracycline have been reported [157].

The photo-, sono- and photosono-catalytic degradation of other organic dyes such as Rhodamine B [158,159], polycyclic aromatic hydrocarbon [160] and Bisphenol A [161] have also been reported. Some of the photo-, sono- and photosono-catalytic degradation of various organic pollutants using semiconductor containing electrospun nanofibers are listed in **Table 1.4** [156, 157, 162-164].

Table 1.4. Photo-, sono- and photosono-catalytic degradation of various organic pollutants using semiconductor containing electrospun nanofibers.

Process	Nanofiber composites	Organic pollutant	Degradation efficiency (%)	Reference
Photo	Polyacrylonitrile@titanium carbide@silver-silver sulphide (PAN/MXene@Ag–Ag_2S) nanofibers	Rhodamine B and Rhodamine 6G	Both 100	[156]
Sono	Zirconium metal organic framework decorated Tin oxide nanofibers (SnO_2 PHNF/UiO-66-NH_2 nanofibers)	tetracycline	98	[157]
Photosono	Polyacrylonitrile/graphitic carbon nitride/cadmium sulphide nanofibers (PAN/g-C_3N_4/CdS Nanofibers)	Rhodamine B	92	[159]
Photo	Titanium dioxide@silver@copper oxide (TiO_2@Ag@Cu_2O nanofibers)	Methylene blue	99	[162]

Sono	Polyacrylonitrile/ β-cyclodextrin nanofibrous membranes/Titanium dioxide/graphene oxide nanofibers (PAN/β-CD/TiO_2/GO nanofiber)	methyl orange (MO) and methylene blue (MB)	94 and 91	[163]
Photosono	Barium titanate@titanium dioxide core-shell nanofibers ($BaTiO_3$@TiO_2 nanofibers)	Methyl Orange (MO)	99	[164]

1.4. The trends followed in this work

1.4.1. Pcs and porphyrin

- Complexes **1** and **2** were studied to compare the the effect of the number of oxygen atoms on the photophysical properties and photocatalytic activity
- Complexes **3** and **5** were studied to compare the number of the oxygen groups
- Complexes **4** and **6** were studied to compare the number of the oxygen groups.
- Complexes **1** and **5** were studied to compare the symmetry.
- Complexes **3**, **4** and **7** were studied to compare the efficiency in degradation of Rhodamine 6G and dichlorophenol (DCP).

1.4.2. Nanoparticles and nanofibers

- Covalently conjugated g-C_3N_4 NS and complexes **3**, **4**, **5** and **6** supported on TiO_2 fibers were studied to compare the amide bond and the number of the oxygen atoms.
- Complex **6** supported on TiO_2 fibers and ZnO fibers were studied to compare the effect of TiO_2 fibers and ZnO fibers.
- The conjugates of complex **5** with g-C_3N_4 nanosheets and $MnFe_2O_4$ NPs when supported to TiO_2 fibers were studied to compare the effect g-C_3N_4 nanosheets and $MnFe_2O_4$ NPs.
- The conjugate of the complex **3**, **4** and **7** and g-C_3N_4 QDs when supported in TiO_2 fibers were compared in degradation of Rhodamine 6G and dichlorophenol (DCP).
- The conjugates of g-C_3N_4 NS and complexes **3** and **4** supported on TiO_2 fibers and the conjugates of g-C_3N_4 QDs and complexes **3** and **4** were studied in degradation of Rhodamine 6G to study the effect of the nanoparticles.

1.5. Aims of the study

This work reports on the design of the phthalocyanine and porphyrin composites for degradation of organic pollutants in water. The list of the specific aims encompasses:

- Synthesis of the phthalocyanines (**3**, **4**, **6** and **7**) and porphyrin (**7**).
- Synthesis of the polymer free TiO_2 and ZnO nanofibers.
- Synthesis of g-C_3N_4 quantum dots and g-C_3N_4 nanosheets.
- Synthesis of $MnFe_2O_4$ nanoparticles
- Conjugation of the phthalocyanines (**3**-**6**) with g-C_3N_4 nanosheets.
- Conjugation of the phthalocyanines (**3**, **4**) and porphyrin (**7**) with g-C_3N_4 quantum dots.
- Conjugation of the phthalocyanine (**5**) with $MnFe_2O_4$ nanoparticles.
- Characterization of the phthalocyanines, porphyrin, nanoparticles and conjugates.
- Functionalization of TiO_2 nanofibers with phthalocyanines (**1**-**6**), porphyrin (**7**), nanoparticles (g-C_3N_4 quantum dots, g-C_3N_4 nanosheets and $MnFe_2O_4$ nanoparticles) and conjugates (**3**@g-C_3N_4 NS, **4**@g-C_3N_4 NS, **5**@g-C_3N_4 NS, **6**@g-C_3N_4 NS, **3**@g-C_3N_4 QDs, **4**@g-C_3N_4 QDs, **7**@g-C_3N_4 QDs and **5**@ $MnFe_2O_4$ NPs)
- Functionalization of the ZnO nanofibers with phthalocyanines (**5**), nanoparticles (g-C_3N_4 NS) and conjugate (**5**@g-C_3N_4 NS).
- Characterization of pristine and functionalized nanofibers.
- Comparison of the photocatalytic activities of phthalocyanines (**3** and **4**), porphyrin (**7**), functionalized fibers (**3**-TiO_2 fibers, **4**-TiO_2 fibers, **7**-TiO_2 fibers, **3**@g-C_3N_4 QDs-TiO_2 fibers, **4**@g-C_3N_4 QDs-TiO_2 fibers and **7**@g-C_3N_4 QDs-TiO_2 fibers) in degradation of dichlorophenol and Rhodamine 6G.

- Comparison of the photocatalytic, sonocatalytic and photosono-catalytic activities of the phthalocyanines (**1**-**6**), pristine fibers (TiO_2 and ZnO fibers), conjugate (**5**@ $MnFe_2O_4$ NPs), functionalized fibers (**1**-TiO_2 fibers, **2**-TiO_2 fibers, **3**-TiO_2 fibers, **4**-TiO_2 fibers, **5**-TiO_2 fibers, **6**-TiO_2 fibers, **1**@g-C_3N_4 NS-TiO_2 fibers, **2**@g-C_3N_4 NS-TiO_2 fibers, **3**@g-C_3N_4 NS-TiO_2 fibers, **4**@g-C_3N_4 NS-TiO_2 fibers, **5**@g-C_3N_4 NS-TiO_2 fibers, **6**@g-C_3N_4 NS-TiO_2 fibers) in degradation of Rhodamine 6G.

Chapter two

This chapter discusses the materials, equipment and methods utilized in this work.

2.1. Chemical reagents

2.1.1. Solvents

Tetrahydrofuran (THF, Merck), dimethyl sulfoxide (DMSO, Merck), Deuterated dimethyl sulfoxide (DMSO-d6), ethanol, methanol (MeOH, Merck), dimethylformamide (DMF, Merck), cyclohexane, glacial acetic acid (AA, Minema Chemicals), Ultra-pure water was obtained from the ELGA, Veolia water PURELAB, flex system,

2.1.2. Reagents for synthesis of the phthalocyanines, nanoparticles, nanofibers and conjugates

3-Aminopropyltriethoxysilane (APTES, Sigma), 1,8-diazobicyclo [5.4.0] undec-7-ene (DBU, Merck), polyvinylpyrrolidone (PVP, Merck), 1-ethyl-3-(3-dimethylaminopropyl)carbodiimide (EDC, Sigma), N, N′-dicyclohexylcarbodiimide (DCC, Sigma), pentanol (Merck), titanium (IV) propoxide (Sigma), zinc acetate dihydrate ($Zn(CH_3CO_2)_2$, Sigma), sodium hydroxide (NaOH, Sigma), manganese chloride pentahydrate ($MnCl_2.5H_2O$, Merck), iron chloride hexahydrate ($FeCl_2.6H_2O$), urea (Sigma), chitosan polymer (Sigma) and glutaraldehyde (Sigma), diaminomalonitrile (DAMN, Sigma), Ethylenediaminetetraacetic acid (EDTA, Sigma). The synthesis of 4-methoxyphenoxyphthalonitrile (complex **A**) [165], 4-(4-carboxyphenoxy)-phthalonitrile (complex **B**) [166], 5-phenoxylpicolinic acid phthalonitrile (**C**) [167] and 4-(3,5-dimethoxyphenoxy) phthalonitrile (**D**) [168] have been reported.

2.1.3. Reagents for photophysical studies and other characterization techniques

Anthracene-9,10-diyl-bis-methylmalonate (ADMA, Sigma), 9,10-dimethylanthracene (DMA), 1,3-diphenylisobenzofuran (DPBF, Sigma), 2,2,6,6-tetramethylpiperidone

(TEMPO, Sigma), Ludox solution (Sigma), 5,5-dimethyl-1-pyrroline N-oxide (DMPO, Sigma), unsubstituted zinc phthalocyanine (ZnPc) standard, quinine sulphate (Fluka), alpha-cyano-4-hydroxycinnamic acid (Merck) and zinc tertaphenylporphyrin (ZnTPP).

2.1.4. Reagents for photocatalytic applications

Peroxymonosulfate (PMS, Sigma), furfuryl alcohol (FFA, Sigma), 4-benzoquinone (BQ, Sigma), *tert*-butyl alcohol (TBA, Merck), humic acid (HA, Merck), Rhodamine 6G, azo-bis-isobutyronitrile (AINB, Aldrich), *tert*-butyl hydrogen peroxide (TBHP, Aldrich), water supplied by ELGA and Rhodamine 6G.

2.2. Equipment

1. Mass spectra were obtained using Bruker AutoFLEX III Smart-beam MALDI TOF/TOF mass spectrometer. α-Cyano-4-hydrocinnamic acid was used as matrix in the positive ion mode.
2. Elemental analyses data were collected from a Vario-Elementar® Microcube ELIII CHNS instrument analyser.
3. Solid state UV-vis spectra were acquired using Perkin-Elmer Lambda 950 UV-vis spectrophotometer.
4. Proton nuclear magnetic resonance (^{1}H NMR) spectra were recorded with Bruker F8 Fourier EduLab, Benchtop FT-NMR.
5. The ultraviolet–visible absorption spectra in solution were recorded using Shimadzu UV-2550 spectrometer.
6. The fluorescence emissions and excitations were using Varian Eclipse spectrofluorometer and 1 cm pathlength quartz cuvette. For all the studies, emission wavelengths were used to acquire excitation spectra.

7. The fluorescence lifetimes were recorded with Time correlation single photon counting (TCSPC) equipped with a Picoquant GmbH containing a LDH-P-670 diode laser with a 44 ps pulse width and 20 MHz rate repetition (**Fig. 2.1**).

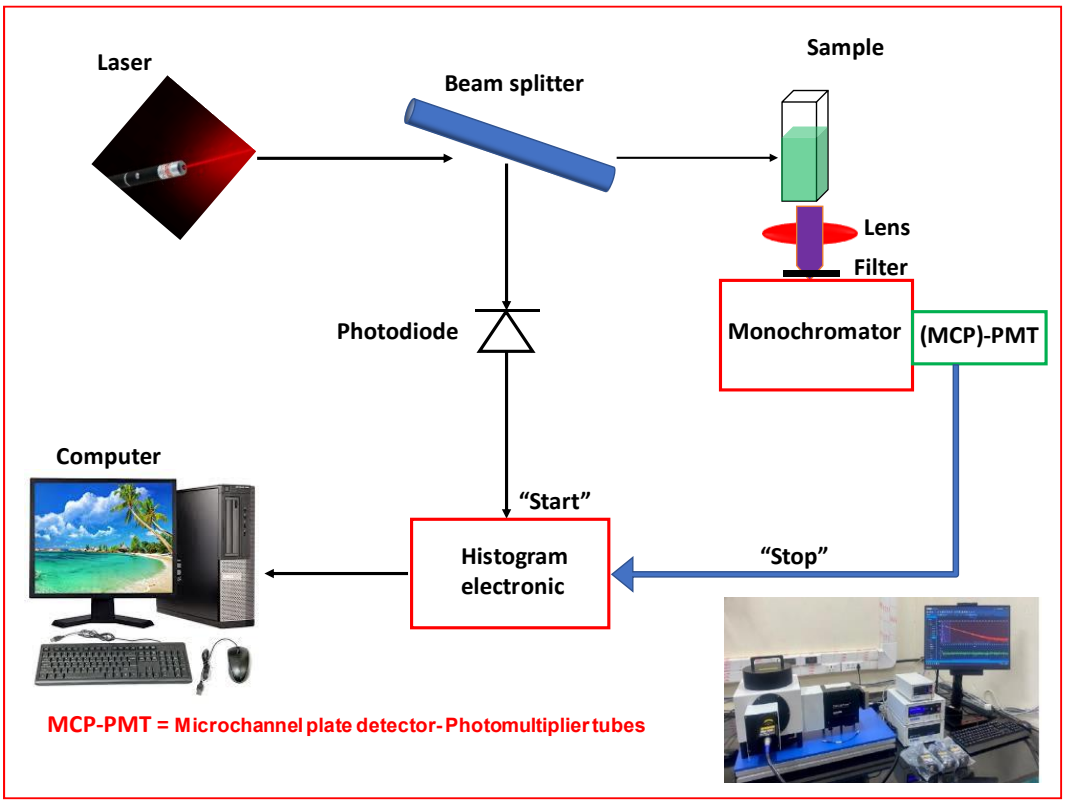

Fig. 2.1. TCSPC set up.

8. The triplet state parameters (triplet quantum yield (Φ_T) and triplet lifetimes (τ_T) were studied with LP980 spectrometer laser flash photolysis equipped with PMT-LP detector and ICCD camera (Andor DH320T-25F03). (**Fig. 2.2**) The signal from the detector was recorded on a Tektronix TDS3012C digital storage oscilloscope. The excitation pulses were produced using a tuneable laser system consisting of an Nd:YAG laser (355 nm, 135 mJ/4–6 ns) pumping an optical parametric oscillator (OPO, 30 mJ/3–5 ns) with a wavelength range of 420–2300 nm (NT-342B, Ekspla). Unsubstituted ZnPc was used as standard. The solutions of the sample and the standard were diluted to an extent that the absorptions of the Q-bands were ~1.5. Argon was used to deaerate samples. Subsequently, the solutions were irradiated

with appropriate excitation wavelength. The wavelength at the crossover of the Q bands of the sample and the standard was used. The triplet lifetimes were obtained by exponential fitting of the kinetic curves using OriginPro 8 software.

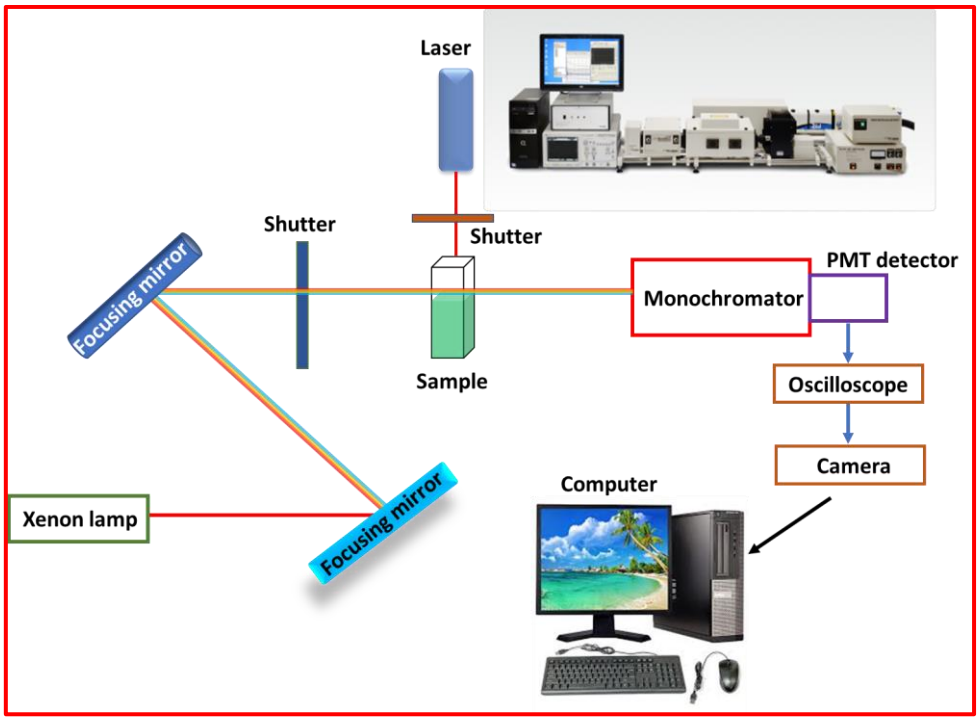

Fig. 2.2. Laser flash photolysis setup

9. Singlet oxygen quantum yield (ϕ_Δ) was determined using halogen lamp (**Fig. 2.3**).

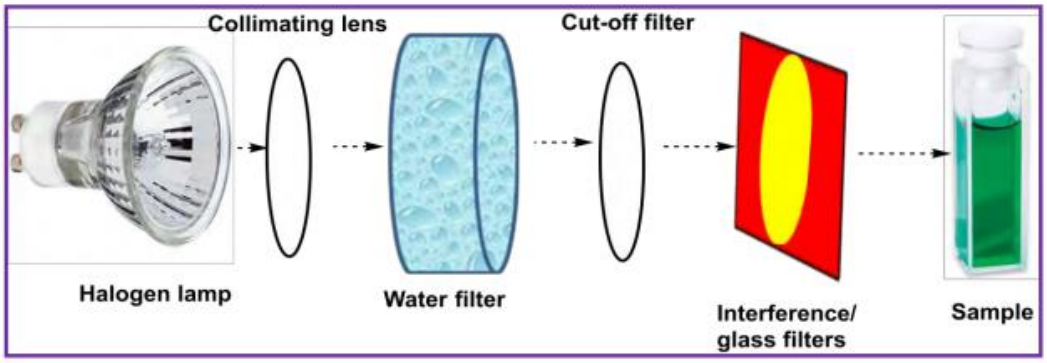

Fig. 2.3. Halogen lamp setup

10. The X-ray diffraction (XRD) spectra were acquired with Bruker D8 diffractometer, equipped with Lynx Eye detector at 2θ range of 10° to 90° at 0.5° per minute.

Samples were placed on a zero-background silicon wafer slide. The X-ray diffraction data was processes using Eva (evaluation curve fitting) software.

11. The Raman spectra were obtained using Bruker Vertex 70-Ram II Raman spectrometer (equipped with a 1064 nm Nd:YAG laser and liquid nitrogen cooled germanium detector).
12. Calcination of all of the nanofibers was conducted using Labotec Precision Furnace (SNOL 3/1100).
13. Electrochemical impedance spectroscopy (EIS) studies were performed with Autolab potentiostat PGSTAT30 equipped with Nova software version 2.1. For EIS measurements were performed between 1 Hz and 10 KHz using a 5 mV rms sinusoidal modulation. The glassy carbon electrode (GCE) was utilized as a working electrode, platinum wire as a counter electrode and silver/silver chloride (3M KCl) as the reference electrode. The catalyst (5 mg) was dispersed in DMSO (2 mL,) to form a homogeneous suspension. 10 µL of the mixture was dropped onto the surface of the working electrode and dried overnight at room temperature. Mott-Schottky measurements were performed using the AC electrochemical impedance method with an AC amplitude of 10 mV at an applied frequency of 1000 Hz at pH 3.
14. X-ray photoelectron spectroscopy (XPS) data was acquired using Kratos Axis Ultra DLD, with an Al (monochromatic) anode, equipped with charge neutralizer. The operational pressure was maintained below 5 x 10^{-9} torr. The resolution was 10 eV pass energy. For XPS wide scan the anode voltage was kept at 15 kV, emission current was maintained at 12.5 mA and the resolution was maintained at 160 eV. The resolution was kept at 40 eV pass energy for higher resolution.

15. The scanning electron microscopy (SEM) images were acquired with JOEL JSM scanning electron microscope (SEM) at an accelerating voltage of 20 kV.
16. The thermal stabilities were examined using Perkin Elmer TGA 8000 instrument, at temperature range of 100-1000 °C. The analyses were initiated by maintaining the temperature at 100 °C for 10 min for removal of moisture under air at 20 mL/min.
17. Electron paramagnetic resonance (EPR) measurements were carried out using the Bruker EMX Plus EPR spectrometer, specifications: model number: EMP-9.5/12B/P. set at 0.632 mW for the microwave power, frequency 9.714 GHz, resolution 2048 points, at centerfield of 3500 and 200 G for the sweep width and time constant of 5.12 for the singlet oxygen, hydroxide and sulfate radicals determination, using TEMPO and DMPO as the quenchers, respectively.
18. A Metrohm Swiss 827 pH meter was used for all pH measurements.
19. Electrostatic potential (ESP) surfaces were mapped onto total electron density isosurfaces at 0.0004 a.u. with Gaussview at the B3LYP/6-31G(d) level of theory to visualize the predicted charge distribution across Pc complexes.
20. Photocatalytic degradation studies done by using Modulight® Medical Laser system (MLS) 7710 channel Turnkey laser system connected to a 2.3 W channel at 680 nm.
21. The ENRAF NONIUS Sonopuls 490B ultrasound medical was used for ultrasound irradiations. Specifications: (ref no.: 1630.905, FREQUS – 1/3 MHz, INTUS – 0-2 W cm^2 continuous, ERAUS-Applicator – 5 cm^2, POWER – 15 W, IPX7).
22. The degradation was constantly monitored using Shimadzu UV-2550 spectrometer.

2.3. Syntheses

2.3.1. Syntheses of the phthalocyanines (Pcs) complexes

As it has already been stated in Table. 1.1, the Pcs **1** [70], **2** [71] and **5** [70] have already been reported before. The synthesis of the Pcs **3**,**4**, **6** and **7** is discussed here.

Synthesis of *z*inc(II)-4-(carboxylic acid phenoxy)-tris-(1,4-methoxyphenoxy) phthalocyanine (3).

Zinc(II)-4-(carboxylic acid phenoxy)-tris-(1,4-methoxyphenoxy) phthalocyanine (**3**) (**Scheme 3.1)** was synthesized by reacting 4-methoxyphenoxyphthalonitrile (complex **A**) (235 mg, 0.943 mmol) and 4-(4-carboxyphenoxy)-phthalonitrile (complex **B**) (747 mg, 2.83 mmol) in boiling pentanol (10 mL). Subsequently, zinc acetate dihydrate (363 mg, 1.98 mmol) was added, followed by the dropwise addition of DBU under vigorous stirring. The mixture was refluxed for 6 h and the product was centrifuged in methanol. Afterwards, the crude product was washed with ethanol for five times. Zinc(II)-4-(carboxylic acid phenoxy)-tris-(1,4-methoxyphenoxy) phthalocyanine (**3**) was purified with 5:1 v/v THF/cyclohexane.

Complex 3: Yield = 36%, UV/Vis (DMF) λ_{max}, nm (log ε): 684 (4.39), 339 (3.73). MALDI-TOF-MS(m/z): Calc = 1128.50 amu, found =1127.90 amu [M+H]; Anal. Calc. for $C_{63}H_{50}N_8O_9$: C, 67.05 %; H, 4.47 %; N, 9.93 %. Found: C, 66.97 %; H, 4.53 %; N, 9.96 %^{1}H NMR (400 MHz, DMSO-d_6): δ, ppm 3.74 (s, 9H, CH_3), 6.39 (m, 8H, Ar), 6.49 (t, 4H, Ar), 6.64 (s, 3H, Ar), 6.93 (d, 2H, Ar), 7.29 (d, 3H, Ar), 7.36 (dd, 4H, Ar), 7.87 (d, 4H, Ar), 11.30 (s, 1H, COOH).

Synthesis of *zinc(II)*-4-(Picolinic acid phenoxy)-tris-(1,4-methoxyphenoxy) phthalocyanine (4).

Zinc(II)-4-picolinic acid phenoxy)-tris-(1,4-methoxyphenoxy) phthalocyanine (**4**) (**Scheme 3.2)** was synthesized by reacting 4-methoxyphenoxyphthalonitrile (complex **A**) (235 mg, 0.943 mmol) and 5-phenoxylpicolinic acid phthalonitrile (compound **C**) (750 mg, 2.83 mmol) in boiling pentanol (10 mL). Zinc acetate dihydrate (363 mg, 1.98 mmol) was subsequently added, followed by the dropwise addition of DBU under vigorous stirring. The mixture was then refluxed for 6 h and the product was centrifuged in methanol. The collected crude product was washed with ethanol for five times. The obtained mixtures of Pcs were separated by column chromatography on silica gel using gradient elution with 5:1 v/v THF/cyclohexane to give complex **4**.

Complex 4: Yield = 34%, UV/Vis (DMF) λ_{max}, nm (log ε): 689 (3.78), 345 (4.53). MALDI-TOF-MS(m/z): Calc = 1129.50 amu, found =1128.29 amu [M+H]; Anal. Calc. for $C_{62}H_{49}N_9O_9$: C, 66.76 %; H, 4.43 %; N, 10.05 %. Found: C, 66.82 %; H, 4.49 %; N, 10.09 %; ^{1}H NMR (400 MHz, DMSO-d_6): δ, ppm 3.80 (s, 9H, CH_3), 6.35 (s, 1H, Ar), 6.39 (d, 6H, Ar), 6.49 (t, 3H, Ar), 6.57 (d, 2H, Ar), 6.69 (m, 2H, Ar), 7.28 (m, 4H, Ar), 7.41 (m, 5H, Ar), 7.87 (m, 4H, Ar), 11.36 (s, 1H, COOH).

Zinc tris(1,3,5-dimethoxyphenoxy)-(5-phenoxylpicolinic acid) phthalocyanine (**6**)

The zinc tris(1,3,5-dimethoxyphenoxy)-(5-phenoxylpicolinic acid) phthalocyanine (**6**) (**Scheme 3.3)** was synthesized by reacting 5-phenoxylpicolinic acid phthalonitrile (compound **C**) and 4-(3,5-dimethoxyphenoxy)phthalonitrile (compound **D**) in a ratio of 1:3 using statistical condensation approach as follows: 4-(3,5-

dimethoxyphenoxy)phthalonitrile (compound **C**) (250 mg, 0.943 mmol) and 4-(3,5-dimethoxyphenoxy)phthalonitrile (compound **D)** (634 mg, 2.83 mmol) were mixed in boiling 1-pentanol (8 mL) followed by addition zinc acetate dihydrate (434 mg, 1.98 mmol). DBU was then added drop wise under vigorous stirring and the resulting mixture was refluxed for 6 h. The crude product was precipitated with methanol through centrifugation and washed 5 times with ethanol. Zinc tris(1,3,5-dimethoxyphenoxy)-(5-phenoxylpicolinic acid) phthalocyanine (**6**) was purified using THF/cyclohexane (5:1 v/v).

Complex 6: Yield = 37%. UV/Vis (DMF) λ_{max} (log ε): 673 (4.21), 607 (3.78), 336 (4.53). MALDI-TOF-MS(m/z): Calc = 1217.33 amu, found =1218.28 amu [M+H]; Anal. Calc. for $C_{65}H_{55}N_9O_{12}$: C, 64.1%; H, 4.55%; N, 10.34%. Found: C, 63.83%; H, 4.63%; N, 10.51%. ^{1}H NMR (400 MHz, DMSO-d_6): δ, ppm 4.50 (s, 18H, CH_3), 6.29 (s, 2H, Ar), 6.36 (d, 3H, Ar), 6.55 (s, 1H, Ar), 6.59 (d, 1H, Ar), 6.80 (d, 3H, Ar), 6.84 (d, 1H, Ar), 7.18 (d, 6H, Ar), 7.34 (d, 2H, Ar), 7.77 (d, 3H, Ar), 7.80 (d, 1H, Ar), 7.91 (d, 1H, Ar), 10.27 (s, 1H, COOH).

Zinc-5-p-carboxyphenyl-10,15,20-(tris-4-pyridyl)-porphyrin (7)

The synthesis of a free base porphyrin (5-p-carboxyphenyl-10,15,20-(tris-4-pyridyl)-porphyrin, **7a**) (**Scheme 3.4)** has been reported before [169]. Complex **7** was then synthesized by dissolving compound **7a** (300 mg, 0.451 mmol) in DMF (5 mL) followed by addition of zinc chloride hexahydrate (200 mg, 0.820 mmol). The mixture was refluxed under vigorous stirring while monitoring the reaction progress with UV-vis absorption spectroscopy. Metalation was confirmed by the collapse of the four Q bands of a free base porphyrin to two of the metallated derivative. The solution was then cooled to room temperature (25 ± 1 °C) before zinc-5-p-carboxyphenyl-10,15,20-

(tris-4-pyridyl)-porphyrin (**7**) was extracted by centrifugation in ethanol, followed by drying in a desiccator.

Complex **7**: Yield = 38%. V-Vis (DMF), λ_{max} nm (log ε): 417 (5.4), 568 (3.6), 609 (3.3). MALDI TOF-MS, calc 724.90 found 725.18 [M+H]. ^{1}H NMR (600 MHz, DMSO-d_6): δ, ppm 5.20-5.24 (d, 2H, pyrrole), 6.09-6.10 (d, 2H, pyrrole), 6.49-6.52 (d, 1H, pyrrole), 6.72-6.77 (d, 1H, pyrrole), 6.90-6.94 (d, 2H, pyrrole), 7.24-7.28 (d, 6H, pyridine), 7.51-7.55 (d, 2H, pyridine), 8.00-8.067 (d, 2H, pyridine), 8.82-8.87 (d, 6H, pyridine), 11.48 (s, 1H, COOH). Anal. Calcd for $C_{42}H_{25}N_7O_2Zn$: C (69.57), H (3.48), N (13.52). Found: C (68.94), H (4.13), N (13.42).

2.3.2 Synthesis of the nanoparticles

The synthesis of g-C_3N_4 quantum dots have been reported before [170]. Briefly, 1 g of diaminomaleonitrile, 0.5 g (1.34 mmol) EDTA and 1 M of NaOH were dissolved in 100 mL of Millipore water. The mixture was then stirred for 1 h to achive complete dispersion. The mixture was then heated at 200 °C in a Teflon-lined hydrothermal reactor for 3 h. After cooling to room temperature. The g-C_3N_4 QDs were filtered and washed with ethanol for five times.

Synthesis of graphitic carbon nitride nanosheets

The g-C_3N_4 nanosheets were synthesized by thermal polymerization of urea as reported in literature with a slight modification [171], **Scheme 3.5**. Typically, 10 g of urea was placed on a porcelain crucible. The crucible was heated to a temperature of 500 °C at a rate of 2 °C/min and maintained at this temperature for 5 h. Afterwards, a light-yellow powder (g-C_3N_4) was cooled down and collected.

Synthesis of spinel manganese ferrites ($MnFe_2O_4$)

Spinel manganese ferrites nanoparticles were synthesized using co-precipitation method as reported in literature with slight modification [172]. Typically, manganese chloride pentahydrate ($MnCl_2.5H_2O$, Merck), iron chloride hexahydrate ($FeCl_2.6H_2O$) were dissolved in 50 mL of 2% acetic acid with a molar ration of 1:2. Subsequently, chitosan polymer (as a coating), was added this solution. The resulting mixture was stirred at room temperature for 24 h. To induce co-precipitation and crosslinking of chitosan, NaOH (5 mL of 0.5 M) and glutaraldehyde (5 mL) were to the above solution. After stirring for 30 min the brown precipitate was collected through centrifuge in ethanol and dried in high vacuum hood.

2.3.3. Synthesis of the electrospun nanofibers

Synthesis of TiO_2 nanofibers

TiO_2 nanofibers were synthesized using electrospinning method already reported in literature [173,174]. Briefly, 10% PVP in ethanol (10 mL) was first prepared. To this solution, 10 mL of titanium (IV) propoxide and 5 mL of glacial acetic acid were added. The solution was magnetically stirred for 3 h. Afterwards, the resulting solution was loaded into a syringe equipped with a stainless-steel needle and connected to a high voltage power supply. An electric voltage of 12 kV was applied between the needle and the stationary aluminium foil collector with the distance between the tip of the needle and the collector being kept at 10 cm. The electrospinning was performed under these parameters: flow rate 1.5 mL h^{-1}; temperature 25.7 °C; humidity 52%. Aluminium foil was used as collector. The collected PVP/TiO_2 nanofibers at 450 °C at a heating rate of 2 °C min^{-1} for 3 h. The calcination process was performed to remove PVP polymer and give polymer free TiO_2 nanofibers.

Synthesis of ZnO nanofibers

ZnO nanofibers were also synthesized using the electrospinning method, already reported with slight modifications [173]. In this method, zinc acetate (2.0 g) was dissolved in a mixture of ethanol (15 mL) and dimethylformamide (DMF, 10 mL). The mixture was then magnetically stirred for 1 h. Subsequently, PVP (4.0 g) was added to the solution and the mixture was magnetically stirred overnight. The electrospinning was performed as stated above.

2.4. Conjugation of the Pcs and porphyrin with nanoparticles

2.4.1. Conjugation of 3, 4, 5 and 6 with g-C_3N_4 nanosheets, Scheme 3.6.

The conjugation of complexes **3**, **4**, **5** and **6** with g-C_3N_4 NS was achieved through an amide bond using DCC and EDC to activate the COOH group of the Pcs as follows: complexes **3** (50 mg, 0.049 mmol), **4** (50 mg, 0.048 mmol), **5** (50 mg, 0.044 mmol) and **6** (50 mg, 0.043 mmol) were dissolved in DMF (10 mL) in separate containers. DCC (50 mg, 0.242 mmol) and EDC (50 mg, 0.322 mmol) were added in each of the containers, then the mixtures were ultrasonicated for 30 min followed by magnetic stirring for 48 h at room temperature. Thereafter, g-C_3N_4 nanosheets (50 mg) were added followed by further stirring for 48 h at room temperature. The conjugates were then collected by centrifugation and labelled as **3**@g-C_3N_4 Ns, **4**@g-C_3N_4 Ns, **5**@g-C_3N_4 Ns and **6**@g-C_3N_4 Ns. Process is illustrated in **Scheme 3.6** using complex **6** as an example.

2.4.2. Conjugation of 3, 4 and 7 with g-C_3N_4 quantum dots, Scheme 3.7.

Conjugation of **3**, **4** and **7** with g-C_3N_4 QDs was carried out by dissolving complexes **3** (50 mg, 0.049 mmol), **4** (50 mg, 0.048 mmol) and **7** (50 mg, 0.069 mmol) in DMF (10 mL), followed by addition of DCC (50 mg, 0.242 mmol) and EDC (50 mg,

0.322 mmol) and ultrasonication for 1 h. Afterwards, the solution was left for 12 h under vigorous stirring. Then, g-C_3N_4 QDs (50 g) were added, followed by additional stirring for 12 h and centrifugation to collect the crude powder. The crude products were named **3**@g-C_3N_4 QDs, **4**@g-C_3N_4 QDs and **7**@g-C_3N_4 QDs. The crude products were then washed with ethanol five times. The process is illustrated in **Scheme 3.7** using complex **7** as an example.

2.4.3. Conjugation of Complex 5 with $MnFe_2O_4$ nanoparticles, Scheme 3.8.

The functionalization of nanoparticles with APTES was achieved as reported before [175]. Briefly, $MnFe_2O_4$ NPs (50 mg) and APTES (30 mg) were mixed in toluene and magnetically stirred at 100 ^oC for 24 h. The APTES functionalized NPs were retrieved by centrifuge in ethanol and dried in high vacuum fume hood. The sample was named $MnFe_2O_4$-APTES [175]. In a separate round bottom flask, the complex **5** (30 mg), N,N′-dicyclohexylcarbodiimide (DCC) (20 mg) and 1-ethyl-3-(3-dimethylaminopropyl) carbodiimide (EDC) (20 mg) were dissolved in dried DMF (3 mL). The mixture was stirred for 24 h, followed by the addition of $MnFe_2O_4$-APTES (30 mg), and stirring for a further 24 h. The resulting **5**@$MnFe_2O_4$ conjugate was retrieved by centrifuge in ethanol and washed five times with ethanol followed by drying in a vacuum fume hood overnight. The process is illustrated in **Scheme 3.8**.

2.5. Functionalization of the nanofibers with Pcs, porphyrin, nanoparticles and conjugates

2.5.1. Functionalization of the nanofibers with Pcs and porphyrin by adsorption, Scheme 4.1.

For functionalization of TiO_2 nanofibers, complexes **1**-**7** (30 mg) were dissolved in 5 mL of THF and stirred for 30 min. Complexes **1**, **2** and **7** were dissolved in THF, whereas

complexes **3**, **4**, **5** and **6** were dissolved in DMF. Subsequently, 50 mg of TiO_2 nanofibers were added and the mixtures were kept in closed containers in the dark for 24 h. The solvent was then evaporated under high vacuum fume hood overnight. The functionalized nanofibers were retrieved and washed with 2 mL ethanol and further dried in high vacuum fume hood for overnight. The functionalized TiO_2 fibers are represented as **1**-TiO_2 and **2**-TiO_2 fibers, **3**-TiO_2 fibers, **4**-TiO_2 fibers, **5**-TiO_2 fibers, **6**-TiO_2 fibers and **7**-TiO_2 fibers for **1**, **2**, **3**, **4**, **5**, **6** and **7**, respectively.

For the functionalization of ZnO fibers with **6**, the similar method used for the functionalization of TiO_2 nanofibers was used. Here, **6**-ZnO fibers were synthesized.

2.5.2. Functionalization of TiO_2 nanofibers with Pcs through conjugation, Scheme 4.2.

TiO_2 fibers were functionalized through conjugation with complexes **3**, **4**, **5** and **6**. 3-Aminopropyltriethoxysilane (APTES) was used as linker. TiO_2 nanofibers were first functionalized with APTES using a procedure reported in literature as follows [176]: APTES (30 mg) was dissolved in DMF and stirred overnight. Subsequently, 50 mg of TiO_2 fibers were added. The mixtures were left in the dark for 48 h. The solvent was then evaporated in a high vacuum. The resultant TiO_2 – fibers-APTES were washed with water three times and left in a fume hood overnight before use.

DCC (50 mg, 0.242 mmol) and EDC (50 mg, 0.322 mmol) were added in each of the solutions of complexes **3** (50 mg, 0.049 mmol), **4** (50 mg, 0.048 mmol), **5** (50 mg, 0.044 mmol) and **6** (50 mg, 0.043 mmol) dried DMF (2 mL). The mixtures were left to stir for 24 h. 50 mg of TiO_2 fibers-APTES were added and mixtures were left in the dark for 24 h. The solvent was evaporated by placing the fibers in a high vacuum fume hood overnight. The functionalized TiO_2 fibers were retrieved and

named **3**@TiO_2 fibers, **4**@TiO_2 fibers, **5**@TiO_2 fibers and **6**@TiO_2 fibers. The process is shown in **Scheme 4.2** using complex **6** as an example (@ was used for covalent bond throughout the thesis).

2.5.3. Functionalization of the nanofibers with nanoparticles

The functionalization of 50 mg of TiO_2 nanofibers with g-C_3N_4 quantum dots, g-C_3N_4 nanosheets, $MnFe_2O_4$ NPs were achieved by physical adsorption as follows: g-C_3N_4 quantum dots, g-C_3N_4 nanosheets, $MnFe_2O_4$ NPs (30 mg) each dissolved in 10 mL DMF and stirred overnight. Subsequently, 50 mg TiO_2 nanofibers were added and mixtures were left in the dark for 24 h. The solvent was evaporated by placing the fibers in a high vacuum fume hood overnight, to give g-C_3N_4 QDs-TiO_2 nanofibers, g-C_3N_4 NS -TiO_2 nanofibers and $MnFe_2O_4$ NPs-TiO_2 nanofibers. The functionalization of ZnO nanofibers with g-C_3N_4 NS was achieved the by the same procedure using ZnO nanofibers with g-C_3N_4 NS. The functionalized nanofibers were named as g-C_3N_4 NS-ZnO nanofibers.

2.5.4. Functionalization of the nanofibers with conjugates

TiO_2 nanofibers (50 mg) were functionalized with (30 mg) of **3**@g-C_3N_4 NS, **4**@g-C_3N_4 NS, **5**@g-C_3N_4 NS and **6**@g-C_3N_4 NS, **3**@g-C_3N_4 QDs, **4**@g-C_3N_4 QDs and **7**@g-C_3N_4 QDs and **5**@$MnFe_2O_4$. The conjugates were dissolved in DMF and stirred for overnight. Subsequently, TiO_2 nanofibers (50 mg) were added and the mixtures were left in the dark overnight. The solvent was evaporated by placing the fibers in a high vacuum fume hood overnight. The functionalized fibers were named **3**@g-C_3N_4 NS-TiO_2 nanofibers, **4**@g-C_3N_4 NS-TiO_2 nanofibers, **5**@g-C_3N_4 NS -TiO_2 nanofibers and **6**@g-C_3N_4 NS-TiO_2 nanofibers, **3**@g-C_3N_4 QDs-TiO_2 nanofibers, **4**@g-C_3N_4 QDs-TiO_2 nanofibers and **7**@g-C_3N_4 QDs-TiO_2 nanofibers and **5**@$MnFe_2O_4$-TiO_2 nanofibers.

The ZnO nanofibers were functionalized with **6**@g-C_3N_4 Ns using the same procedure. The functionalized nanofibers were named **6**@g-C_3N_4 NS-ZnO nanofibers.

2.6. Photophysical properties of the Pcs and conjugates

2.6.1. Fluorescence quantum yield (Φ_F) and fluorescence Lifetime (τ_f)

Φ_F is the ratio of the number of photons emitted via fluorescence to those absorbed. Φ_F can be determined using comparative method [177]. In this thesis, Φ_F was calculated using comparative methods reported in literature [177], **Eq. 2.1**.

$$\Phi_F = \Phi_F^{Std} \frac{F.A^{Std}.n^2}{F^{Std}.A.(n^{Std})^2} \qquad \textbf{2.1}$$

Where, Φ_F^{Std} and Φ_F are fluorescence quantum yields of the standard used, zinc-phthalocyanine (ZnPc) in DMSO (Φ_F^{std} = 0.20) [178], zinc-tetraporphyrin (ZnTPP) in DMSO (Φ_F^{std} = 0.039) [179] and quinine sulphate in 0.1 M H_2SO_4 (Φ_F^{std} = 0.5) [180] were used as standards for Pcs, porphyrin and g-C_3N_4 NPs, respectively. A^{Std} and A represent the absorbance of the standard and the sample at excitation wavelength, respectively. F^{Std} and F represent the areas of the fluorescence curves of the standard and the sample, respectively and n^{Std} and n represent the refractive indices of the solvents for the standard and samples, respectively.

The excitation and emission measurements were obtained using a 1 cm path length quartz cuvette. The absorbances were adjusted to ≤ 0.05 intensity using vibronic band and Soret band for Pcs and porphyrins, respectively. The τ_F of the Pcs and conjugates were studied using TCSPC analysis.

2.6.2. Triplet quantum yield (Φ_T) and triplet state lifetimes (τ_T)

The triplet quantum yields were determined in DMSO using a comparative method, and ZnPc as a standard in DMSO (Φ_T = 0.65) [181], using **Eq. 2.2**.

$$\Phi_T = \Phi_T^{std} \frac{\Delta A_T \, \varepsilon_T^{std}}{\Delta A_T^{std} \varepsilon_T} \qquad \textbf{2.2}$$

Where Φ_T^{std} is the triplet quantum yield of the standard, ΔA_T and ΔA_T^{std} are the changes in the triplet state absorbances of the sample and the standard, respectively, ε_T and ε_T^{std} are the triplet state molar extinction coefficients for the sample and the standard, respectively.

For τ_T and Φ_T measurements, the solutions (standard or sample) in 1 cm UV-Vis cuvette were first degassed using argon 15 min. Thereafter the solutions were sealed and irradiated with an appropriate excitation wavelength which was the crossover wavelength of the standard and the sample was ~623 nm. The absorbances of the Q-bands were maintained at ~1.5 intensity. The maximum triplet absorption wavelength was determined from the transient curve.

2.6.3. Singlet oxygen quantum yield (Φ_Δ)

Singlet oxygen quantum yields (Φ_Δ) of the Pcs, porphyrin and conjugates were studied using comparative method. The **Eq. 2.3** was used to calculate the Φ_Δ in DMSO.

$$\Phi_\Delta = \Phi_\Delta^{Std} \cdot \frac{\mathrm{B.I^{Std}}}{\mathrm{B^{Std}.I}} \qquad \textbf{2.3}$$

Where Φ_Δ^{std} is the singlet oxygen quantum yield of the standard; B and B^{Std} represent the singlet oxygen quencher DMSO photobleaching rates of the sample and the standard, respectively; I and I^{Std} represent the rates of light absorption by the sample and standard, respectively. 1,3-Diphenylisobenzofuran (DPBF) and dimethylanthracene (DMA) were used as the singlet oxygen quenchers for phthalocyanines and porphyrins, respectively. ZnPc (Φ_Δ^{std} = 0.67) and ZnTPP (Φ^{std} = 0.53) were used as standards in DMSO for Pcs and porphyrin, respectively [181].

For determination of the Φ_Δ of the functionalized nanofibers, the direct chemical method was used due to lack of the standards [182]. anthracene-9,10-diyl-bis-methylmalonate (ADMA) was used as a singlet oxygen quencher. The functionalized nanofibers were immersed in solution and irradiated. The extinction coefficient of ADMA (ε = 12589) [183] at 380 nm was used. **Eq. 2.4** was first used to calculate the quantum yield of ADMA (Φ_{ADMA}).

$$\Phi_{ADMA} = \frac{(C_O - C_t)\, V_R}{I_{Abs}.t} \qquad \textbf{2.4}$$

Where C_o and C_t represent the concentrations of ADMA before and after irradiation, respectively; V_R is the volume of the solution; t is the irradiation time per cycle and I_{Abs} is defined by **Eq. 2.5**.

$$I_{abs=\frac{\alpha AI}{N_A}} \qquad \textbf{2.5}$$

where $\alpha = I\text{-}I0^{-A(\lambda)}$, $A(\lambda)$ is the absorbance of the sensitizer at the irradiation wavelength, A is irradiated area (2.5 cm^2), I is the intensity of light (3.20×10^{16} photons cm^{-2} s^{-1}) and N_A is Avogadro's constant. The light measured refers to the light reaching the spectrophotometer cell, and it is expected that some of the light may be scattered, hence the values of the Pcs are estimates. Subsequently, the Φ_Δ values of the composites were calculated using **Eq. 2.6**:

$$\frac{1}{\Phi_{ADMA}} = \frac{1}{\Phi_\Delta}\left(1 + \frac{k_d}{k_a}.\frac{1}{[ADMA]}\right) \qquad \textbf{2.6}$$

Where K_a is the rate constant for the reaction of DMA with $^1O_2$ ($^1\Delta_g$), and K_d is the singlet oxygen decay constant.

2.7. Photosono-catalytic degradation studies

The photocatalytic degradation studies of Rhodamine 6G and dichlorophenol (5 mL of 6.63 x 10^{-5} M) were performed using Modulight® Medical Laser system (MLS) 7710-680 channel Turnkey laser system, **Fig 2.4**. The sonocatalytic studies were done using sonopuls sonicator at 2 MHz:1 $W.cm^{-1}$ frequency. Recently, the effect of the ultrasound on the stability of MPcs using the following ultrasonication parameters (frequency: power): (i) 1 MHz; 1 $W.cm^{-2}$; (ii) 1 MHz: 2 $W.cm^{-2}$; (iii) 3 MHz: 1 $W.cm^{-2}$ and (iv) 3 MHz: 2 $W.cm^{-2}$ had been studied. The parameter combination: 1 MHz: 1 $W.cm^{-2}$ showed minimal degradation of the Pc, and hence it is employed in this work [184]. The degradation studies were performed at pH 9 [185] for Rhodamine 6G and pH 5 for dichorophenol because the degrdatioin of these pollutants have been outlined to be efficient under these pH values [186]. The UV-vis spectral changes recorded during degradation of Rhodamine 6G at 525 nm [187] and dichlorophenol at 283 nm [188] and were used to evaluate degradations of Rhodamine 6G and dichlorophenol, respectively. The **Eq. 2.7** was used to calculate the degradation efficiency (%). The pH of the solution was adjusted using 0.1 M NaOH.

$$\textbf{Degradation efficiency}\ (\%) = \left(\frac{C_o - C_t}{C_o}\right) x\ 100 \qquad \textbf{2.7}$$

Where, C_o is the initial concentration of Rhodamine 6G, C_t is the concentration at time t during degradation. Irradiations were first performed in the absence of the catalysts. Subsequently, they were performed in the presence of the catalysts. Rate constants (k_{obs}) were obtained from slopes from kinetics plots. The following catalysts wereused in degradation of organic pollutants: phthalocyanines (**1**-**6**), pristine fibers (TiO_2 and ZnO fibers), conjugate (**5**@ $MnFe_2O_4$ NPs) and functionalized fibers (**1**-TiO_2 fibers, **2**-TiO_2 fibers, **3**-TiO_2 fibers, **4**-TiO_2 fibers, **5**-TiO_2 fibers, **6**-TiO_2 fibers, **1**@g-C_3N_4 NS-

TiO_2 fibers, **2**@g-C_3N_4 NS-TiO_2 fibers, **3**@g-C_3N_4 NS-TiO_2 fibers, **4**@g-C_3N_4 NS-TiO_2 fibers, **5**@g-C_3N_4 NS-TiO_2 fibers and **6**@g-C_3N_4 NS-TiO_2 fibers), porphyrin (**7**) and **7**@g-C_3N_4 QDs-TiO_2 fibers.

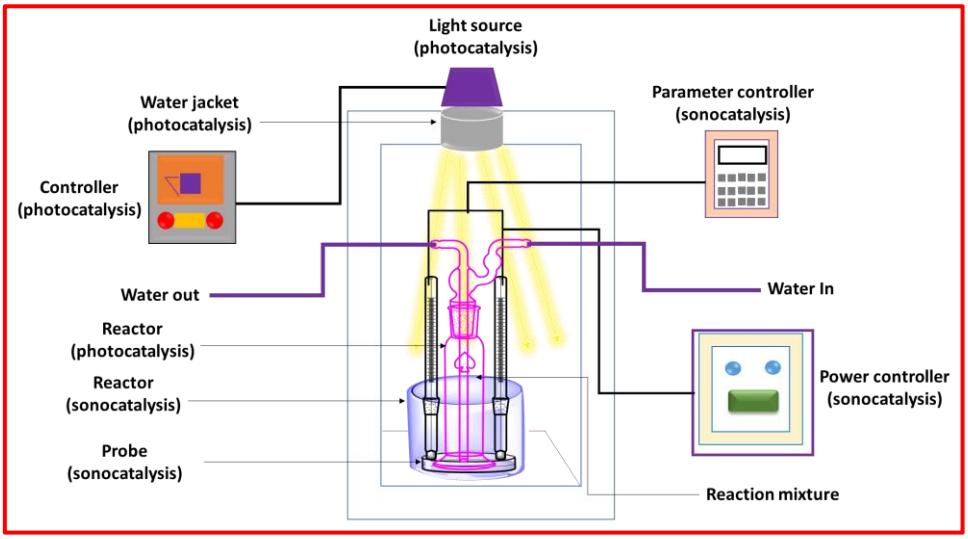

Fig. 2.4. Set up for the photosono-catalytic degradation of Rhodamine 6G.

Chapter three

This chapter provides details on the syntheses and characterisation of the Pcs, porphyrin, NPs as well as their respective conjugates.

Publications

The results discussed in this thesis have been published or submitted for publication in peer reviewed journals.

1. **S.T. Mkhondwane**, R. Matshitse, T. Nyokong, Porphyrin-graphitic carbon nitride quantum dots decorated titanium dioxide on electrospun nanofibers for photocatalytic degradation of organic pollutants, J. Coord. Chem., 75 (2022), 15-16.

2. **S.T. Mkhondwane**, S. Mgidlana, Y. Openda, L.C. Nene, T. Nyokong, Photosono catalytic behaviour of phthalocyanine when supported on electrospun nanofibers: The effect of radical initiators, Synth. Met. 299 (2023) 117484.

3. **S.T. Mkhondwane**, S. Mgidlana, Y. Openda, N. Nwahara, T. Nyokong, Phthalocyanine conjugated manganese ferrite nanoparticles embedded in TiO_2 fibers for photo-, sono- and photosono-catalytic degradation of Rhodamine 6G, Catal. Today, 432 (2024), 114644.

4. **S.T. Mkhondwane**, G. Sebiawu, S. Mgidlana, Y. Openda, N. Nwahara, J. Mack, T. Nyokong, Photosono activation of peroxymonosulfate using A_3B phthalocyanines supported on titanium dioxide nanofibers for degradation of Rhodamine 6G, Synth. Met., 307 (2024), 117699

5. **S.T. Mkhondwane**, S. Mgidlane, T. Nyokong, Asymmetric phthalocyanine-graphitic carbon nitride nanosheets conjugate on zinc oxide fibers for combined ultrasound and visible light driven degradation of Rhodamine 6G, J. Photochem. Photobiol. A:, 447 (2024), 115245

6. **S.T. Mkhondwane**, T. Nyokong, Phthalocyanines@g-C_3N_4 nanosheets conjugate synergic Z-scheme heterojunction and intersystem crossing induced charge separation supported on TiO_2 fibers for photosono-catalytic degradation of Rhodamine 6G, Diamond and Related Comp., 153 (2025) 112067.

3.1. Syntheses of porphyrin and phthalocyanines

3.1.1. Phthalocyanines (Pcs)

As has already been outlined in the previous chapters, the synthesis of complexes **1**, **2** and **5** have been reported before [70,71]. Hence, their synthesis and characterizations were not discussed in this chapter. The syntheses and characterization of complexes **3**, **4**, **6** and **7** are discussed in this chapter. An illustrative synthetic route for novel complexes **3**, **4** and **6** are shown in **Schemes 3.1-3.3**. The 4-methoxyphenoxyphthalonitrile (**A**) [165], 4-(4-carboxyphenoxy)-phthalonitrile (**B**) [166], 5-phenoxylpicolinic acid phthalonitrile (**C**) [167] and 4-(3,5-dimethoxyphenoxy) phthalonitrile (**D**) [168] used have already been reported. The 3:1 equivalent of the phthalonitriles in the presence of DBU as a base and ZnAOc were refluxed in the presence of argon **Schemes 3.1-3.3**. Column chromatography was used to separate the mixtures on silica gel using 5:1 v/v THF/cyclohexane. The mass spectra of complexes **3**, **4** and **6** are shown in **Fig. 3.1-3.3**.

The integrations of the ^{1}H NMR spectra (**Appendixes 1-3**) of the complexes **3**, **4** and **6** also confirmed the structures of these complexes. As anticipated, complex **4** is one proton shorter than complex **3** due to the presence of the N atom in phenoxy picolinic acid in complex **4** compared to the C atom in phenoxy carboxylic acid in complex **3**. Complexes **3**, **4** and **6** displayed a single peak at a higher chemical shift (between 10 ppm-11.5 ppm) which is due to the OH group of the COOH group. In addition, the compositions of the complexes were also confirmed with elemental analysis (CHNS). For all the as-synthesized complexes, the ratios of C:H:N obtained corresponded to anticipated ratios.

The MALDI-TOF spectra (run in positive mode) of complexes **3**, **4** and **6** are shown in **Appendix 4-6**. All the spectra show single peaks at m/z = 1127.90 amu, 1128.29 amu

and 1218.90 amu for complexes **3**, **4** and **6**, respectively corresponding to the calculated m/z of the respective Pcs. This proves that the Pcs were successfully synthesized and purified.

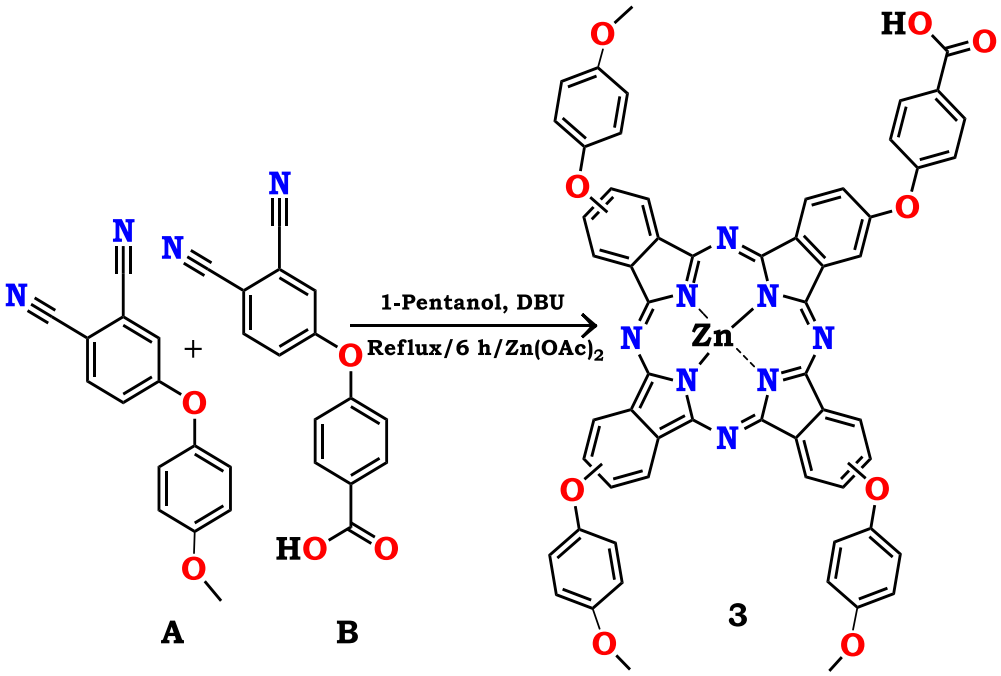

Scheme 3.1. Synthesis of complex **3**.

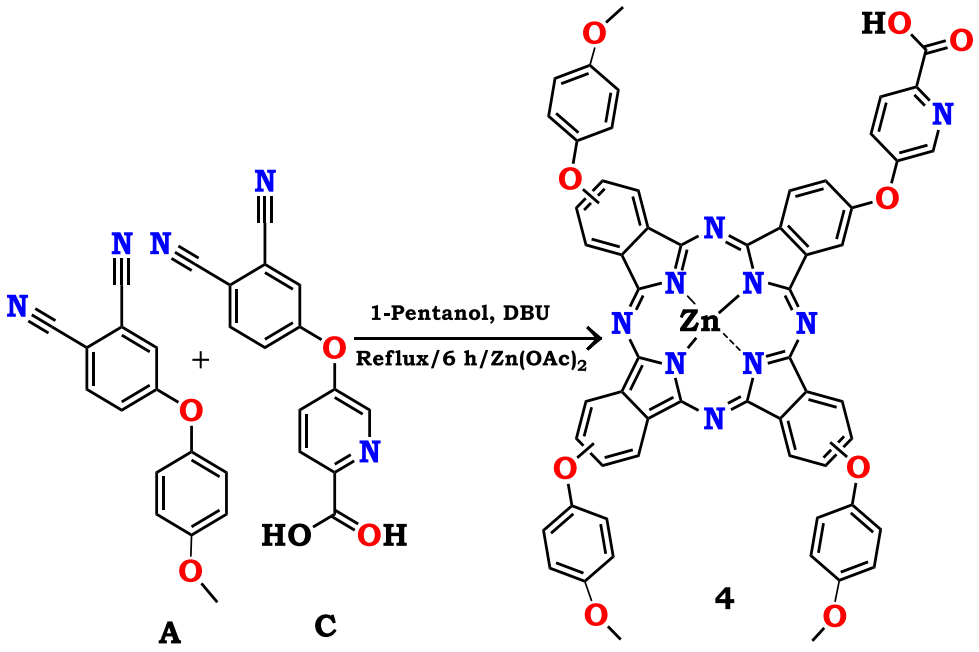

Scheme 3.2. Synthesis of complex **4**.

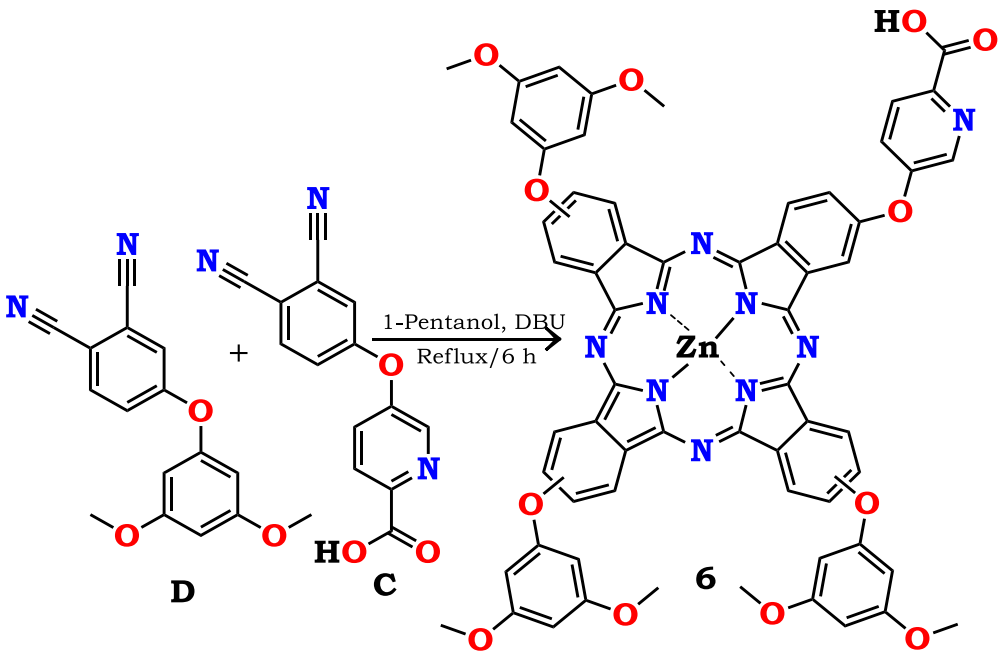

Scheme 3.3. Synthesis of complex **6**.

3.1.2. Porphyrin (7)

The illustrative synthesis route of the porphyrin (**7**) used in this study is shown in **Scheme 3.4**. The synthesis of 5-p-carboxyphenyl-10,15,20-(tris-4-pyridyl)-porphyrin (free base porphyrin, named complex **7a**) has been reported before hence it is not shown [169].

^{1}H NMR (**Appendix 7**) also displayed an anticipated number of protons and chemical shifts. The structure of the complex **7** was further confirmed using MALDI-TOF mass spectroscopy. The mass spectrum is shown in **Appendix 8**. The obtained mass was m/z = 725.17 amu which is close to the anticipated m/z of 724.90 amu. The CHN content obtained from elemental analysis were close to the anticipated elemental composition.

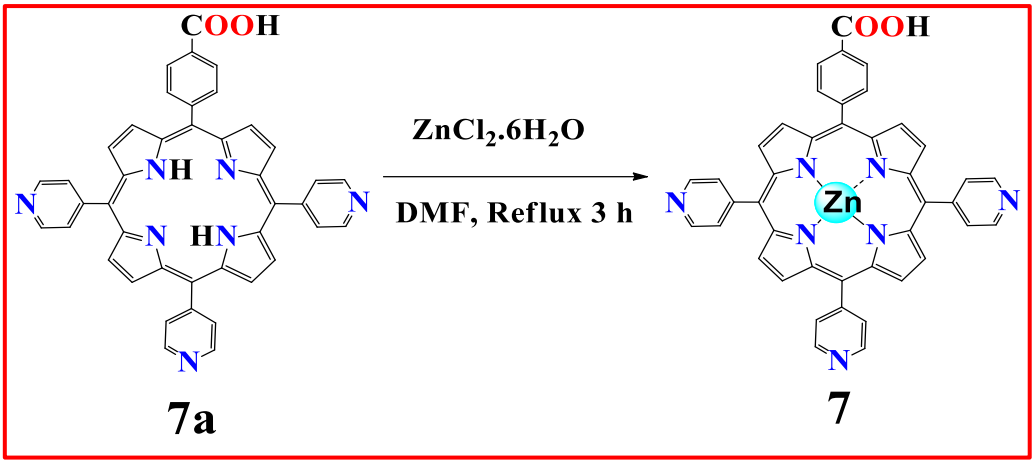

Scheme 3.4. Synthesis of complex **7**.

3.2. Syntheses of the nanoparticles

3.2.1. Syntheses of g-C_3N_4, Scheme 3.5.

As previously mentioned, the synthesis of g-C_3N_4 quantum dots have been reported before [170]. The synthesis of g-C_3N_4 NS was achieved by thermal polymerization of urea. The process is illustrated in **Scheme 3.5**.

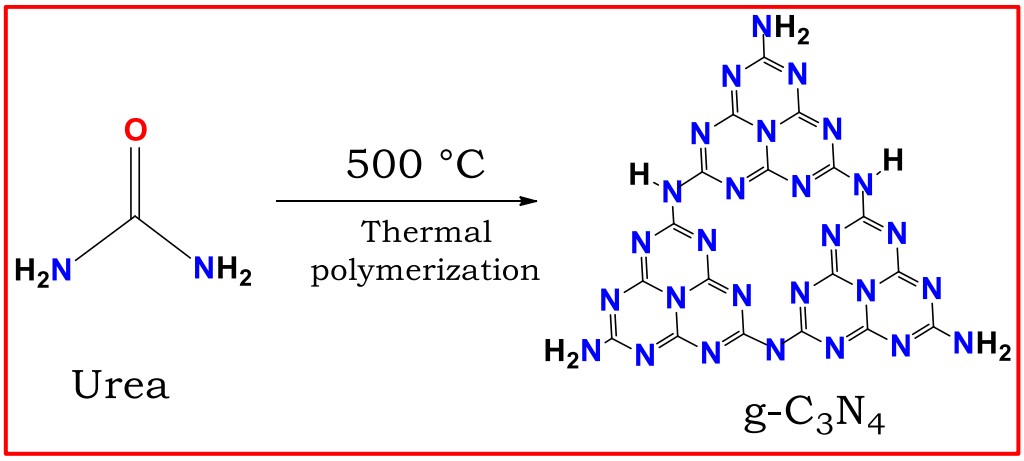

Scheme 3.5. Synthesis of graphitic carbon nitride by thermal polymerization.

3.2.2. Syntheses of $MnFe_2O_4$ nanoparticles.

Spinel manganese ferrite nanoparticles were synthesized using the co-precipitation method as reported in the literature [172].

3.3. Syntheses of the conjugates

3.3.1. Conjugation of 3, 4, 5 and 6 with g-C_3N_4 nanosheets, Scheme 3.6.

Scheme 3.6 shows the synthetic route for the conjugation of complexes **3**, **4**, **5**, and **6** with g-C_3N_4 nanosheets using complex **6** as an example. The -COOH group of the Pcs were first activated with DCC and EDC. The conjugation was achieved by means of an amide bond. The conjugates were named as **3**@g-C_3N_4 NS, **4**@g-C_3N_4 NS, **5**@g-C_3N_4 NS and **6**@g-C_3N_4 NS as listed in **Table 1.1**.

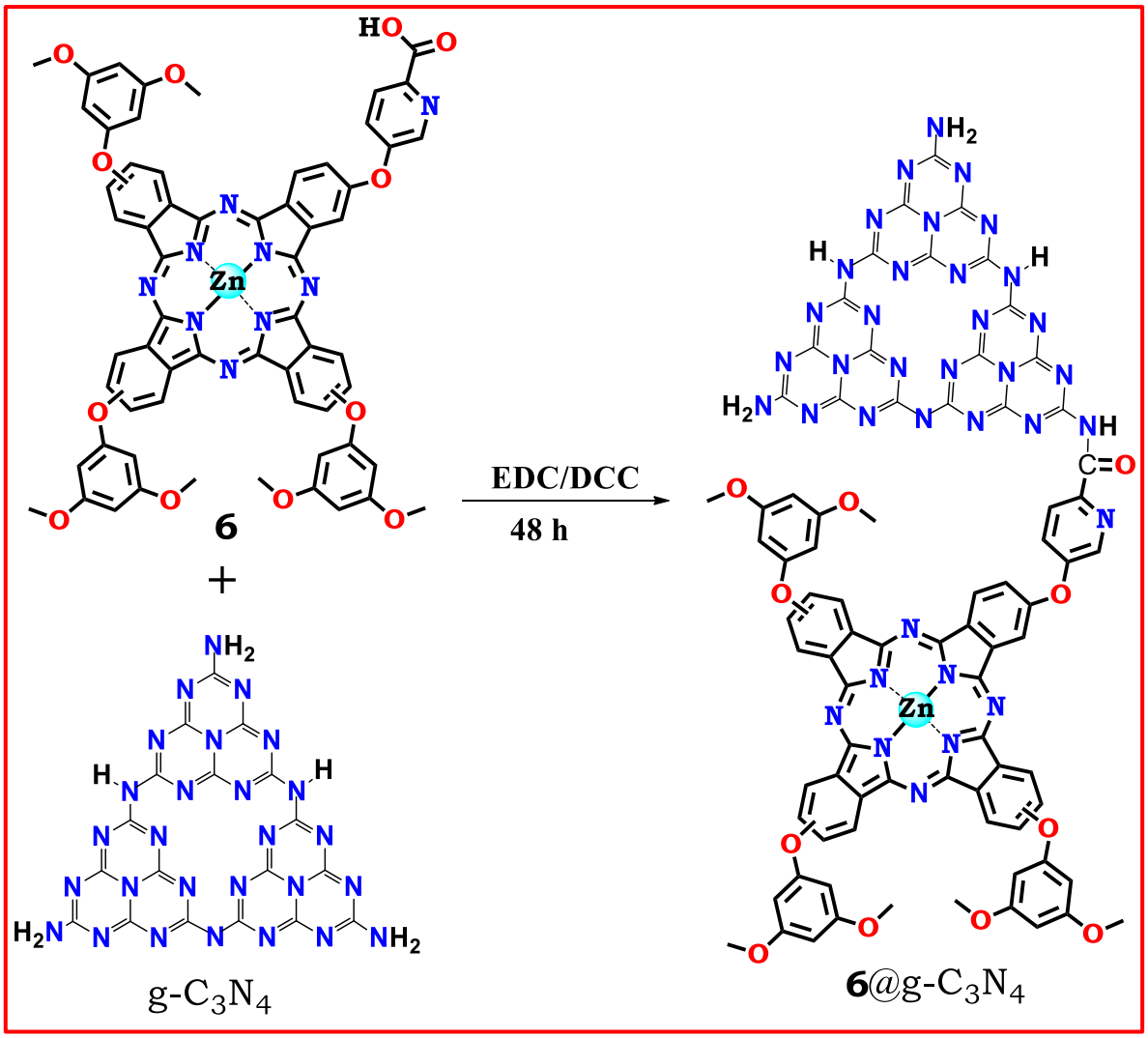

Scheme 3.6. The conjugation of complex **6** with g-C_3N_4 nanosheets

3.3.2. Conjugation of 3, 4, and 7 with g-C_3N_4 quantum dots

Scheme 3.7 shows the synthetic route for the conjugation of complexes **3**, **4** and **7** with g-C_3N_4 quantum dots using complex **7** as an example. The g-C_3N_4 quantum dots were synthesized using diaminomaleonitrile (DAMN) [172]. The ~COOH groups of the complexes **3**, **4** and **7** activated with DCC and EDC. The conjugation was achieved by covalent linkage by means of an amide bond. The conjugates were named **3**@g-C_3N_4 QDs, **4**@g-C_3N_4 QDs and **7**@g-C_3N_4 QDs.

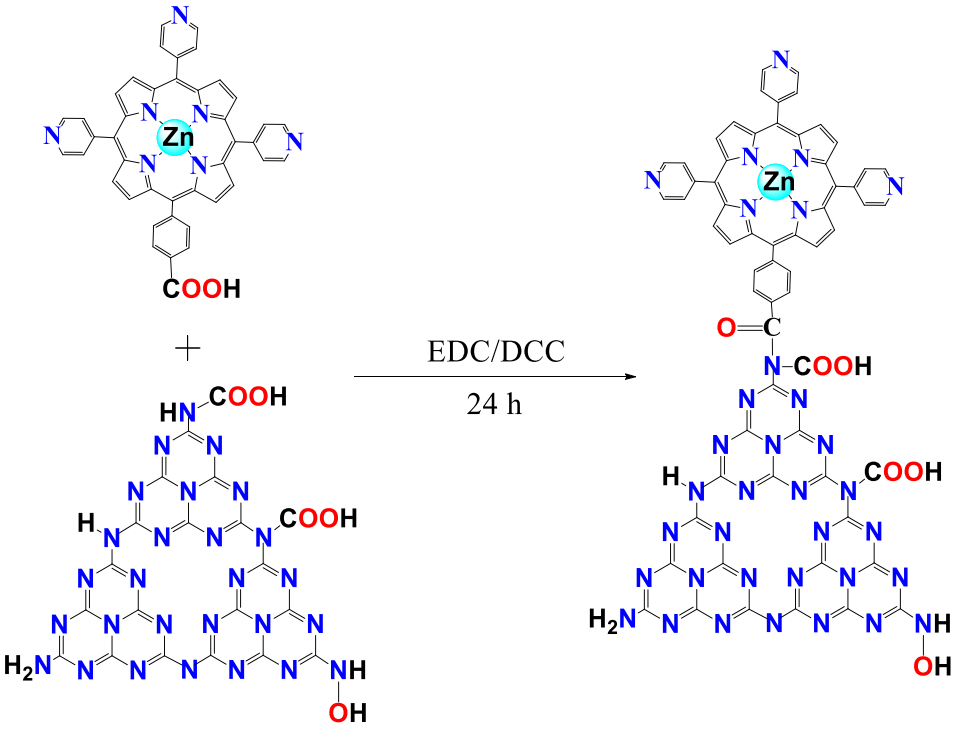

Scheme 3.7. The conjugation of complex **7** with g-C_3N_4 quantum dots

3.3.3. Conjugation of 5 with $MnFe_2O_4$ nanoparticles

Scheme 3.8 shows the conjugation of complex **5** with $MnFe_2O_4$ nanoparticles. APTES was used as a linker between the complex **5** and the $MnFe_2O_4$ nanoparticles. The functionalization of the $MnFe_2O_4$ nanoparticles with the APTES was adopted using the reported method [175]. DCC (20 mg) and EDC were used to activate the ~COOH

group of the complex **5**. The conjugation was achieved by covalent linkage through an amide bond.

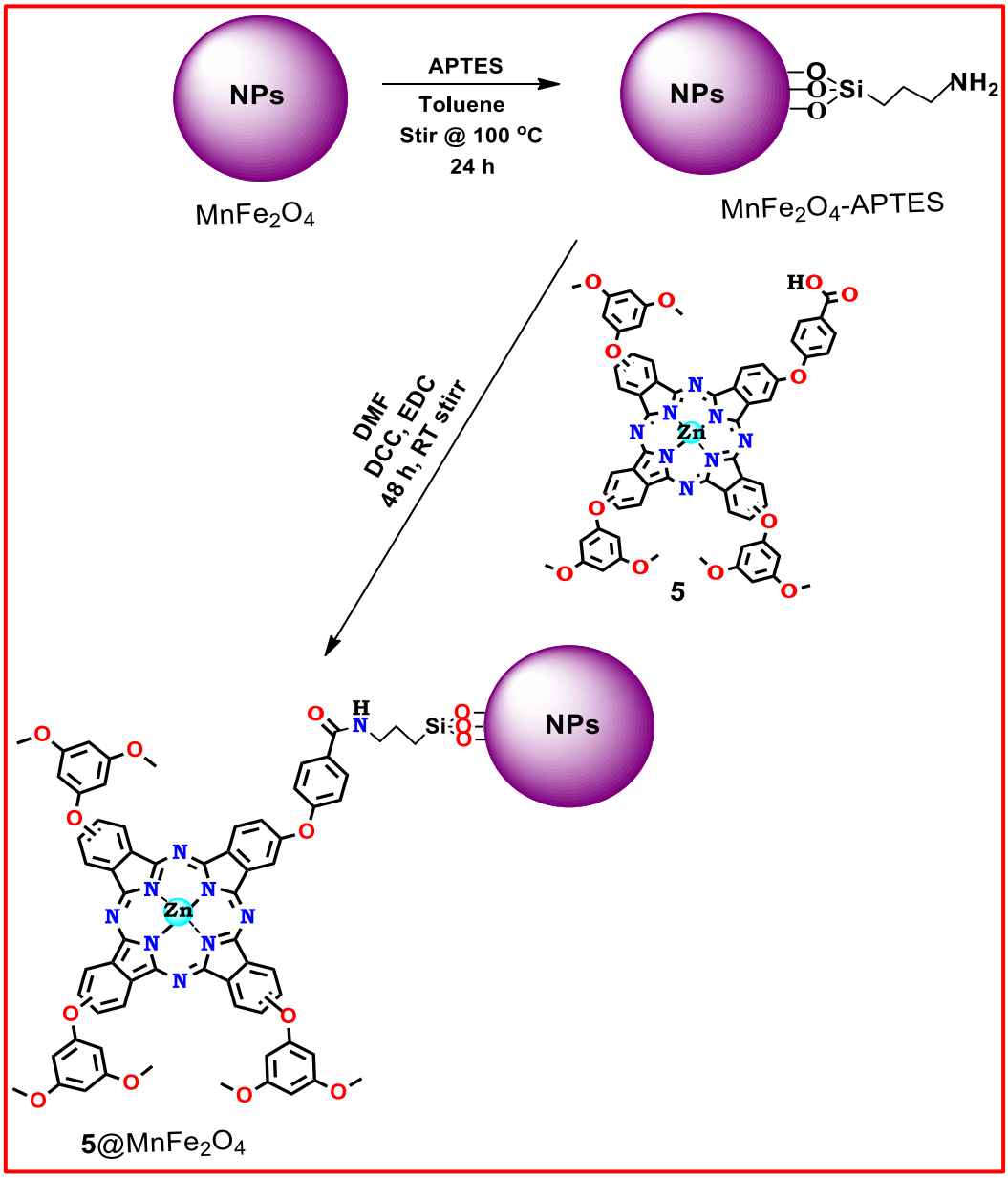

Scheme 3.8. The conjugation of complex **5** with $MnFe_2O_4$ nanoparticles

3.4. Optical properties

3.4.1. Porphyrin and Pcs alone

The UV-Vis absorption spectra of the Pcs (complexes **1**-**6**) are shown in **Fig. 3.1** in DMF and the values are listed in **Table 3.1**. Complex **2** was blue-shifted compared to complex **1**, **Fig. 3.1A**. Complex **1** has tetrakis-3,5-dimethoxyphenoxy substituents whereas complex **2** has tetrakis-3,4,5-trimethoxyphenoxy substituents. Therefore, the additional methoxy group in complex **2** is responsible for the blue-shift perceived in comparison to complex **1** (**Table 3.1**).

Complex **4** was red-shifted compared to complex **3**, **Fig. 3.1B**. Complex **4** has a picolinic acid phenoxy substituent, whereas complex **3** has carboxylic acid phenoxy. Therefore, picolinic acid phenoxy substituent endorsed a shift in absorption towards a higher wavelength. Nitrogen-containing compounds are known to red-shift the Q-band [189]. Complex **3** shows a red-shifted Q band compared to complex **5**, and complex **4** is red-shifted compared to **6**. This suggests that 1,4-methoxyphenoxy substituents in complexes **3** and **4** resulted in a red shift compared to 1,3,5-dimethoxyphenoxy substituents in complexes **5** and **6** (**Table 3.1**).

The band gap energies of complexes **1** and **2** were calculated from Tauc plots. The Tauc plots of complexes **1** and **2** are displayed in **Fig. 3.1A** and listed in **Table 3.1**. The results showed that there is no difference in band gap energies of complexes **1** and **2**. The band gap energies of complexes **3**, **4**, **5**, and **6** (**Fig. 3.1B**) obtained from Tauc plots revealed that band gap energies of complexes **3** and **4** were lower than those obtained from complexes **5** and **6**, **Table 3.1**.

Table 3.1. Optical properties of the complexes **1**, **2**, **3**, **4**, **5**, **6** and **7** and respective conjugates.

Samples	λ_{max} (nm)	Band gap (eV)
1	679	3.0
2	674	3.0
3	684	3.2
4	689	3.2
5	669	3.4
6	670	3.4
7a	417	2.9
7	424	2.8
g-C_3N_4 NS	327	2.8
g-C_3N_4 QDs	327	2.7
$MnFe_2O_4$ NPs	330	2.5
3@g-C_3N_4 NS	688	3.0
4@g-C_3N_4 NS	691	2.7
5@g-C_3N_4 NS	672	3.0
6@g-C_3N_4 NS	674	2.9
3@g-C_3N_4 QDs	690	2.3
4@g-C_3N_4 QDs	693	2.6
7@g-C_3N_4 QDs	426	2.6
5@$MnFe_2O_4$	676	2.8

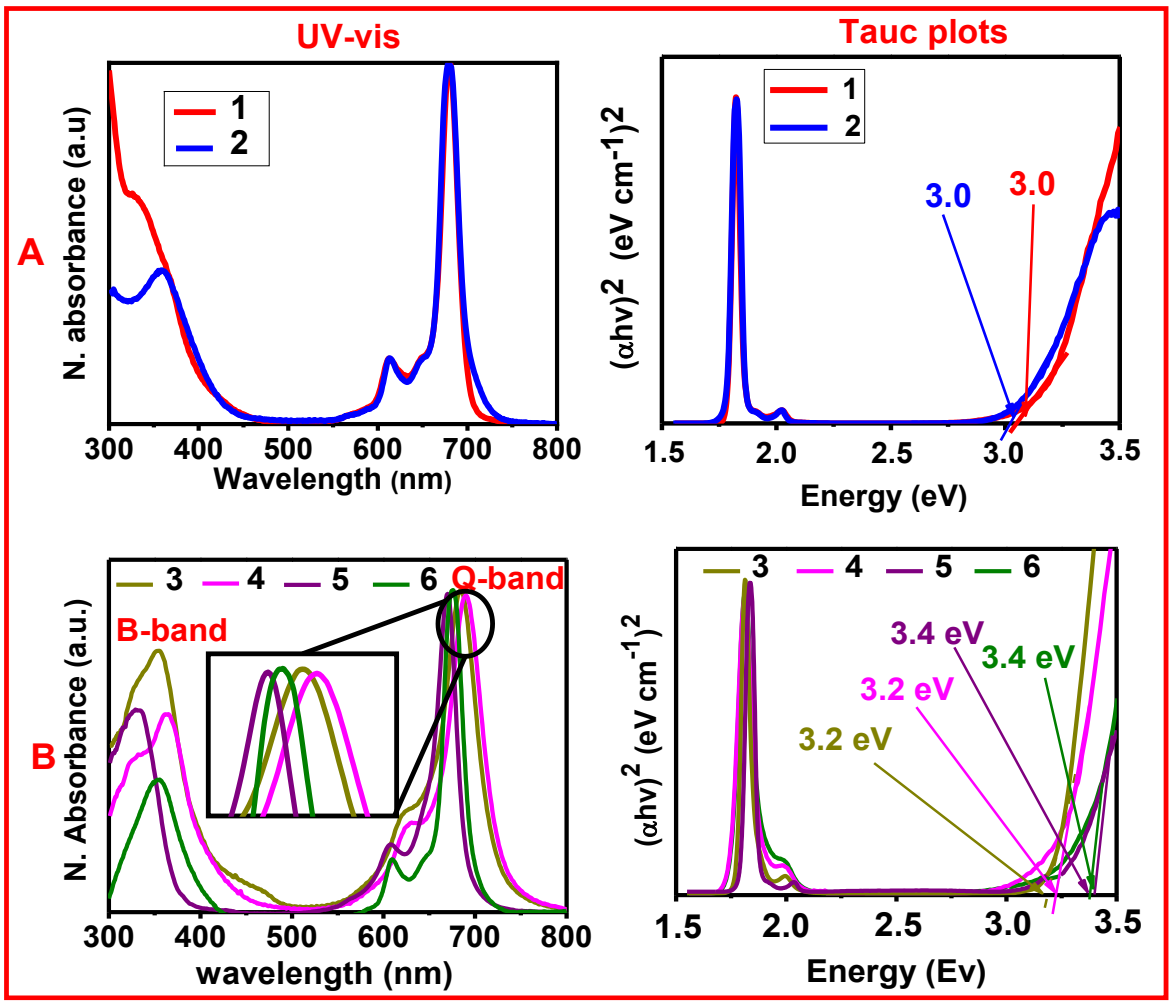

Fig. 3.1. UV-Vis spectra and Tauc plots of complexes **1** and **2** (**A**) and complexes **3**, **4**, **5** and **6** (**B**) in DMF.

The UV-Vis spectra of complex **7a** (unmetalled porphyrin) and **7** (metallated Por) are shown in **Fig. 3.2** and values are listed in **Table 3.1**. The complex **7a** had four Q-bands. Complex **7** (metallated **7a**) had two Q-bands. In addition, the Soret band was of **7** red-shifted compared to that of complex **7a**. The introduction of a metal such as zinc could result in a degree of perturbation and electron delocalization within the porphyrin macrocycle, resulting in redshifts in absorption spectra [190].

Tauc plots of complexes **7**a and **7** are shown in **Fig. 3.2** and **Table 3.1**. The band gap energy of the complex **7** was lower than that of the complex **7a.** This could be due to the fact that complex **7** was red-shifted compared to complex **7a**.

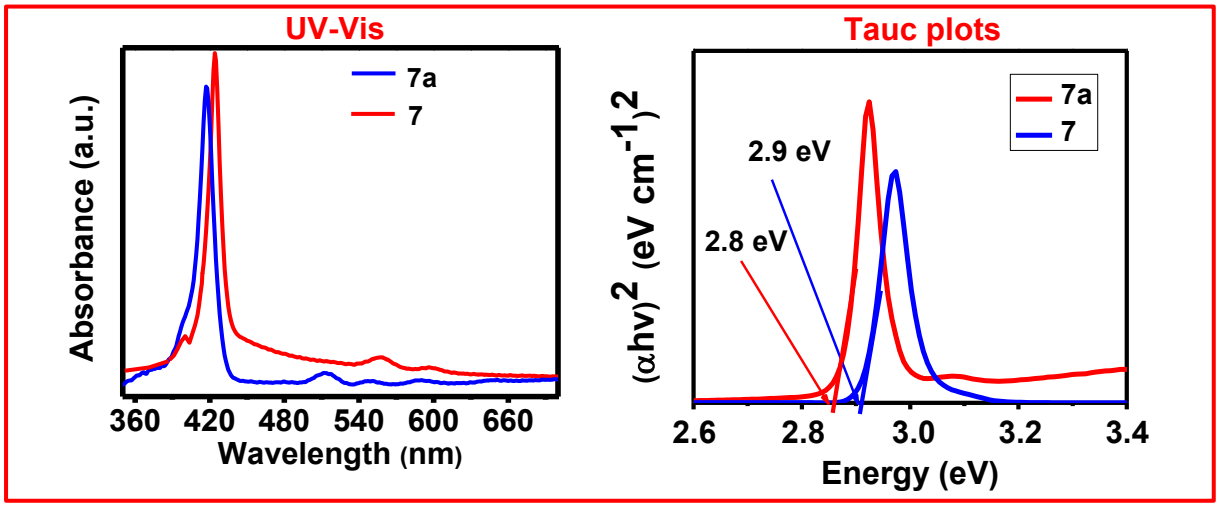

Fig. 3.2. UV-Vis spectra and Tauc plots of complexes **7a** and **7** in DMF.

3.4.2. g-C_3N_4 nanosheets and their conjugates

As stated before, complexes **3**, **4**, **5,** and **6** were conjugated to g-C_3N_4 NS. The UV-vis absorption properties of g-C_3N_4 NS, **3**@g-C_3N_4 NS, **4**@g-C_3N_4 NS, **5**@g-C_3N_4 NS, and **6**@g-C_3N_4 NS conjugates in DMF are displayed in **Fig. 3.3** and **Table 3.1**. The Q-bands of the conjugates are red-shifted compared to complexes **3**, **4**, **5,** and **6** alone. The observed red-shift is due to the molecular flattening reported in porphyrin-like complexes when conjugated with graphene-like materials [191].

The band gap energies of the synthesized conjugates were obtained from Tauc plots. The plots are shown in (**Fig. 3.3**), and values are listed in **Table 3.1**. The band gap energies of conjugates were lower than those obtained from respective complexes **3**, **4**, **5**, and **6** alone. However, the difference was not significant.

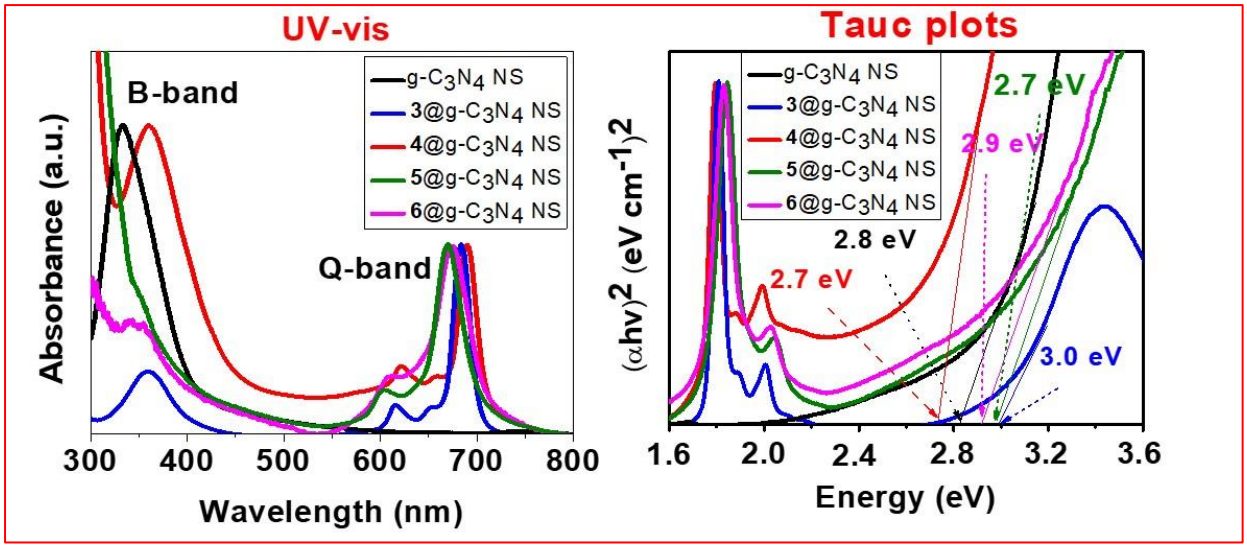

Fig. 3.3. UV-Vis spectra and Tauc plots of g-C_3N_4 NS, **3**@g-C_3N_4 NS, **4**@g-C_3N_4 NS, **5**@g-C_3N_4 NS and **6**@g-C_3N_4 NS in DMF.

3.4.3. g-C_3N_4 QDs and their respective conjugates

Complexes **3**, **4**, and **7** were conjugated to g-C_3N_4 QDs. The UV-Vis spectra and respective Tauc plots of g-C_3N_4 QDs, **3**@g-C_3N_4 QDs, and 4@g-C3N4 QDs were compared in **Fig. 3.4A** and **Table 3.1**. The g-C_3N_4 QDs display absorption at 327 nm (**Table 3.1**). This absorption band is attributed to n→π transition, which originated from an electron transfer from a nitrogen nonbonding orbital to an aromatic antibonding orbital of g-C_3N_4 QDs. The UV-Vis spectra of **3**@g-C_3N_4 QDs and **4**@g-C_3N_4 QDs display absorption peaks corresponding to B-bands and Q-bands. The conjugates displayed a red-shift than individual complexes **3** and **4**, **Table 3.1**. The observed red-shift compared to porphyrins alone is due to the molecular flattening in porphyrin light complexes when conjugated to graphene-like materials [191] as stated above.

The band gap energies obtained from Tauc plots (**Fig. 3.4A)** are listed in **Table 3.1**. The band gap energies of the conjugates are lower than those of the corresponding

individuals **3** and **4**. This suggests that the conjugation of complexes **3** and **4** with g-C_3N_4 QDs resulted in a decrease in band gap energies compared to those of **3** and **4**.

The UV-vis absorption spectra of g-C_3N_4 QDs and **7**@g-C_3N_4 QDs conjugates in DMF are compared in **Fig. 3.4B**. The absorption spectrum of **7**@g-C_3N_4 QDs shows a Soret-band at 426 nm. There is a shift in the porphyrin Soret band towards a higher wavelength upon conjugation. The observed red-shift B-band compared to that of the **7b** alone is due to molecular flattening, which is often reported in porphyrin-graphene conjugates [191].

The band gap energies of g-C_3N_4 QDs and **7**@g-C_3N_4 QDs calculated from Tauc plots (**Fig. 3.4B**) are listed in **Table 3.1**. The band gap energies of g-C_3N_4 QDs and **7**@g-C_3N_4 QDs were 2.7 and 2.6 eV, respectively. The band gap energy obtained in **7**@g-C_3N_4 QDs was slightly lower than that obtained in pristine **7**, suggesting that the conjugation resulted in a decrease in band gap energy.

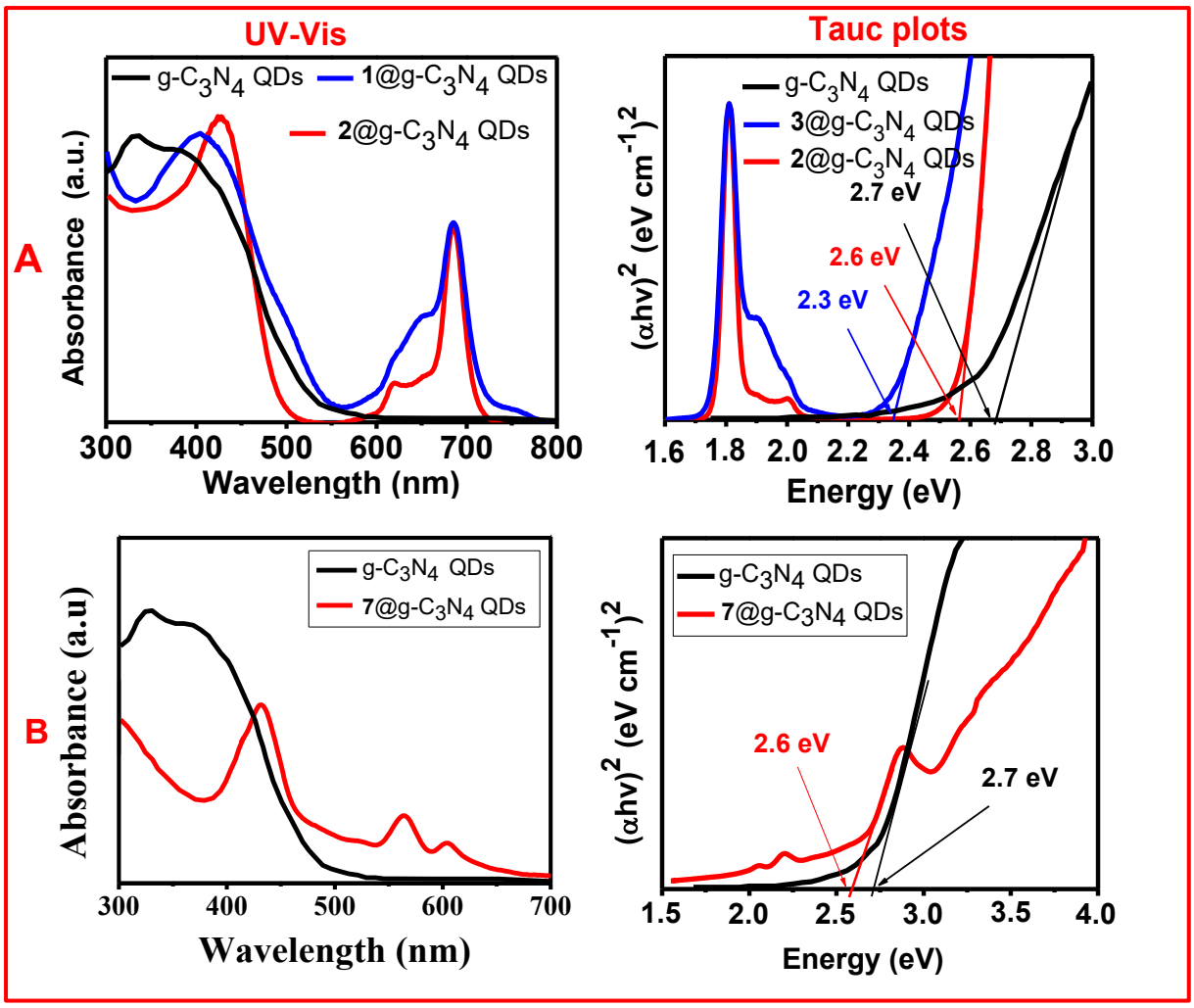

Fig. 3.4. UV-Vis spectra and Tauc plots of g-C_3N_4 QDs, **1**@g-C_3N_4 QDs and **2**@g-C_3N_4 QDs in DMF.

3.4.4. $MnFe_2O_4$ NPs and 5@$MnFe_2O_4$ NPs conjugates

The UV-Vis absorption spectra of **5**, $MnFe_2O_4$ and **5**@$MnFe_2O_4$ conjugate in DMF are shown in **Fig. 3.5**. The $MnFe_2O_4$ NPs display absorption at 330 nm. **5**@$MnFe_2O_4$ conjugate in DMF displays the B-band at 360 nm and the Q bands at 676 nm, **Table 3.1**. The conjugate was red shift compared to complex **5** alone, which was attributed to molecular flattening [191].

The band gap energies (**Fig. 3.5** and **Table 3.1.**) of $MnFe_2O_4$ nanoparticles and **5@**$MnFe_2O_4$ conjugate (using the B-band for the Pcs) show that the conjugate has lower band gap energy than complex **5** alone. This suggests that conjugation of the complex **5** and $MnFe_2O_4$ NPs resulted in a decrease in band gap energy compared to that of the **5**.

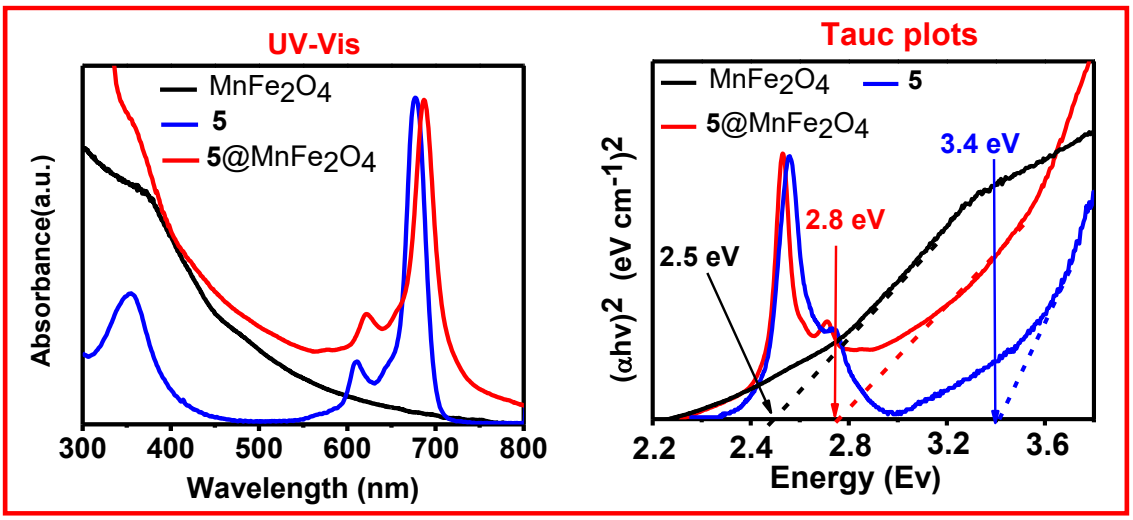

Fig. 3.5. UV-Vis spectra and Tauc plots of **5**, $MnFe_2O_4$ and **5**@$MnFe_2O_4$ conjugate in DMF.

3.5. Fourier transform infrared spectroscopy (FT-IR)

FT-IR was used to study surface bonding and interaction between g-C_3N_4 QDs and complexes **3**, **4** and **7** in **3**@g-C_3N_4 QDs, **4**@g-C_3N_4 QDs and **7**@g-C_3N_4 QDs respectively. The FT-IR spectra of g-C_3N_4 QDs, **3**@g-C_3N_4 QDs and **4**@g-C_3N_4 QDs conjugates are displayed in **Fig. 3.6**. The spectrum of g-C_3N_4 QDs display three peaks at 1302, 1472 and 1784 cm^{-1}, which are indexed to C-N, N-H and C=O vibration frequencies, respectively [192]. The spectra of **3**@g-C_3N_4 QDs and **4**@g-C_3N_4 QDs conjugate shows an enhanced C-N peak with an additional C=O peak corresponding to the presence of an amide bond and confirming successful conjugation. C-O peaks are also observed for both **3**@g-C_3N_4 QDs and **4**@g-C_3N_4 QDs conjugate which corresponds to methoxy group of the complexes **3** and **4**.

The spectra of g-C_3N_4 QDs, complex **7** and **7**@g-C_3N_4 QDs are compared in **Fig. 3.7**. The spectrum of g-C_3N_4 QDs display three peaks at 1302 cm^{-1}, 1472 cm^{-1} and 1784 cm^{-1}, which are indexed C-N, N-H and C=O vibration frequencies, respectively (cycled in red) [192]. The FT-IR spectrum of complex **7** showed peaks at 3000 cm^{-1} and 2957 cm^{-1} corresponding to O-H and C-H of the porphyrin, respectively. Another intense absorption band is oberved at 1772 cm^{-1} which is due to C=O stretching frequencies. The FT-IR spectra of **7**@g-C_3N_4 QDs show peaks at 3000 and 2957 cm^{-1}, which are due to O-H and C-H vibrations of complex **7**. Another peak was observed at 1772 cm^{-1} which is due to C=O stretching frequencies. The band confirming the presence of an amide bond is at 1564 cm^{-1}, which can be indexed to the C-N stretching of the amide bond [193]. The FT-IR analysis of the conjugates of the Pc complexes, g-C_3N_4 NS, or g-C_3N_4 QDs were not performed. Instead, Raman spectroscopy and X-ray spectroscopy (XPS) were used to investigate the interaction

between the Pcs, g-C_3N_4 NS, and g-C_3N_4 QDs. XPS is more sensitive than FT-IR in identifying surface bonding. Hence, it was used instead of FT-IR.

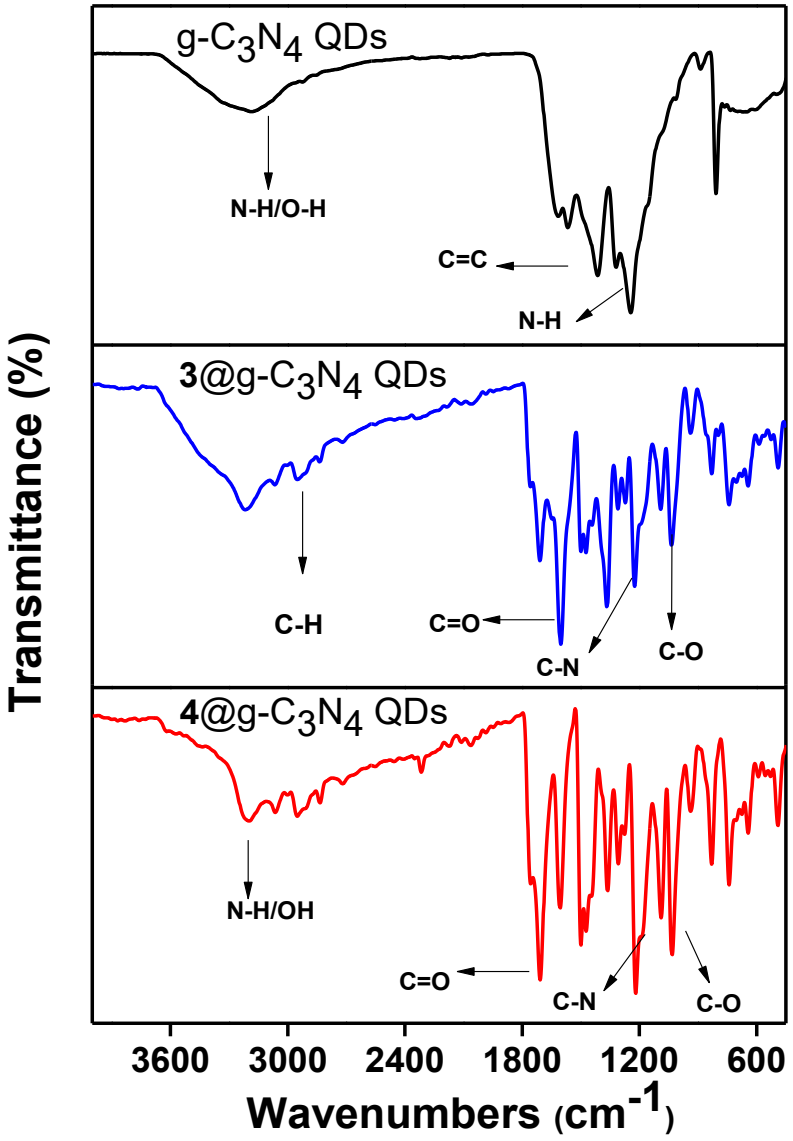

Fig. 3.6. FT-IR spectra of g-C_3N_4 QDs, **3** and **3**@g-C_3N_4 QDs conjugates

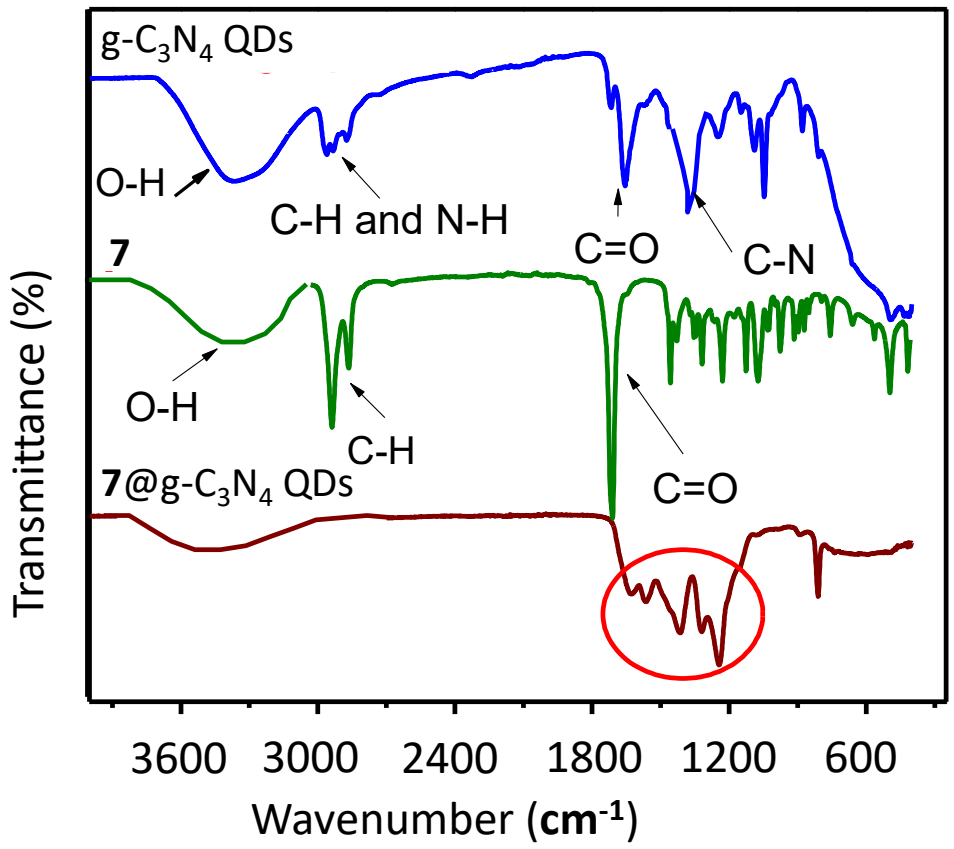

Fig. 3.7. FT-IR spectra of g-C_3N_4 QDs, **7** and **7**@g-C_3N_4 QDs conjugates.

3.6. Raman spectroscopy analysis

Raman spectroscopy was used to investigate the interaction between Pc complexes, g-C_3N_4 NS and g-C_3N_4 QDs. Typically, the interaction between the Pc and g-C_3N_4 QDs or g-C_3N_4 NS results in the formation of defect sites in g-C_3N_4 QDs or g-C_3N_4 NS. The defect sites are observed by changes in Raman peaks of g-C_3N_4 QDs and g-C_3N_4 NS. Hence, Raman spectroscopy was used to study the interaction between Pcs and g-C_3N_4 QDs or g-C_3N_4 NS.

3.6.1. g-C_3N_4 NS and their conjugates

Raman spectroscopy of g-C_3N_4 NS and their respective conjugates was studied to gain insight into the molecular interaction between g-C_3N_4 NS and Pcs. The Raman spectra of g-C_3N_4 NS and **3**@g-C_3N_4 NS, **4**@g-C_3N_4 NS, **5**@g-C_3N_4 NS and **6**@g-C_3N_4 NS are presented in **Fig. 3.8**. The spectrum of g-C_3N_4 NS show peaks at 1280 cm^{-1} and 1600 cm^{-1}, which are due to D-band (sp^3) and G-band (sp^2), respectively. The G-band is due to in-plane vibrations of sp^2 carbon nitride groups and the D-band is due to out-of-plane vibrations [194]. The conjugation of g-C_3N_4 with Pc complexes resulted in a shift in both D- and G-bands to high frequencies. This is due to strong interaction between the Pcs and g-C_3N_4 NS [195]. The I_D: I_G ratio of g-C_3N_4 NS, **4**@g-C_3N_4 NS, **5**@g-C_3N_4 NS and **6**@g-C_3N_4 NS were 0.21, 0.87, 0.88, 0.91 and 0.90, respectively. Thus, there is an increase in the I_D:I_G ratio of the conjugates compared to g-C_3N_4 NS alone. This also shows a strong interaction between the Pcs and g-C_3N_4 NS and an increase in the level of disorder upon conjugation.

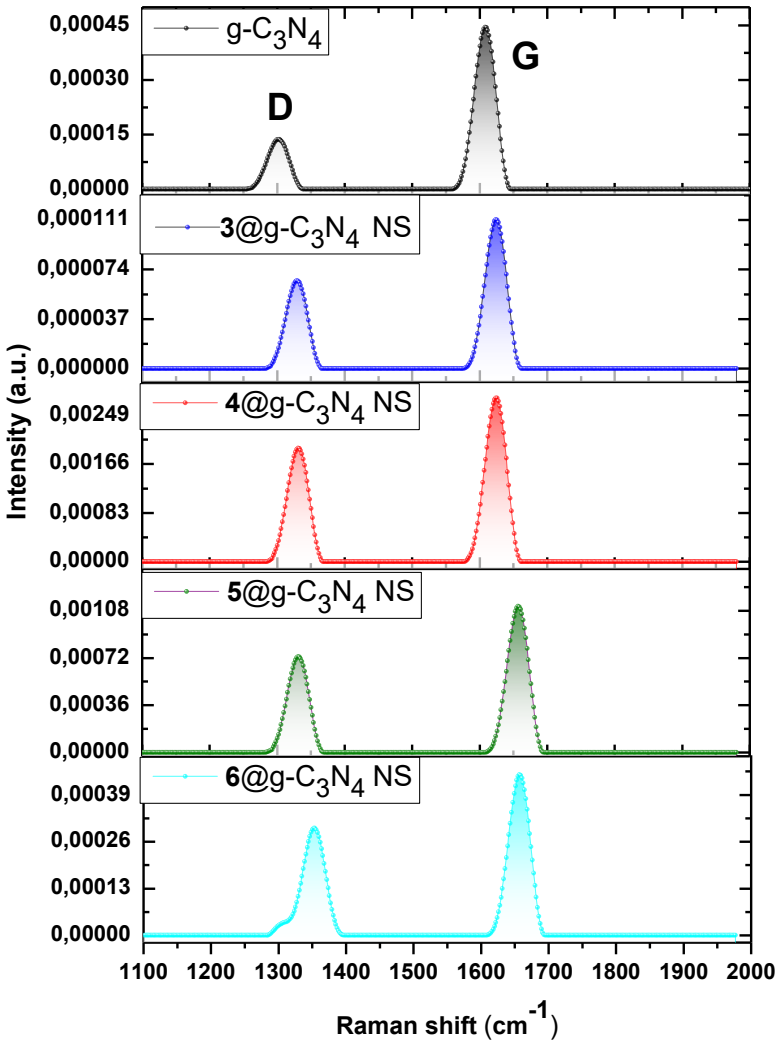

Fig. 3.8. Ramana spectra of g-C_3N_4 NS, **3**@g-C_3N_4 NS, **4**@g-C_3N_4 NS, **5**@g-C_3N_4 NS and **6**@g-C_3N_4 NS conjugates.

3.6.2. g-C_3N_4 QDs and their conjugates

The Raman spectra of g-C_3N_4 QDs and **3**@g-C_3N_4 QDs and **4**@g-C_3N_4 QDs are compared in **Fig. 3.9**. The Raman spectrum of g-C_3N_4 QDs display peaks at 1280 cm^{-1} and 1600 cm^{-1}, which are due to D-band (sp^3) and G-band (sp^2), respectively. The conjugation of the g-C_3N_4 QDs with complexes **3** and **4** resulted in a

shift in D and G bands to high frequencies. The calculated I_D: I_G ratio of g-C_3N_4, **3**@g-C_3N_4 QDs and **4**@g-C_3N_4 QDs, were 0.21, 0.84, 0.86, respectively.

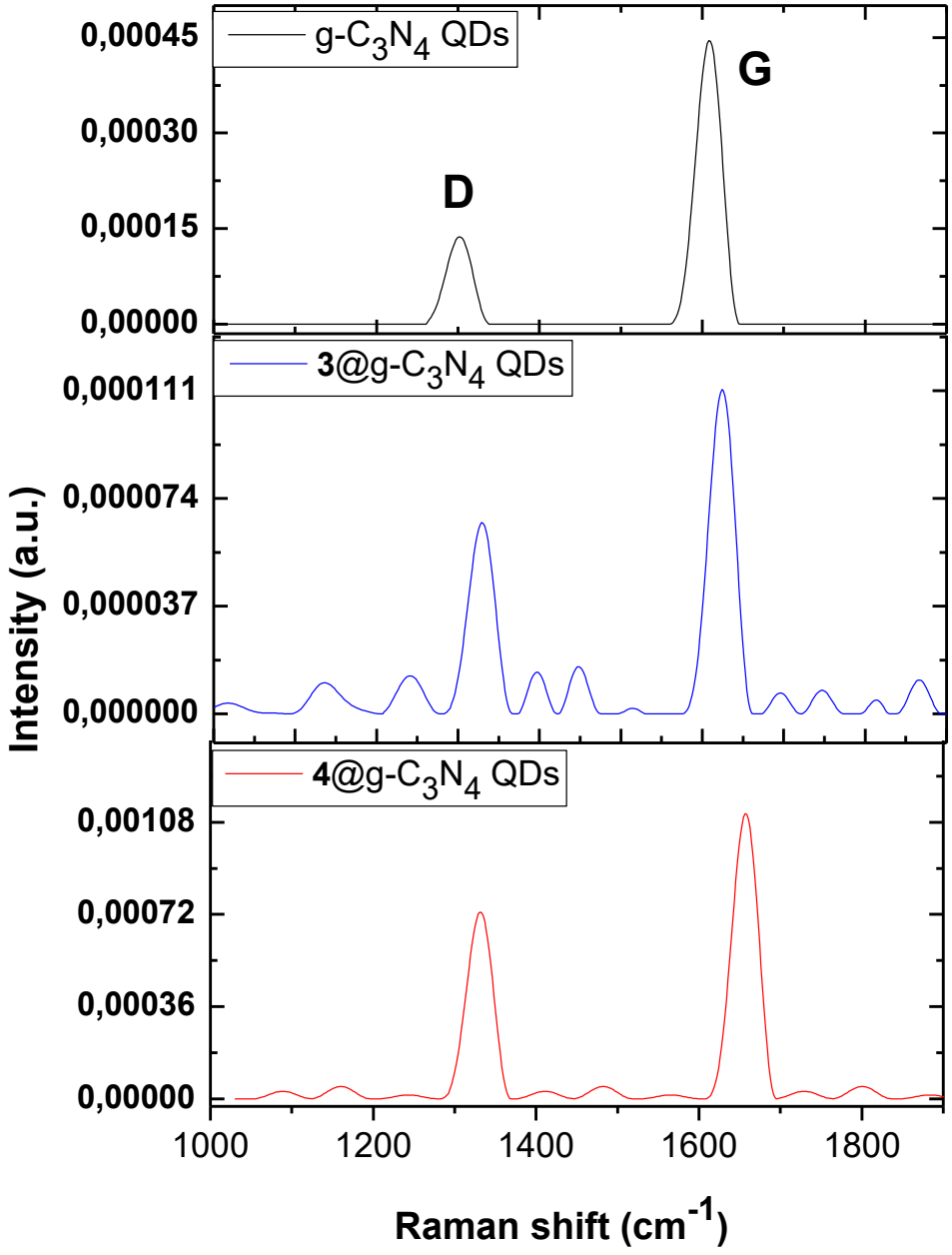

Fig. 3.9. Ramana spectra of g-C_3N_4 QDs, **3**@g-C_3N_4 QDs and **4**@g-C_3N_4 QDs conjugates.

3.7. X-ray photoelectron spectroscopy (XPS) analysis

3.7.1. XPS of g-C_3N_4 NS and respective conjugates

XPS was used to confirm the successful conjugation between g-C_3N_4 NS and Pc complexes by investigating the chemical states of the complex **6**, g-C_3N_4 NS and **6**@g-C_3N_4 NS (and used as an example for the rest of the conjugates). The results are shown in **Fig. 3.10**. The elemental survey spectra of the complex **6**, g-C_3N_4NS and **3**@g-C_3N_4 NS display peaks corresponding to carbon (C), nitrogen (N) and oxygen (O) at 386.9, 399.4 and 532,8 eV, respectively.

The C and N peaks were deconvoluted to identify the different bonding states. The high-resolution spectra of the C 1s and N 1s spectra of both g-C_3N_4 NS, **6** and conjugates are shown in **Fig 3.10**. The C1s of g-C_3N_4 displayed bonding states at 284.2 eV and 285.6 eV corresponding to C=C and C-N/C=N, respectively. These Gaussian peaks have been previously reported for g-C_3N_4 [196,197]. The deconvoluted N1s spectrum of g-C_3N_4 NS displays two bonding states at 399.9 eV and 401.0 eV corresponding to (sp^2) C-N=C and the intercalated graphitic N atoms, respectively.

The bonding states for C 1s of complex **6** were observed at 284.1, 284.6, 285.4, 286.8 and 288.2 eV corresponding to C=C, C-H, C-N/C=N, C-O and C=O, respectively [198]. For N1s, two bonding states were observed at 399.9 eV and 401.0 eV, which correspond to the C=N bond and graphitic N, respectively. The C 1s spectrum of **6**@g-C_3N_4 NS had similar bonding states observed in the deconvoluted C1s spectrum of the complex **6**. However, the intensity of the C-N/C=N at 285.7 eV was significantly enhanced due to the formation of an amide bond. To further confirm the formation of an amide bond the deconvoluted N 1s spectrum of **6**@g-C_3N_4NS was obtained. An

additional peak was observed at 402.1 eV, corresponding to -N-C=O bond of an amide.

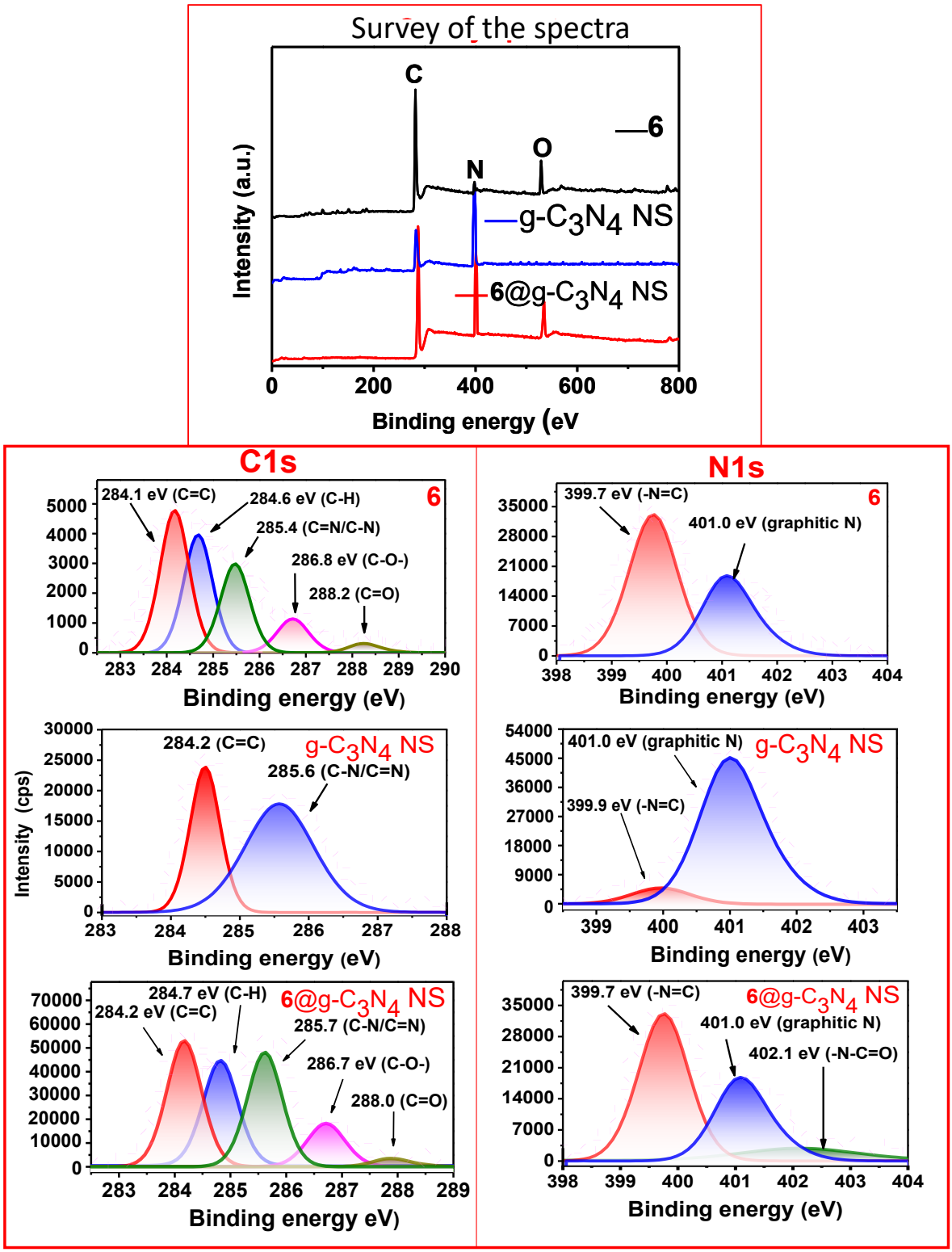

Fig. 3.10. XPS spectra of complex **6**, g-C_3N_4 NS and **6**@g-C_3N_4 NS.

3.7.2. $MnFe_2O_4$ and the respective conjugate

XPS analyses were performed to confirm the conjugation between complex **5** and $MnFe_2O_4$. The wide scan spectra of $MnFe_2O_4$-APTES and **5**@$MnFe_2O_4$ are shown in **Fig. 3.11**. The wide scan spectrum of $MnFe_2O_4$-APTES shows the presence of Mn, Fe, O, Si, C, and N elements. The **5**@$MnFe_2O_4$ spectrum shows the presence of Zn from complex **5** in addition to the peaks of $MnFe_2O_4$-APTES.

To confirm the conjugation through an amide bond, the C 1s and N 1s were deconvoluted in $MnFe_2O_4$-APTES and **5**@$MnFe_2O_4$ conjugate. The high-resolution C 1s spectrum of $MnFe_2O_4$-APTES shown in **Fig. 3.11** was deconvoluted to C-C/C-H and C-N peaks at 284.6 and 286.5 eV, respectively. The N 1s for $MnFe_2O_4$ in **Fig. 3.11** was deconvoluted to –N-H and –N-C at 397.4 and 398.9 eV, respectively. The C 1s spectrum of **5**@$MnFe_2O_4$ was deconvoluted to C=C, C-C/C-H, C-N/C=N, C-O- and C=O at 284.0, 284.6, 285.3, 286.3 and 287.2 eV, respectively. The N 1s spectrum of **5**@$MnFe_2O_4$ was deconvoluted to –N-H, pyridinic N, pyrrolic N and –N-C=O at 397.8, 399.0, 400.1 and 401.1 eV corresponding, respectively. The –N-C=O bond confirms the successful conjugation between **5** and $MnFe_2O_4$ [199].

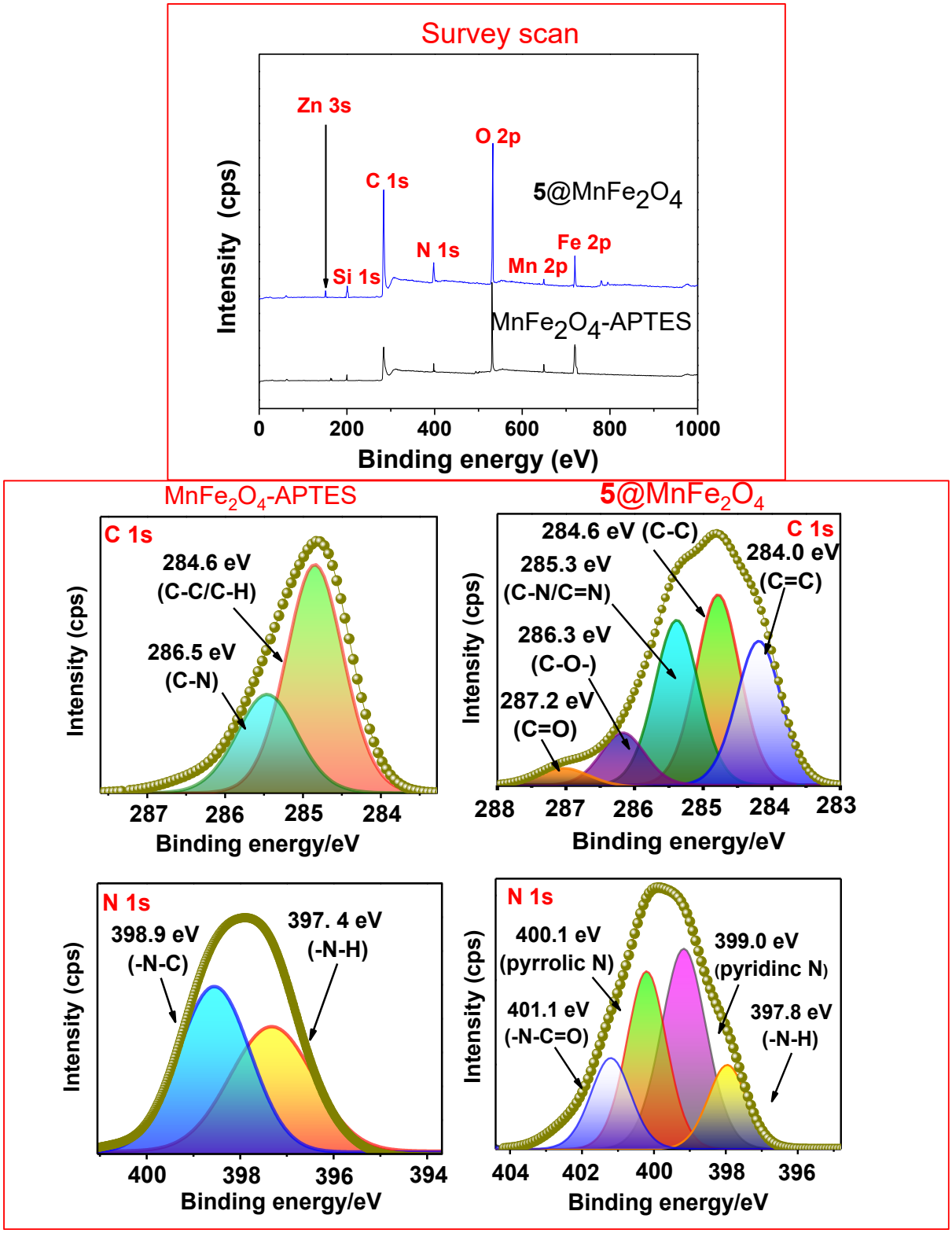

Fig. 3.11. XPS spectra of complex **5**, and **5**@$MnFe_2O_4$ conjugate.

3.8. X-ray diffraction (XRD)

3.8.1. g-C_3N_4 NS and respective conjugates

The XRD spectrum of the g-C_3N_4 NS displays a broad diffraction peak at 2θ = 27.4° corresponding to (002) plane (**Fig. 3.12**). The spectra of **3**@g-C_3N_4 NS, **4**@g-C_3N_4 NS, **5**@g-C_3N_4 NS, and **6**@g-C_3N_4 NS also show diffraction peaks corresponding to the (002) plane. However, the peak has low intensity which suggests that the conjugation resulted in a decrease in crystallinity [192].

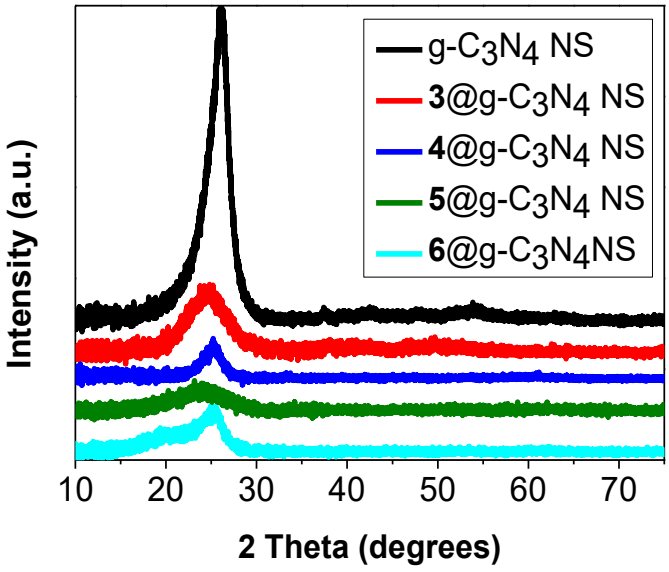

Fig. 3.12. XRD spectra of g-C_3N_4 NS **3**@g-C_3N_4 NS, **4**@g-C_3N_4 NS, **5**@g-C_3N_4 NS and **6**@g-C_3N_4 NS.

3.8.2. g-C_3N_4 QDs and conjugates

The XRD spectra of g-C_3N_4 QDs and **3**@g-C_3N_4 QDs and **4**@g-C_3N_4 QDs conjugates are displayed in **Fig. 3.13A**. The XRD spectrum of the g-C_3N_4 QDs displays a broad diffraction peak at 2θ = 27.4° corresponding to (002) plane. The spectra of **3**@g-C_3N_4 QDs and **4**@g-C_3N_4 QDs conjugates show that the conjugation resulted in decrease in crystallinity observed by a decrease in (002) peak intensity.

The XRD spectra of g-C_3N_4 QDs and **7**@g-C_3N_4 QDs are shown in **Fig. 3.13B**. Upon conjugation of g-C_3N_4 with complex **7** to form **7**@g-C_3N_4, the (002) peak of the g-C_3N_4 was significantly broadened. This is probably due to the overlap between the (002) peak of the g-C_3N_4 and the amorphous peak of the porphyrin (complex **7**).

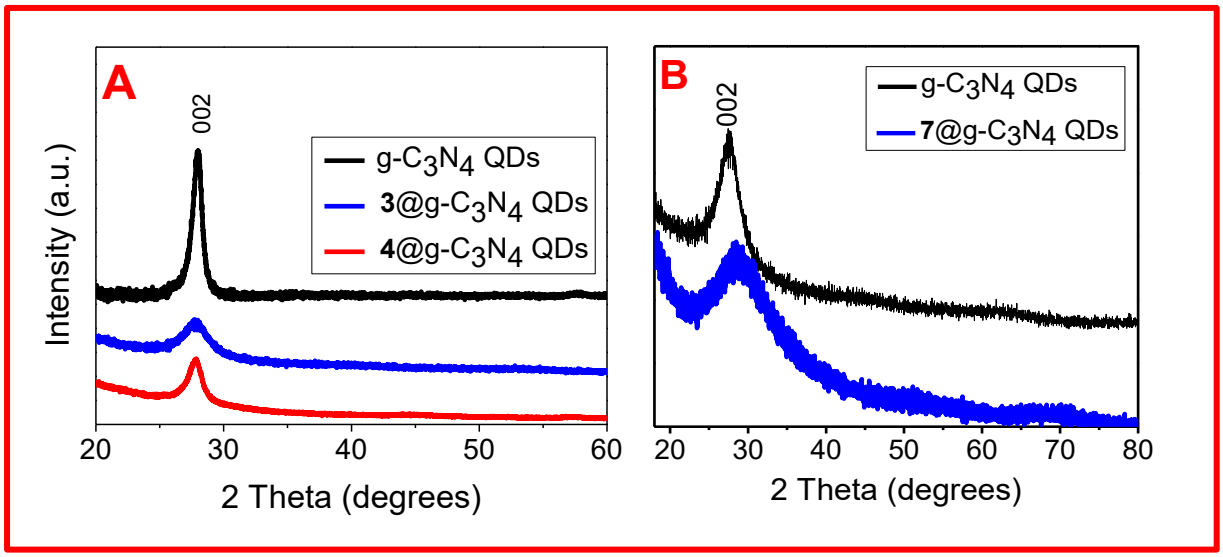

Fig. 3.13. XRD spectra of g-C_3N_4 QDs, **3**@g-C_3N_4 QDs and **4**@g-C_3N_4 NS **(A)** and g-C_3N_4 QDs and **7**@g-C_3N_4 QDs **(B)**.

3.8.3. $MnFe_2O_4$ nanoparticles and respective conjugates

X-ray diffraction of $MnFe_2O_4$ NPs and **5**@$MnFe_2O_4$ are displayed in **Fig. 3.14**. The XRD spectrum of $MnFe_2O_4$ display peaks at 2θ = 30.38°, 35.14°, 37.29°,43.31, 53.86°, 57.41° and 63.03° corresponding to (220), (311), (222), (400), (422), (511) and (440) spinel phase (JCPDS No. 10–0319) [200]. The spectrum of **5**@$MnFe_2O_4$ displays an additional broad, amorphous peak that can be observed at 2θ = 18.31°, which is typical for Pcs [201].

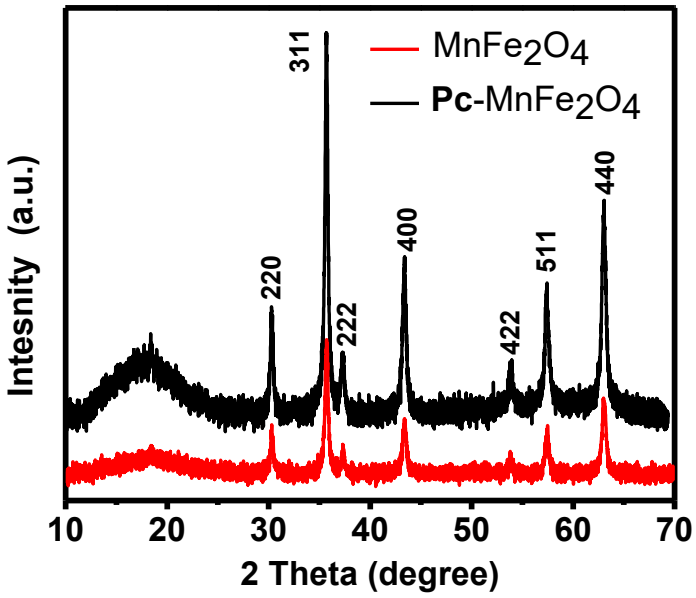

Fig. 3.14. XRD spectra of $MnFe_2O_4$, and **5**@$MnFe_2O_4$

3.9. Transmission electron microscopy (TEM) analysis

Transmission electron microscopy was used to study the morphologies of the synthesized nanomaterials (g-C_3N_4 NS and $MnFe_2O_4$). TEM analysis of g-C_3N_4 QDs have been reported before, hence, were not studied in this thesis [170].

3.9.1. g-C_3N_4 NS and 6@g-C_3N_4 NS

The morphologies of the synthesized g-C_3N_4 were confirmed by TEM analysis. The TEM analysis of pristine g-C_3N_4 NS, g-C_3N_4 QDs and **6**@g-C_3N_4 NS was performed. The TEM analysis of **6**@g-C_3N_4 NS was used as an example for all the conjugates. **Fig. 3.15(a)** shows TEM image of the g-C_3N_4 NS, which appears as thin sheets with slight segregation. **Fig. 3.15(b**) shows the TEM image of **6**@g-C_3N_4 NS, which appears to be slightly aggregated with regard to pristine g-C_3N_4 NS due to the interaction between complex **6** and g-C_3N_4 NS. The **Fig. 3.15(c)** shows the morphology of the spherical dots. The morphology of **3**@g-C_3N_4 QDs, **4**@g-C_3N_4 QDs

and **7**@g-C_3N_4 QDs is not anticipated to differ from that of g-C_3N_4 QDs, hence TEM analyses of **3**@g-C_3N_4 QDs, **4**@g-C_3N_4 QDs and **7**@g-C_3N_4 QDs was not performed.

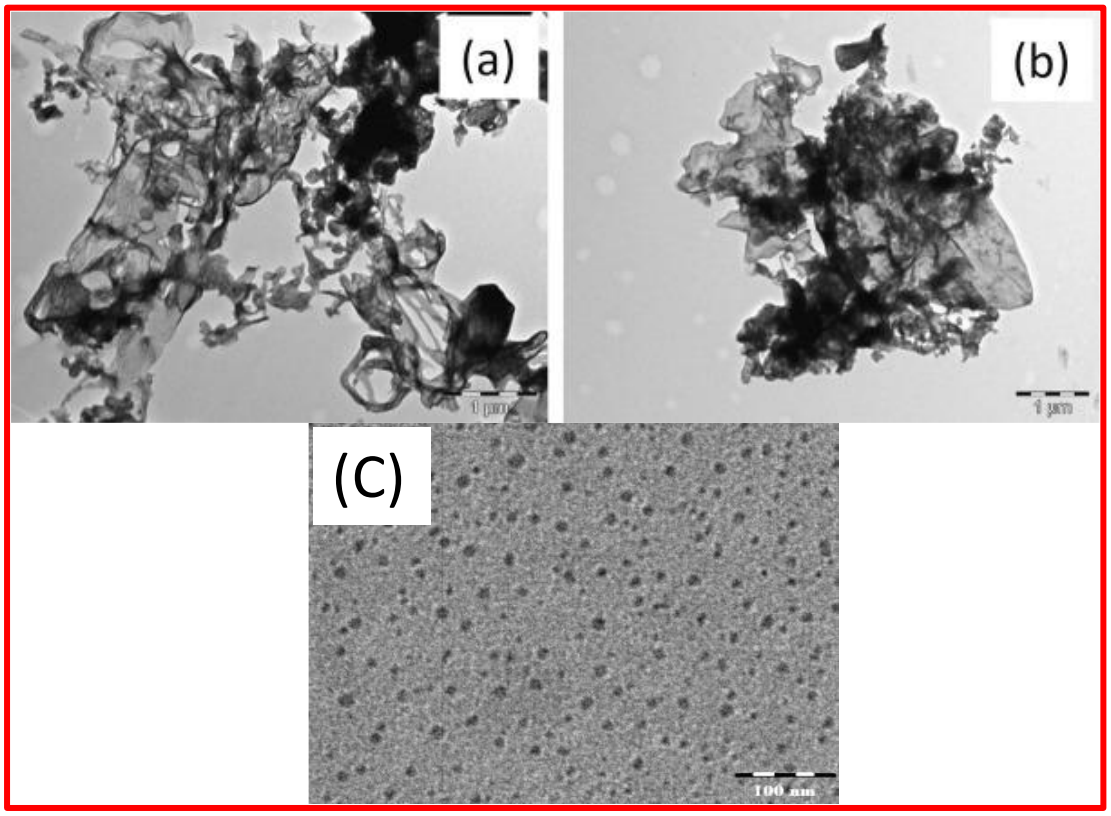

Fig.3.15. TEM images of g-C_3N_4 NS **(a)** and **6**@g-C_3N_4 NS **(b)**, g-C_3N_4 QDs

3.9.2. $MnFe_2O_4$ NPs and 5@$MnFe_2O_4$ conjugate

The TEM images (**Fig. 3.16A**) of the $MnFe_2O_4$ nanoparticles and **5**@$MnFe_2O_4$ conjugate show that the nanoparticles were segregated and irregular shaped. The average diameter (**Fig. 3.16B**) of the $MnFe_2O_4$ nanoparticles calculated from TEM results was 7.0 nm. The particles of the **5**@$MnFe_2O_4$ conjugate appeared to be highly aggregated with an average particle diameter of 35 nm. An increase in average particle diameter upon conjugation with the **5** complex is due to aggregation.

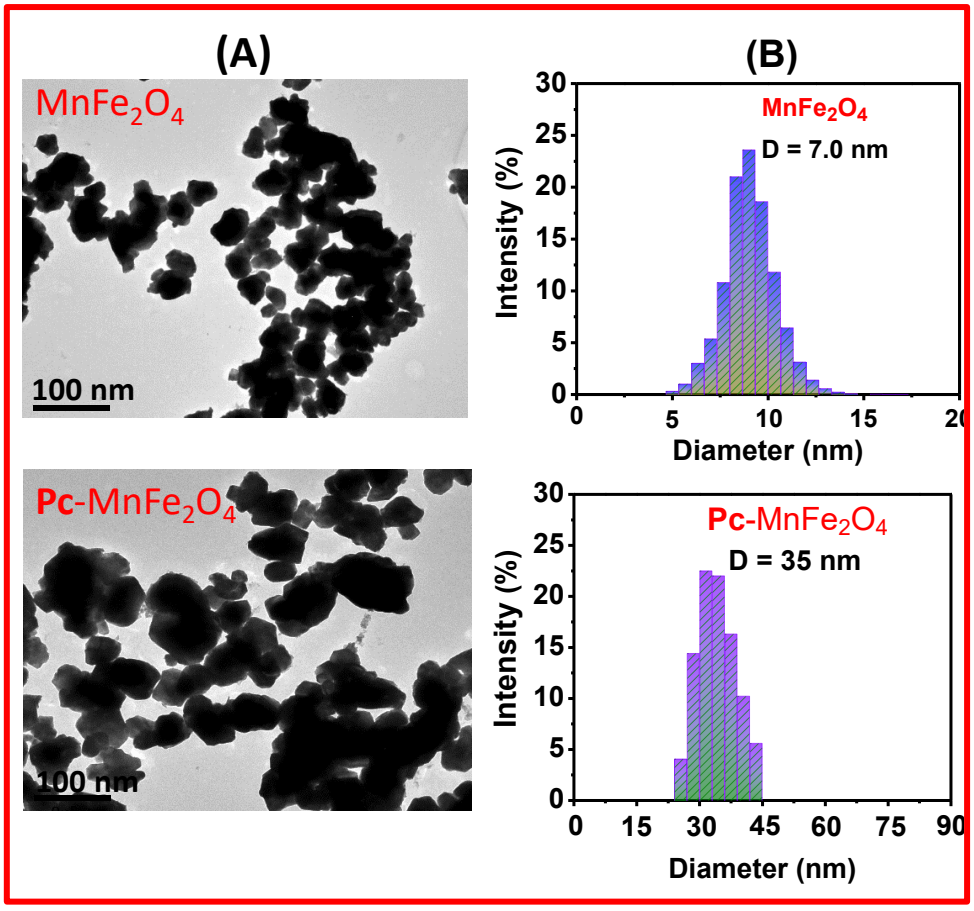

Fig.3.16. TEM images of $MnFe_2O_4$ NPs and **5**@$MnFe_2O_4$ conjugate **(a)** and respective particle sizes histograms **(b)**

3.10. Dynamic light scattering (DLS) analysis

3.10.1. DLS analysis of g-C_3N_4 QDs and 7@g-C_3N_4 QDs

The DLS spectra of the pristine g-C_3N_4 QDs and the conjugate of the complex **7** and g-C_3N_4 QDs in DMSO are shown in **Fig. 3.17**. The particle size of the pristine g-C_3N_4 QDs was recorded to be 23.6 nm. Upon conjugation of complex **7** with g-C_3N_4 QDs an increase in particle size was recorded. The particle size of the **7**@g-C_3N_4 QDs conjugate was recorded to be 39.2 nm, with the increase being most like due to aggregation.

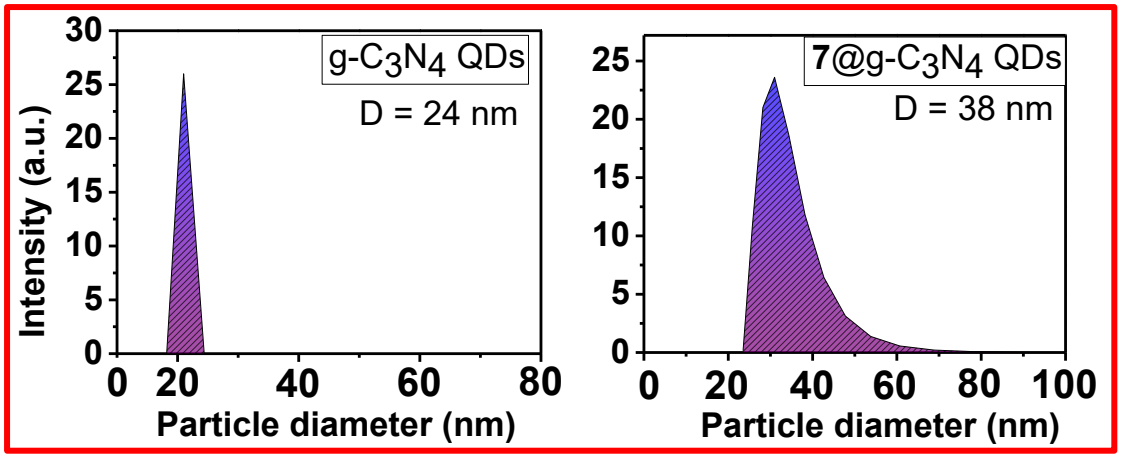

Fig. 3.17. DLS spectra of g-C_3N_4 QDs and **7**@g-C_3N_4 QDs conjugate

3.10.2. DLS analysis of $MnFe_2O_4$ NPs and 5@$MnFe_2O_4$ conjugate

The DLS was used to examine the average particle sizes of the $MnFe_2O_4$ NPs and **5**@$MnFe_2O_4$ conjugate. The DLS spectra in water are shown in **Fig. 3.18**. In general, catalysts with smaller particle sizes tend to be more catalytically active due to the large number of available active sites [202]. The average particle size of the $MnFe_2O_4$ NPs was found to be 17.1 nm and for **5@**$MnFe_2O_4$ conjugate was 26.3 nm. An apparent increase in particle diameter upon conjugation is due to the large number of the complex **5** molecules binding to the nanoparticles [169] and possibly aggregation.

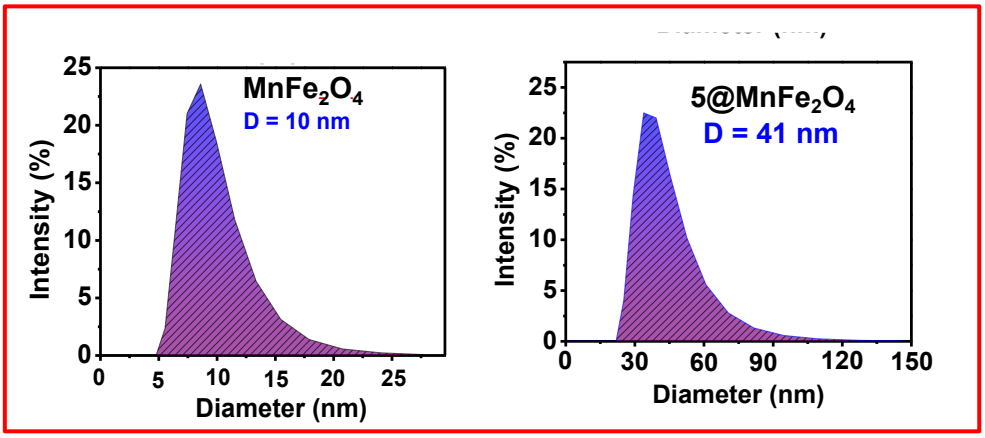

Fig.3.18. DLS spectra of $MnFe_2O_4$ NPs and **5**@$MnFe_2O_4$ conjugate

3.11. Summary of the chapter

In this Chapter, the syntheses of a porphyrin (**7**) and some phthalocyanines (**1-6**) and their characterizations were discussed. The conjugates of complexes **3-6** with g-C_3N_4 NS, complexes **3**, **4** and **7** with g-C_3N_4 QDs and complex **5** with $MnFe_2O_4$ nanoparticles through an amide bond were successfully synthesized as shown by FT-IR and XPS. The ground state electronic absorption of complexes and their corresponding conjugates were studied using UV-Vis absorption. The interaction between the Pc complexes and g-C_3N_4 nanoparticles were studied using Raman spectroscopy. The particle diameters, crystalline structures and morphologies were studied using dynamic light scattering, XRD and TEM analysis.

Chapter four

This chapter provides details on the synthesis and characterisation of the nanofibers and their functionalized hybrids.

4.1. Functionalization of the electrospun nanofibers

In this study, TiO_2 nanofibers and ZnO nanofibers were utilized. TiO_2 nanofibers were first functionalized with complexes **1**-**7** through physical adsorption as described in **Section 2.5.1** and **Scheme 4.1**. TiO_2 nanofibers were also functionalized with complexes **3**-**6** through covalent linkage with an amide bond as described in **Section 2.5.2** and **Scheme 4.2**. The nanofibers were also functionalized with g-C_3N_4 NS, g-C_3N_4 QDs, $MnFe_2O_4$ NPs, and their respective conjugates as described in **Section 2.5.3**. The ZnO nanofibers were functionalized with complex **6**, g-C_3N_4 NS and **6**@g-C_3N_4 NS. The pristine and functionalized fibers were compared using various spectroscopic and microscopic techniques, **Table 5.1**.

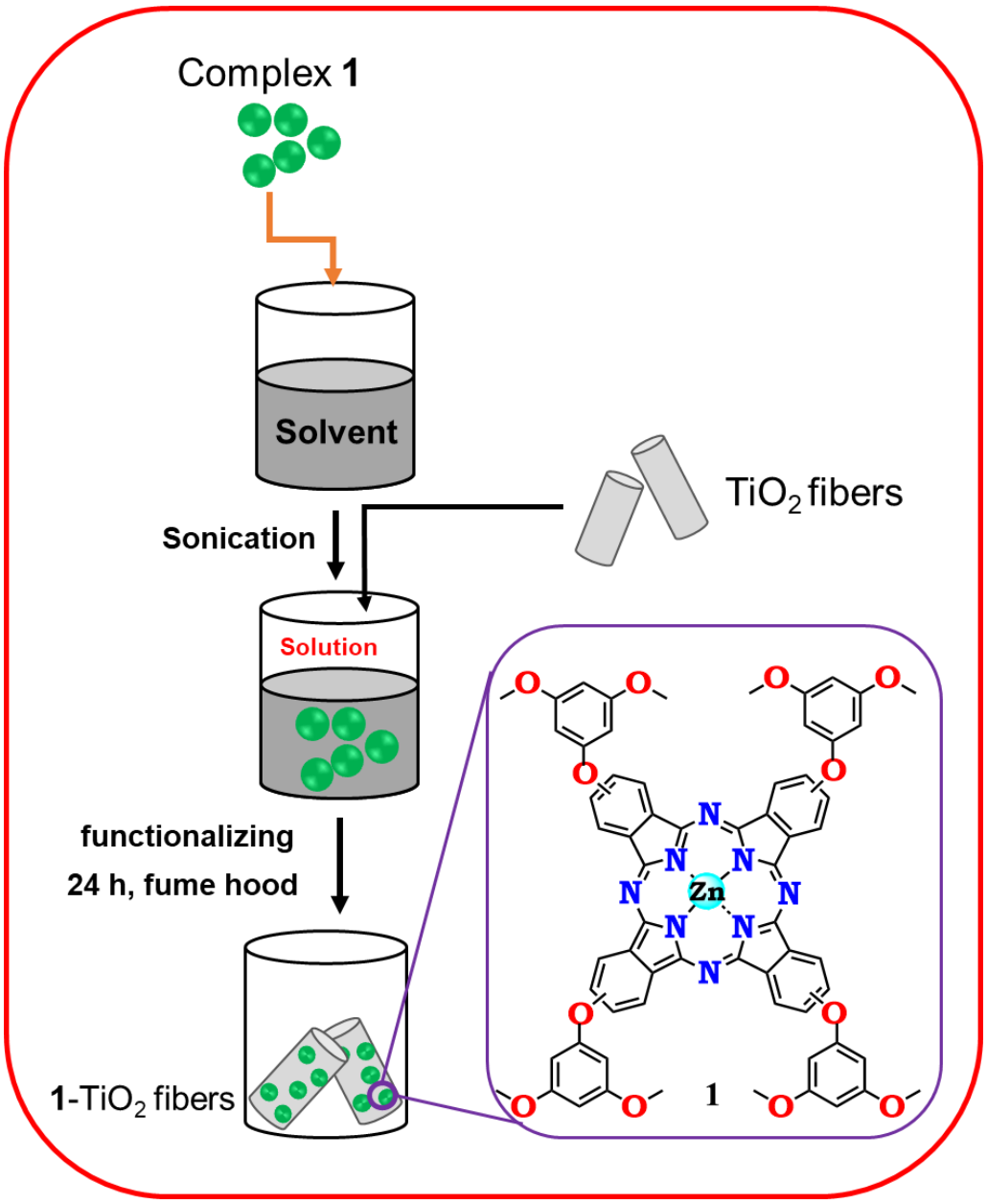

Scheme 4.1. Functionalization of TiO_2 fibers with complexes **1** as an example.

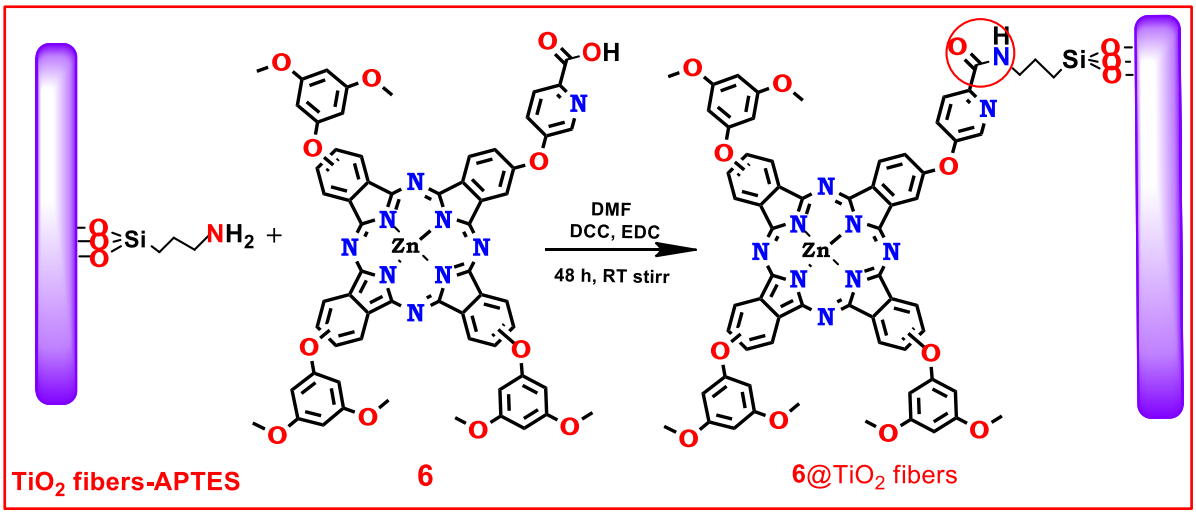

Scheme. 4.2. Functionalization of TiO_2 fibers with complex **6** through covalent linkage

4.2. Characterization of the electrospun nanofibers

Electrospun nanofibers were characterized by various spectroscopic and microscopic techniques to investigate their physicochemical properties prior to and post-functionalization with Pcs, NPs, and respective conjugates. The characterization of TiO_2 fibers, **1**-TiO_2 fibers and **2**-TiO_2 fibers were compared since complexes **1** and **2** are both A_4 complexes (tetra substituted Pcs). The characterization of physically adsorbed complexes **3**-**6** functionalized TiO_2 fibers (**3**-TiO_2 fibers, **4**-TiO_2 fibers, **5**-TiO_2 fibers, and **6**-TiO_2 fibers) are also compared since these complexes are all asymmetrical, and the functionalization of the fibers was through physical absorption. The properties of covalently linked TiO_2 fibers and **3**-**6** functionalized TiO_2 fibers (**3**@TiO_2 fibers, **4**@TiO_2 fibers, **5**@TiO_2 fibers, and **6**@TiO2 fibers) are compared since complexes **3**-**6** are asymmetrical Pcs and they were supported on nanofibers through covalent linkage.

The physicochemical properties of TiO_2 fibers and physically adsorbed complex **7** functionalized TiO_2 fibers (**7**-TiO_2 fibers) are compared separately since complex **7** is

a porphyrin and complexes **1**-**6** are Pcs. The physicochemical properties of the ZnO fibers and physically adsorbed complex **6** functionalized ZnO fibers are compared. The characterizations of g-C_3N_4 NS, g-C_3N_4 QDs and $MnFe_2O_4$ NPs functionalized TiO_2 are compared since they are all nanoparticles. The properties of ZnO fibers and g-C_3N_4 NS functionalized ZnO fibers are compared. Lastly, the properties of the functionalized TiO_2 fibers and ZnO fibers are compared.

4.2.1. Optical properties

Symmetrical Pcs, physically adsorbed on TiO_2 fibers

The absorption properties of the pristine TiO_2 fibers **1**-TiO_2 and **2**-TiO_2 fibers were characterized using solid-state UV-Vis spectroscopy or diffuse reflectance spectroscopy (DRS). The spectra are shown in **Fig. 4.1A**. The pristine TiO_2 fibers showed a peak at 347 nm, **Table 4.1**. Upon functionalization with complexes **1** and **2** to form **1**-TiO_2 fibers and **2**-TiO_2 fibers, Q-band absorption peaks (split bands) between 500 nm and 800 nm were observed in the solid-state spectra. The Q-bands are split due to aggregation, with the low energy peak being due to the monomer and the high energy peak being due to the aggregate. This is typical for MPcs in the solid state [203]. The B bands are observed at 347 nm and overlap with the peak for TiO_2 fibers.

The band gap energies of TiO2 fibers, **1**-TiO_2 and **2**-TiO_2 fibers were calculated using Tauc plots. The plots are presented in **Fig. 4.1B** and **Table 4.1**. The comparison of the band gap energies of the pristine TiO_2 fibers and functionalized fibers suggests that the functionalization of the fibers resulted in a decrease in band gap energies. This phenomenon is highly beneficial in photocatalytic processes [204] since it induces visible light photo-response properties of the semiconductor materials. In addition, the **2**-TiO_2 fibers displayed lower band gap energy than the **1**-TiO_2 fibers.

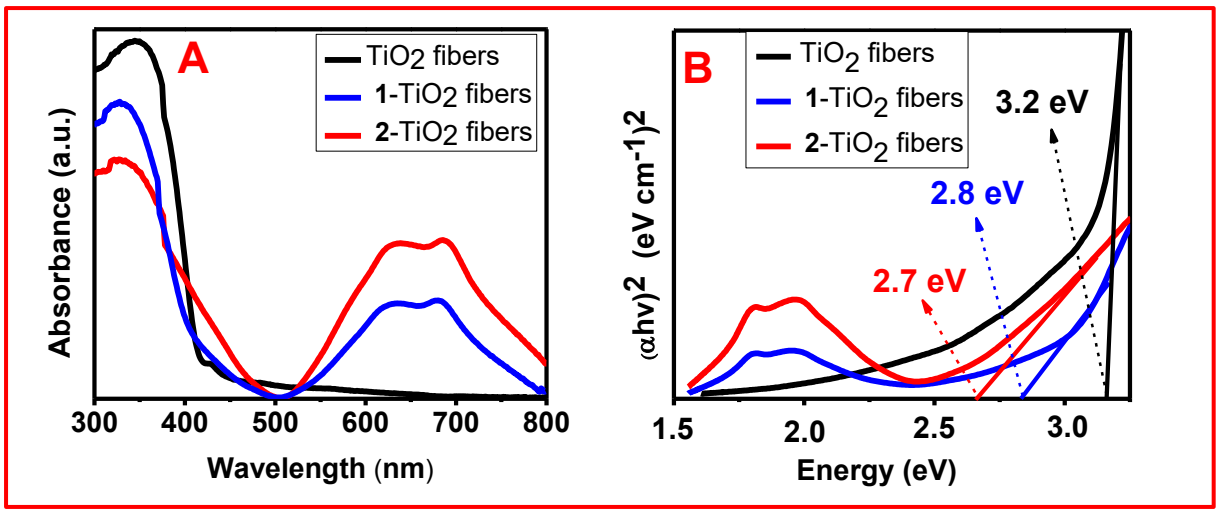

Fig. 4.1. Solid state UV-Vis absorption **A** and Tauc plots **B** of TiO_2 fibers, **1**-TiO_2 fibers and **2**-TiO_2 fibers

Table 4.1. Maximum absorption, band gap energies, diameters, surface area and pore volumes of the fibers.

Samples	λ_{max} (nm)	Band gap (eV)	Diameters (μm) SEM	BET surface area (m^2 g^{-1})	Pore volumes (cm^3 g^{-1})
TiO_2 fibers	347	3.2	0.5	14.60	0.281
1-TiO_2 fibers	500-800[b]	2.8	0.8	12.49	0.173
2-TiO_2 fibers	500-800[b]	2.7	0.8	11.55	0.159
3- TiO_2 fibers	550-750[b]	2.8	---	---	---
4- TiO_2 fibers	550-750[b]	2.7	---	---	---
5-TiO_2 fibers	550-750[b]	2.8	0.9	---	---
6- TiO_2 fibers	550-750[b]	2.8	---	---	---
7-TiO_2 fibers	424[a]	2.7	1.2	---	---
3@TiO_2 fibers	550–750[b]	2.5	0.7	12.3	0.187
4@TiO_2 fibers	550–750[b]	2.4	0.7	12.8	0.182
5@TiO_2 fibers	550–750[b]	2.3	0.7	11.7	0.173
6@TiO_2 fibers	550–750[b]	2.4	0.7	12.1	0.151
g-C_3N_4 NS-TiO_2 fibers	<400	2.7	1.1	12.7	0.194
3@g-C_3N_4 NS-TiO_2 fibers	550 -750[b]	2.7	1.7	10.3	0.143
4@g-C_3N_4 NS-TiO_2 fibers	550 -750[b]	2.7	1.6	10.8	0.107
5@g-C_3N_4 NS-TiO_2 fibers	550 -750[b]	2.8	1.7	10.4	0.092

Samples	λ_{max} (nm)	Band gap (eV)	Diameters (μm)	BET surface area (m^2 g^{-1})	Pore volumes (cm^3 g^{-1})
6@g-C_3N_4 NS-TiO_2 fibers	550 -750[b]	2.8	1.8	12.7	0.064
g-C_3N_4 QDs-TiO_2 fibers	400	2.7	1.4	---	---
3@g-C_3N_4 QDs-TiO_2 fibers	550 -750[b]	2.7	---	---	---
4@g-C_3N_4 QDs-TiO_2 fibers	550 -750[b]	2.7	---	---	---
7@g-C_3N_4 QDs-TiO_2 fibers	450[a]	2.1	1.6	---	---
$MnFe_2O_4$-TiO_2 fibers	360	2.5	1.1	2.79	0.181
5@$MnFe_2O_4$-TiO_2 fibers	550 -750[b]	2.5	1.5	9.37	0.143
ZnO fibers	380	3.4	1.1	13.3	0.28
g-C_3N_4 NS-ZnO fibers	380	3.3	1.3	11.7	0.14
6-ZnO fibers	550 -750[b]	2.5	1.7	12.4	0.11
6@g-C_3N_4 NS-ZnO fibers	550 -750[b]	2.3	2.0	9.11	0.064

a = Soret band, b = Q- band

Asymmetrical Pcs, physically adsorbed on TiO_2 fibers

The solid-state UV-Vis absorption spectra of TiO_2 fibers and **3**-TiO_2 fibers, **4**-TiO_2 fibers, **5**-TiO_2 fibers, and **6**-TiO_2 fibers obtained through physical adsorption are shown in **Fig. 4.2A**. The **3**-TiO_2 fibers, **4**-TiO_2 fibers, **5**-TiO_2 fibers, and 6-TiO2 fibers display broad, split absorption peaks between 550 and 750 nm assigned to the Q-bands of the aggregated Pcs [203].

The band gap energies were obtained from Tauc plots. The band gap energies are displayed in **Fig. 4.2B** and **Table 4.1**. The band gap energies of the functionalized TiO_2 fibers were lower than those of pristine TiO_2 fibers.

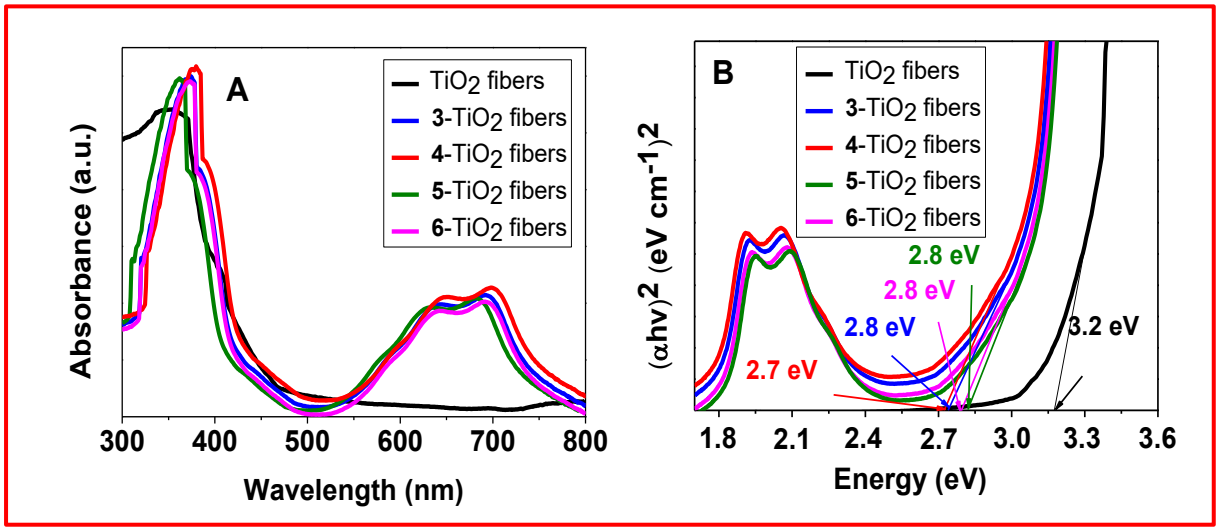

Fig. 4.2. Solid state UV-Vis absorption **A** and Tauc plots **B** of TiO_2 fibers, **3**-TiO_2 fibers, **4**-TiO_2 fibers, **5**-TiO_2 fibers and **6**-TiO_2 fibers

Asymmetrical Pcs, covalently linked on TiO_2 fibers

The solid-state UV-Vis absorption spectra of TiO_2 fibers and **3**@TiO_2 fibers, **4**@TiO_2 fibers, **5**@TiO_2 fibers and **6**@TiO_2 fibers obtained through covalent linkage using an amide bond are shown in **Fig. 4.3A**. The functionalized fibers (**3**@TiO_2 fibers, **4**@TiO_2

fibers, **5**@TiO_2 fibers, and 6@TiO_2 fibers), with respect to pristine TiO_2 fibers, display broad Q-bands between 520 nm and 750 nm. Which are split due to aggregation.

The band gap energies obtained from Tauc plots are displayed in **Fig. 4.3B** and **Table 4.1.** The functionalization of TiO_2 fibers (3.20 eV) resulted in a decrease in band gap energies compared to that obtained from pristine TiO_2 fibers.

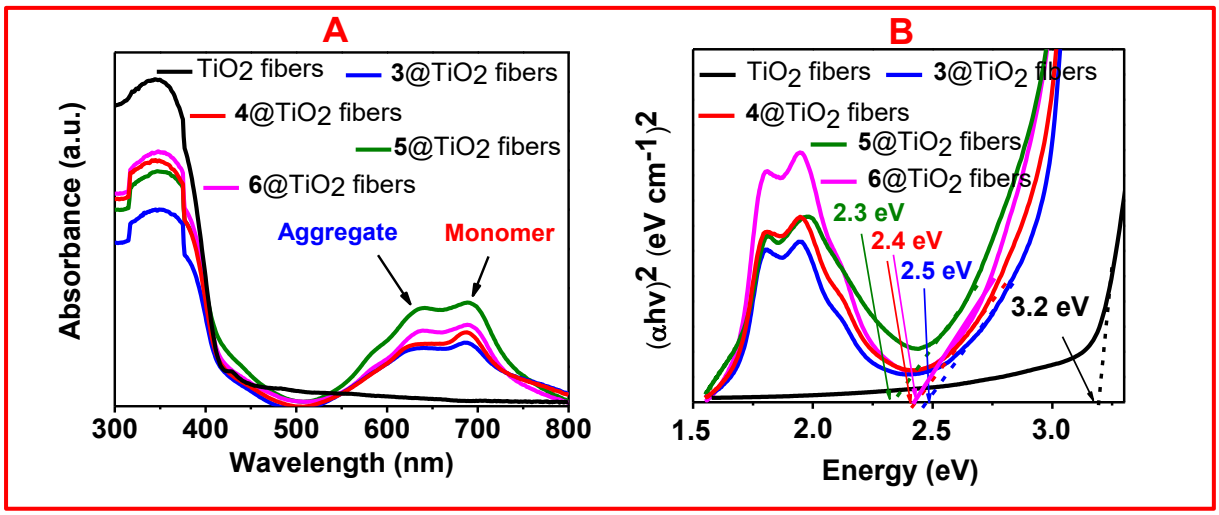

Fig. 4.3. Solid state UV-Vis absorption **A** and Tauc plots **B** of TiO_2 fibers, **3**@TiO_2 fibers, **4**@TiO_2 fibers, **5**@TiO_2 fibers and **6**@TiO_2 fibers

Asymmetric Pcs covalently linked to g-C_3N_4 NS and adsorbed on TiO_2 fibers

The absorption spectra of g-C_3N_4 NS-TiO_2 fibers display absorption below 400 nm. The solid-state UV-Vis spectra of **3**@g-C_3N_4 NS-TiO_2 fibers, **4**@g-C_3N_4 NS-TiO_2 fibers, **5**@g-C_3N_4 NS-TiO_2 fibers, **6**@g-C_3N_4 NS-TiO_2 fibers display absorption below 400 nm which is due to B-band and broad split bands between 550 nm and 750 nm which are due to Q-bands of the aggregated Pcs (**Fig. 4.4A**). The band gap energies are shown in **Fig. 4.4B** and **Table 4.1**. The band gap energies of **3**@g-C_3N_4 NS-TiO_2 fibers, **4**@g-C_3N_4 NS-TiO_2 fibers, **5**@g-C_3N_4 NS-TiO_2 fibers and **6**@g-C_3N_4 NS-TiO_2 fibers were lower than those obtained from pure TiO_2 fibers.

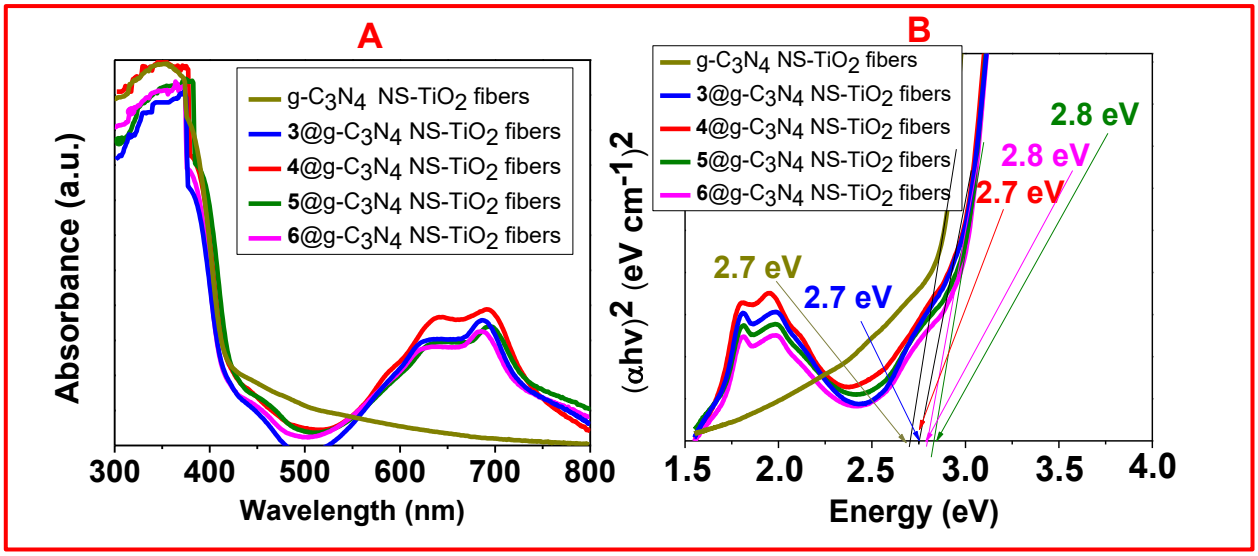

Fig. 4.4. Solid state UV-Vis absorption **A** and Tauc plots **B** g-C_3N_4 NS-TiO_2 fibers, **3**@g-C_3N_4 NS-TiO_2 fibers, **4**@g-C_3N_4 NS-TiO_2 fibers, **5**@g-C_3N_4 NS-TiO_2 fibers and **6**@g-C_3N_4 NS-TiO_2 fibers

Pcs covalently linked to g-C_3N_4 QDs and adsorbed on TiO_2 fibers

The absorption spectra of TiO_2 fibers, g-C_3N_4 QDs-TiO_2 fibers display absorption below 400 nm. The solid-state UV-Vis spectra of **3**@g-C_3N_4 QDs-TiO_2 fibers, **4**@g-C_3N_4 QDs-TiO_2 fibers display absorption below 400 nm due to B-band and broad split bands between 550 and 750 nm which are due to Q-bands of the aggregated Pcs (**Fig. 4.5A** and **Table 4.1**). The band gap energies (**Fig. 4.5B** and **Table 4.1**) of the composites were remarkably lower than those obtained from pure TiO_2 fibers.

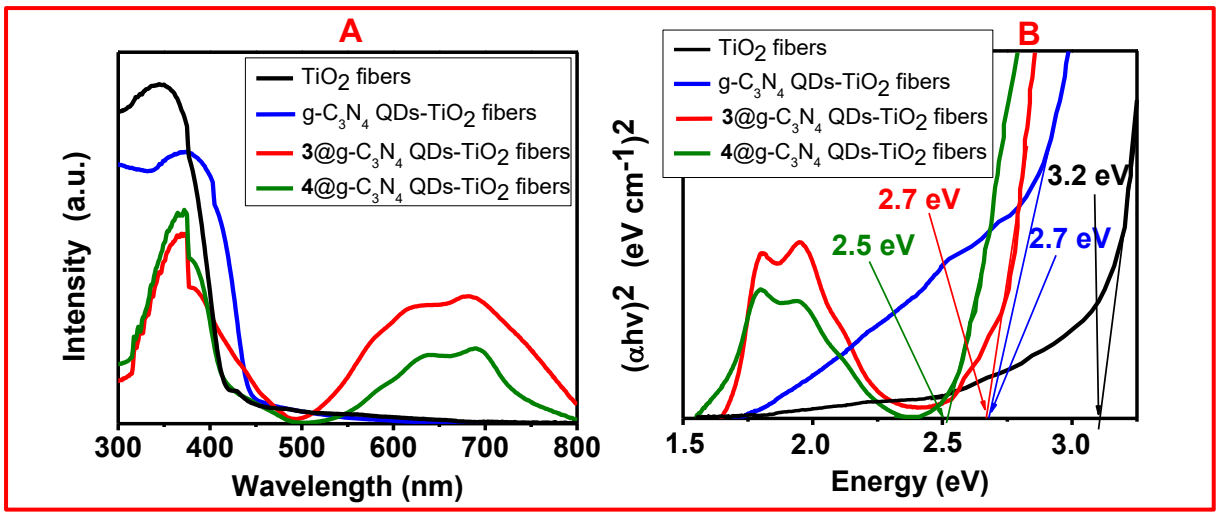

Fig. 4.5. Solid state UV-Vis absorption **A** and Tauc plots **B** of TiO_2 fibers, g-C_3N_4 QDs-TiO_2 fibers, **3**@g-C_3N_4 QDs-TiO_2 fibers, **4**@g-C_3N_4 QDs-TiO_2 fibers.

Complex 5 linked to $MnFe_2O_4$ and adsorbed on TiO_2 fibers

5-TiO_2 fibers, $MnFe_2O_4$-TiO_2 fibers and **5**@$MnFe_2O_4$-TiO_2 fibers showed broad bands below 400 nm due to the presence of TiO_2 fibers and the B-band. The spectra of **5**-TiO_2 and **5**@$MnFe_2O_4$-TiO_2 fibers showed broad and split Q bands between 550 and 750 nm, typical of Pcs in the solid state (**Fig. 4.6A** and **Table 4.1**).

The hybridization of TiO_2 fibers with $MnFe_2O_4$ NPs, **5** and **5**@$MnFe_2O_4$ resulted in a decrease in band gap energies of $MnFe_2O_4$-TiO_2 fibers, **5**-TiO_2 fibers and **5**@$MnFe_2O_4$-TiO_2 fibers compared to pristine TiO_2 fibers. The results reveal a decreased band gap energy for **5**@$MnFe_2O_4$-TiO_2 fibers (**Fig. 4.6B** and **Table 4.1**).

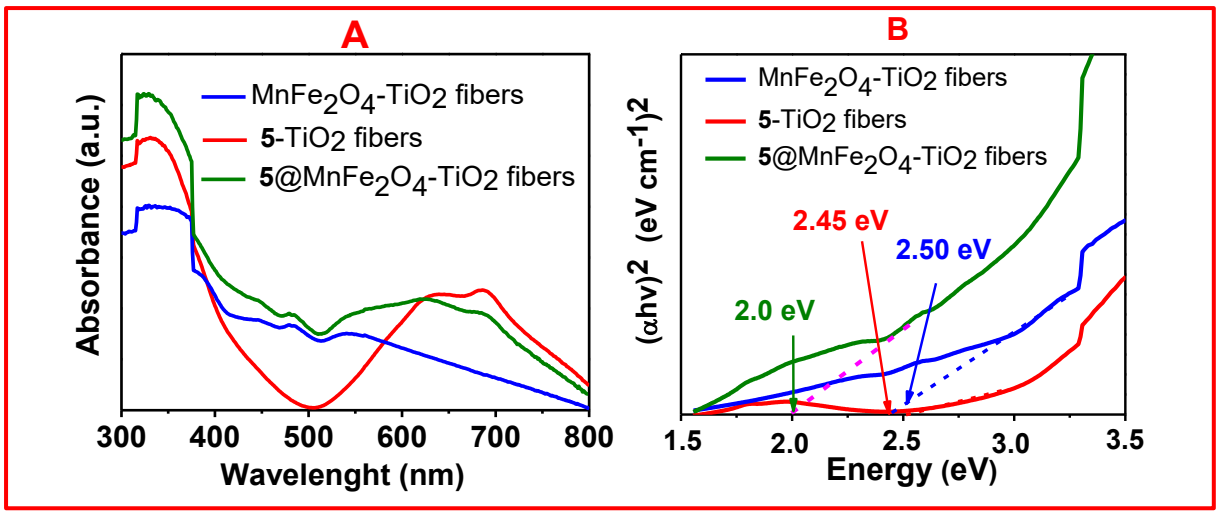

Fig. 4.6. Solid state UV-Vis absorption **A** and Tauc plots **B** of $MnFe_2O_4$ NPs-TiO_2 fibers, **5**-TiO_2 fibers and **5**@$MnFe_2O_4$ NPs-TiO_2 fibers

Porphyrin linked to g-C_3N_4 QDs and adsorbed to TiO_2 fibers

The absorption spectrum of **7**-TiO_2 fibers shows an additional band at 437 nm which is due to the Soret band of the porphyrin, **Fig. 4.1**. Two additional bands were observed for **7**-TiO_2 fibers at 564 nm and 613 nm, corresponding to porphyrin Q-bands. The absorption spectrum of **7**@g-C_3N_4 QDs-TiO_2 fibers shows shifted Q bands at 580 and 628 nm compared to **7**-TiO_2 fibers and a shift in the Soret band to 450 nm, (**Fig. 4.7A** and **Table 4.1**). The band gap energy of **7**@g-C_3N_4 QDs-TiO_2 fibers was lower than those obtained from g-C_3N_4 QDs-TiO_2 fibers and **7**-TiO_2 fibers, **Table 4.1**.

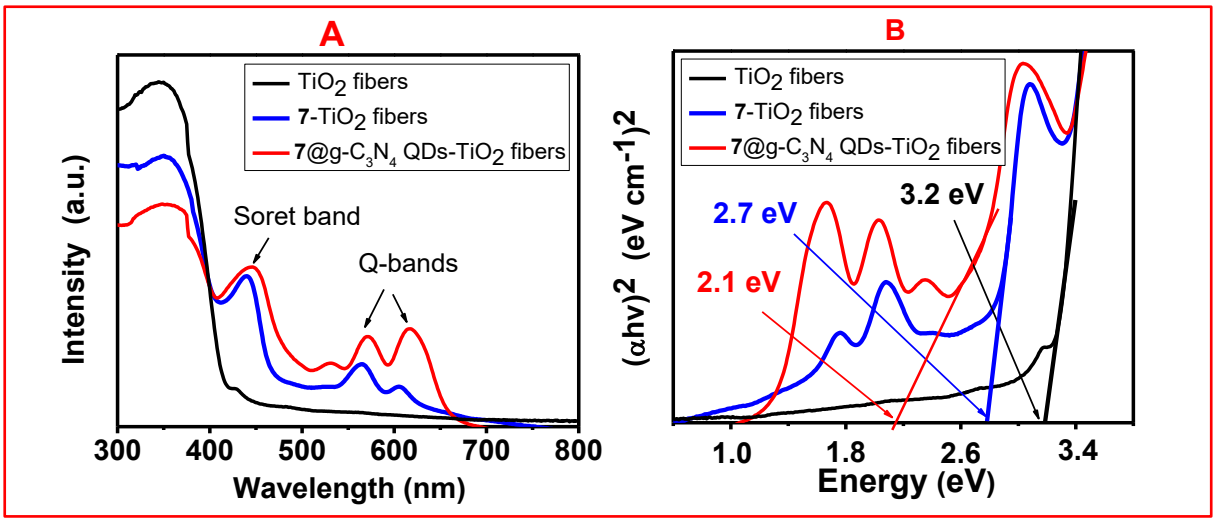

Fig. 4.7. Solid state UV-Vis absorption **A** and Tauc plots **B** of TiO_2 fibers, **7**-TiO_2 fibers and **7**@g-C_3N_4 QDs-TiO_2 fibers.

Complex 6 linked to g-C_3N_4 NS and adsorbed on ZnO fibers

The absorption properties of ZnO fibers, g-C_3N_4 NS-ZnO fibers, **6**-ZnO fibers and **6**@g-C_3N_4 NS-ZnO fibers are shown **Fig. 4.8A**. The ZnO fibers and g-C_3N_4 NS-ZnO fibers show absorption below 400 nm. The **6**-ZnO fibers and 6@g-C3N4 NS-ZnO fibers show an anticipated broad absorption band (Q-band) between 550 and 750 nm due to the presence of complex **6**.

The band gap energies of the ZnO fibers, g-C_3N_4 NS-ZnO fibers, **6**-ZnO fibers and **6**@g-C_3N_4-ZnO fibers (**Fig. 4.8B** and **Table 4.1**) were 3.4, 3.3, 2.5 and 2.3 eV, respectively. The functionalization of the fibers resulted in a decrease in band gap energy, which is more apparent in the presence of complex **6**.

ZnO fibers have slightly higher band gap energy than TiO_2 fibers. This difference in band gap is primarily due to the different atomic orbitals involved in the valence and conduction bands of each material [205].

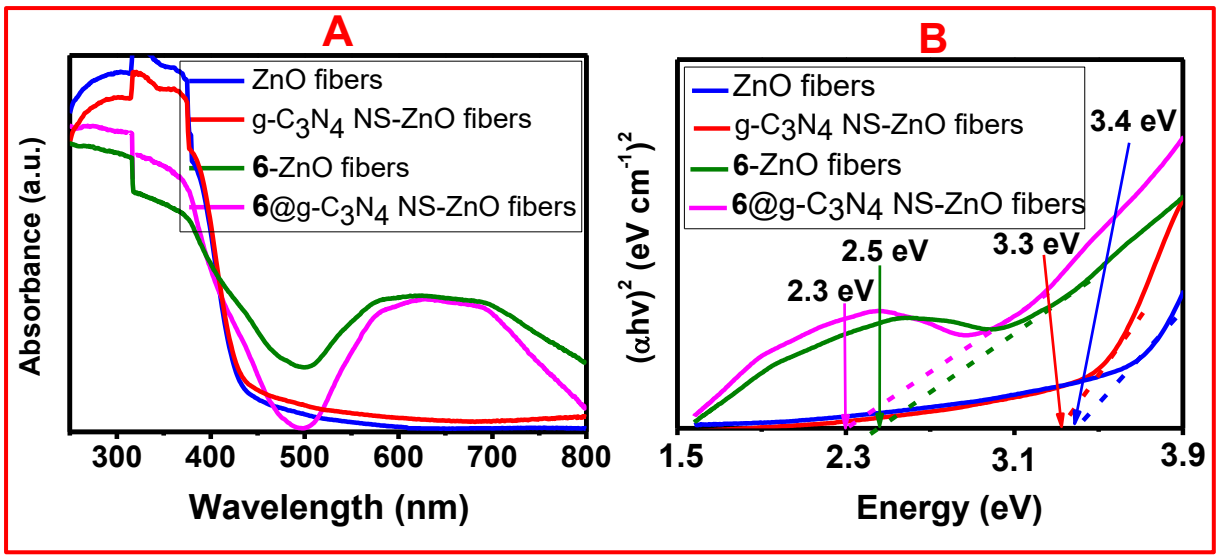

Fig. 4.8. Solid state UV-Vis absorption **A** and Tauc plots **B** of ZnO fibers, g-C_3N_4 QDs-ZnO fibers, **6**-ZnO fibers and **6**@g-C_3N_4 QDs- ZnO fibers.

4.2.2. X-Ray photoelectron spectroscopy (XPS)

XPS was used to confirm the conjugation between complexes **3** and **6** with TiO_2 fibers in **3**@TiO_2 fibers and **6**@TiO_2 fibers as examples (**Fig. 4.9**). The results were used for all the hybrids. The XPS survey scan spectra of **3**@TiO_2 fibers and **6**@TiO_2 fibers (**Fig. 4.9**) confirm the presence of Ti, Si, O, C and N elements. The C 1s and N 1s were deconvoluted to identify bonding states (**Fig. 4.9**). The C 1s spectra show bonding states corresponding to C-C, C=C, C-N/C=N, C-O- and C=O bonds [206] for both **3**@TiO_2 fibers and **6**@TiO_2 fibers. The deconvoluted N 1s spectra show the bonding states corresponding to N-C, N=C and N-C=O bonds, respectively [199]. The presence of C-N/C=N in the deconvoluted C 1s spectra, N-C and N-C=O in the N 1s spectra confirm the successful formation of an amide bond between TiO_2 fibers and the **Pc** complexes.

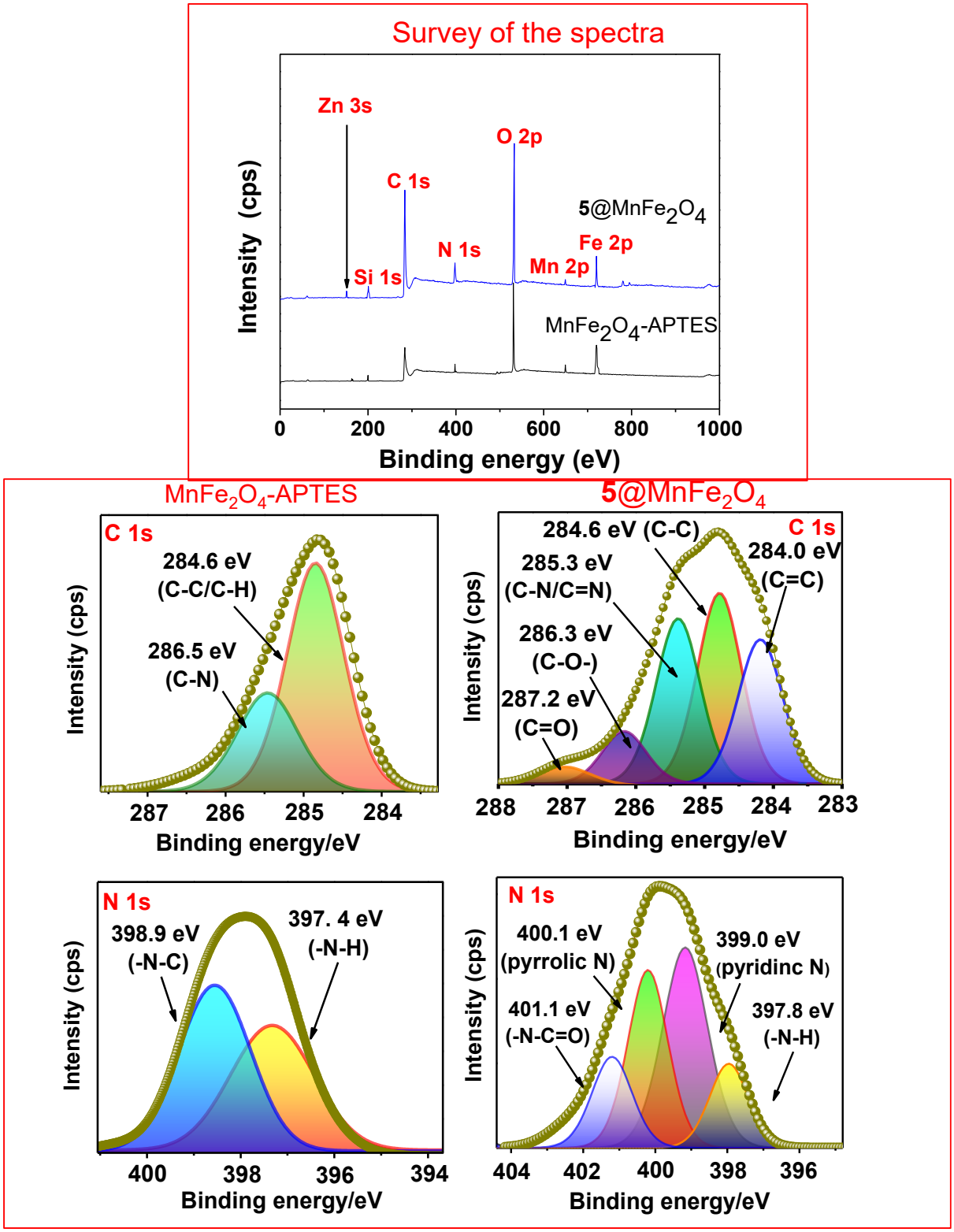

Fig. 4.9. XPS survey spectra, deconvulated C 1s and N 1s spectra of **3**@TiO_2 fibers and **6**@TiO_2 fibers

4.2.3. X-ray diffraction (XRD)

The XRD properties of the fibers were studied to identify phases of the fibers and the effect of functionalization on crystallinity. The XRD properties of TiO_2 fibers, **1**-TiO_2 and **2**-TiO_2 fibers (containing symmetrical Pc) were first compared. Afterward, the XRD properties of TiO_2 fibers, **3**@TiO2, **4**@TiO2 fibers, **5**@TiO2 fibers, and **6**@TiO_2 fibers were compared. The XRD properties of g-C_3N_4 NS-TiO_2 fibers, **3**@g-C_3N_4 NS-TiO_2 fibers, **4**@g-C_3N_4 NS-TiO_2 fibers, **5**@g-C_3N_4 NS-TiO_2 fibers and **6**@g-C_3N_4 NS-TiO_2 fibers were compared followed by comparison of TiO_2 fibers, g-C_3N_4 QDs-TiO_2 fibers, **3**@g-C_3N_4 QDs-TiO_2 fibers, **4**@g-C_3N_4 QDs-TiO_2 fibers. The XRD patterns of TiO_2 fibers, $MnFe_2O_4$ NPs-TiO_2 fibers, **5**-TiO_2 fibers and **5**@$MnFe_2O_4$ NPs-TiO_2 fibers were compared. To investigate the effect of the complex **7** and g-C_3N_4 QDs, the XRD properties of g-C_3N_4 QDs-TiO_2 fibers, **7** -TiO_2 fibers and **7**@g-C_3N_4 QDs-TiO_2 fibers were compared. To investigate the effect of the complex **6** and g-C_3N_4 NS on the properties of ZnO fibers, the XRD patterns of ZnO fibers, g-C_3N_4 QDs-ZnO fibers, **6**-ZnO fibers and **6**@g-C_3N_4 QDs-ZnO fibers were compared.

TiO_2 fibers, 1-TiO_2 and 2-TiO_2 fibers

The XRD spectra of the pristine TiO_2 fibers, **1**-TiO_2 and **2**-TiO_2 fibers are shown in **Fig. 4.10**. The spectra display sharp diffraction peaks characteristic of the highly crystalized, pure and structural ordered material at 2θ = 25.2, 37.3, 48.5, 54.7, 55.8, 63.3, 69.3, 70.1, 75.8 and 83.2° corresponding to (101), (004), (200), (105), (211), (204), (116), (220), (215) and (303) of tetragonal planes of anatase TiO_2 [207,208]. (JCPDS file no. 21–1272) [208].

The functionalization of TiO_2 fibers with complexes **1** and **2** resulted in a decrease in the crystalline structure of the fibers. This was observed by a notable decrease in XRD

peak intensities. The Pc peaks, which are usually broad due to amorphous nature with a peak near 2θ = 30° [201], could not be observed probably due to the small amount of Pc complexes compared to TiO_2 fibers.

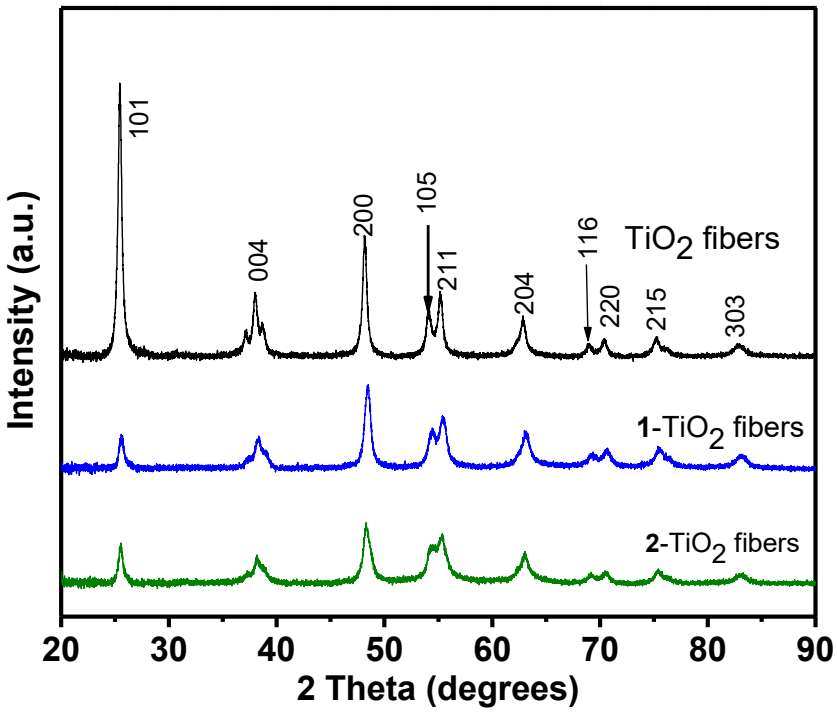

Fig. 4.10. XRD patterns of TiO_2 fibers, **1**-TiO_2 fibers, **2**-TiO_2 fibers, **1**-TiO_2 fibers used photo, **2**-TiO_2 fibers used photo, **1**-TiO_2 fibers used sono, **2**-TiO_2 fibers used sono.

3@TiO_2 fibers, 4@TiO_2 fibers, 5@TiO_2 fibers and 6@TiO_2 fibers

TiO_2 fibers display intense diffraction peaks corresponding to the anatase phase. The **3**@TiO_2 fibers, **4**@TiO_2 fibers, **5**@TiO_2 fibers and **6**@TiO_2 fibers also display peaks corresponding to anatase with reduced intensity, suggesting that functionalization through an amide bond also resulted in a decrease in crystallinity of TiO_2 fibers, **Fig. 4.11**.

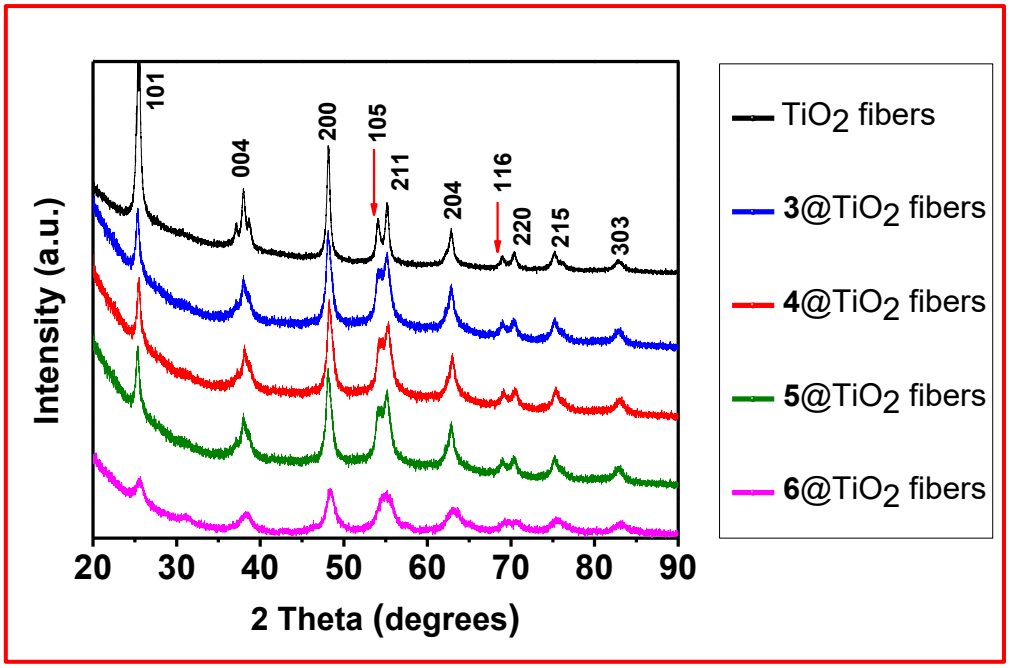

Fig. 4.11. XRD patterns of TiO_2 fibers, **3**@TiO_2 fibers, **4**@TiO_2 fibers, **5**@TiO_2 fibers and **6**@TiO_2 fibers.

g-C_3N_4 NS-TiO_2 fibers, 3@g-C_3N_4 NS-TiO_2 fibers, 4@g-C_3N_4 NS-TiO_2 fibers, 5@g-C_3N_4 NS-TiO_2 fibers and 6@g-C_3N_4 NS-TiO_2 fibers

The XRD spectra of TiO_2 fibers, g-C_3N_4 NS-TiO_2 fibers, **3**@g-C_3N_4 NS-TiO_2 fibers, **4**@g-C_3N_4 NS-TiO_2 fibers, **5**@g-C_3N_4 NS-TiO_2 fibers and **6**@g-C_3N_4 NS-TiO_2 fibers are shown in **Fig.4.12**. All the spectra show peaks corresponding to the anatase phase. The intensities of the peaks of the functionalized fibers were low, most significantly for **6**@g-C_3N_4 NS-TiO_2 fibers.

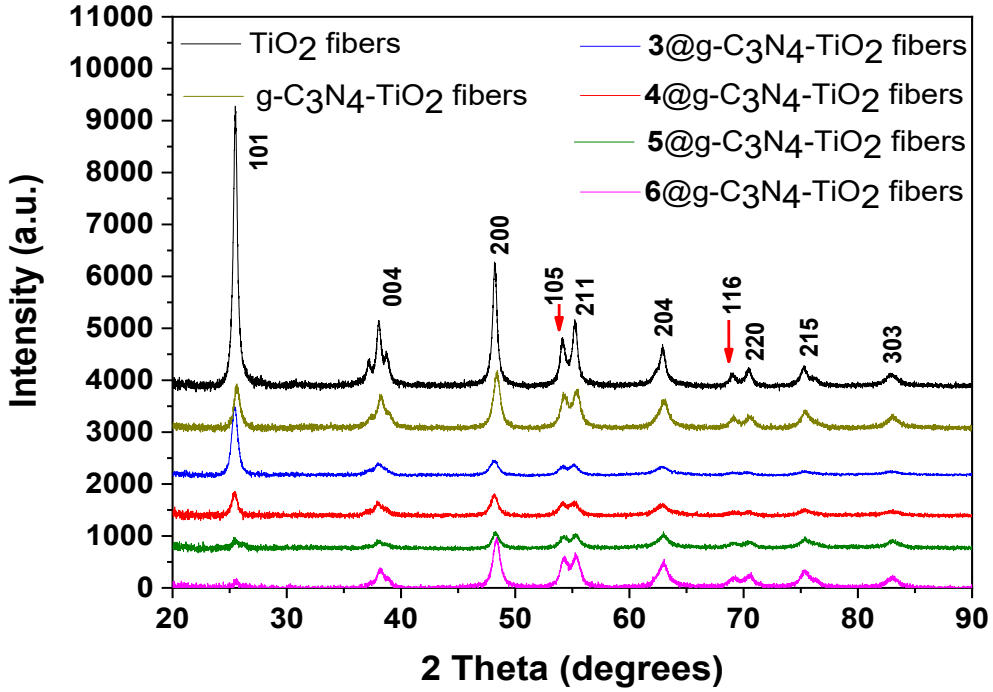

Fig. 4.12. XRD patterns of TiO_2 fibers, g-C_3N_4 NS-TiO_2 fibers, **3**@g-C_3N_4 NS-TiO_2 fibers, **4**@g-C_3N_4 NS-TiO_2 fibers, **5**@g-C_3N_4 NS-TiO_2 fibers and **6**@g-C_3N_4 NS-TiO_2 fibers.

g-C_3N_4 QDs-TiO_2 fibers, 3@g-C_3N_4 QDs-TiO_2 fibers, 4@g-C_3N_4 QDs-TiO_2 fibers

The XRD spectra of **3**@g-C_3N_4 QDs-TiO_2 fibers and **4**@g-C_3N_4 QDs-TiO_2 fibers are shown in **Fig. 4.13** and compared to that of pure TiO_2 fibers. All the spectra show peaks corresponding to the anatase phase. The intensities of the peaks of **3**@g-C_3N_4 QDs-TiO_2 fibers, **4**@g-C_3N_4 QDs-TiO_2 fibers were low compared to those of pristine TiO_2 fibers.

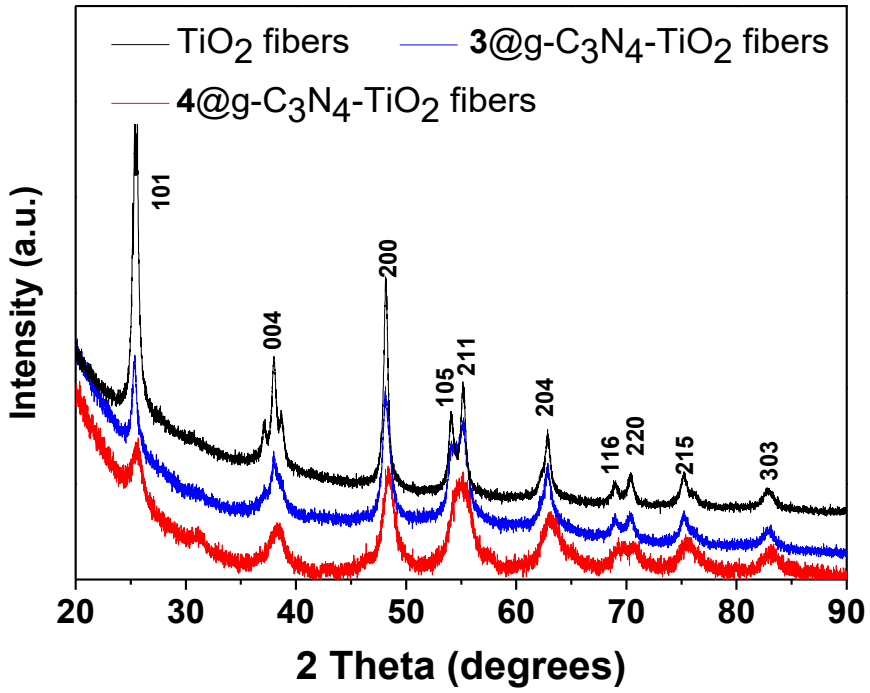

Fig. 4.13. XRD patterns of TiO_2 fibers, **3**@g-C_3N_4 QDs-TiO_2 fibers, **4**@g-C_3N_4 QDs-TiO_2 fibers

5-TiO_2 fibers, $MnFe_2O_4$-TiO_2 fibers, 5@$MnFe_2O_4$-TiO_2 fibers

5@TiO_2 fibers, $MnFe_2O_4$-TiO_2 fibers and **5**@$MnFe_2O_4$-TiO_2 fibers are shown in **Fig. 4.14** and compared to pure TiO_2 fibers. The spectrum of **5**-TiO_2 fibers also displays similar properties to pure TiO_2 fibers, however there is a decrease in crystallinity as judged by a significant decrease in XRD peak intensities. A similar observation was also noticed in the XRD spectra of $MnFe_2O_4$-TiO_2 fibers and **5**@$MnFe_2O_4$-TiO_2 fibers. In addition, two additional peaks corresponding to (220) and (400) miller indices of the spinel phase of $MnFe_2O_4$ are observed for $MnFe_2O_4$-TiO_2 fibers and **5**@$MnFe_2O_4$-TiO_2 fibers at 2θ = 30.3 and 44.9°, respectively.

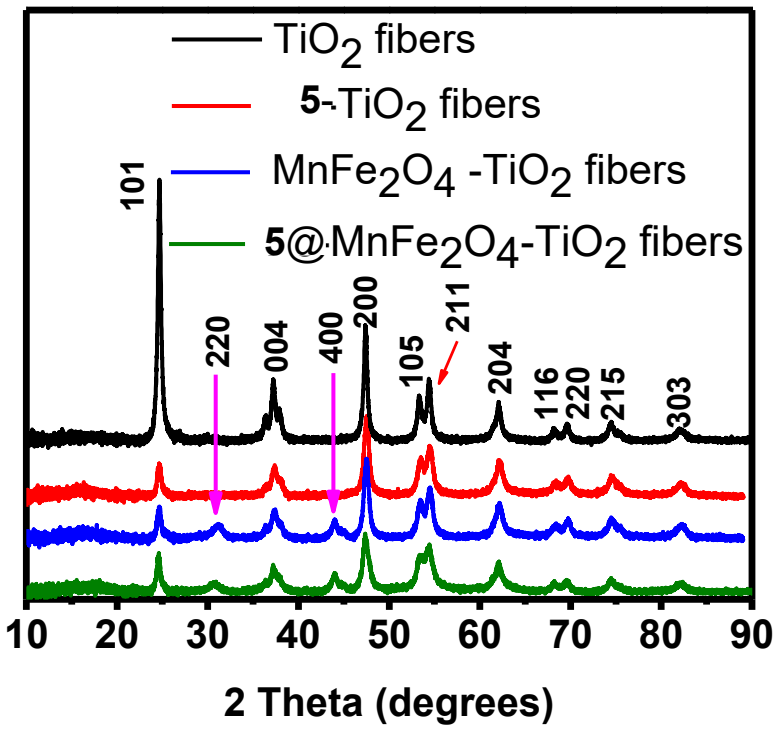

Fig. 4.14. XRD patterns of TiO_2 fibers, **5**-TiO_2 fibers, $MnFe_2O_4$-TiO_2 fibers, **5**@$MnFe_2O_4$-TiO_2 fibers

7-TiO_2 fibers, g-C_3N_4 QDs-TiO_2 fibers, 7@g-C_3N_4 QDs -TiO_2 fibers

The XRD spectrum of TiO_2 fibers was not discussed since it has been discussed in the previous sections. The XRD spectra of **7**-TiO_2 fibers and g-C_3N_4 QDs-TiO_2 fibers **(Fig. 4.15)** are compared with TiO_2 fibers. The XRD spectrum of **7**@g-C_3N_4 QDs-TiO2 fibers (**Fig. 4.15**) displays an additional broad diffraction peak at 27.5° which is due to the overlap between (002) peak of g-C_3N_4 QDs and a porphyrin, since porphyrins are known to display a broad diffraction peak below 30 °C.

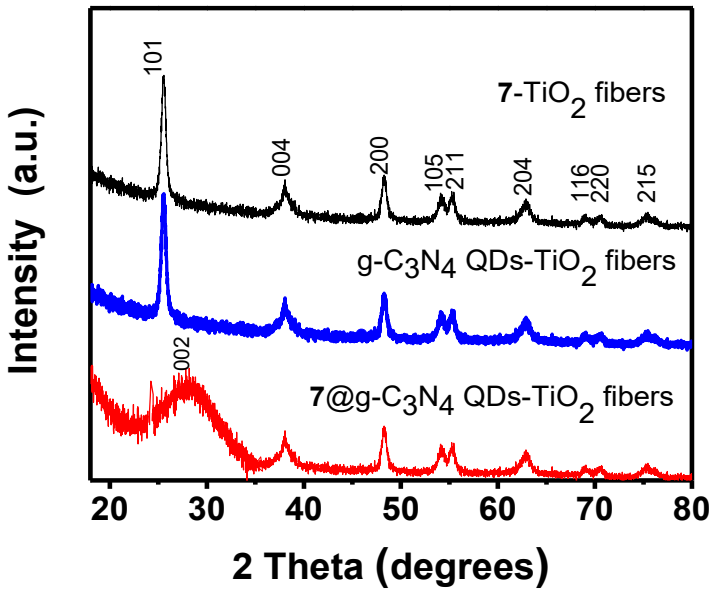

Fig. 4.15. XRD patterns of **7**-TiO_2 fibers, g-C_3N_4 QDs-TiO_2 fibers, **7**@g-C_3N_4 QDs-TiO_2 fibers

ZnO fibers, 6@ZnO fibers, g-C_3N_4 NS-TiO_2 fibers, 6@g-C_3N_4 NS - ZnO fibers

The XRD spectra of ZnO fibers, **6**@ZnO fibers, g-C_3N_4 NS- ZnO fibers and **6**@g-C_3N_4 NS-ZnO fibers are shown in **Fig. 4.16**. Al the spectra display peaks at 2θ = 31.61, 34.39, 36.88, 47.91, 56.82, 63.85, 68.93 and 69.69° corresponding to (100), (002), (101), (102), (110), (103), (112) and (201) miller indices of hexagonal wurtzite of crystalline ZnO phase (JCPDS card no. 36–1451) [209]. No peaks corresponding to g-C_3N_4 NS and complex **6** were observed suggesting that the peaks are weak to be detected by XRD.

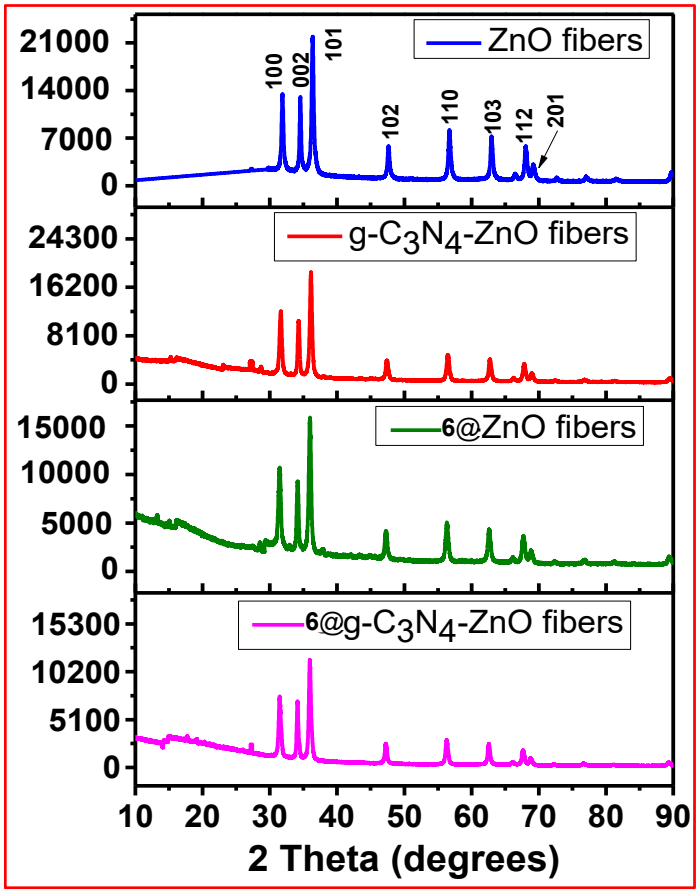

Fig. 4.16. XRD patterns of ZnO fibers, 6@ZnO fibers, g-C_3N_4 NS-TiO_2 fibers, 6@g-C_3N_4 NS - ZnO fibers

4.2.4. Scanning electron microscopy (SEM)

The morphology, topography and diameters of the fibers were studied with SEM. Energy dispersive X-ray spectroscopy was also used for some of the composites to study the composition of the fibers.

TiO_2 fibers and their composites

The morphology and topography of TiO_2 fibers and their composites were investigated using scanning electron microscopy (SEM). The SEM images and diameters histograms of **1**-TiO_2 fibers, **2**-TiO_2 fibers, **5**@TiO_2 fibers, $MnFe_2O_4$-TiO_2 fibers, **5**@$MnFe_2O_4$-TiO_2 fibers, **7**-TiO_2 fibers, g-C_3N_4 QDs-TiO_2 fibers and **7**@g-C_3N_4 QDs-TiO_2 fibers are shown in **Appendix 9-11**. The diameters of TiO_2 fibers were observed

to vary with each set of fibers, suggesting that diameters of the fibers were not uniform. The smallest diameters (0.5 μm) obtained were used here (**Table 4.1**).

The SEM images of TiO_2 fibers, g-C_3N_4 NS-TiO_2 fibers, **3**@g-C_3N_4 NS-TiO_2 fibers, **4**@g-C_3N_4 NS-TiO_2 fibers, **5**@g-C_3N_4 NS-TiO_2 fibers and **6**@g-C_3N_4 NS-TiO_2 fibers were studied using scanning electron microscopy (SEM) (**Fig. 4.17** and **Table 4.1**). The SEM images (taken at 5 kV) shown in **Fig. 4.17** display properties of a coiled cylindrical material with a smooth surface. The average diameters (**Fig. 4.17** (insert plots) and **Table 4.1**) of TiO_2 fibers, g-C_3N_4 NS-TiO_2 fibers, **3**@g-C_3N_4 NS -TiO_2 fibers, **4**@g-C_3N_4 NS -TiO_2 fibers, **5**@g-C_3N_4 NS -TiO_2 fibers and **6**@g-C_3N_4-TiO_2 fibers were 0.5, 1.1, 1.7, 1.6, 1.7 and 1.8 μm, respectively. The average diameters increased upon functionalization. There was no significant difference between the SEM images in **Fig. 4.17** and the rest of the diameters in **Table 4.1**.

The SEM images of **7**-TiO_2 fibers and **7**@g-C_3N_4 QDs-TiO_2 fibers display small particles at the surface which were presumed to be **7** and **7**@g-C_3N_4 QDs, respectively. The particle diameters are also listed in **Table 4.1**, **Appendix 11**.

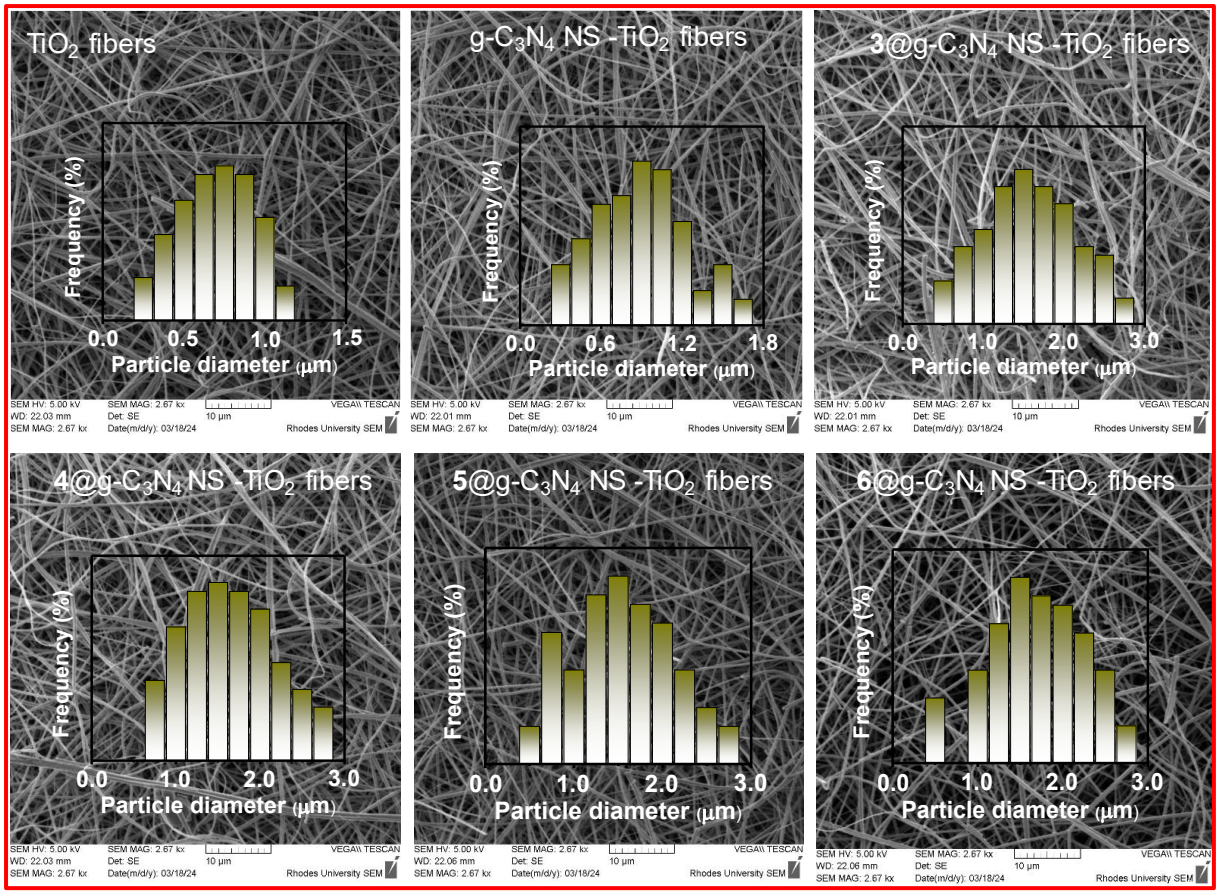

Fig. 4.17. SEM images of TiO_2 fibers, g-C_3N_4 NS-TiO_2 fibers, **3**@g-C_3N_4 NS-TiO_2 fibers, **4**@g-C_3N_4 NS-TiO_2 fibers, **5**@g-C_3N_4 NS-TiO_2 fibers and **6**@g-C_3N_4 NS-TiO_2 fibers (Insert = histograms).

ZnO fibers and their composites

The SEM images of pristine ZnO fibers, g-C_3N_4 NS-ZnO fibers, **6**-ZnO fibers, **6**@g-C_3N_4 NS-ZnO fibers and their corresponding particle size histograms (inserted plots) are displayed in **Fig. 4.18A**. The images show the characteristics of coiled cylindrical materials with smooth surfaces. The diameters (insert plots) of ZnO, g-C_3N_4 NS -ZnO, **6**-ZnO and **6**-g-C_3N_4 NS-ZnO fibers are 1.1, 1.3, 1.7 and 2.0 μm, respectively, **Fig. 4.18** and **Table 4.1**. g-C_3N_4 NS-ZnO fibers, **6**-ZnO fibers and **6**@g-C_3N_4 NS -ZnO fibers show an increase in average diameters with respect to pristine

ZnO fibers. This is due to the incorporation of the complex **6,** g-C_3N_4 and **6**@g-C_3N_4 NS conjugate.

The EDX spectra of ZnO fibers, **6**-ZnO fibers, g-C_3N_4 NS-ZnO fibers and **6**@g-C_3N_4 NS-ZnO fibers are shown in **Fig. 4.18B**. The EDX spectrum of ZnO fibers displays Zn and O with traces of C. The C emanates from the carbon tape used during the analysis. The spectrum of g-C_3N_4 NS -ZnO fibers displays increase in C emanating from g-C_3N_4 NS. The spectrum of **6**-ZnO fibers shows the presence of C, Zn, and O fibers, and **6**@g-C_3N_4 NS-ZnO fibers showed Zn, C, N and O, as expected. The anticipated N element in **6**-ZnO fibers was not observed, probably due to the fact that Zn and O are more abundant in the sample than N.

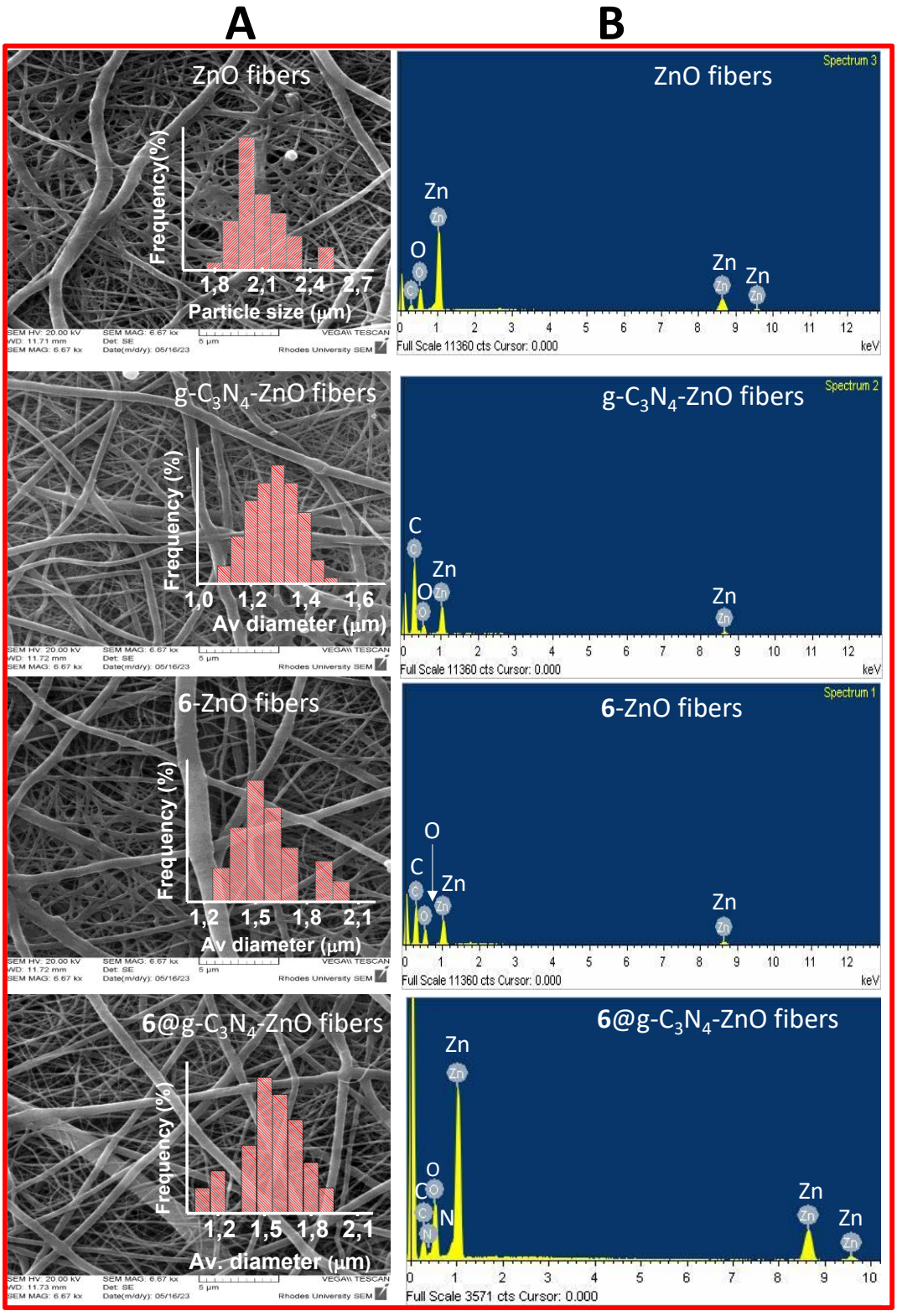

Fig. 4.18. SEM images **A** and EDX spectra **B** of ZnO fibers, g-C_3N_4 NS-ZnO fibers, **6**-ZnO fibers, **6**@g-C_3N_4 NS-ZnO fibers (Inset = histograms).

4.2.5. Breanuer-Emmett and Teller (BET) surface analysis

TiO_2 fibers, ZnO fibers and composites

BET surface area analysis was used to study the surface areas and pore volume of pristine and functionalized nanofibers. The surface areas and pore volumes of the nanofibers are listed in **Table 4.1**. The isotherms are displayed in **Fig. 4.19** and **Appendixes 12-14**. All the isotherms revealed that fibers are type IV materials with hysteresis loops, which suggests the existence of mesopores [210].

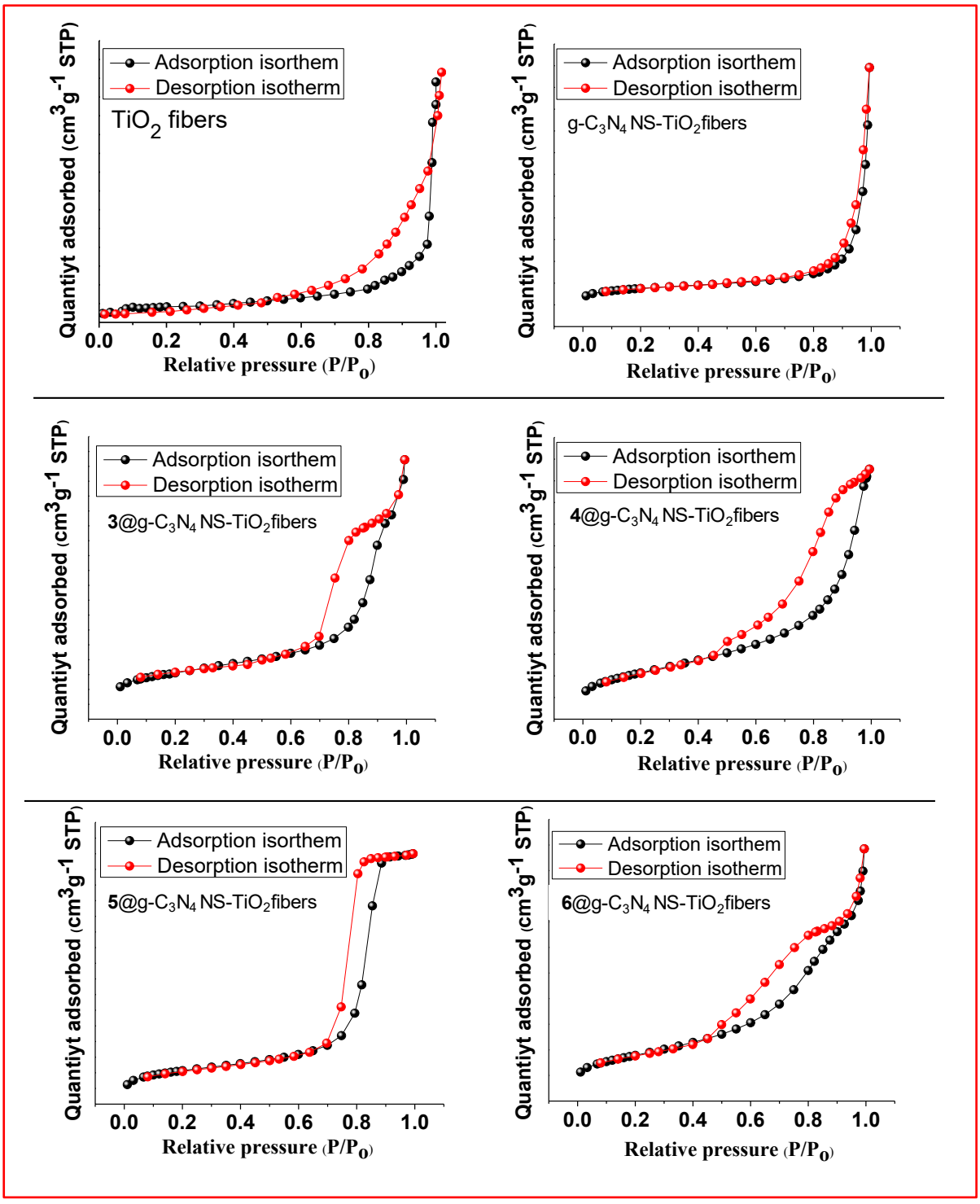

Fig. 4.19. BET isotherms of TiO_2 fibers, g-C_3N_4 NS-TiO_2 fibers, **3**@g-C_3N_4 NS-TiO_2 fibers,**4**@g-C_3N_4 NS-TiO_2 fibers, **5**@g-C_3N_4 NS-TiO_2 fibers and **6**@g-C_3N_4 NS-TiO_2 fibers

ZnO fibers and composites

The BET isotherms obtained from the ZnO fibers, g-C_3N_4-ZnO fibers, **6**-ZnO fibers and **6**@g-C_3N_4-ZnO fibers are shown in **Fig. 4.20**. The isotherms show that fibers are type IV materials with a hysteresis loop which proves the existence of the mesopores [211]. The surface areas of ZnO fibers, g-C_3N_4-ZnO fibers, **6**-ZnO fibers and **6**@g-C_3N_4-ZnO fibers were 13.3, 11.7, 12.4 and 9.11 $m^2\ g^{-1}$, respectively, **Table 4.1**. The results reveal that the functionalization of the fibers resulted in a decrease in the surface area of the fibers. The pore volumes were recorded to be 0.28, 0.14, 0.11 and 0.064 $cm^3\ g^{-1}$ for ZnO fibers, g-C_3N_4-ZnO fibers, **6**-ZnO fibers and **6**@g-C_3N_4-ZnO fibers, respectively, **Table 4.1**. The pores volumes also decreased upon functionalization of the ZnO fibers, suggesting that complex **6,** g-C_3N_4 and **6**@g-C_3N_4 occupy the pores of the ZnO fibers.

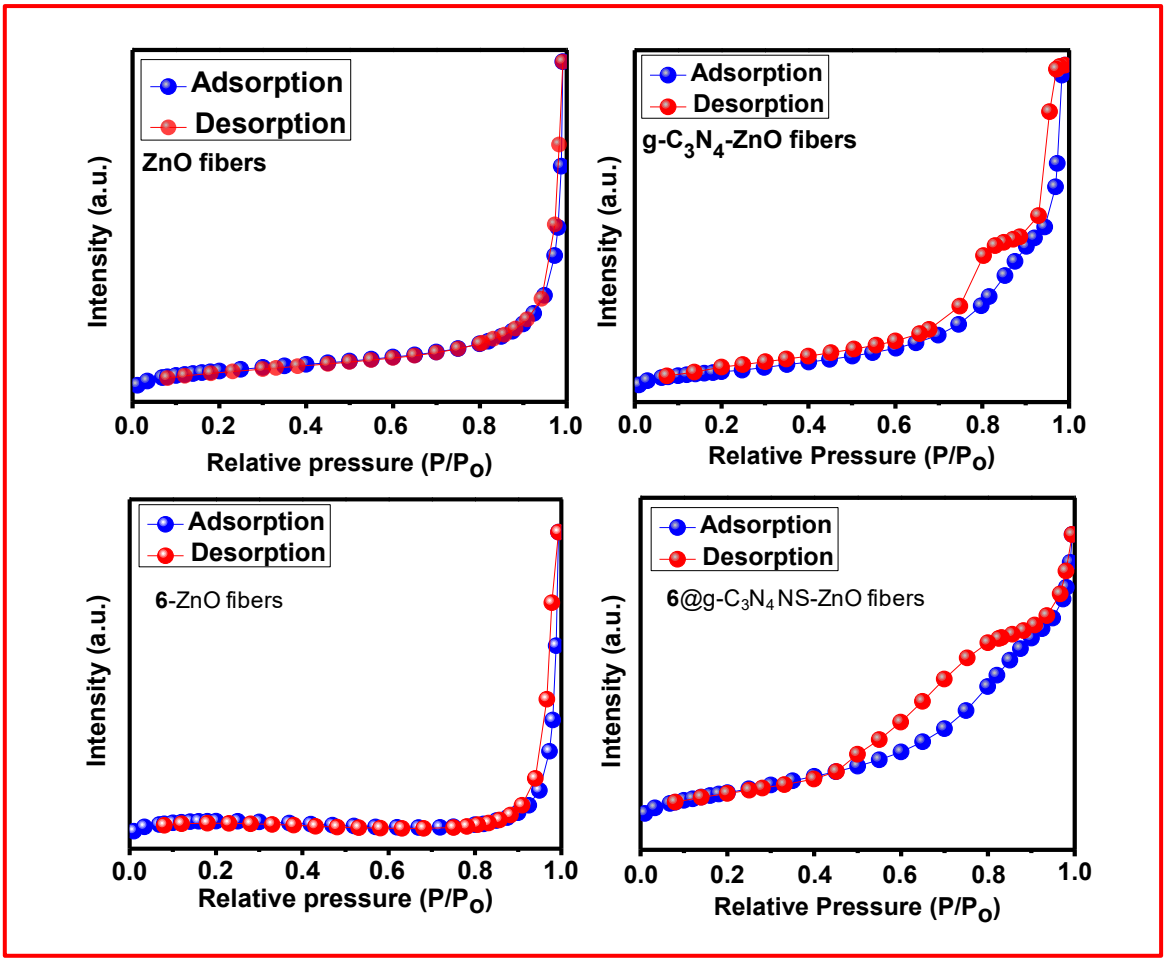

Fig. 4.20. BET isotherms of ZnO fibers, g-C_3N_4 NS-ZnO fibers, **6**-ZnO fibers and **6**@g-C_3N_4 NS-ZnO fibers

4.2.6. Thermal gravimetric analysis (TGA)

Pcs, TiO_2 fibers and composites

TGA analysis were used to study the effect of functionalization of the fibers on thermal stability. The thermal stabilities of TiO_2 fibers, **1**-TiO_2 fibers and **2**-TiO_2 fibers were compared **Fig. 4.21** upon heating from 50 to 1000 °C. The TGA of the pristine TiO_2 fibers display tremendous thermal stability up to 1000 °C without significant weight loss. Both the complexes **1** and **2** and functionalized TiO_2 fibers displayed slight weight loss between 50 and 150 °C, which is due to the loss of the adsorbed H_2O molecules. The TGA thermogram for complexes **1** and **2** display another weight loss

of 24 and 19%, respectively, between 500 and 700 °C, which is due to the decomposition of the Pc structure. The functionalized TiO_2 fibers displayed tremendous thermal stabilities compared to complexes **1** and **2** with weight losses of only 3 and 2% for **1**-TiO_2 fibers and **2**-TiO_2 fibers between 500 and 700 °C.

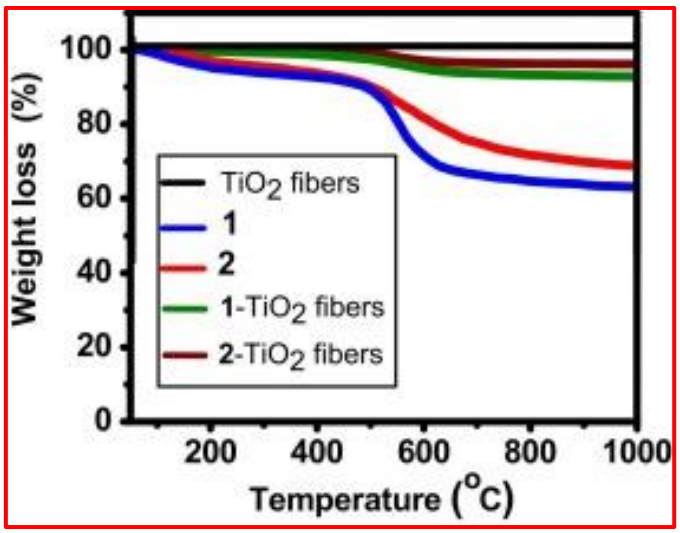

Fig. 4.21. TGA spectra of TiO_2 fibers, **1**, **2**, **1**-TiO_2 fibers and **2**-TiO_2 fibers.

The thermal stabilities of complexes **3**, **4**, **5**, and **6** were compared with the stabilities of TiO_2 fibers, **3**@TiO_2 fibers, **4**@TiO_2 fibers, **5**@TiO_2 fibers, and **6**@TiO_2 fibers at a temperature range of 30 to 500 °C. The TGA spectra of **3**, **4**, **5** and **6** are shown in **Fig. 4.22A.** The TGA spectra of TiO_2 fibers, **3**@TiO_2 fibers, **4**@TiO_2 fibers, **5**@TiO_2 fibers and **6**@TiO_2 fibers are shown in **Fig. 4.22B**. The thermograms of the complexes alone display weight loss between 30 °C and 100 °C which are due to the loss of the surface adsorbed H_2O molecules. Another weight loss was observed between 150 and 500 °C, which can be attributed to the decomposition of the Pc core. The overall weight losses observed from complexes **3**, **4**, **5** and **6** were 27, 31, 17 and 22 %, respectively, at 500 °C. There is no significant weight loss observed from TiO_2 fibers. The conjugation of the complexes and TiO_2 fibers significantly enhanced the thermal stabilities of

the complexes. The overall weight losses observed for **3**@TiO_2 fibers, **4**@TiO_2 fibers, **5**@TiO_2 fibers and **6**@TiO_2 fibers were 8 , 11 , 5 and 6 %, respectively.

The comparison of all the phthalocyanines used shows that the **5** is more stable than **1**, suggesting that symmetry improves thermal stability. The comparison of complex **3** and **4** shows that the latter is more thermally stable, suggesting that the presence of picolinic acid in **4** as substituent improves thermal stability. The comparison of complexes **5** and **6**, suggests that the presence of picolinic acid in complex 6 did not improve thermal stability, since complex **5** is more thermally stable.

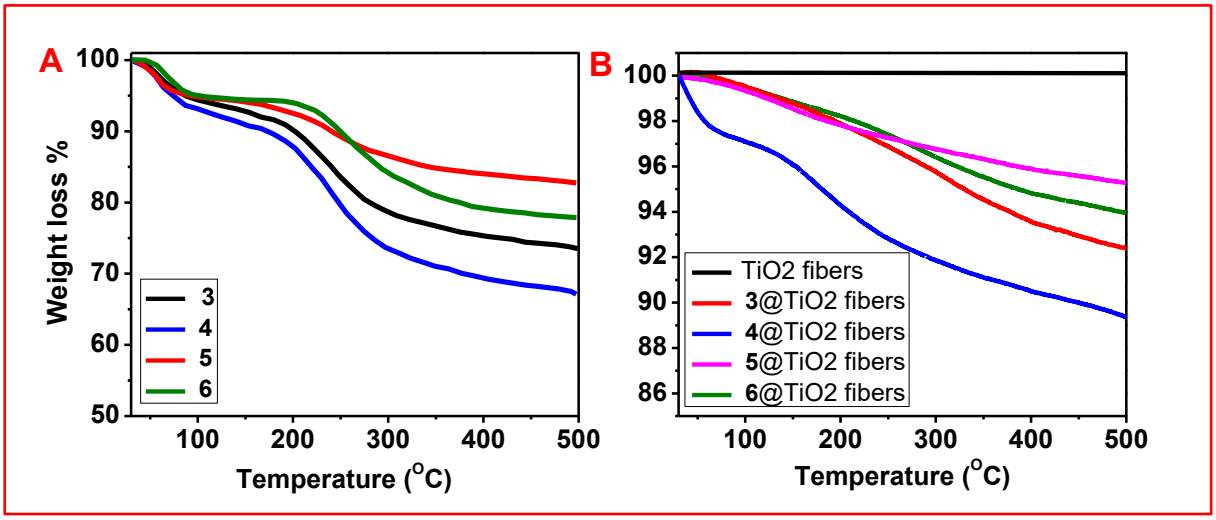

Fig. 4.22. TGA spectra of **3**, **4**, **5**, **6**, **A**, and TiO_2 fibers, **3**@TiO_2 fibers, **4**@TiO_2 fibers, **5**@TiO_2 fibers and **6**@TiO_2 fibers, **B**.

ZnO fibers and composites

The thermograms of powders of complex **6**, pristine g-C_3N_4 NS and **6**-g-C_3N_4 NS conjugate are presented in **Fig. 4.23A**. The thermograms show weight losses of 4%, 12%, and 8% for complex **6**, g-C_3N_4 NS, and **6**@g-C_3N_4 NS conjugate, respectively, between 50 and 180 °C attributed to the loss of physically adsorbed H_2O molecules with complex **3** exhibiting more thermal stability than pristine g-C_3N_4 NS and

corresponding **3**@g-C_3N_4 NS analogue. The pristine g-C_3N_4 NS exhibits an additional major weight loss of 80% between 500 and 800 ^oC which is attributed to the decomposition of g-C_3N_4 NS to carbon and nitrogen. Complex **6** also displays another weight loss of 17% between 500 and 600 ^oC. Similar to g-C_3N_4, the **6**@g-C_3N_4 NS thermogram exhibits a major weight loss of 60% between 500 and 800 ^oC, which is due to the decomposition of both g-C_3N_4 NS and complex **6**. Complex **6** exhibits higher thermal stability than both pristine g-C_3N_4 NS and **6**@g-C_3N_4 NS. The conjugation of complex **6** with g-C_3N_4 NS proved to be beneficial in enhancing the thermal stability of g-C_3N_4 NS since the weight loss decreased from 80% to 60%. This could be attributed to the fact that bond formation between the complex **6** and g-C_3N_4 NS results in the conjugate bearing properties of both compounds and breaking the bond, thus requires greater thermal energy.

TGA analysis of ZnO fibers, g-C_3N_4 NS-ZnO fibers, **6**-ZnO fibers and **6**@g-C_3N_4 NS-ZnO fibers are displayed in **Fig. 4.23B**. The analyses were performed in the temperature range of 0 to 1000 °C. All the materials display weight losses between 50 and 200 °C, which are due to the removal of the adsorbed H_2O molecules. Above 200 °C the TGA spectra of ZnO fibers showed stability without significant weight loss. The g-C_3N_4 NS-ZnO fibers display a weight loss of 55 % between 500 °C and 790 °C, which is due to the decomposition of g-C_3N_4. The **6**-ZnO fibers also display another weight loss of 8 % between 490 and 570 °C, which is due to the decomposition of complex **6**. The **6**@g-C_3N_4 NS-ZnO fibers display a weight loss of 28 % between 540 and 670 °C, which is due to the decomposition of complex **6** and g-C_3N_4 NS. This suggests that supporting **6**@g-C_3N_4 NS on ZnO fibers was beneficial in enhancing the stability of the hybrid.

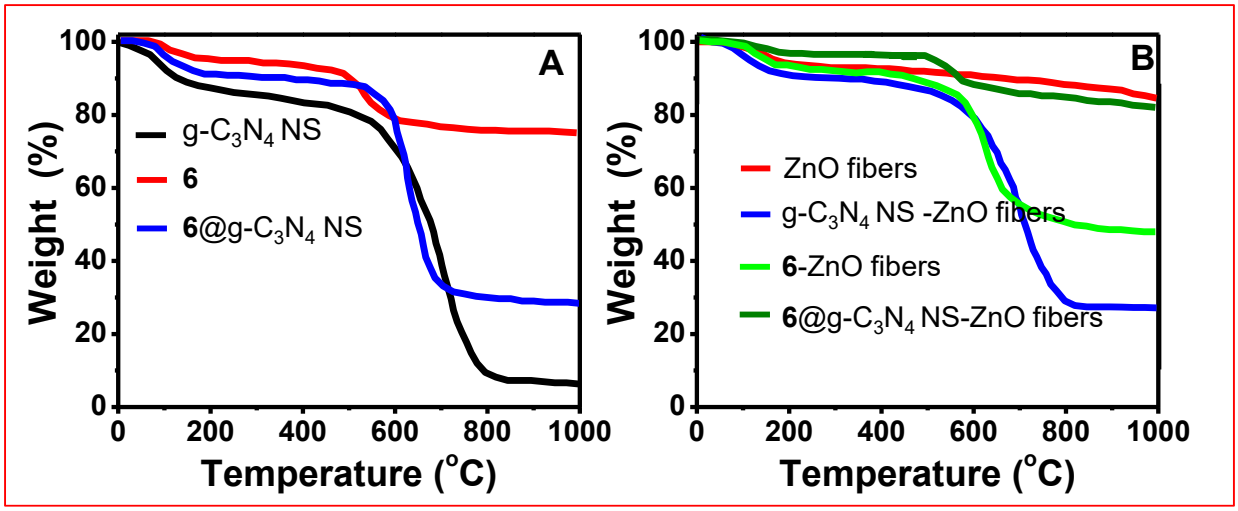

Fig. 4.23. TGA plots of **(A)** powders: (i) g-C_3N_4 NS, (ii) complex **6** and (iii) **6**@g-C_3N_4 NS conjugate and **(B)** fibers: (i) ZnO fibers, (ii) g-C_3N_4 NS -ZnO fibers, (iii) **6**-ZnO fibers, (iv) **6**@g-C_3N_4 NS-ZnO fibers.

4.3. Density functional theory (DFT)

DFT was performed to study the behaviour of Pcs, conjugates and their hybrids. The methods used are discussed in **Appendix 15**.

DFT calculations were carried out to predict trends in the chemical activities of complexes **3**-**6**. Among the parameters that can be obtained from DFT calculations are the highest occupied molecular orbital (HOMO) and lowest unoccupied molecular orbital (LUMO) energies, which are of crucial importance in photosono-catalytic processes. The HOMO−LUMO gap energies are shown together with their respective band structure alignments are shown in **Fig. 4.24A**. In general, the compound or molecule with the smallest HOMO−LUMO gap is anticipated to have highest chemical activity, while the compound with the highest gap is expected to be the least chemically active since the HOMO−LUMO energy gap is equivalent to the band gap energy of

the molecule. Therefore, the relationship between the HOMO−LUMO gap and the photosono-catalytic processes activity can be determined from the band gap energy.

The HOMO energies of complexes **3** and **4** are calculated to be -5.34 eV, while those of complexes **5** and **6** lie at -4.98 eV. The LUMO energies of these sets of complexes lie at -2.15 and -1.57 eV, respectively, with band gap energies of 3.19 eV for complexes **3** and **4** and 3.41 eV for complexes **5** and **6**. The calculated HOMO−LUMO band gap energies correlate with those obtained from Tauc plots. The complexes **3** and **4** have smaller band gap energy than **5** and **6** hence complexes **3** and **4** are anticipated to be more catalytically active. The electrostatic potential (ESP) maps of the complexes (**Fig. 4.24B**) were also calculated by DFT. All the complexes showed electron rich regions (red). The electron rich regions act as electron corridors during electron transfer. This is even more beneficial in this work because the electron rich regions were used to conjugate the Pc complexes with TiO_2 fibers. The electron rich regions facilitate the electrostatic attraction between the catalyst and Rhodamine 6G, since the later is positively charged. The ESP maps demonstrate that the central Zn(II) ions of the complexes are electron deficient and can hence readily undergo axial ligation to facilitate the photosono-catalysis.

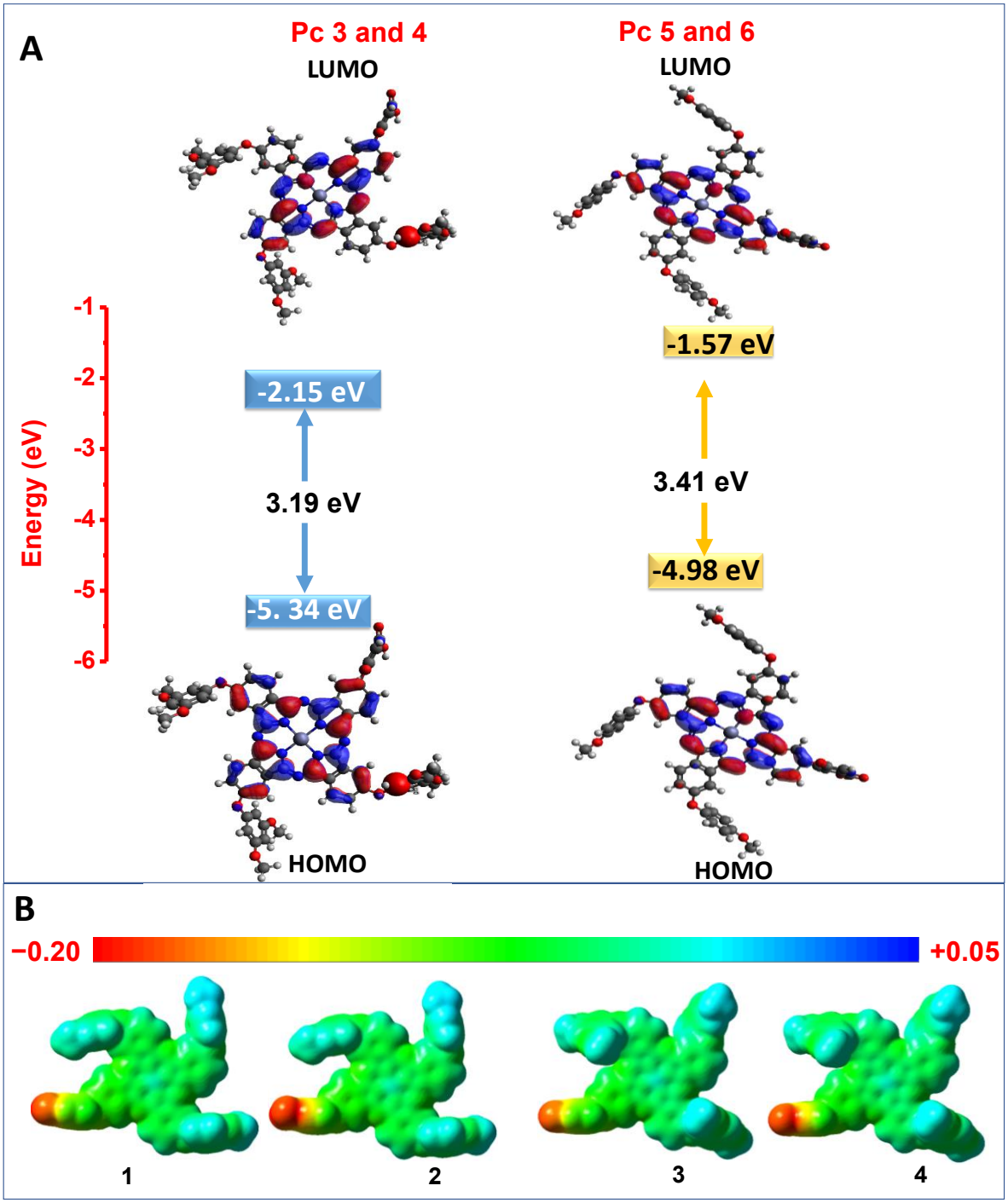

Fig. 4.24. Trends in the HOMO and LUMO energies, the HOMO−LUMO energy gaps and band structure alignments **A** and electrostatic potential (ESP) maps **B** of Pc complexes **3-6**. The MO angular nodal patterns are plotted at an isosurface of 0.02 a.u. The ESP surfaces were mapped onto total electron density isosurfaces at 0.0004 a.u.

4.4. Summary of the chapter

The functionalizationof the fibers (TiO_2 fibers and ZnO fibers) was successfully achieved. The conjugation of TiO_2 fibers with Pcs, through an amide bond was confirmed by XPS analysis. The absorption of properties of the fibers were stidied using solid-state UV-Vis spectroscopy. The phases, morphologies, surface areas, thermal stabilities were studied using XRD, SEM, BET and TGA respectively. DFT theory also corroborated with experimental results.

Chapter five

This chapter discusses photophysics of the phthalocyanines, porphyrin and their respective conjugates. It also discusses the photophysics of the functionalized nanofibers with phthalocyanines, porphyrin and conjugates.

5.1. Φ_F and τ_F

In general, when phthalocyanine/porphyrin is illuminated with light of adequate wavelength, electrons in the highest occupied molecular orbital (HOMO) become excited to the lowest unoccupied molecular orbital (LUMO). Subsequently, the electrons in the LUMO orbitals either recombine with holes to produce fluorescence or undergo intersystem crossing to the forbidden triplet state. The rate of the recombination of the electrons (e^-) and holes (h^+) is measured by fluorescence quantum yield (Φ_F) and fluorescence lifetimes (τ_F) studies [212]. By definition, the Φ_F is the ratio of the photons absorbed to photons emitted through fluorescence. The (τ_f) is the time a compound spends in its excited state before it undergoes fluorescence or intersystem crossing [213]. Hence, the fluorescence quantum yield (Φ_F) of the complexes **1**-**7** and their respective conjugates were studied. Afterwards, fluorescence lifetimes (τ_F) of the complexes **3**-**6** and their conjugates were compared (**Table 5.1**). The τ_F of the complex **7** was not studied because porphyrins have low or insignificant τ_F. The Φ_F and τ_F of the nanofibers were not studied because they do not dissolve in any solvent.

5.1.1. Pcs alone

The Φ_F of the complexes **1** has been reported to be 0.25 [70]. The Φ_F of the complexes **2** was calculated to be 0.24, **Table 5.1**. The Φ_F of the complexes **3**, **4**, and **6** were calculated to be 0.54, 0.53 and 0.19, respectively. The Φ_F of the complex **5** has been reported to be 0.22 [70]. The Φ_F of complexes **1** and **2** were lower than those obtained from complexes **3** and **4**. The Φ_F of complexes **5** and **6** were lower than those obtained from complexes **3** and **4.** This suggests that the recombination of electron-hole pairs is lower in complexes **5** and **6** than in **3** and **4**. In addition, the recombination

in complex **1** and **2** is lower than in **3** and **4**. Time correlation single photon counting (TCSPC) fluorescence lifetime decay curve of complex **6** is shown in **Fig. 5.1** and is used as an example for all the complexes for τ_F determination. The Φ_F of the complexes **3** and **4** were higher than those obtained from complexes **1** and **2**, suggesting that asymmetric Pcs had improved Φ_F.

The τ_F value of complex **1** has been reported to be 3.1 ns [70]. The τ_F of complex **2** was obtained to be 3.2 ns, **Table 5.1**. The τ_F value for complexes **3**, **4** and **6** were 6.2 ns and 6.8 ns and 3.6 ns respectively. The τ_F of complex **5** has been reported to be 3.0 ns [70]. The τ_F of complexes **5** and **6** are shorter than those obtained from complexes **3** and **4**, which corresponds to Φ_F. Asymmetric Pcs had improved τ_F. In addition, complexes **3** and **4** had higher τ_F than **5** and **6**, respectively, suggesting that carboxy phenoxy carboxylic acid substituents improved τ_F.

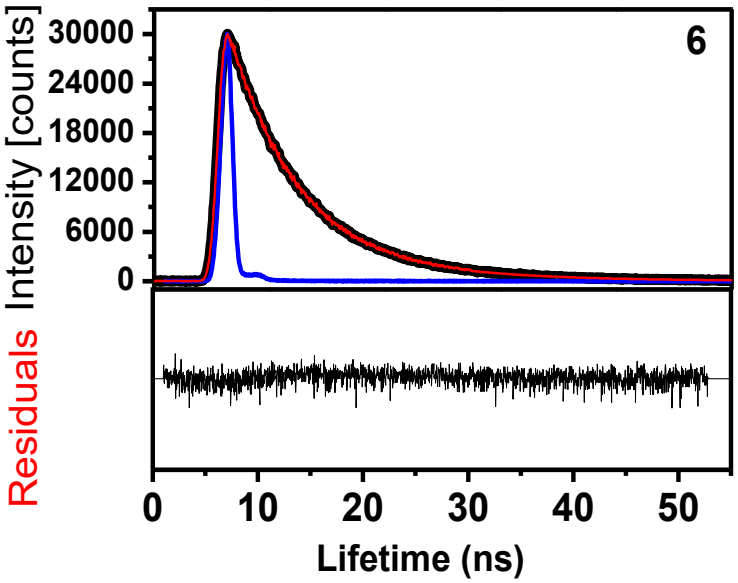

Fig. 5.1. TCSPC Fluorescence lifetime decay curve fitting for complex **6** in DMSO, using LUDOX HS-40 colloidal silica as a scatter sample.

Table. 5.1. Photophysical properties of phthalocyanines, porphyrin, conjugates and functionalized fibers.

Samples	Φ_F	$\tau_{F(ns)}$	Φ_T	$\tau_T(\mu s)$	Φ_Δ
Pcs and porphyrin complexes in DMSO					
1	0.25[a]	3.1[a]	0.69	190	0.58
2	0.24	3.2	0.66	187	0.63
3	0.54	6.2	0.39	340	0.53
4	0.53	6.8	0.37	355	0.41
5	0.22[a]	3.0[a]	0.69	271	0.58[a]
6	0.19	3.6	0.62	198	0.56
7	0.03	---	---	---	0.53
NPs and conjugates in DMSO					
g-C_3N_4	0.39	6.3	---	---	---
3@g-C_3N_4 NS	0.11	3.3	0.91	260	0.65
4@g-C_3N_4 NS	0.09	3.1	0.88	272	0.63
5@g-C_3N_4 NS	0.05	2.6	0.97	158	0.71
6@g-C_3N_4 NS	0.02	2.4	0.96	151	0.69
3@g-C_3N_4 QDs	0.24	3.6	0.71	197	0.59
4@g-C_3N_4 QDs	0.18	3.4	0.63	206	0.57
7@g-C_3N_4 QDs	0.01	---	---	---	0.62
5@$MnFe_2O_4$	0.12	1.4	0.89	163	0.69

Samples	Φ_F	$\tau_{F(ns)}$	Φ_T	$\tau_T(\mu s)$	Φ_Δ
Functionalized nanofibers in water					
1-TiO_2 fibers	---	---	---	---	0.41
2-TiO_2 fibers	---	---	---	---	0.45
3@TiO_2 fibers	---	---	---	---	0.39
4@TiO_2 fibers	---	---	---	---	0.35
5@TiO_2 fibers	---	---	---	---	0.46
6@TiO_2 fibers	---	---	---	---	0.37
6@ZnO fibers	---	---	---	---	0.26
3@g-C_3N_4 NS-TiO_2 fibers	---	---	---	---	0.46
4@g-C_3N_4 NS-TiO_2 fibers	---	---	---	---	0.40
5@g-C_3N_4 NS-TiO_2 fibers	---	---	---	---	0.53
6@g-C_3N_4 NS-TiO_2 fibers	---	---	---	---	0.50
3@g-C_3N_4 QDs-TiO_2 fibers	---	---	---	---	0.40
4@g-C_3N_4 QDs-TiO_2 fibers	---	---	---	---	0.41
7@g-C_3N_4 QDs-TiO_2 fibers	---	---	---	---	0.47
6@g-C_3N_4 NS-ZnO fibers	---	---	---	---	0.42

5.1.2. Conjugates of the Pcs

The Φ_F of **3**@g-C_3N_4 NS, **4**@g-C_3N_4 NS, **5**@g-C_3N_4 NS and **6**@g-C_3N_4 NS were calculated to be 0.11, 0.09, 0.05 and 0.02, respectively. The Φ_F of the conjugates was significantly less than that of the **Pc** complexes, suggesting that the conjugation resulted in fluorescence quenching of the **Pc**. This effect minimizes re-combination of the electron-hole pairs and enhances the generation of the reactive oxygen species (ROS).

The Φ_F of **3**@g-C_3N_4 QDs and **4**@g-C_3N_4 QDs (Table **5.1**) were calculated to be 0.24 and 0.18, respectively, which were lower than those of complexes **4** and **5**, respectively. This also suggests that the conjugation resulted in charge separation.

The Φ_F value for **5**@$MnFe_2O_4$ was calculated to be Φ_F = 0.12, (Table **5.1**). The Φ_F value for **5**@$MnFe_2O_4$ was significantly lower than that of the complex **5**. This is due to fluorescence quenching in **5**@$MnFe_2O_4$ conjugate, as a result of the heavy atom effect of the nanoparticles. This suggests that the conjugation of **5** and $MnFe_2O_4$ resulted in the separation of the electron-hole pairs.

The τ_F values for **3**@g-C_3N_4 NS, **4**@g-C_3N_4 NS, **5**@g-C_3N_4 NS and **6**@g-C_3N_4 NS (**Table 5.1**) are 3.3 ns, 3.1 ns, 2.6 ns and 2.4 ns, respectively. The τ_F value of the conjugates were noticeably lower than that of individual Pc complexes. This proves that the conjugation resulted in charge separation either by electron transfer or intersystem crossing to the forbidden triplet state. The τ_F values of **3**@g-C_3N_4 QDs and **4**@g-C_3N_4 QDs were 3.6 ns and 3.4 ns. The τ_F of the conjugates were shorter than those of individual complexes **3** and **4**, respectively. The τ_F of

the **5**@$MnFe_2O_4$ conjugate was recorded to be 1.4 ns, which is shorter than that of the **Pc.** This collaborates with the fluorescence quantum yield studies.

5.1.3. Porphyrin and its conjugate

The Φ_F of **7** and **7**@g-C_3N_4 QDs were investigated in DMSO. Both **7** and **7**@g-C_3N_4 QDs were excited at ~420 nm. The Φ_F value for **7** was found to be 0.03. The Φ_F value for **7**@g-C_3N_4 was found to be 0.01, which is not too different from that obtained for **7** within error limits. The Φ_F and τ_F of the Pcs, porphyrin and the conjugate were in **Table 5.1** lower than those obtained from g-C_3N_4 nanoparticles, suggesting that electron-hole recombination is higher in g-C_3N_4 nanoparticles.

5.2. Triplet quantum yields (Φ_T) and triplet lifetime (τ_T) studies

In general, when the Pcs are excited, they can either fluorescence or undergo intersystem crossing (ISC) to a forbidden triplet state (T_1) to generate ROS, including singlet oxygen ($^1O_2$). The efficiency of the ISC on the molecules can be studied using triplet quantum yield (Φ_T) and triplet lifetime studies (τ_T). Hence, Φ_T and τ_T of the Pcs and corresponding conjugates were studied. The Φ_T and τ_T of the fibers were not studied because they did not dissolve.

5.2.1. Pcs alone

The Φ_T indicates the number of molecules that undergo intersystem crossing to the forbidden triplet state [214]. The Φ_T of the complexes **1** and **2** were 0.69 and 0.66, respectively. The Φ_T values (**Table 5.1**) of complexes **3**-**6** and their conjugates were compared. The Φ_T of **3**, **4**, **5** and **6** were 0.39, 0.37 and 0.69 and 0.62 respectively.

The triplet lifetime (τ_T) studies were also determined in order to probe the time in microseconds the molecules spend in their triplet forbidden states before they either

react with O_2 and organic compounds or transfer their energies to O_2 to generate ROS. The triplet lifetime curve of the complex **6** is shown in **Fig. 5.2**. The τ_T values for **1** and **2** were 190 and 187 μs, respectively. The τ_T values for **3**, **4**, **5** and **6** are 340, 355, 271 and 198 μs, respectively. Surprisingly, the τ_T of complex **1** was lower than for complex **5**, which was not anticipated, since they have the same Φ_T.

5.2.2. Conjugates of the Pcs

The Φ_T of **3**@g-C_3N_4 NS, **4**@g-C_3N_4 NS, **5**@g-C_3N_4 NS and **6**@g-C_3N_4 NS were 0.91, 0.88, 0.97, and 0.96, respectively. The Φ_T of the **3**@g-C_3N_4 QDs and **4**@g-C_3N_4 QDs were 0.71 and 0.63 μs, respectively. The Φ_T of the conjugates were higher than those of the corresponding Pcs due to the electron electron-donating of g-C_3N_4. Electron donating groups have been reported to increase intersystem crossing in Pcs [215]. The Φ_T of the **5**@$MnFe_2O_4$ was 0.89, which was higher than that of the complex **5** alone. This suggests that the conjugation of **5** and $MnFe_2O_4$ promotes the intersystem crossing of the Pc to the forbidden triplet state.

The τ_T of **3**@g-C_3N_4 NS, **4**@g-C_3N_4 NS, **5**@g-C_3N_4 NS and **6**@g-C_3N_4 NS were 260, 272, 158, and 151, respectively. The τ_T of the **3**@g-C_3N_4 QDs and **4**@g-C_3N_4 QDs were 197 and 206 μs, respectively. The conjugates had a shorter life than their corresponding Pcs counterparts. This was anticipated because an increase in Φ_T has been reported to result in a decrease in τ_T [216]. The τ_T of **5**-$MnFe_2O_4$ conjugate was 163 μs. The conjugate (**5**@$MnFe_2O_4$) had a shorter-lifetimes than **5** as expected, with an increase in triplet quantum yield.

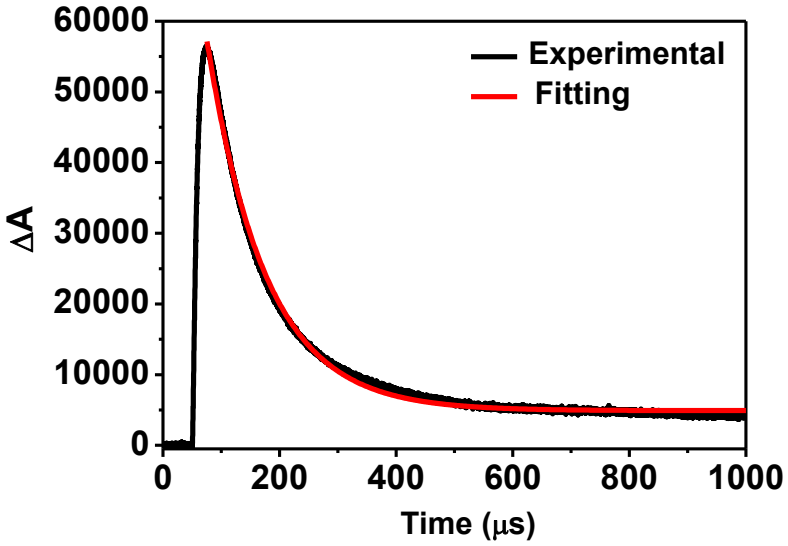

Fig. 5.2. Triplet lifetime curve for complex **6** in DMSO.

5.3. Singlet oxygen quantum yield studies

Singlet oxygen ($^1O_2$) is one of the most important reactive species that are generated by phthalocyanine under light illumination. This is usually measured using singlet oxygen quantum yield (Φ_Δ). In this study, singlet oxygen quantum yields of the complexes **1**-**7** and their respective conjugates were studied. The singlet oxygen quantum yield of the functionalized fibers with Pcs, porphyrin and their respective conjugates were also studied.

5.3.1. Pcs and conjugates

The singlet oxygen quantum yields (Φ_Δ) for Pcs and respective conjugates in DMSO were investigated using the comparative method. DPBF (9.13 $\times 10^{-6}$ M) and unsubstituted ZnPc (Φ^{std} = 0.67) were used as singlet oxygen quencher and standard, respectively [213]. The DPBF spectral changes during photodegradation in the presence **5**@$MnFe_2O_4$ conjugate are shown in **Fig. 5.3**. The Q-band was not affected

during the degradation of DPBF, which suggests that the **Pc** (complex **5)** remained stable during degradation.

The Φ_Δ values are shown in **Table 5.1**. The Φ_Δ of complexes **1** and **2** were 0.58 and 0.63, respectively. The Φ_Δ of complexes **3**, **4 and 6** were calculated to be 0.53, 0.41 and 0.58, respectively. The Φ_Δ of complex **5** has been reported to be 0.56 [70]. There was not difference between Φ_Δ complex **1** and **5**, suggesting that symmetry did not affect singlet quantum yield.

The Φ_Δ of **3**@g-C_3N_4 NS, **4**@g-C_3N_4 NS, **5**@g-C_3N_4 NS and **6**@g-C_3N_4 NS were 0.65, 0.63 and 0.71 and 0.69, respectively. The Φ_Δ of **3**@g-C_3N_4 QDs, **4**@g-C_3N_4 QDs were 0.59 and 0.57, respectively. There was an increase in Φ_Δ for the conjugates compared to Pcs alone. This suggests that conjugation promotes the generation of singlet oxygen.

The Φ_Δ of **5**@$MnFe_2O_4$ conjugate was calculated to be 0.69. The Φ_Δ of the **5**@$MnFe_2O_4$ conjugate was higher than that of the complex **5** (0.56). This was highly anticipated since **5**@$MnFe_2O_4$ conjugate had a higher triplet quantum yield.

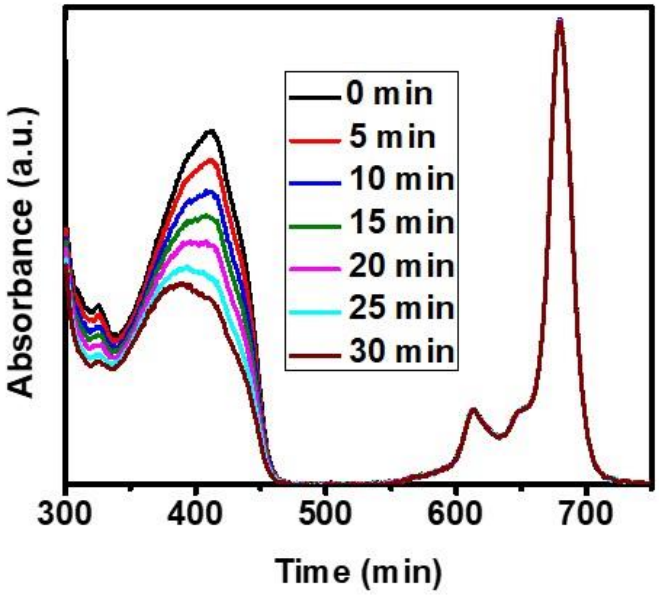

Fig. 5.3. UV-vis spectral changes for photo-degradation of DPBF (6.92 x 10^{-5} M) in DMSO in the presence of **5**@$MnFe_2O_4$ conjugate.

5.3.2. Porphyrin and its conjugate

The Φ_Δ in DMF for **7** and its conjugate **7**@g-C_3N_4 QDs were investigated using comparative methods reported [217]. DMA was used as the singlet oxygen quencher using ZnTPP (Φ^{std} = 0.53) in DMSO as a standard [181]. The generation of the singlet oxygen was confirmed by degradation of DMA with time as shown in **Fig. 5.4**. The porphyrin (complex **7**) exhibited high stability which was observed by trivial change in its Soret and Q bands upon degradation. The Φ_Δ of the unmetallated (**7a**) porphyrin has been reported to be 0.34 [169]. The Φ_Δ of the complex **7** was calculated to be 0.53. The Φ_Δ (**Table 5.1**) of **7** is higher than for **7** due to the relatively heavy Zn (in the former) which encourages intersystem crossing to the triplet state, from where singlet oxygen is generated. The Φ_Δ obtained in **7**@g-C_3N_4 QDs was 0.62. Therefore, Φ_Δ further increased when **7** was conjugated with g-C_3N_4 QDs. Electron donating groups are known to increase intersystem crossing in porphyrin-like complexes [215,218], hence the increase in singlet oxygen quantum yield in **7**@g-C_3N_4 QDs.

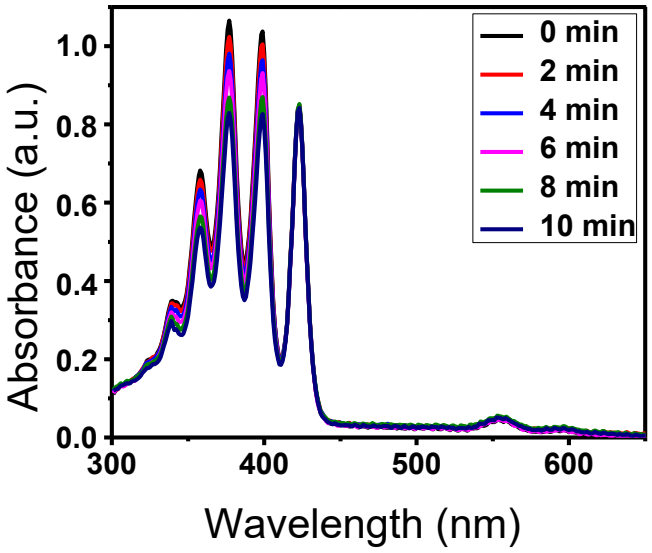

Fig. 5.4. UV-vis spectral changes for photo-degradation of DMA (9.11 x 10^{-5} M) in the presence of **7**@g-C_3N_4 QDs.

5.3.3. Functionalized fibers

The Φ_Δ of the functionalized TiO_2 fibers was studied using the absolute method, the equations **2.4**-**2.6** [182]. ADMA (5.42 × 10^{-6} M) was used as a quencher in aqueous solution. The spectral changes of ADMA during degradation in the presence **6**@g-C_3N_4 NS-TiO_2 fibers are shown in **Fig. 5.5**. The Φ_Δ values for **1**@TiO_2 fibers and **2**@TiO_2 fibers were calculated to be 0.41 and 0.45, respectively. The Φ_Δ values for **3**@TiO_2 fibers, **4**@TiO_2 fibers, **5**@TiO_2 fibers and **6**@TiO_2 fibers were calculated to be 0.39, 0.35, 0.46 and 0.37, respectively, **Table 5.1**. The calculated Φ_Δ values were lower for functionalized fibers than for corresponding Pc complexes alone. This is because the Φ_Δ studies of the functionalized fibers were done in aqueous solutions and Φ_Δ studies of the Pc complexes were performed in DMSO. Water is the known quencher for $^1O_2$ [218]. The Φ_Δ values obtained in **5**@TiO_2 fibers was higher than that obtained from **1**@TiO_2 fibers, suggesting asymmetric Pc generated higher singlet oxidation quantum than its analogue in water.

The Φ_Δ of **3**@g-C_3N_4 NS-TiO_2 fibers, **4**@g-C_3N_4 NS-TiO_2 fibers, **5**@g-C_3N_4 NS-TiO_2 fibers and **6**@g-C_3N_4 NS-TiO_2 fibers were 0.46, 0.40, 0.53 and 0.50, respectively. The Φ_Δ of **3**@g-C_3N_4 QDs-TiO_2 fibers, **4**@g-C_3N_4 QDs-TiO_2 fibers were 0.40 and 0.41, respectively, **Table 5.1**.

The Φ_Δ values obtained for **7**@g-C_3N_4 QDs-TiO_2 fibers was 0.47, which was lower than those obtained from complex **7** and **7**@g-C_3N_4 QDs. The Φ_Δ of complex **7** and **7**@g-C_3N_4 QDs were performed in DMF, whereas the Φ_Δ was performed in water. Hence, this is not surprising since water is the known $^1O_2$ quencher.

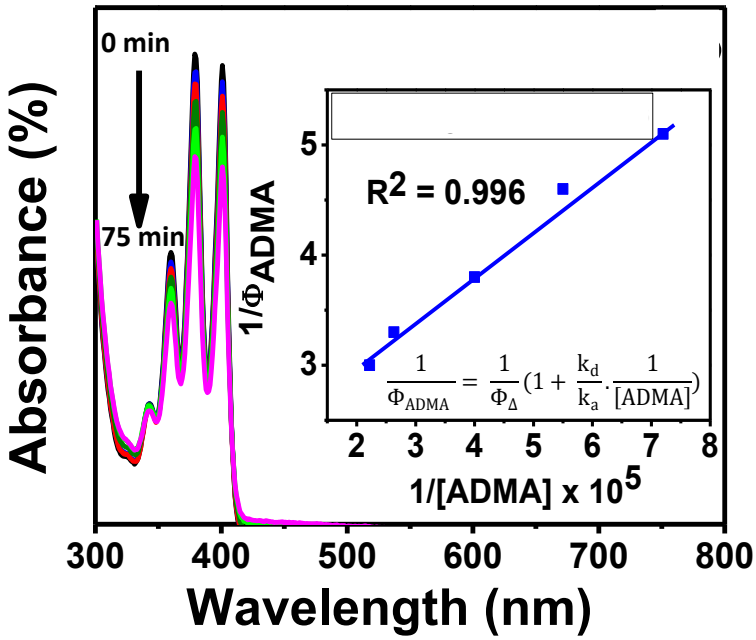

Fig. 5.5. UV-vis spectral changes for photo-degradation of ADMA (6.11 X 10^{-5} M) in water (insert plot is 1/[ADMA] against $1/\Phi_{ADMA}$) for **6**@g-C_3N_4 -ZnO fibers in water

5.4. Summary of the chapter

The photophysical properties of a porphyrin and the phthalocyanines were successfully studies, so were those of the conjugates and functionalized fibers. The conjugates had lower fluorescence quantum yield and enhanced singlet oxygen

quantum yield. The functionalized fibers had lower singlet oxygen quantum yield than their corresponding conjugations due to singlet oxygen quenching effect of H_2O.

Chapter six

This chapter discusses photo-, sono- and photosono-catalytic degradation of Rhodamine 6G using various Pcs, porphyrin and functionalized fibers. It also discusses photo-catalytic degradation of dichlorophenol using various Pcs, porphyrin and functionalized fibers

6.1. Photo-, sono- and photosono-catalytic-degradation of Rhodamine 6G

6.1.1. Symmetrical complexes 1 and 2 and their functionalized TiO_2 nanofibers

The degradation of the Rhodamine 6 G (6.63×10^{-5} M) was evaluated by recording the spectral changes (**Fig. 6.1**) at 525 nm, which is typically where Rhodamine 6 G absorbs [219]. The studies were performed at pH 9 because Rhodamine 6G degradation has been reported to be enhanced at this pH [185,219]. The studies were performed for 270 min at 30 min intervals. Before degradation, the catalysts and Rhodamine 6G solution were left in the dark overnight to reach adsorption-desorption equilibrium. When Rhodamine 6 G was irradiated in the absence of the catalyst, no spectral changes were observed. When pristine TiO_2 fibers were used only a minor decrease in peak intensity was observed, which suggests that TiO_2 fibers are not catalytically active for the degradation of Rhodamine 6 G. However, when complexes **1** and **2** (as powders) and **1**-TiO_2 fibers and **2**-TiO_2 fibers were used, a significant decrease in spectral peak intensity was observed (**Fig. 6.1**). This suggests that the catalysts play a profound role in instigating both photo-, sono- and photosono-catalytic degradation and the degradation does not transpire in the absence of the catalyst.

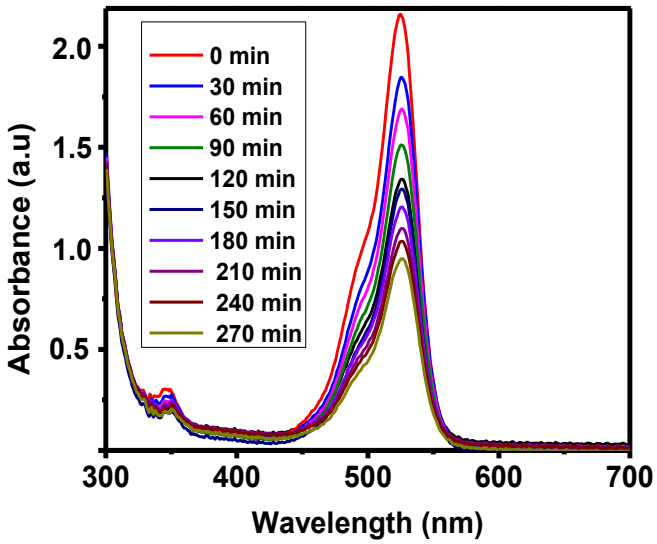

Fig. 6.1. Spectral changes for photosonocatalytic degradation of Rhodamine 6 G (6.63×10^{-5} M) in H_2O using **2**-TiO_2 fibers.

The degradation efficiency was calculated using equation **6.1**.

$$\textbf{Degradation efficiency}\ (\%) = \left(\frac{C_o - C_t}{C_o}\right) x\ 100 \qquad (\textbf{6.1})$$

Where C_o is the initial concentration of Rhodamine 6G, C_t is the concentration at time t during degradation.

The degradation results and kinetics are displayed in **Table 6.1** and **Figs. 6.2** and **6.3**. Among the catalysts used, pristine TiO_2 fibers displayed poor catalytic activity with degradation efficiencies of 4, 7 and 11% for photo-, sono- and photosono- catalytic degradation processes, respectively after 270 min. This is not surprising since TiO_2 fibers exhibit poor visible light absorption [173]. Complexes **1** and **2** showed improved degradation efficiency with 11, 16 and 19% using complex **1** and 14, 21 and 23% using complex **2** for photo-, sono- and photosono-catalytic degradation processes, respectively. Higher catalytic activity is observed under ultrasound (sono-catalytic process) and combined ultrasound and light (photosono-catalytic process) compared to light alone. It has been reported before [220] and will be shown below,

that ultrasound generates hydroxyl radicals in addition to singlet oxygen, while light only generates singlet oxygen. Among the two Pc complexes studied, complex **2** exhibited higher catalytic activity. The higher catalytic activity of complex **2** can be attributed to its higher singlet oxygen quantum yield as shown in **Table 5.1**.

The **1**-TiO_2 fibers and **2**-TiO_2 fibers displayed higher catalytic activities than their corresponding pristine MPc analogous. **2**-TiO_2 fibers displayed higher catalytic activity with 37, 54 and 63% conversions compared to **1**-TiO_2 fibers at 34, 49 and 58% conversions for photo-, sono- and photosono-catalytic degradation processes, respectively. The values are higher for **2** for reasons given above. The degradation curves obtained from TiO_2 fibers, **1**-TiO_2 fibers and **2**-TiO_2 fibers are displayed in **Fig**. **6**.**2**.

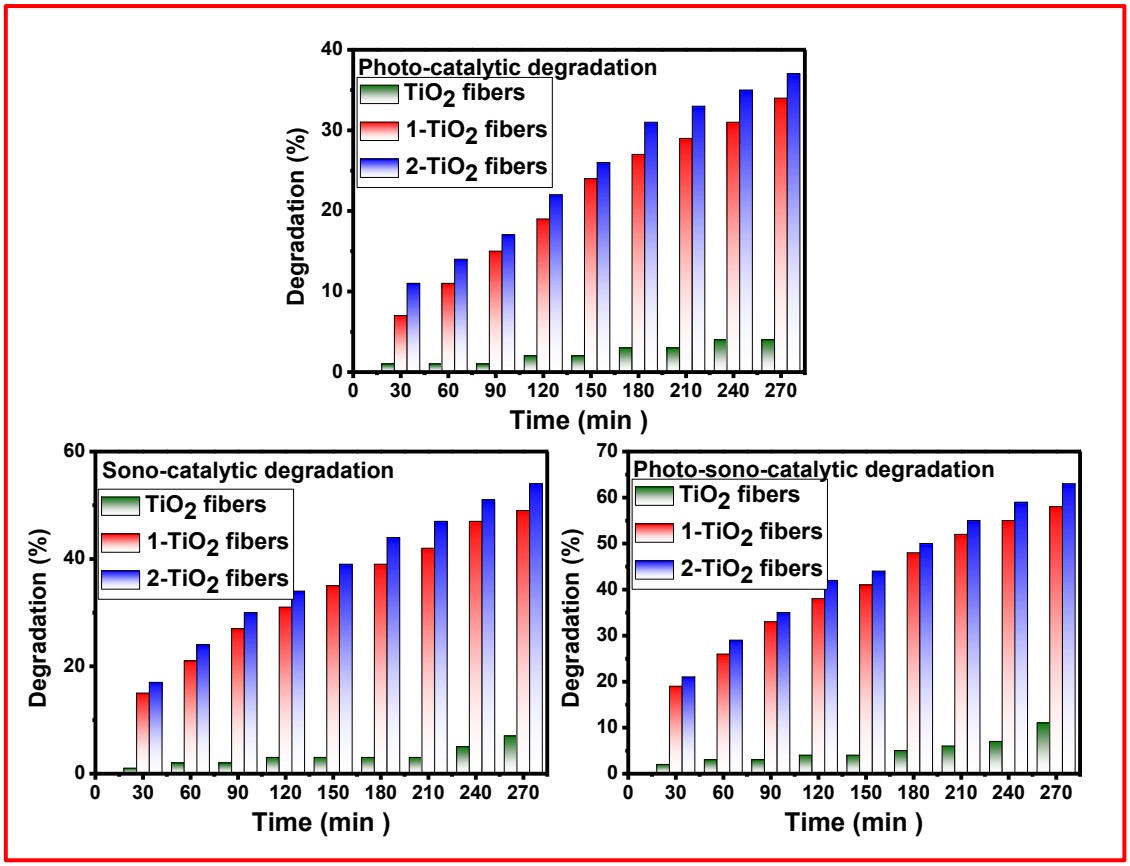

Fig. 6.2. Degradation plots for photo-, sono- and photosono- catalytic degradation of Rhodamine 6 G (6.63×10^{-5} M) in H_2O using TiO_2 fibers, **1**-TiO_2 fibers and **2**-TiO_2 fibers at pH = 9.

6.1.1.1. Kinetic studies

Kinetic studies of Rhodamine 6 G (6.63×10^{-5} mol.L^{-1}) were performed for photo-, sono- and photosono-catalytic degradation processes to establish kinetics of the degradation processes. The kinetic data plots for TiO_2 fibers, **1**-TiO_2 fibers and **2**-TiO_2 fibers catalysed reactions are shown in **Fig. 6.3** and the data are listed in **Table 6.1**. The plots of $\ln(C_O/C)$ versus irradiation time display properties of the pseudo-first-order kinetics with a linear fit. The rate constants (k_{obs}) obtained from the sonocatalytic degradation process are higher (half-lives are lower) than those obtained from photocatalytic degradation processes. Also, the rate constants (k_{obs}) obtained from

photosono-catalytic degradation process are higher than those obtained from sonocatalytic degradation processes. The highest rate constant (k_{obs}) and lowest $\tau_{1/2}$ was obtained using **2**-TiO_2 fibers suggesting that **2**-TiO_2 fibers displayed higher catalytic activity.

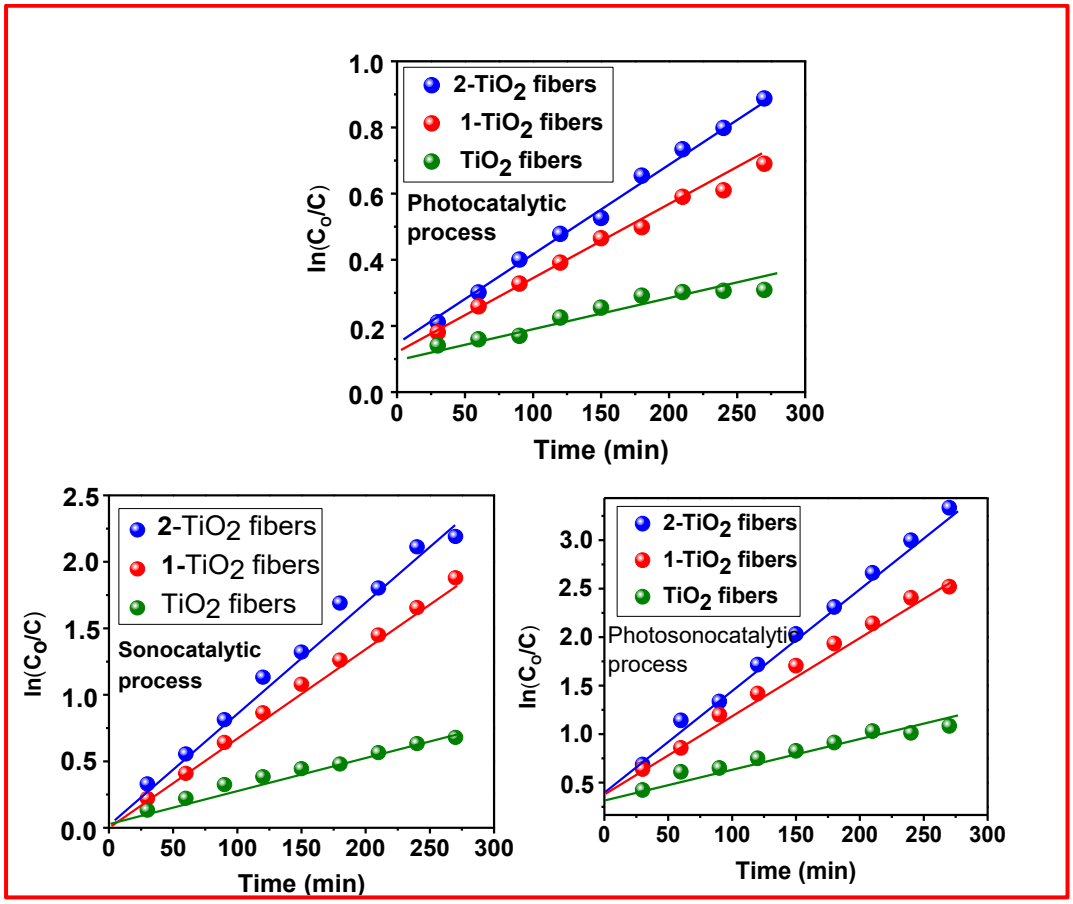

Fig. 6.3. Reaction kinetics for photo-, sono- and photosono- catalytic degradation of Rhodamine 6 G (6.63×10^{-5} M) in H_2O using TiO_2 fibers, **1**-TiO_2 fibers and **2**-TiO_2 fibers at pH = 9.

Table 6.1. Degradation efficiency and reaction kinetics properties for photosono-catalytic degradation of Rhodamine 6G (6.63×10^{-5} M) at using TiO_2 fibers, **1**-TiO_2 fibers and **2**-TiO_2 fibers at pH = 9.

[Rhodamine 6G]	Degradation efficiency (%)			k_{obs} (min^{-1}) x10^{-4}			$\tau_{1/2}$		
	Photo	Sono	Photosono	Photo	Sono	Photosono	Photo	Sono	Photosono
TiO_2 fibers	4	7	11	0.8	1.1	1.7	8663	6300	4076
1	11	16	19	1.7	1.8	4.1	4076	3871	1732
2	14	21	23	3	6	9	2310	1155	770
1-TiO_2 fibers	34	49	58	29	33	36	239	210	193
2-TiO_2 fibers	37	54	63	30	38	41	231	182	169

The Langmuir-Hinshelwood rate expression **(Eq. 6.2)** was subsequently utilized to establish the kinetics of solid–liquid reactions [221].

$$\frac{1}{r_O} = \frac{1}{k_r K_A}\frac{1}{C_O} + \frac{1}{k_r} \qquad (6.2)$$

Where r_o is the rate of the initial degradation reaction, C_o is the initial concentration of the Rhodamine 6G, K_A is the adsorption coefficient and k_r represents the reaction rate constant. The plots of the reciprocal of the initial concentration of Rhodamine 6G against the reciprocal of the initial rate using **1**-TiO_2 fibers and **2**-TiO_2 fibers hybrid catalyst for fibers for photo-, sono-, and photosono- catalytic degradation processes are shown in **Fig. 6.4**. The plots are linear suggesting that Rhodamine 6G degradation reactions obey Langmuir–Hinshelwood kinetics model. The adsorption coefficient (K_A) values were determined from the slope, whereas k_r values were calculated from the intercept using **Eq. 6.2**. The results indicate that both K_A and k_r are larger for photosono-catalytic degradation processes than for sono- and photocatalytic degradation **Table 6.2**, for the reasons provided above, furthermore, the **2**-TiO_2 fibers hybrid obtained higher K_A and k_r than **1**-TiO_2 fibers. This could be one of the contributing factors toward the perceived improved degradation efficiency of the former.

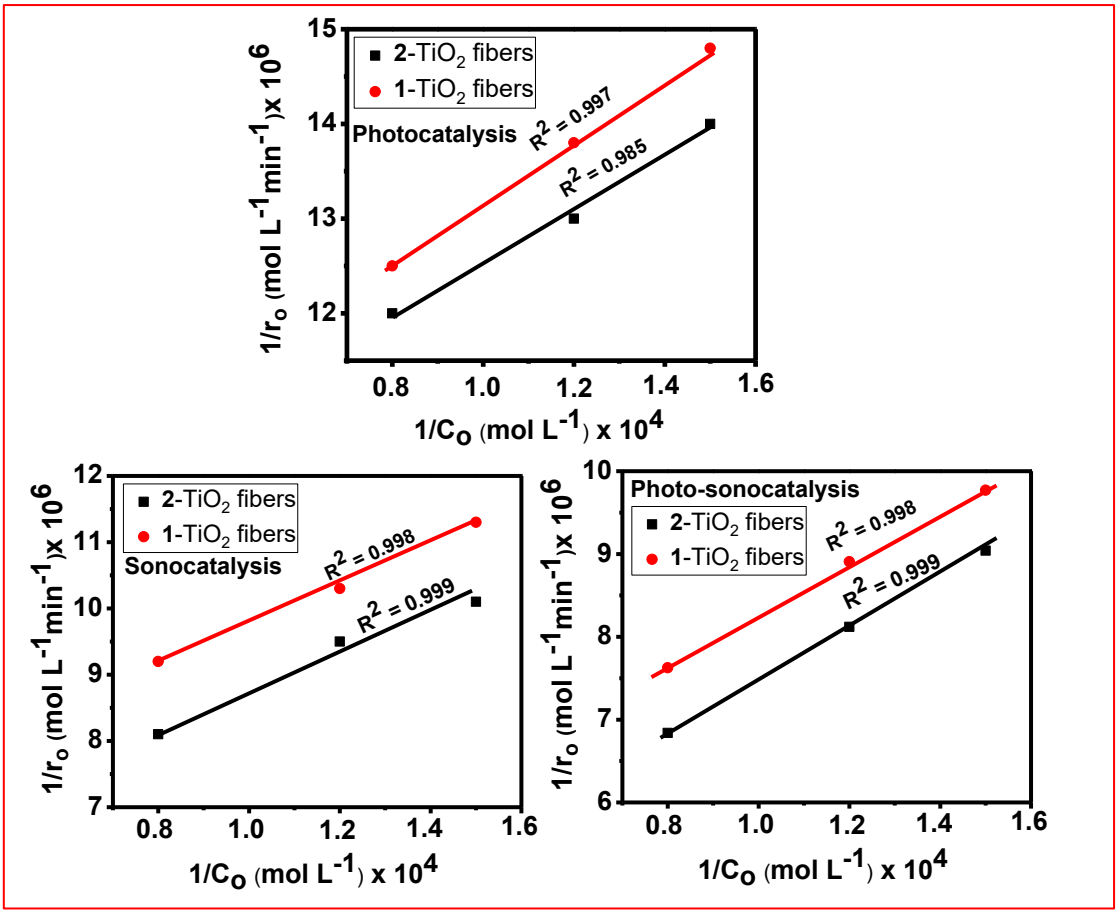

Fig. 6.4. Plots of the reciprocal of initial reaction rate versus the reciprocal of the initial concentration for the sonocatalytic and photocatalytic degradation of Rhodamine 6 G in H_2O using **1**-TiO_2 fibers and **2**-TiO_2 fibers.

Table 6.2. Langmuir-Hinshelwood parameters photo-, sono, and photosono- catalytic degradation of Rhodamine 6 G (pH 9) using **1**-TiO_2 fibers and **2**-TiO_2 fibers.

Degradation process	**Catalysts**	**k_r (mol L^{-1} min^{-1}) 10^{-7}**	**K_A (mol^{-1} L) × 10^4**	**R^2**
Photocatalytic degradation	**1**-TiO_2 fibers	8.13	2.8	0.997
	2-TiO_2 fibers	8.62	3.0	0.985
Sonocatalytic degradation	**1**-TiO_2 fibers	11.4	3.6	0.998
	2-TiO_2 fibers	12.7	3.7	0.999
Photosono-catalytic degradation	**1**-TiO_2 fibers	14.8	4.1	0.998
	2-TiO_2 fibers	15.7	4.8	0.999

6.1.1.2. Singlet oxygen and hydroxide radicals trapping experiments

Electron paramagnetic resonance (EPR) was used to study the generation of both $^1O_2$ and $^{\bullet}OH$ radicals. TEMPO and DMPO were used as $^1O_2$ and $^{\bullet}OH$ quenchers, respectively, **Fig. 6.5**. The generation of both $^1O_2$ and $^{\bullet}OH$ was observed by the appearance of the peaks between 3400 and 3550 G upon the addition of a quencher. Increased yields of both $^1O_2$ and $^{\bullet}OH$ radicals result in increased peak signals. For comparison purposes, the $^1O_2$ and $^{\bullet}OH$ radicals generation was investigated in the absence of the catalysts, the presence of TiO_2 fibers, complexes **1** and **2** and MPc functionalized TiO_2 fibers.

The EPR spectra of the photo- and sono- catalytic processes using TEMPO or DMPO alone in the absence of the catalysts or using pristine TiO_2 fibers showed no formation of $^1O_2$ species and $^{\bullet}OH$ radicals. However, when MPc complexes were used for both photo- and sono-catalytic processes in the presence of TEMPO, the spectral peaks corresponding to the $^1O_2$ species were observed for both complexes **1** and **2** alone (suspended as powder) or on TiO_2 fibers. The intensity of the signals is higher in the

presence of the MPc-TiO_2 fibers. When DMPO was used in the sonocatalytic process in the presence of MPc complexes alone or on TiO_2 fibers, the spectral peaks corresponding to •OH radicals were observed. No signal was observed for DMPO for the photocatalytic process. This suggests that the •OH radicals were generated in the sonocatalytic process but not in photocatalytic process. Typically, TiO_2 exhibits a strong •OH signal upon illumination with UV light. However, in this study no •OH species were observed for TiO_2 alone. This is not surprising because the excitation wavelength used in this study in the photo-catalytic degradation process is 680 nm and TiO_2 fibers absorb below 400 nm.

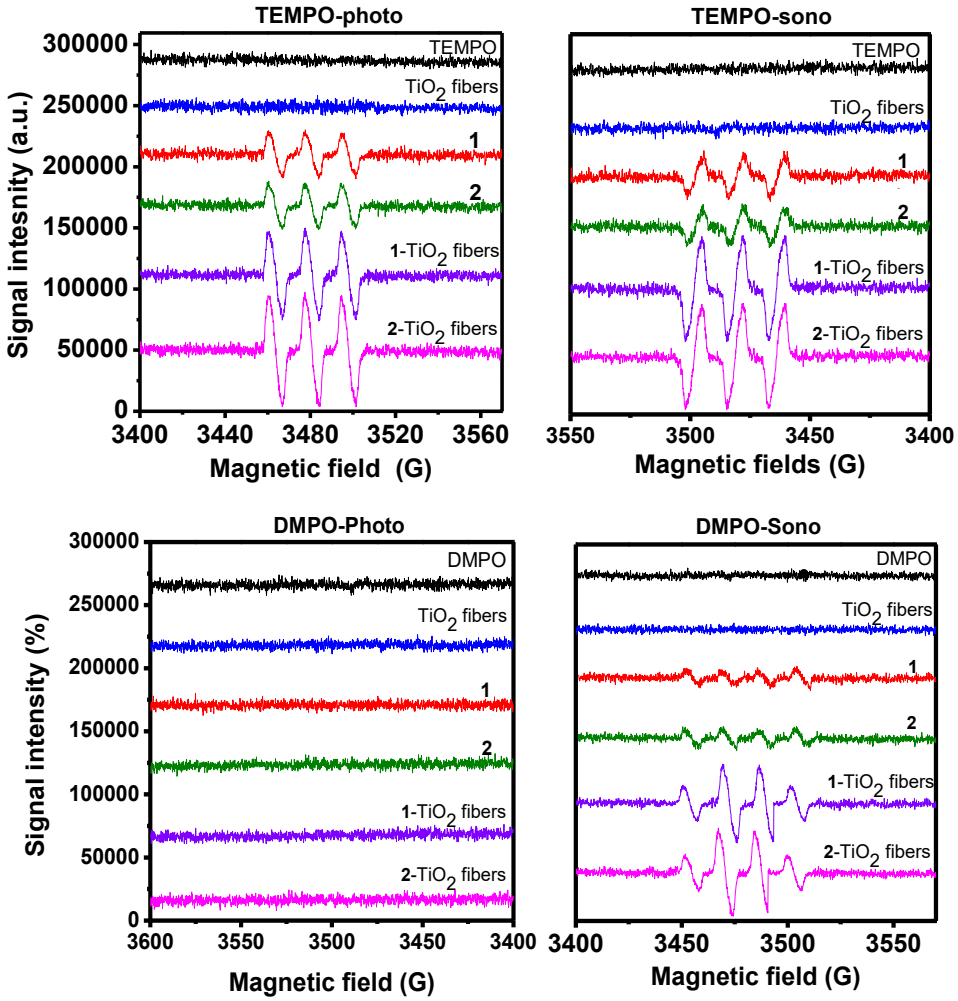

Fig 6.5. EPR spectra of the blank, TiO_2 fibers, complexes **1**, **2**, **1**-TiO_2 fibers and **2**-TiO_2 fibers using TEMPO and DMPO as quenchers.

6.1.2. Asymmetric complexes 3-6 and their functionalized TiO2 nanofibers through covalent linkage

The Rhodamine 6G (6.63×10^{-5} M) degradations were also performed using complexes **3**-**6** (as powders) and their functionals fibers through covalent linkage (**3**@TiO_2 fibers, **4**@TiO_2 fibers, **5**@TiO_2 fibers and **6**@TiO_2 fibers). The studies were done at pH 9 for 300 min. The results were recorded in 60 min intervals. As stated above, before degradation, the mixtures were left in the dark overnight to reach adsorption-desorption equilibrium. To evaluate the photosono-catalytic effect of the as-synthesized catalysts, degradation studies in the absence of the catalysts for photo, sono and photosono-degradation of Rhodamine 6G (6.63×10^{-5} M) in the absence of the catalyst, in the presence of TiO_2 fibers, **3**, **4**, **5**, **6** alone and in the presence of **3**@TiO_2 fibers, **4**@TiO_2 fibers, **5**@TiO_2 fibers and **6**@TiO_2 fibers. When photo, sono and photosono degradation studies were performed in the absence of the catalysts, no spectral changes were recorded. This suggests that degradation does not occur in the absence of the catalyst as was the case above.

Rhodamine 6G degradation data and kinetics are provided in **Table 6**.**3**. The plots for photo- and sono-catalytic degradation processes using complexes TiO_2 fibers, **3**, **4**, **5**, **6** alone are shown in **Appendix 16**. The plots for photo- and sono-catalytic degradation processes **3**@TiO_2 fibers, **4**@TiO_2 fibers, **5**@TiO_2 fibers and **6**@TiO_2 fibers are displayed in **Appendix 17**. The plots for photosono-catalytic degradation processes using TiO_2 fibers, **3**, **4**, **5**, **6**, **3**@TiO_2 fibers, **4**@TiO_2 fibers, **5**@TiO_2 fibers and **6**@TiO_2 fibers are shown in **Fig**. **6**.**6** and **Table 6**.**3**.

Rhodamine 6G degradation efficiencies obtained using TiO_2 fibers were 4%, 7% and 11% for photo, sono and photosono processes as stated above, respectively.

When **3**, **4**, **5** and **6** complexes were used alone, noticeable degradation efficiencies were observed. The degradation efficiencies obtained using **3**, **4**, **5** and **6** complexes were 24 **,** 26 **,** 29 and 31 % for photocatalytic degradation**,** 32 **,** 36 **,** 43 and 45 % for sonocatalytic degradation and 42 , 44 , 53 and 57 % for photosono-catalytic degradation processes, respectively. This suggests that the Pc complexes were more catalytically active than bare TiO_2 fibers.

When **3**@TiO_2 fibers, **4**@TiO_2 fibers, **5**@TiO_2 fibers and **6**@TiO_2 fibers were used, the degradation efficiencies further improved. The degradation efficiencies obtained using **3**@TiO_2 fibers, **4**@TiO_2 fibers, **5**@TiO_2 fibers and **6**@TiO_2 fibers were 39 **,** 43 **,** 54 and 57 % for the photocatalytic degradation process, 55 , 59 , 72 and 76 % for sono-catalytic degradation process. The degradation efficiencies obtained using **3**@TiO_2 fibers, **4**@TiO_2 fibers, **5**@TiO_2 fibers and **6**@TiO_2 fibers were 68 **,** 73 **,** 85 and 88 % for photosono-catalytic process, respectively. The functionalized fibers were more catalytically active than individual Pc complexes alone. The photosono catalytic process showed higher degradation efficiency than photo and sonocatalytic processes.

The kinetic studies were performed in order to determine the order of the reaction. The plots of ln(C_O/C) versus irradiation time for photo, sono and photosono degradation processes showed pseudo first-order kinetics with linear fit for all the catalysts, **Fig.6.6, Table 6.3** and **Appendix 16** and **17**. The rate constants (k_{obs}) in the photosono-catalytic process were higher for all the catalysts than in photo and sono-catalytic processes, whereas half-lives were lower. The higher k_{obs} was obtained with **6**@TiO_2 fibers. This was anticipated since the higher degradation efficiency was also obtained with **6**@TiO_2 fibers catalyst.

The higher catalytic activity of complex **6** compared to complexes **3** and **4** could be attributed to higher singlet oxygen quantum yield for the former. A higher degradation efficiency was observed for complex **6** compared to complex **5**, even though the latter had a slightly higher singlet oxygen quantum yield value. This could be due to the presence of nitrogen lone pairs on the substituent of the former complex. The presence of nitrogen in complexes **4** and **6** provides abundant lone pair electrons, which subsequently promote n→π* transition [222]. This can result in H-abstraction from the organic compound which is the first step in the degradation of organic pollutants. For the same reason, complex **4** has a higher degradation efficiency than **3**, even though the latter has a higher singlet oxygen quantum yield.

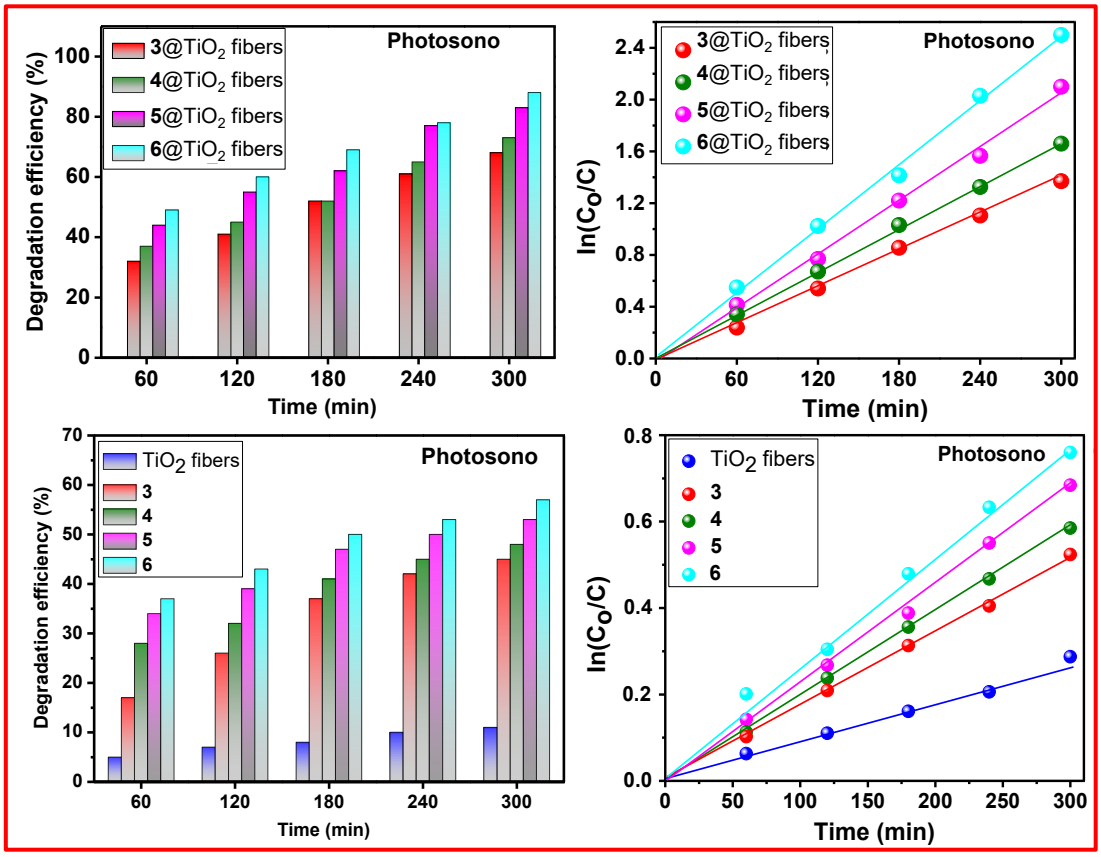

Fig. 6.6. Rhodamine 6G percentage degradations **A**, and kinetics **B,** plots for photosono-catalytic process using TiO_2 fibers, Pc complexes and functionalized TiO_2 fibers (Rhodamine 6G = 6.63×10^{-5} M) at pH 9.

Table 6.3: Degradation efficiencies of Rhodamine 6G using various catalysts at pH 9.

Catalyst	Degradation efficiency (%)			k_{obs} (min^{-1}) x10^{-4}			$\tau_{1/2}$		
	Photo	Sono	Photosono	Photo	Sono	Photosono	Photo	Sono	Photosono
Phathalocyanines alone									
3	24	32	42	11	23	31	630	301	224
4	26	36	44	13	30	33	533	231	210
5	29	43	53	19	32	39	365	216	178
6	31	45	57	21	28	42	330	248	165
7	---	---	---	52	---	---	133	---	---
TiO_2 fibers alone									
TiO_2 fibers	4	7	11	0.8	1.1	1.7	8663	6300	4076
Pcs-TiO_2 fibers conjugated through an amide bond									
3@TiO_2 fibers	39	55	68	29	35	49	239	198	141
4@TiO_2 fibers	43	59	73	31	37	51	224	187	134
5@TiO_2 fibers	54	72	85	34	49	65	203	141	107
6@TiO_2 fibers	57	76	88	36	54	68	193	128	102
Pcs supported on TiO_2 fibers through physical adsorption									
3-TiO_2 fibers	32	52	64	23	36	46	301	203	150
4-TiO_2 fibers	37	55	68	28	37	49	248	198	141
5-TiO_2 fibers	50	66	83	34	39	59	253	176	117
6-TiO_2 fibers	52	69	85	33	48	60	210	144	116
g-C_3N_4 supported to TiO_2 fibers									
g-C_3N_4 NS–TiO_2 fibers	52	61	66	37	42	47	187	165	147
g-C_3N_4 QDs–TiO_2 fibers	46	---	---	32	---	---	244	---	---
Pcs conjugated with g-C_3N_4 NS and supported on TiO_2 fibers									
3@g-C_3N_4 NS-TiO_2 fibers	75	87	100	57	65	78	133	112	89
4@g-C_3N_4 NS-TiO_2 fibers	78	88	100	58	67	81	122	103	86
5@g-C_3N_4 NS-TiO_2 fibers	83	91	100	60	69	84	116	77	83
6@g-C_3N_4 NS-TiO_2 fibers	86	96	100	64	73	91	81	94	76

Catalyst	Degradation efficiency (%)			k_{obs} (min^{-1}) x10^{-4}			$\tau_{1/2}$		
	Photo	Sono	Photosono	Photo	Sono	Photosono	Photo	Sono	Photosono
Pcs and porphyrin conjugated with g-C_3N_4 QDs and supported on TiO_2 fibers									
7		---	---		---	---		---	---
3@g-C_3N_4 QDs-TiO_2 fibers	79	---	---	58	---	---	122	---	---
4@g-C_3N_4 QDs-TiO_2 fibers	86	---	---	61	---	---	115	---	---
7-TiO_2 fibers	---	---	---	63	---	---	177	---	---
7@g-C_3N_4 QDs-TiO_2 fibers	---	---	---	67	---	---	157	---	---
Complex **5 conjugated to $MnFe_2O_4$ nanoparticles and supported to TiO_2 fibers**									
$MnFe_2O_4$ NPs	14	24	33	2.3	4.7	7.6	2961	1474	911
5@$MnFe_2O_4$	58	63	76	31	35	54	219	194	128
$MnFe_2O_4$-TiO_2 fibers	21	30	39	6.3	08	10	1100	855	666
5@$MnFe_2O_4$-TiO_2 fibers	65	72	90	41	55	68	168	124	102
ZnO fibers and its comoposites									
ZnO fibers	6	9	13	0.6	2.3	3.9	12375	3013	
g-C_3N_4 NS –ZnO fibers	29	47	56	13	38	41	521	181	168
6- ZnO fibers	59	68	86	42	49	62	162	139	112
6@g-C_3N_4 NS – ZnO fibers	74	85	97	59	72	93	117	96	75

6.1.3. Complexes 3-6 and their g-C3N4 NS conjugates functionalized TiO2 nanofibers

The photo-, sono- and photosono-catalytic degradation efficiencies of **3**, **4**, **5**, and **6** (as powders) and their functionalized TiO_2 fibers (**3**-TiO_2 fibers, **4**-TiO_2 fibers, **5**-TiO_2 fibers, **6**-TiO_2 fibers) were compared with their respective conjugates (**3**@g-C_3N_4 NS-TiO_2 fibers, **4**@g-C_3N_4 NS-TiO_2 fibers, **5**@g-C_3N_4 NS-TiO_2 fibers and **6**@g-C_3N_4 NS-TiO_2 fibers) functionalized fibers in degradation of Rhodamine 6G (6.63 ×10^{-5} M). The studies were performed for 300 min and the readings were taken 60 min intervals. Before degradation studies were performed, the catalysts and the Rhodamine 6G solution mixture were left in the dark for 120 min to achieve adsorption-desorption

equilibrium. The equilibrium was reached after 60 min. The degradation activities of **3**@g-C_3N_4 NS, **4**@g-C_3N_4 NS, **5**@g-C_3N_4 NS and **6**@g-C_3N_4 NS conjugates were not investigated because they were soluble in an aqueous solution as stated above.

The photo-, sono- and photsono-catalytic degradation efficiencies and kinetics values for **3**-TiO_2 fibers, **4**-TiO_2 fibers, **5**-TiO_2 fibers and **6**-TiO_2 fibers are listed in **Table 6.3**. The degradation efficiencies obtained with **3**-TiO_2 fibers, **4**-TiO_2 fibers, **5**-TiO_2 fibers and **6**-TiO_2 fibers were 32**,** 37**,** 50 and 52% for photo-catalytic degradation process, 52, 55, 66 and 69% for sono-catalytic degradation process and 64**,** 68**,** 83, and 85% for photosono-catalytic degradation process (**Table. 6.3**). The degradation efficiencies obtained with **3**-TiO_2 fibers, **4**-TiO_2 fibers, **5**-TiO_2 fibers and **6**-TiO_2 fibers were lower than degradation results obtained using **3**@TiO_2 fibers, **4**@TiO_2 fibers, **5**@TiO_2 fibers and **6**@TiO_2 fibers. This suggests that functionalization of TiO_2 fibers through covalent linkage promoted Rhodamine 6G degradation. This is presumably due to facilitated charge transfer from the Pc to TiO_2 fibers in covalent linkage than in physical adsorption.

The degradation efficiencies and kinetics of g-C_3N_4 NS-TiO_2 fibers, **3**@g-C_3N_4 NS-TiO_2 fibers, **4**@g-C_3N_4 NS-TiO_2 fibers, **5**@g-C_3N_4 NS-TiO_2 fibers and **6**@g-C_3N_4 NS-TiO_2 fibers are shown in **Fig. 6.7** and **Table 6.3**. The degradation efficiencies obtained using g-C_3N_4 NS-TiO_2 fibers were 52, 61 and 66% for photo, sono and photosono-catalytic degradation processes, respectively. The catalytic degradation efficiencies of **3**@g-C_3N_4 NS-TiO_2 fibers, **4**@g-C_3N_4 NS-TiO_2 fibers, **5**@g-C_3N_4 NS-TiO_2 fibers and **6**@g-C_3N_4 NS-TiO_2 fibers (**Fig. 6.7**) and (**Table 6.3**) were 75**,** 78**,** 83 and 86% for photo-catalytic process, 87, 88, 91 and 96% for sono-catalytic process. The efficacy obtained in photosono-catalytic efficiency using **3**@g-C_3N_4 NS-TiO_2 fibers, **4**@g-C_3N_4 NS-TiO_2

fibers, **5**@g-C_3N_4 NS-TiO_2 fibers and **6**@g-C_3N_4 NS-TiO_2 fibers were 100%. The obtained degradation efficiencies in photo, sono and photosono-catalytic degradation processes were higher for **3**@g-C_3N_4 NS-TiO_2 fibers, **4**@g-C_3N_4 NS-TiO_2 fibers, **5**@g-C_3N_4 NS-TiO_2 fibers and **6**@g-C_3N_4 NS-TiO_2 fibers than for **3**, **4**, **5**, **6** and **3**-TiO_2 fibers, **4**-TiO_2 fibers, **5**-TiO_2 fibers, **6**-TiO_2 fibers. This suggests that the conjugation conjugation of Pc complexes with g-C_3N_4 enhanced Rhodamine 6G degradation.

The kinetic studies reveal that all the reactions follow first-order kinetics with respect to the catalysts used. This is observed by the linear plots of the natural logarithm of the initial concentration over the concentration at time t against time, **Fig. 6.7**. As anticipated, the largest k_{obs} was obtained using **6**@g-C_3N_4 NS-TiO_2 fibers, since the highest efficiency was observed using the same catalyst. In addition, the shortest half-life ($\tau_{1/2}$) was obtained using the same catalyst. Since the combination of photosono-catalytic process and **6**@g-C_3N_4 NS-TiO_2 fibers showed higher efficacy, they were used in subsequent studies. Although complete degradations were obtained in photosono-catalytic degradation process by all the catalysts, results in **Table 6.3** suggest that the highest k_{obs} was obtained using **6**@g-C_3N_4 NS-TiO_2 fibers. This suggests that **6**@g-C_3N_4 NS-TiO_2 fibers were the most active catalysts in photosono-catalytic process.

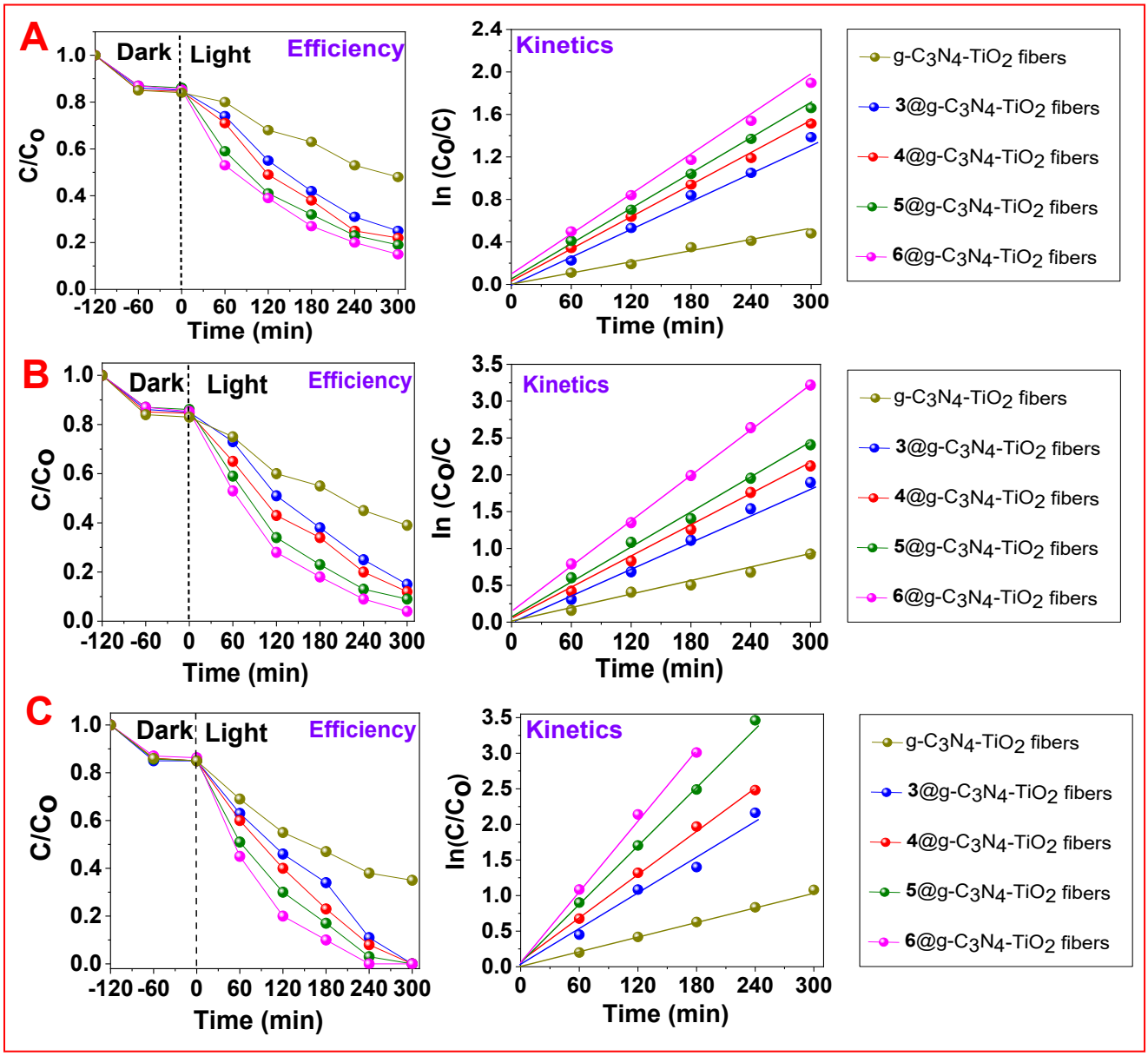

Fig. 6.7. Catalytic efficiencies and kinetics of Photo **A**, sono **B** and photosono **C** degradation processes using g-C_3N_4 NS-TiO_2 fibers, **3**@g-C_3N_4 NS-TiO_2 fibers, **4**@g-C_3N_4 NS-TiO_2 fibers, **5**@g-C_3N_4 NS-TiO_2 fibers and **6**@g-C_3N_4 NS-TiO_2 fibers in degradation of Rhodamine 6G.

6.1.4. Complexes 3, 6 and 7 and their g-C_3N_4 QDs conjugates functionalized TiO2 nanofibers

The photocatalytic degradation of Rhodamine 6G (6.63 x 10^{-5} M) was studied using g-C_3N_4 QDs-TiO_2 fibers, **3**@g-C_3N_4 QDs-TiO_2 fibers and **4**@g-C_3N_4 QDs-TiO_2 fibers, **7**, **7**-TiO_2 fibers and **7**@g-C_3N_4 QDs-TiO_2 fibers (5 mg) at pH 9. Using g-C_3N_4 QDs-TiO_2 fibers, **3**@g-C_3N_4 QDs-TiO_2 fibers and **4**@g-C_3N_4 QDs-TiO_2 fibers, the degradation studies were performed for 300 min. However, using **7**, **7**-TiO_2 fibers and **7**@g-C_3N_4 QDs-TiO_2 fibers, the degradation studies were performed for 75 min. The kinetics (k_{obs}) were used to compare degradation results. The catalysts and the solution of the pollutant were left in the dark for 120 min to reach adsoption-desoption equilibrium. Afterward, the pollutant was irradiated in the absence of the catalysts. Sono- and photosono-catalytic processes were not performed for complex **7** and g-C_3N_4 QDs-TiO_2 fibers and **7**@g-C_3N_4 QDs-TiO_2 fibers.

The activities of g-C_3N_4 QDs and **3**@g-C_3N_4 QDs and **4**@g-C_3N_4 QDs and **7**@g-C_3N_4 QDs were not studied because they were soluble in aqueous solutions. When irradiations were performed in the absence of the catalysts, no spectral changes were perceived. The degradation results are shown in **Fig. 6.8** and **Tables 6.3**.

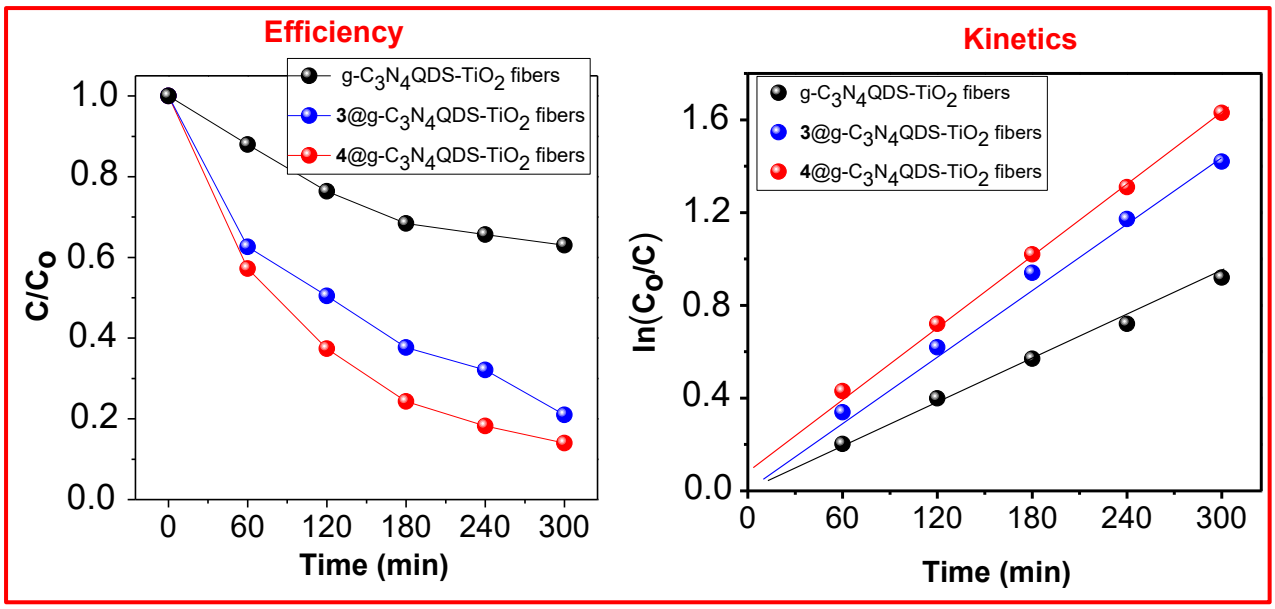

Fig. 6.8. Catalytic efficiencies and kinetics of Photo-catalytic degradation of Rhodamine 6G using g-C_3N_4 QDs-TiO_2 fibers, **3**@g-C_3N_4 QDs-TiO_2 fibers, **4**@g-C_3N_4 QDs-TiO_2 fibers.

When g-C_3N_4 QDs-TiO_2 fibers, **3**@g-C_3N_4 QDs-TiO_2 fibers and **4**@g-C_3N_4 QDs-TiO_2 fibers were used, degradation efficiencies of 46, 79 and 86%, respectively were obtained. The degradation efficiencies obtained using **3**@g-C_3N_4 QDs-TiO_2 fibers and **4**@g-C_3N_4 QDs-TiO_2 fibers in Rhodamine 6G were higher than degradation efficiencies obtained using **3**, **4**, **3**-TiO_2 fibers and **4**-TiO_2 fibers, **Table 6.3**. This suggests that the conjugation of complexes **3** and **4** with g-C_3N_4 QDs resulted in enhanced degradation. Surprisingly, the degradation efficiencies of **3**@g-C_3N_4 QDs-TiO_2 fibers and **4**@g-C_3N_4 QDs-TiO_2 fibers in photo-catalytic process were higher than those of **3**@g-C_3N_4 NS-TiO_2 fibers and **4**@g-C_3N_4 NS-TiO_2 fibers. This was not anticipated because nanosheets are known to be more catalytically active than QDs [223].

The kinetic plots shown in **Table. 6.3** and **Fig. 6.8**. The largest k_{obs} were obtained using **4**@g-C_3N_4 QDs-TiO_2 fibers. As anticipated, the shortest half-life ($\tau_{1/2}$) was obtained using **4**@g-C_3N_4 QDs-TiO_2 fibers since the highest degradation was obtained with the same catalyst.

6.1.5. Complex 5 conjugate to $MnFe_2O_4$ NPs and supported to TiO_2 nanofibers

The photo-, sono- and photosono-catalytic degradation of Rhodamine 6G (6.63×10^{-5} M) were performed using **5**@$MnFe_2O_4$-TiO_2 fibers at pH 9. The degradation studies were performed for 270 min. The spectral changes were recorded in 30 min intervals. The catalyst and the solution of the pollutant were left in the dark for overnight to establish adsorption-desorption equilibrium. For comparison purposes, the catalytic degradation efficiencies of **5**, $MnFe_2O_4$, **5**@$MnFe_2O_4$ (powders) and TiO_2 fibers, **5**-TiO_2 fibers, and $MnFe_2O_4$-TiO_2 fibers were also studied and compared with the results obtained from **5**@$MnFe_2O_4$-TiO_2 fibers.

The degradation efficiencies and kinetics plots for photosono-catalytic degradation process are displayed in **Table. 6.3** and **Fig. 6.9**. The degradation efficiencies and kinetics plots for the degradation process for photo- and sono-catalytic processes are shown in **Appendix 18** and **Table. 6.3**.

The $MnFe_2O_4$ NPs (powder) achieved 14%, 24% and 33% degradation efficiencies for photo-, sono- and photosono-catalytic processes, respectively. The **5**@$MnFe_2O_4$ NPs gave much higher degradation efficiencies of 58%, 63% and 76% for photo-, sono- and photosono-catalytic processes, respectively, showing the benefit of the combination of $MnFe_2O_4$ NPs and **5**.

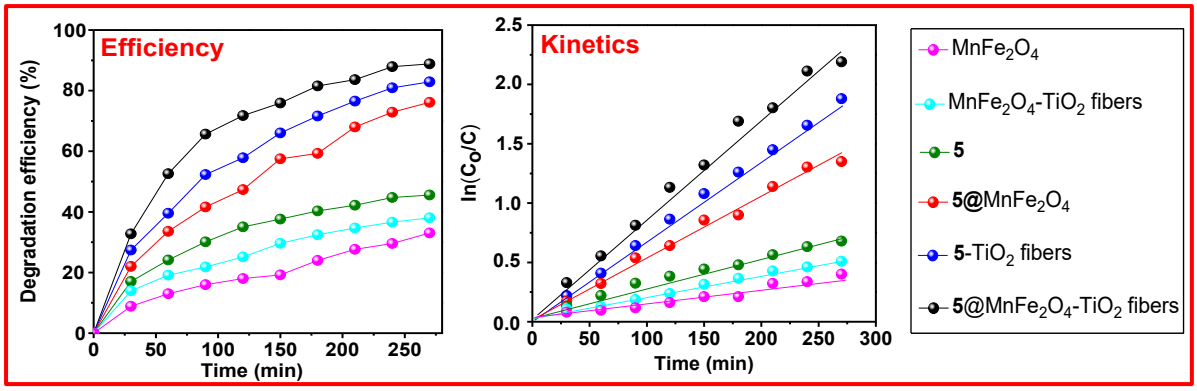

Fig. 6.9. Degradation efficiencies and reaction kinetics plots of Rhodamine 6 G (6.63 $\times 10^{-5}$ M) degradation for photosono-catalytic process using various catalysts.

The catalytic activities of TiO_2 fibers were 4, 7 and 11% for photo-, sono- and photosono-catalytic degradation processes, respectively as stated above. The percentage degradation efficiency obtained with $MnFe_2O_4$-TiO_2 fibers were 21, 30 and 39% for photo-, sono- and photosono-catalytic processes, respectively. Thus $MnFe_2O_4$-TiO_2 fibers hybrid was more catalytically active than TiO_2 fibers. The observed catalytic activity can be attributed to an apparent decrease in the band gap energy of the $MnFe_2O_4$-TiO_2 fibers with respect to the band gap energy of pristine TiO_2 fibers, which resulted in improved visible light absorption of the hybrid compared to pristine TiO_2 fibers. For **5**-TiO_2 fibers, 50, 66 and 83% were obtained for photo-, sono- and photosono- degradation processes, respectively. Thus the **5**-TiO_2 fibers displayed more catalytic activity than $MnFe_2O_4$- TiO_2 fibers. This can be attributed to the presence of **5** in **5**-TiO_2 fibers. Complex **5** is highly conjugated and exhibits good visible light absorption through B- and Q-bands. The **5**@$MnFe_2O_4$-TiO_2 fibers outperformed all the catalysts with conversions of 65, 72 and 90%. Higher degradation efficiencies were observed for photosono-catalysis compared to photo- and sono-catalysis. The reason will be provided below. In general, the fibers gave larger

degradation efficiencies than the powders, this could be due to the distribution of the powders in solution.

Kinetic plots suggest that the degradation of Rhodamine 6 G follows the pseudo-first-order kinetics with respect to the catalysts used for photo-, sono- and photosono-catalytic degradation processes (**Fig. 6.9**), as judged by the proper fit of the ln (C_O/C) versus irradiation time plots. The k_{obs} was the highest for **5**@$MnFe_2O_4$-TiO_2 fibers, with the shortest half-life. In addition, k_{obs} was also higher for photosono-catalytic degradation process compared to photo- and sono-catalytic processes. This was anticipated since **5**@$MnFe_2O_4$-TiO_2 fibers outperformed all the catalysts and photosono-catalytic process achieved higher degradation efficiency than its individual analogous.

The higher catalytic efficiency obtained using **5**@$MnFe_2O_4$-TiO_2 fibers compared to individual components can be envisaged from photophysical properties. The low Φ_F was recorded for **5**@$MnFe_2O_4$ compared to that obtained from **5** alone. This is due to fluorescence quenching in **5**@$MnFe_2O_4$ which minimizes the recombination of the electrons and holes. In addition, the presence $MnFe_2O_4$ also resulted in an enhanced intersystem crossing to the forbidden triplet state. This phenomenon enhanced singlet oxygen quantum yield since the singlet oxygen quantum yield obtained in **5**@$MnFe_2O_4$ conjugate was higher than the one obtained in **5** alone. The decoration of TiO_2 fibers with **5**@$MnFe_2O_4$ resulted in a significant decrease in band gap energy of the **5**@$MnFe_2O_4$-TiO_2 fibers compared to that of the pure TiO_2 fibers. This effect also improved the catalytic activity of the **5**@$MnFe_2O_4$-TiO_2 fibers.

6.1.6. Complex 6 conjugated and supported on ZnO nanofibers

The photo-, sono- and photosono-catalytic degradation of Rhodamine 6G (6.63×10^{-5} M) were studied using **6**@g-C_3N_4 NS-ZnO fibers composite. For comparison purposes, photo-, sono- and photosono-catalytic activities of complex **6** (as powder), and fibers: ZnO fibers, g-C_3N_4 NS-ZnO fibers, **6**-ZnO fibers. The catalytic studies of **6**@g-C_3N_4 NS were not investigated because they were soluble in aqueous solution. The studies were performed at pH 9 for 270 min. The degradation efficiencies were assessed in 30 min intervals. When the studies were performed in the blank (in the absence of the catalyst), no degradations were observed. However, in the presence of complex **6**, ZnO fibers, g-C_3N_4 NS-ZnO fibers, **6**-ZnO fibers and **6**@g-C_3N_4 NS-ZnO fibers Rhodamine 6G degradation occurred.

The UV-Vis spectral changes and degradation efficiencies are displayed in **Appendixes 19** and **20**. The photosono-catalytic degradation plots and kinetics are shown in **Fig. 6.10** and **Table 6.3**. The photo- and sono-catalytic degradation plots and corresponding kinetics are shown in **Appendix 19** and **Table 6.3**. The degradation efficacies of the ZnO_2 fibers alone were 6, 9 and 13 % for photo-, sono- and photosono-catalytic processes, respectively. The degradation efficacies of the complex **6** were 31, 45 and 57% for photo-, sono- and photosono-catalytic processes, respectively. The high catalytic activity of complex **6** is due to the fact that Pcs have an ability to generate both singlet oxygen ($^1O2$) and hydroxide radicals ($^{\bullet}OH$) [224], the latter only under sono- irradiation.

The degradation efficacies of g-C_3N_4 NS-ZnO fibers were 29, 47 and 56% for photo-, sono- and photosono-processes, respectively. The degradation efficiency of g-C_3N_4 NS-ZnO fibers is higher than that of ZnO fibers. The degradation efficacies of **6**-ZnO

fibers were 59, 68 and 86% for photo-, sono- and photosono-catalytic processes, respectively. The **6**-ZnO fibers were more catalytically active than ZnO fibers, complex **6** and g-C_3N_4 NS-ZnO fibers.

The **6**@g-C_3N_4 NS-ZnO fibers outperformed all the catalysts with degradation efficacies of 74, 85 and 97% for photo-, sono- and photosono-catalytic processes, respectively, **Table 6.3**. The kinetic studies revealed that the degradation follows the first order with respect to the catalysts used. Amongst the catalysts used, **6**@g-C_3N_4 NS-ZnO fibers also gave the largest k_{obs} and shortest $t_{1/2}$ in for all the catalytic processes suggesting that the formation of the hybrid of **6**@g-C_3N_4 NS-ZnO fibers played a pivotal role in enhancing Rhodamine 6G degradation efficiency, **Table 6.3**.

ZnO fibers were less catalytically active than TiO_2 fibers. This can be attributed to the fact that the band gap energy of TiO_2 fibers were lower than that of the ZnO fibers. Eventhough, **6**@g-C_3N_4 NS-ZnO fibers have lower band gap than **6**@g-C_3N_4 NS-ZnO fibers, however, **6**@g-C_3N_4 NS-ZnO fibers are more catalytically active. This is due to the fact that **6**@g-C_3N_4 NS-ZnO fibers have higher singlet oxygen quantum yield than **6**@g-C_3N_4 NS-ZnO fibers.

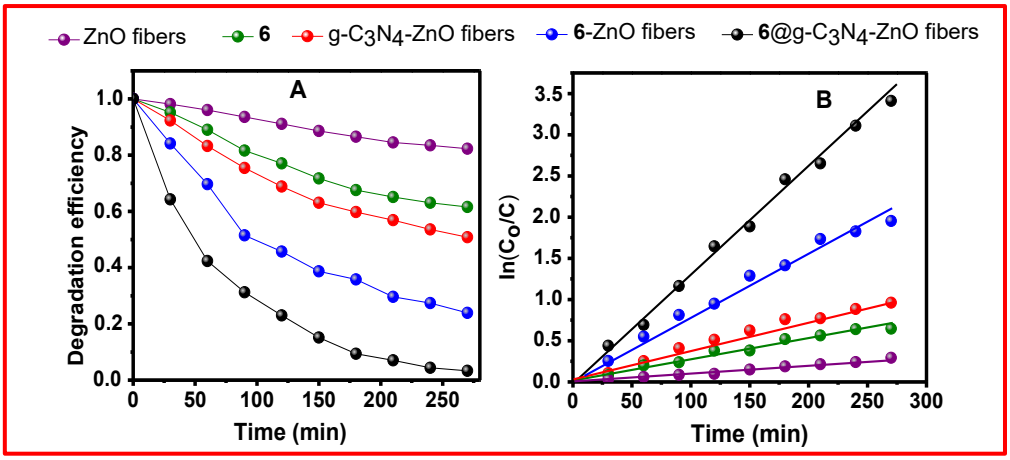

Fig. 6.10. Degradation efficiencies **(A)** and reaction kinetics **(B)** plots of Rhodamine 6 G (6.63 $\times 10^{-5}$ M) degradation for photosono-catalysis process using various catalysts.

6.2. Degradation of 2,4-dichlorophenol

The photocatalytic degradations of 2,4-dichlorophenol (6.63 x 10^{-5} M) in the presence of TiO_2 fibers, **3**, **4**, **7**, g-C_3N_4 QDs-TiO_2 fibers, **7**-TiO_2 fibers, **3**-TiO_2 fibers**,** **4**-TiO_2 fibers, **3**@g-C_3N_4 QDs-TiO_2, **4**@g-C_3N_4 QDs-TiO_2 and **7**@g-C_3N_4 QDs-TiO_2 fibers were investigated at pH 5. Using the composites of complexes **3** and **4**, the degradation were performed for 300 min, which using the composites of complex **7**, the kinetics were performed for 75 min. The kinetic results are shown in **Fig. 6.11** and **Table 6.4**. When TiO_2 fibers, g-C_3N_4 QDs-TiO_2 fibers, **3**, **4, 3**-TiO_2 fibers, **4**-TiO_2 fibers, **3**@g-C_3N_4 QDs-TiO_2 fibers and **4**@g-C_3N_4 QDs-TiO_2 fibers were used, efficiencies of 4, 38, 17, 19, 22, 25, 63 and 77% were obtained in dichlorophenol degradation, respectively.

The k_{obs} obtained using TiO_2 fibers, **7**, g-C_3N_4 QDs-TiO_2 fibers and **7**-TiO_2 fibers were 0.62 x10^{-4}, 36 x10^{-4}, 33 x10^{-4} and 39 x10^{-4} min^{-1}, respectively. The k_{obs} obtained from **7**@g-C_3N_4 QDs-TiO_2 fibers 44 x10^{-4} min^{-1}. The k_{obs} obtained in this study using **7** was higher than those obtained using **3** and **4** alone, suggesting that **7** was more catalytically active.

The k_{obs} obtained using **7**-TiO_2 fibers was higher than those obtained using **3**-TiO_2 fibers and **4**-TiO_2 fibers, which suggests that **7**-TiO_2 fibers was more catalytically acative than **3**-TiO_2 fibers and **4**-TiO_2 fibers. The k_{obs} for **3**@g-C_3N_4 QDs-TiO_2 fibers and **4**@g-C_3N_4 QDs-TiO_2 fibers composites were higher than those obtained from **7**@g-C_3N_4 QDs-TiO_2 fibers, which suggests that **3**@g-C_3N_4 QDs-TiO_2 fibers and **4**@g-C_3N_4 QDs-TiO_2 fibers were more active than **7**@g-C_3N_4 QDs-TiO_2 fibers (**Table 6.4**).

The degradation results from complexes **3**, **4**, **3**-TiO_2 fibers and **4**-TiO_2 fibers for 2,4-dichlorophenol and Rhodamine 6G suggest that the Pcs and their corresponding hybrids were more catalytically active towards Rhodamine 6G degradation than 2,4-dichlorophenol. This is due to the fact that Rhodamine 6G is positively charged, whereas 2,4-dichlorophenol in has an electron rich O-H region. Using electrostatic potential (ESP) maps (**Fig. 4.24**) it was shown that the Pc complexes showed electron rich regions. The electrostatic attraction between the Pcs with Rhodamine 6G transpires which facilitate degradation. On the other hand, electrostatic repulsion transpires between 2,4-dichlorophenol and Pcs which reduces degradation. The extent of overlap between the emission spectrum of the light source and the absorption bands of different photosensitizers is also assumed to be the main contributing factor in differences in photocatalytic activity.

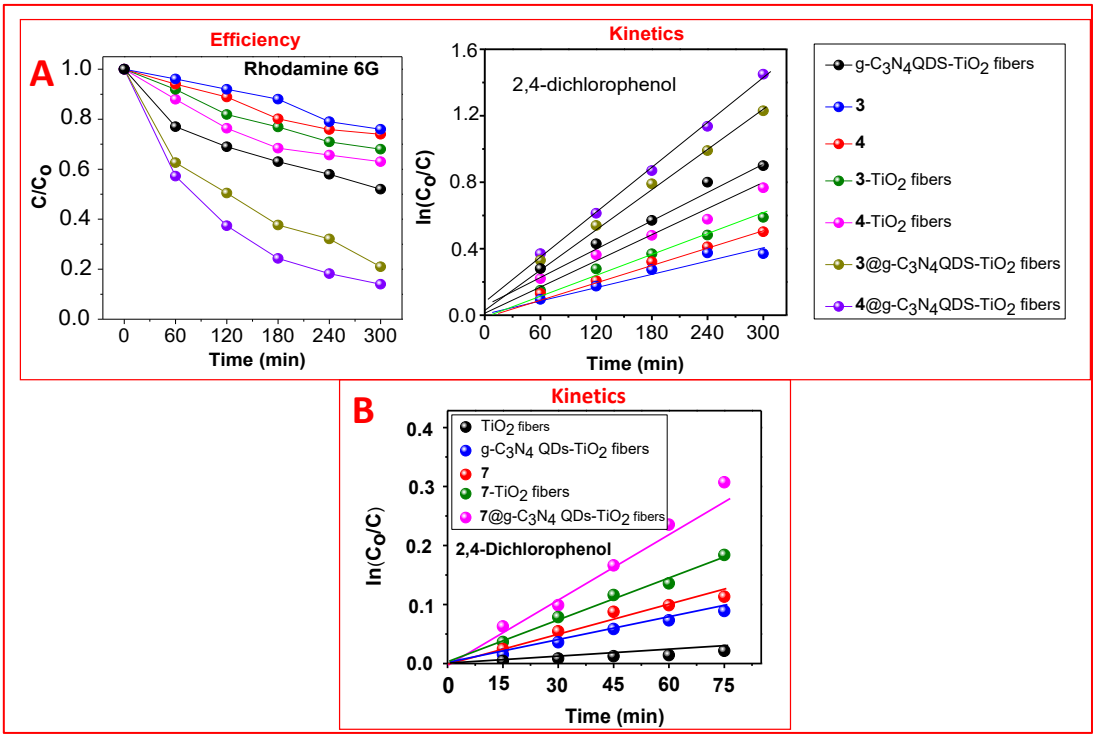

Fig. 6.11. Degradation efficiencies and kinetics **A** and kinetics **B** for photocatalytic degradation of 2,4-dichlorophenol using various catalysts.

Table 6.4: Degradation of 2,4-dichlorophenol using various catalysts at pH 5.

Catalysts	Efficiency (%)	k_{obs} (min^{-1}) x10^{-4}	$\tau_{1/2}$
TiO_2 fibers	4	0.62	11177
3	17	09	770
4	19	10	693
3-TiO_2 fibers	22	16	433
4-TiO_2 fibers	25	23	301
g-C_3N_4 QDs– TiO_2 fibers	38	33	210
3@g-C_3N_4 QDs-TiO_2 fibers	63	48	144
4@g-C_3N_4 QDs-TiO_2 fibers	77	45	114
7	---	36	192
7-TiO_2 fibers	---	39	177
7@g-C_3N_4 QDs-TiO_2 fibers	---	44	157

The adsorption co-efficiencies of Rhodamine 6G on **7**-TiO_2 fibers and **7**@g-C_3N_4 QDs -TiO_2 fibers hybrid were probed using Langmuir-Hinshelwood model (**Eq. 6.2**) [225-226]. The Langmuir-Hilshelwood model proposes that the reactant species first adsorb to the surface of the catalyst followed by the reaction of the reactants to form the intermediates and products [221]. The K_A and k_r values are presented in **Table 6.5**. The results indicate that both K_A and k_r are larger for **7**@g-C_3N_4 QDs -TiO_2 fibers than for **7**-TiO_2 fibers. These results advocate that the adsorption of 2,4-dichlorophenol is

favored in **7**@g-C_3N_4 QDs -TiO_2 fibers more than in **7**-TiO_2 fibers. The results obtained from re-used catalysts suggests that both **7**-TiO_2 fibers and **7**@g-C_3N_4 QDs -TiO_2 fibers demonstrated high catalytic stability.

Table 6.5. Langmuir–Hinshelwood parameters for the photodegradation of Rhodamine 6G and 2,4-dichlorophenol.

	Catalyst	**k(mol L^{-1} min^{-1}) 10^{-7}**	**K_A(mol^{-1} L) ×10^5**
2,4-dichlorophenol	**7**-TiO_2 fibers	1.07	3.04
		1.13	3.17
	7@g-C_3N_4 QDs-TiO_2 fibers	2.75	3.91
		2.63	3.79
The values in the highlighted rows are for reused catalysts			

6.3. Catalyst stability and reusability

In order so investigate the stability and re-usability of the photosono catalysts, the catalytic degradation studies were repeated for five times using **3**@g-C_3N_4-TiO_2 fibers and **6**@g-C_3N_4-TiO_2 fibers in Rhodamine 6G degrdation. The results are shown in **Fig. 6.12**. The photosono-catalytic degradation efficiency obtained after five cycles using **3**@g-C_3N_4-TiO_2 fibers was 68, whereas 86% was obtained using **6**@g-C_3N_4-TiO_2 fibers. The results suggests that the catalysts demonstrated sufficient stability even after five cycles.

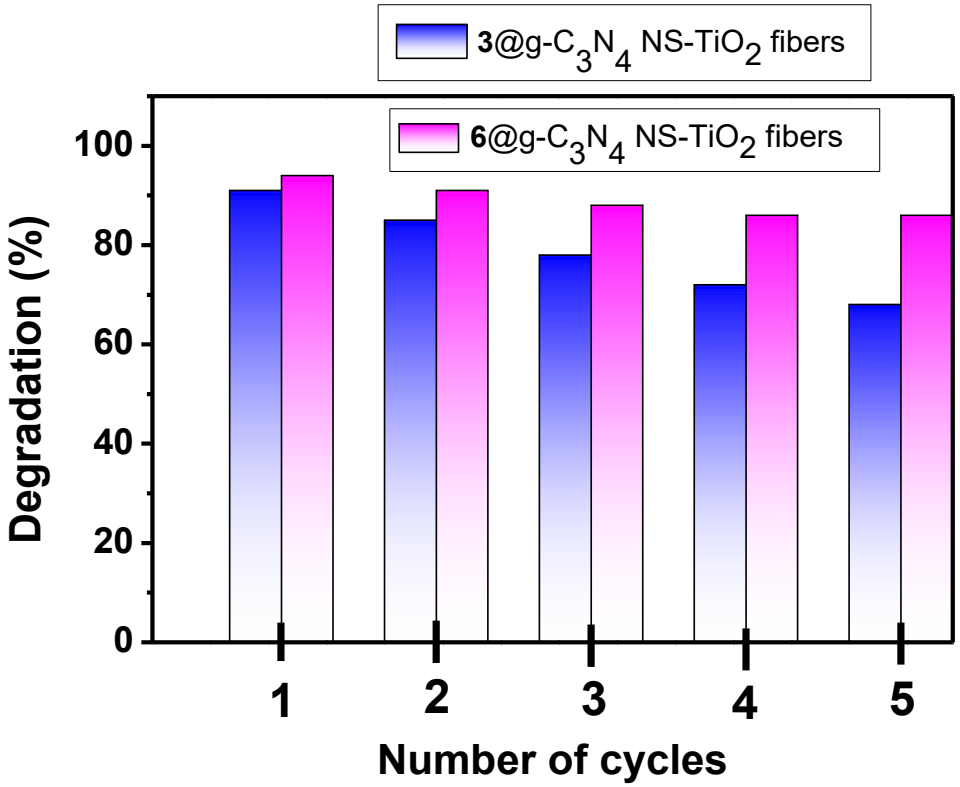

Fig. 6.12. Catalyst stability and re-usability studies of **3**@g-C_3N_4-TiO_2 fibers and **6**@g-C_3N_4-TiO_2 fibers in photosono-catalytic process after five cycles.

6.4. Photo-electrochemical studies

Photo-electrochemical studies of the complexes **3**, **4**, **5** and **6** and the conjugates were performed to investigate photo-electrochemical properties such as charge mobility, conductivity properties and photocurrent response.

6.4.1. Pc complexes

The transient photocurrent, electrochemical impedance spectroscopic (EIS) properties of complexes **3**, **4**, **5** and **6** were studied to determine the charge mobility, conductivity properties, and photocurrent response. The Nyquist plots are shown in **Fig. 6.13A**. The Nyquist plot gives information about the charge transfer resistance (R_{ct}). The smaller R_{ct} means higher conductivity. High R_{ct} values suggest poor electron transfer. The R_{ct} values for complexes **3**, **4**, **5** and **6** were 964, 842, 609 and 545 Ω, respectively.

From R_{ct} values, the conductivity of complex **4** is higher than that of complex **3** and that of complex **6** is higher than that of complex **5**.

This suggests that the presence of nitrogen in the phenoxy picolinic acid substituents in complexes **4** and **6** resulted in enhanced conductivity. The R_{ct} value of complex **5** is lower than **3** and that of **6** lower than for **4**. This suggests that the number of methoxy groups also play the crucial role in facilitating charge mobility. Complexes **3** and **4** each have only one methoxy group as the substituent, whereas, the complexes **5** and **6** each have two methoxy groups as substituents.

The transient photocurrent response plots (**Fig. 6.13B**) suggest that complexes **3** and **4** are more photoactive than complexes **5** and **6**. This can be attributed to smaller band gap energies of complexes **3** and **4** compared to **5** and **6**.

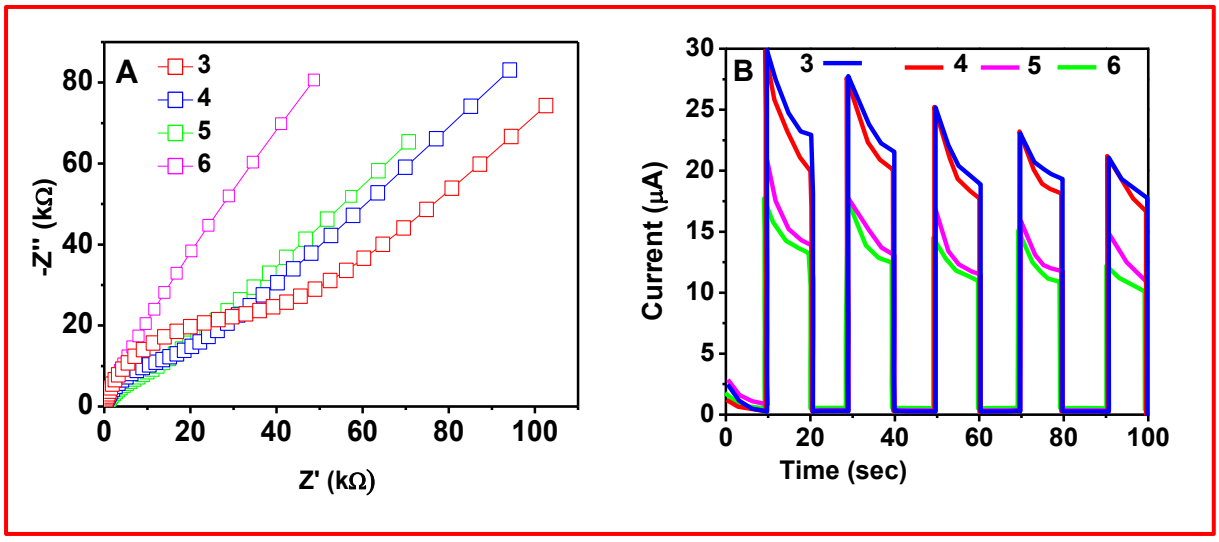

Fig. 6.13. Nyquist plots of electrochemical impedance spectroscopy (EIS) (**A)** and transient photocurrent (i-t) response (**B**) of the complexes **3**, **4**, **5** and **6**.

6.4.2. g-C_3N_4 NS and conjugates

The transient photocurrent and electrochemical impedance spectroscopic (EIS) properties of g-C_3N_4 NS, **1**@g-C_3N_4 NS, **2**@g-C_3N_4 NS, **3**@g-C_3N_4 NS and **4**@g-C_3N_4 NS conjugates were studied to observe the effect of conjugation.

The Nyquist plots for g-C_3N_4 NS, **1**@g-C_3N_4 NS, **2**@g-C_3N_4 NS, **3**@g-C_3N_4 NS and **4**@g-C_3N_4 NS conjugates were 366, 213, 199, 119 and 101 Ω, respectively are shown in **Fig. 6.14A.** The results revealed that the charge resistances are lower for the conjugates compared to corresponding Pcs and g-C_3N_4 NS alone. This suggests that the conjugation resulted to an improved charge transfer and possible separation of the charge transfer. The transient photocurrent response plots of the conjugates (**Fig. 6.14B**) suggest that the conjugates are more photo active than g-C_3N_4 alone. Therefore, the conjugation resulted in improved photocatalytic efficiency. The **6**@g-C_3N_4 NS conjugate appears to be more photo-active than all the other conjugates.

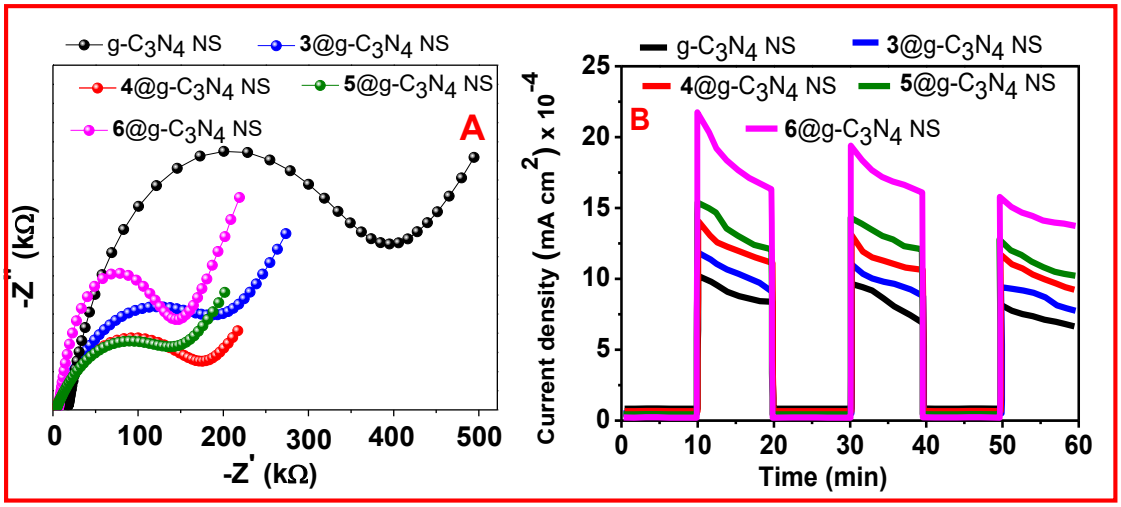

Fig. 6.14. Nyquist plots of electrochemical impedance spectroscopy (EIS) (**A)** and transient photocurrent (i-t) response (**B**) of the conjugates.

6.5. Summary for the Chapter

The functionalized fibers were studied in photo-, sono- and photosono-degradation of Rhodamine 6G. The functionalized fibers were more effective that pristine fibers and corresponding Pcs and nanoparticles. Photosono-degradation process was more effective than photo- and sono-degradation process. The porphyrin and Pcs functionalized fibers were used in photocatalytic degradation of Rhodamine 6G and 2,4-dichlorophenol. The fibers were more active towards Rhodamine 6G degradation than 2,4-dichlorophenol degradation.

Chapter seven

This chapter discusses the effect of the various parameters such as pH, initial concentration of the pollutant and addition of the radicals' initiators on degradation efficiency.

7.1. The effect of radical's initiators

7.1.1. Tert-butyl hydrogen peroxide (TBHP) and azo-bis-isobutyronitrile (AINB)

The *tert*-butyl hydrogen peroxide (TBHP) and azo-bis-isobutyronitrile (AINB) (1 mL of 0.3 M) were used as radical initiators in photo-, sono- and photosono-catalytic degradation of Rhodamine 6G using **1**-TiO_2 fibers and **2**-TiO_2 fibers. TBHP, AINB are decomposed at high temperatures or in the presence of the catalysts, to highly reactive carbon cantered and $^{\bullet}OH$ radicals.

The degradation efficiencies obtained in the absence radicals initiators are displayed in **Table 7.1** for comparison purposes even though they have been shown in **Table 6.1**. The degradation efficiencies obtained in the presence of TBHP and AINB are also displayed in **Table 7.1**.

A significant increase in Rhodamine 6G degradation efficiencies was observed upon the addition of the radical initiators, **Table 7.1**. Among the radical initiators used, TBHP exhibited higher reactivity than AINB with percentage conversions of 71% and 74% for photolytic using **1**-TiO_2 and **2**-tiO_2 fibers, 88% and 92% for sonocatalytic using **1**-TiO_2 and **2**-tiO_2 fibers and 100% for photosono-catalytic degradation process for both **1**-TiO_2 and **2**-TiO_2 fibers **Table 7.1**. The sonocatalytic exhibited higher efficiency than photolytic process. This can be rationalized by the reaction conditions under which these processes are operated. The sonocatalytic degradation process encompasses a significant increase in temperature during "hotspot" which subsequently promotes the decomposition of both AINB and TBHP. In contrast, photolytic degradation utilizes visible light, which is not as effective for AINB and TBHP decomposition as compared to the sonocatalytic process, hence, the sonocatalytic process was highly efficient in the latter.

Table 7.1. Percentage degradation efficiencies of Rhodamine 6G in the presence of pristine TiO_2 fibers, MPc complexes and functionalised fibers, in the presence and absence of AINB and TBHP.

Catalysts	Degradation efficiency (%)								
	Photo-catalytic degradation			Sono-catalytic degradation			Photosono-catalytic degradation		
	Photo	Photo + AINB	Photo +TBHP	Sono	Sono + AINB	Soo + TBHP	Photo +sono	Photosono + AINB	Photosono+ TPHP
TiO_2 fibers	4	9	13	7	19	26	11	38	43
1	11	21	29	16	33	41	19	62	69
2	14	25	32	21	37	44	23	64	71
1-TiO_2 fibers	34	67	71	49	79	88	58	100	100
2-TiO_2 fibers	37	69	74	54	84	92	63	100	100

AINB = azo-bis-isobutyronitrile, TBHP = *tert*-butyl hydrogen peroxide

Despite AINB and TBHP being both radical initiators, decomposition pathways are different. The AIBN is decomposed to two cyanopropyl radicals and N_2, **Eqs. 7.1** and **7.2** [227,228].

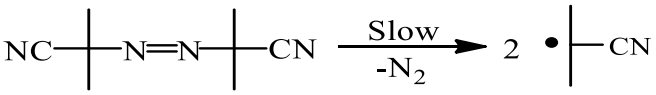

(7.1)

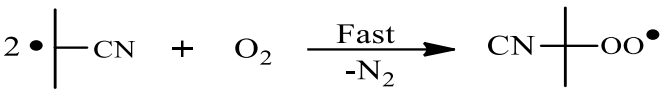

(7.2)

The carbon-centred cyanopropyl radicals are highly reactive, and they either instigate H abstraction, which is a first step in the degradation of organic pollutants, or react with O_2 to generate peroxy radicals. In contrast, TBHP undergoes homolytic cleavage to generate $^{\bullet}OH$ radicals and other radicals, **Eqs. 7.3-7.5** [227,228]

$$(CH_3)_3COOH \rightarrow (CH_3)_3CO^{\bullet} + {}^{\bullet}OH \quad \textbf{(7.3)}$$

$(CH_3)_3CO^{\bullet} + (CH_3)_3COOH \rightarrow (CH_3)_3COH + (CH_3)_3COO^{\bullet}$ **(7.4)**

$2(CH_3)_3COO^{\bullet} \rightarrow 2(CH_3)_3CO^{\bullet} + O_2$ **(7.5)**

Taking into account of the results, it can be presumed that **1**-TiO_2 and **2**-TiO_2 fibers promote the TBHP O-O cleavage. This rationalizes the higher Rhodamine 6G conversion obtained in the presence of TBHP than when AINB was utilized for both photolytic and sonocatalytic degradation processes.

7.1.2. Peroxymonosulfate

The effect of peroxymonosulfate (PMS) (0.5 mL of 0.1 mol. L^{-1}) in Rhodamine 6G (6.63×10^{-5} M) degradation efficiency was investigated in photo, sono and photosono-catalytic degradation processes using **3**@TiO_2 fibers, **4**@TiO_2 fibers, **5**@TiO_2 fibers and **6**@TiO_2 fibers at pH 9. For comparison purposes, the studies were first performed in the presence of PMS alone (blank, without light or ultrasound). Subsequently, the studies were performed in the presence of PMS and visible light alone (photo), ultrasound alone (sono) and combined visible light and ultrasound (photosono).

7.1.2.1. Degradation efficiency

The degradation and kinetic results for the photo-, sono and photosono-catalytic degradation process are shown in **Fig. 7.1** and **Tables 7.2** and **7.3**. For comparison purposes, the results for Rhodamine 6G degradation in the absence of PMS using **3**@TiO_2 fibers, **4**@TiO_2 fibers, **5**@TiO_2 fibers and **6**@TiO_2 fibers are shown **Table 7.2** even though they have already been listed in **Table 6.3**. When degradation studies were performed for PMS alone using photo, sono and photosono processes, degradation efficiencies of 13 %, 21 % and 25 % were obtained, respectively. This suggests that ultrasound and light activate peroxymonosulfate during degradation, which subsequently enhances degradation. When PMS was used in conjunction with

functionalized TiO_2 fibers, degradation efficiencies further improved. The degradation efficiencies obtained in photo-catalytic process were 72 **,** 77**,** 81 and 85 %, for **3**@TiO_2 fibers, **4**@TiO_2 fibers, **5**@TiO_2 fibers and **6**@TiO_2 fibers, respectively (**Fig. 7.1** and **Table 7.3**). The degradation efficiency obtained in the sono-catalytic process was 100 % after 240 min using **3**@TiO_2 fibers, **4**@TiO_2 fibers, **5**@TiO_2 fibers and **6**@TiO_2 fibers.

In the photosono-catalytic process 100 % degradation efficiencies were obtained after 180 min using **3**@TiO_2 fibers, **4**@TiO_2 fibers, **5**@TiO_2 fibers and **6**@TiO_2 fibers. The results suggest that the combination of ultrasound, light and catalysts plays a profound role in activating PMS. The kinetic studies showed pseudo first order kinetics with linear fit for all the catalysts, **Fig. 7.1**. Higher k_{obs} was obtained using **4**@TiO_2 fibers.

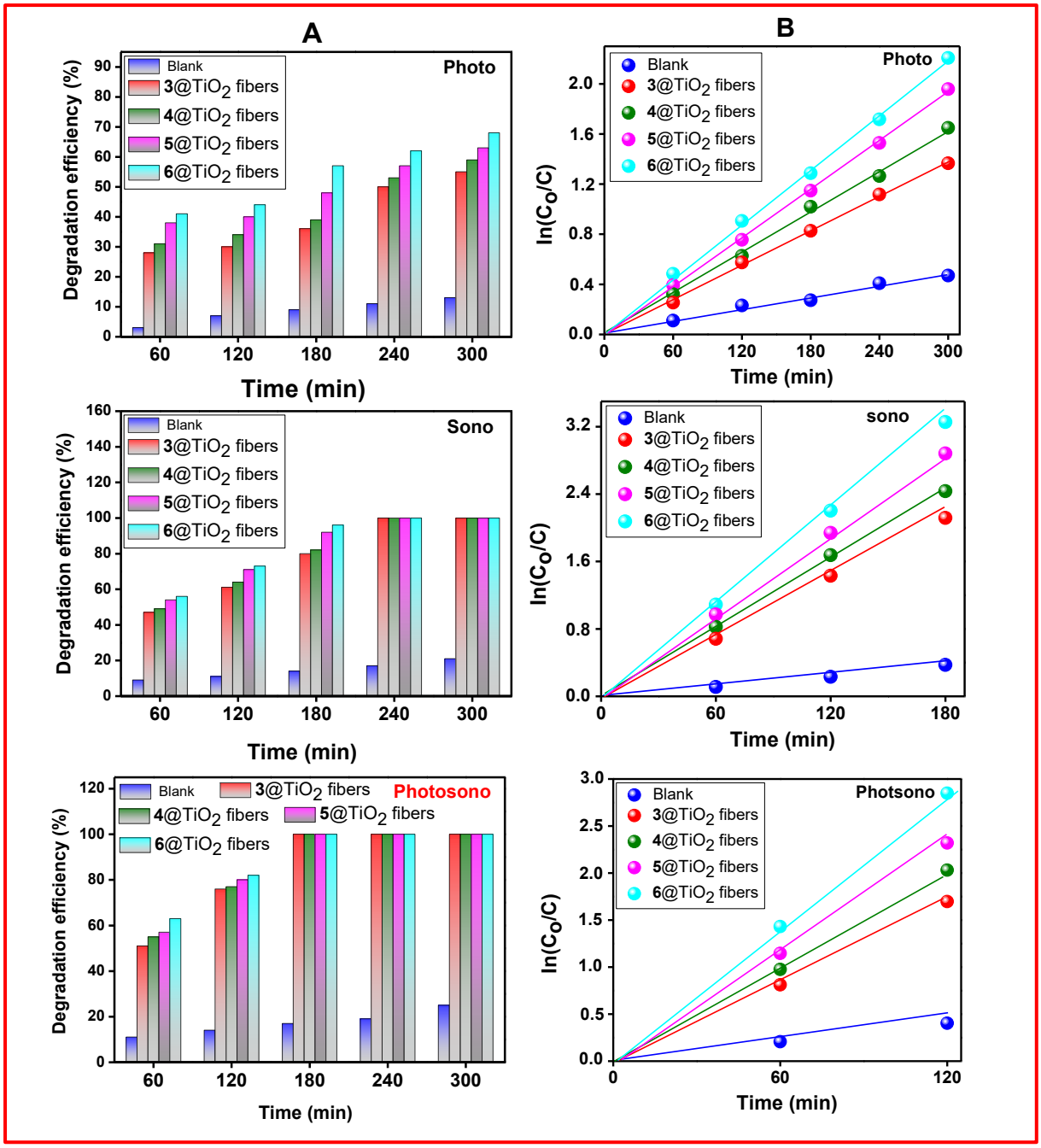

Fig 7.1. Rhodamine 6G (6.63×10^{-5} M) percentage degradations **A** and kinetics **B** plots for photosono-catalytic process using functionalized TiO_2 fibers in the presence of PMS at pH 9. Blank = degradation in PMS alone. [PMS] = 0.1 mol. L^{-1}, pH = 9.

Table 7.2: Degradation efficiencies, rate constant (k_{obs}) and half-life of the photo, sono and photosono-catalytic degradation processes of the various catalysts at pH 9 in the absence of PMS.

Catalysts	Degradation efficiency (%)			k_{obs} (min^{-1}) x10^{-4}			$\tau_{1/2}$		
	Photo	Sono	Photosono	Photo	Sono	Photosono	Photo	Sono	Photosono
3@TiO_2 fibers	39	55	68	29	35	49	239	198	141
4@TiO_2 fibers	43	59	73	31	37	51	224	187	134
5@TiO_2 fibers	54	72	85	34	49	65	203	141	107
6@TiO_2 fibers	57	76	88	36	54	68	193	128	102

Table 7.3: Degradation efficiencies, rate constant (k_{obs}) and half-life of photosono-catalytic degradation processes in various pH solutions at pH 9 in the presence of PMS. [PMS] = 0.1 mol. L^{-1}.

Catalysts	Degradation efficiency (%)			k_{obs} (min^{-1}) x10^{-4}			$\tau_{1/2}$		
	Photo	Sono	Photosono	Photo	Sono	Photosono	Photo	Sono	Photosono
PMS (blank)	13	21	25	1.93	8	12	3590	866	577
3@TiO_2 fibers	72	100	100	48	92	113	144	75	61
4@TiO_2 fibers	77	100	100	56	96	119	124	72	58
5@TiO_2 fibers	81	100	100	60	102	129	115	67	54
6@TiO_2 fibers	85	100	100	65	106	133	106	65	52

7.1.2.2. Investigation of the reactive species

The electron paramagnetic resonance (EPR) and reactive species quenching experiments were performed to investigate the reactive species participating in photo, sono and photosono processes and identify the most reactive species in each of these reactions. The plots are shown in **Fig 7.2**. TEMPO (1.0 mL of 0.1 M in water) was used as $^1O_2$ and DMPO (1.0 mL of 0.1 M in water) was used as $^{\bullet}OH$ and $SO_4^{-\cdot}$ quencher.

The **6**@TiO_2 fibers were used as the catalyst in the presence of PMS. The EPR spectra in the presence of TEMPO for photo, sono and photosono processes display peaks corresponding to $^1O_2$. This suggests that $^1O_2$ was involved in photo, sono and photosono processes. The EPR spectra in the presence of DMPO for photo, sono and photosono processes displayed peaks corresponding to $SO_4^{\bullet-}$ suggesting that the sulfate radicals also participated in all the processes. However, the EPR peaks corresponding to $^\bullet OH$ were only observed in sono and photosono-catalytic processes. Therefore, the photo-catalytic process was instigated by $^1O_2$ and $SO_4^{\bullet-}$ only, whereas the sono and photosono-catalytic processes were instigated by $^\bullet OH$, $^1O_2$ and $SO_4^{\bullet-}$. Therefore, the higher catalytic degradation efficiencies obtained in the presence of PMS were due to the generation of $^\bullet OH$, $^1O_2$ and $SO_4^{\bullet-}$.

Quenching experiments were performed in order to investigate the most reactive species in each of photo, sono and photosono processes. The plots are shown in **Appendix 21**. The reaction was limited to 180 min, since complete degradation was obtained after 180 min. Furfuryl alcohol (FFA), 4-benzoquinone (BQ), tert-butyl alcohol (TBA) and methyl alcohol (MeOH) as $^1O_2$, $O_2^{\bullet-}$, $SO_4^{\bullet-}$ and $^\bullet OH$ trapping agents, respectively. When FFA, BQ, TBA and MeOH (0.1 M, 0.5 mL) were added in photo-catalytic process, the obtained degradation efficiencies were 38%, 69%, 78% and 100%. The results show that the $^1O_2$ is the most dominant reactive species in the photo-catalytic process since the addition of FFA resulted to a significant decrease in degradation efficiency compared to other trapping agents. $^\bullet OH$ did not participate in the photo-catalytic process. When FFA, BQ, TBA and MeOH were added in sono-catalytic degradation process 64%, 84%, 67% and 56%, respectively. This suggests that $^\bullet OH$ is the most dominant species in the sono-catalytic process. In photosono-catalytic process, the degradation efficiencies of 78%, 89%, 52% and 42% in the

presence of FFA, BQ, TBA and MeOH, respectively, suggesting that •OH is still the most dominant reactive species in photosono-catalytic process. In general, •OH are more reactive than $^1O_2$. This rationalizes the higher degradation efficiency obtained in sono and photosono-degradation process compared to photo-catalytic processes. $SO_4^{\bullet-}$ participated in all processes (photo-, sono- and photosono-catalysis)

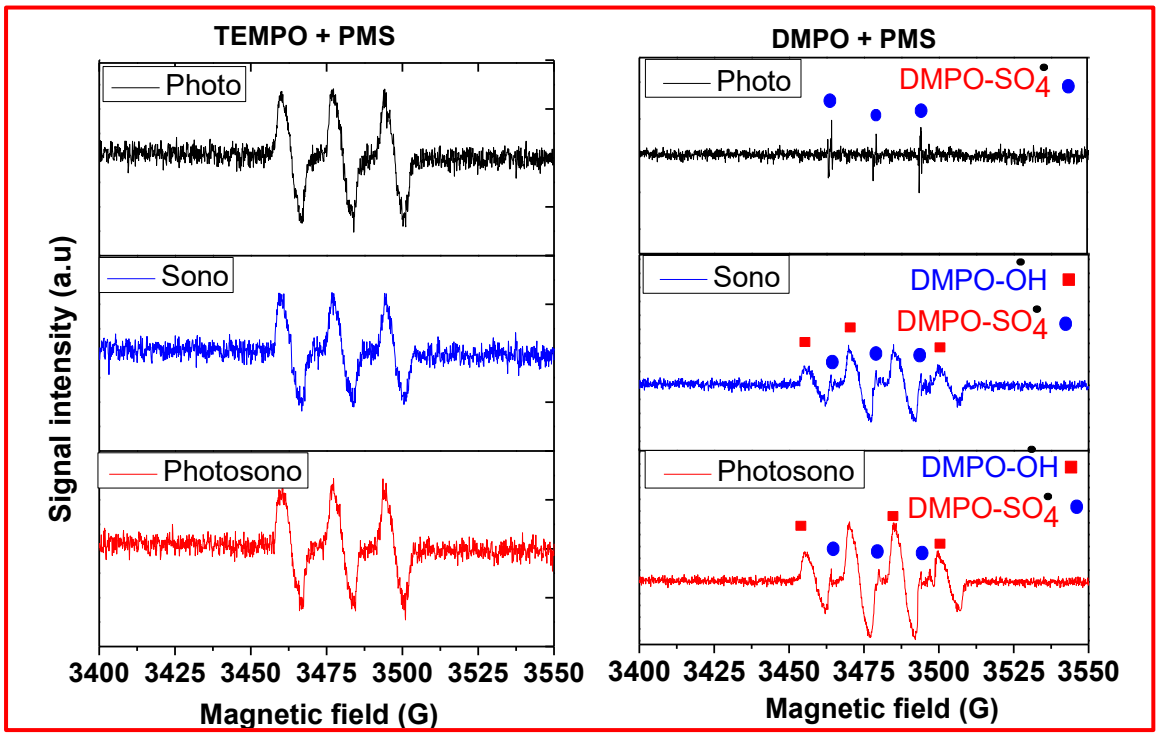

Fig 7.2. EPR plots of the photo, sono and photosono-catalytic processes in the presence of TEMPO and DMPO in the presence of PMS using **6**@TiO_2 fibers.

7.1.2.3. Effect of anions and dissolved organic matter

Ubiquitous anions and dissolved organic matter such as chlorides (Cl^-), bicarbonates (HCO_3^-), nitrates (NO_3^-) and humic acid (HA) co-exist with organic pollutants and play an inhibitory or promoting role in degradation efficiency of the organic pollutants. Hence, the photosono-degradation of Rhodamine 6G (6.63×10^{-6} M) was performed in the presence of Cl^-, HCO_3^-, NO_3^- and HA (1 mL of 0.3 mM, 3 mM, 30 mM and 300

mM) using **6**@TiO_2 fibers at pH 9 in PMS. The degradation was limited to 180 min, since complete degradation was obtained after 180 min. The degradation plots are shown in the **Fig. 7.3**.

The results suggest that, the concentration of the anions and dissolved organic matter affect Rhodamine 6G degradation efficiency. When 0.3 and 3.0 mM of Cl^- was added, 96 and 89%, degradation efficiencies, respectively, were recorded. However, when 30 and 300 mM were added, 100% degradation was maintained. This suggests that lower concentration of Cl^- reduces degradation while, higher concentrations have no effect. At lower concentrations, Cl^- has been reported to quench $SO_4^{\bullet-}$ and $^{\bullet}OH$ to generate $Cl^{\bullet}$ and $ClHO^{\bullet-}$ which are less reactive than the former, hence possessing a negative impact on degradation efficiency. However, at higher concentrations Cl^- promotes degradation by generating HOCl and Cl_2 which have longer lifetimes than $SO_4^{\bullet-}$ and $^{\bullet}OH$ [229].

The addition of 0.3 and 3 mM of HCO_3^- resulted to a decrease in degradation efficiency to 91 and 84%, respectively. When the concentration of HCO_3^- was increased to 30 and 300 mM, 100% degradation was obtained. The HCO_3^- quenches could $SO_4^{\bullet-}$ and $^{\bullet}OH$ to form carbonate radicals ($HCO_3^{\bullet}$), which reduces the degradation.

HCO_3^- can react with $SO_4^{\bullet-}$ at higher concentrations to generate percabonates (HCO_4). The HCO_4^- has been reported to increase degradation efficiency of various organic pollutants.

At 0.3 and 3 mM of NO_3^-, the Rhodamine 6G degradation efficiencies of 94 and 88%, respectively. As the concentration of NO_3^- was raised to 30 and 300 mM, a further decrease in degradation efficiency to 81 and 72%, respectively, were observed. The

NO_3^- can quench $SO_4^{\bullet-}$ and $^{\bullet}OH$ to generate less reactive nitrate radicals. When Rhodamine 6G was degraded in the presence of HA (0.3, 3, 30 and 300 mM), 100% degradation efficiency was maintained. This is because HA can improve electron transfer and the oxidation process. A similar observation has been reported before. In addition, HA contains quinone groups, which act as redox shuttles, hence improving degradation efficiency.

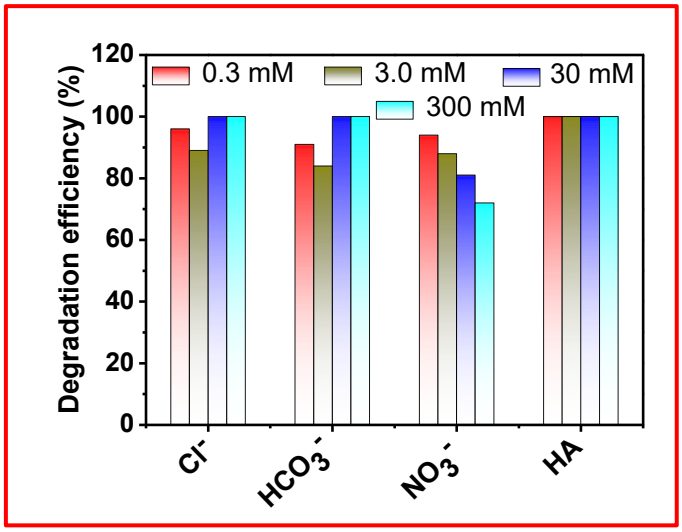

Fig. 7.3. Degradation efficiencies for Rhodamine 6G (6.63×10^{-6} M) using photosono-catalytic degradation process using **6**@TiO_2 fibers in the presence of PMS and various concentrations of organic anions and acids.

7.1.2.4 Stability of and re-usability of the catalysts

The catalysts stability was evaluated in five cycles in photo, sono and photosono-catalytic degradation processes in the presence of PMS at pH 9 using **6**@TiO_2 fibers. The degradation studies were limited to 180 min. Degradation plots are displayed in **Fig. 7.4**. The degradation efficiencies obtained after five cycles in photo, sono- and photosono-catalytic processes were 62, 84 and 79%, respectively. The results suggests that the **6**@TiO_2 fibers catalyst exhibit adequate stability after five cycles.

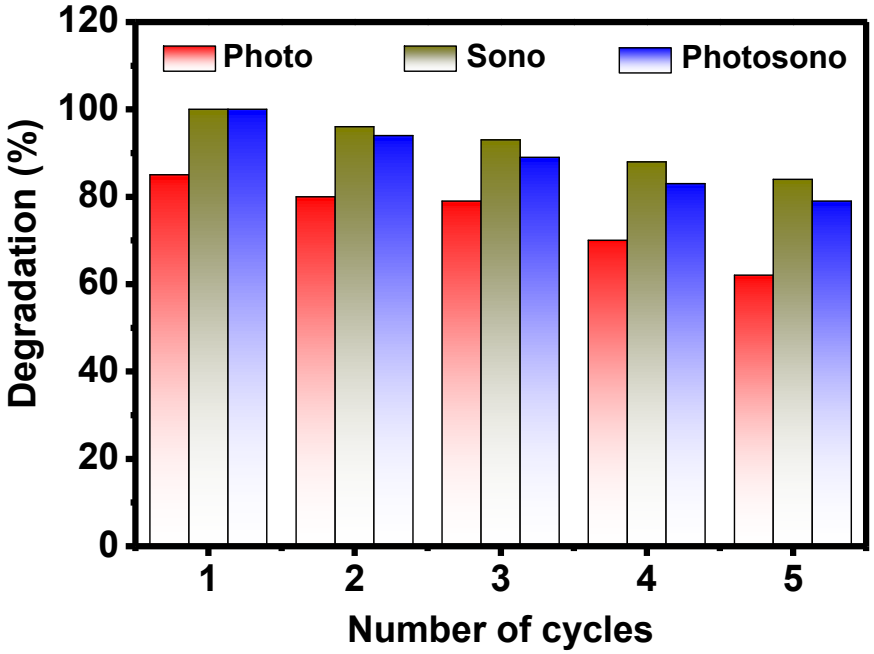

Fig. 7.4. Stability test of **6**@TiO_2 fibers after 5 cycles in the presence of PMS at pH 9 after 180 min.

7.2. The effect of the initial concentration

7.2.1. The effect of the initial Rhodamine 6G concentration in 1-TiO_2 and 2-TiO_2 fibers catalysed photo, sono- and photosono-catalytic processes

Three different concentrations of Rhodamine 6G: 6.63×10^{-5}, 8.14×10^{-5} and 1.23×10^{-4} $mol.L^{-1}$ were studied for photo-, sono- and photosono- catalytic degradation processes to establish kinetics of the degradation processes. The studies were performed at pH 9. The kinetic data plots of the **1**-TiO_2 fibers and **2**-TiO_2 fibers catalysed reactions are shown in **Fig. 7.5** and the data is listed in **Tables 7.4-7.6**. The plots for ln (C_O/C) versus irradiation time for photosono-catalytic degradation processes using **1**-TiO_2 and **2**-TiO_2 fibers display properties of the pseudo first-order kinetics with linear fit. The initial rate of degradation and rate constants (k_{obs}) obtained from sonocatalytic degradation processes are higher than those obtained from photocatalytic degradation processes. Subsequently, the initial rate of degradation

and rate constants (k_{obs}) obtained from photosono-catalytic degradation process degradation process are higher than those obtained from sonocatalytic degradation processes. The k_{obs} was found to decrease, whereas initial rates and half-lives were found to increase with an increase in Rhodamine 6G concentration. This suggests that an increase in concentration resulted to a decrease in degradation efficiencies since k_{obs} decreased.

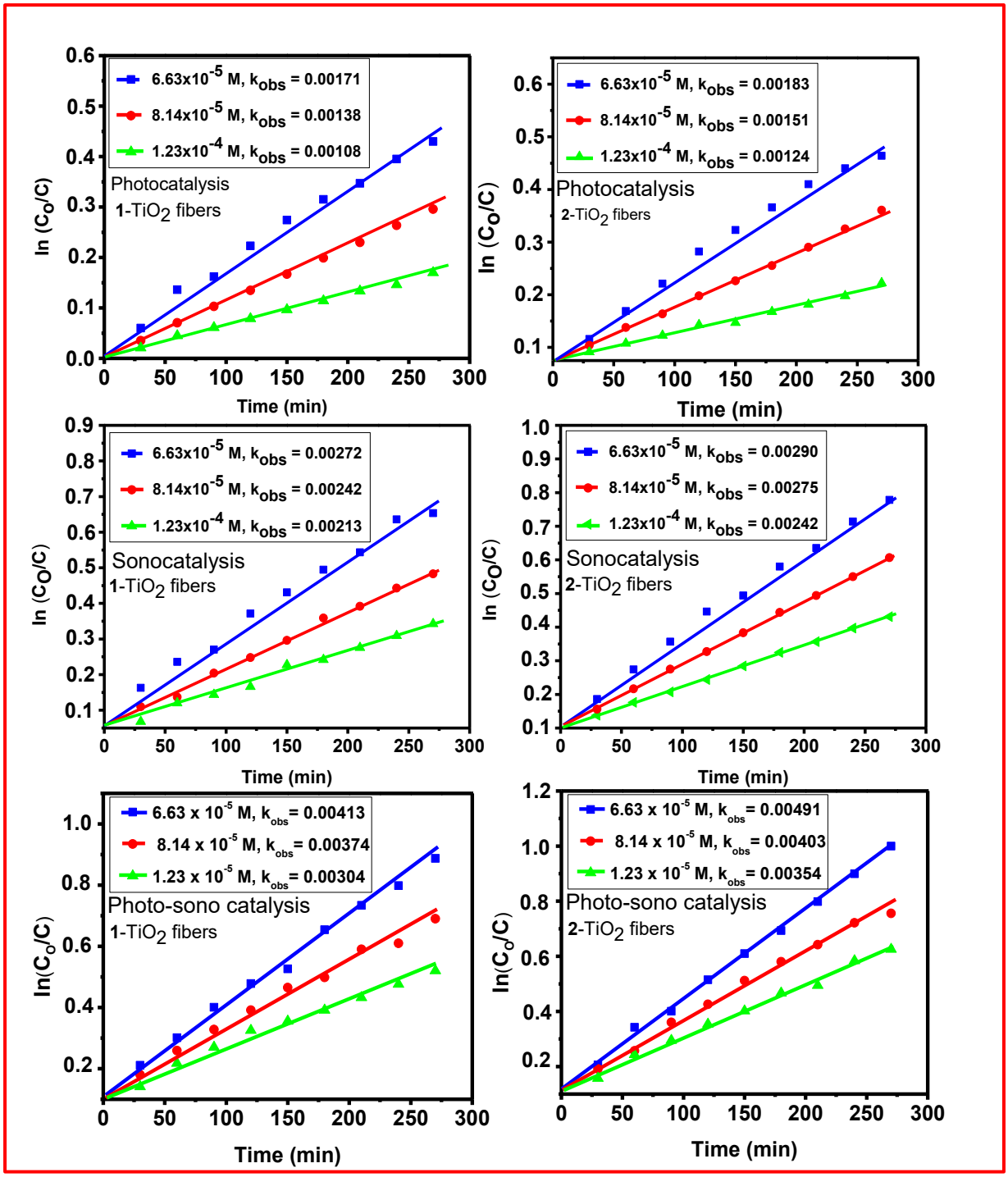

Fig. 7.5. Pseudo first order kinetics plots for the degradation of 6.63 X 10^{-5}, 8.14 X 10^{-5} and 1.23 X 10^{-4} M of Rhodamine 6G at pH 9 using **1**-TiO_2 fibers and **2**-TiO_2 fibers for photo-, sono-, and photosono- catalytic degradation processes.

Table 7.4: Reaction kinetics properties for photocatalytic degradation of Rhodamine 6G at pH 9 using **1**-TiO_2 fibers and **2**-TiO_2 fibers.

[Rhodamine 6G]	**k_{obs} (min^{-1})** x10^{-4}		**Initial rates (×10^{-8} mol L^{-1} min^{-1})**		**$\tau_{1/2}$ (min)**	
	1-TiO_2 fibers	**2**-TiO_2 fibers	**1**-TiO_2 fibers	**2**-TiO_2 fibers	**1**-TiO_2 fibers	**2**-TiO_2 fibers
6.63×10^{-5}	17.1	18.3	7.61	8.76	405	378
8.14×10^{-5}	13.8	15.1	9.22	11.2	502	458
1.23×10^{-4}	10.8	12.4	11.8	14.1	641	491

Table 7.5: Reaction kinetics properties for sonocatalytic degradation of Rhodamine 6G (pH 9) using **1**-TiO_2 fibers and **2**-TiO_2 fibers.

[Rhodamine 6G]	**k_{obs} (min^{-1})** x10^{-4}		**Initial rates (×10^{-8} mol L^{-1} min^{-1})**		**$\tau_{1/2}$(min)**	
	1-TiO_2 fibers	**2**-TiO_2 fibers	**1**-TiO_2 fibers	**2**-TiO_2 fibers	**1**-TiO_2 fibers	**2**-TiO_2 fibers
6.63×10^{-5}	27.2	29.0	21.7	23.7	254	239
8.14×10^{-5}	24.2	27.5	24.9	27.1	286	252
1.23×10^{-4}	21.3	24.2	27.3	31.3	325	286

Table 7.6: Reaction kinetics properties for photosono-catalytic degradation of Rhodamine 6G (pH 9) using **1**-TiO_2 fibers and **2**-TiO_2 fibers.

[Rhodamine 6G]	**k_{obs} (min^{-1})** x10^{-4}		**Initial rates (×10^{-8} mol L^{-1} min^{-1})**		**$\tau_{1/2}$(min)**	
	1-TiO_2 fibers	**2**-TiO_2 fibers	**1**-TiO_2 fibers	**2**-TiO_2 fibers	**1**-TiO_2 fibers	**2**-TiO_2 fibers
6.63×10^{-5}	41.3	49.1	35.8	39.1	167	141
8.14×10^{-5}	37.6	40.3	38.7	42.7	185	172
1.23×10^{-4}	30.4	35.4	40.3	44.9	227	227

7.2.2. The effect of the initial Rhodamine 6G concentration in 6@TiO_2 fibers catalysed photosono-catalytic processes

To evaluate the effect of the initial concentration of **6**@TiO_2 fibers catalysed Rhodamine 6G degradation, four different concentrations: Rhodamine 6G: 6.63×10^{-5}, 8.14×10^{-5}, 1.23×10^{-4} and 5.48×10^{-4} M were studied in a photosono-catalytic process in the presence of PMS. The degradation efficiency plots with respective kinetics plots are shown in **Fig. 7.6** and **Table 7.7**. The degradation studies were performed for 180 min. The degradation efficiencies obtained using 6.63×10^{-5} and 8.14×10^{-5} M were 100%, suggesting that a slight increase in Rhodamine 6G concentration did not alter degradation efficiency. However, a further increase in Rhodamine 6G concentration to 1.23×10^{-4} M and 5.48×10^{-4} M resulted in a decrease in degradation efficiencies to 91 and 88%, respectively. This suggests that a further increase in Rhodamine 6G concentration resulted in a slight decrease in degradation efficiency. The kinetic plots followed first-order kinetics with respect to the initial concentration of Rhodamine 6G. k_{obs} decreased with an increase in Rhodamine 6G concentration, whereas the half-life increased. The reusability studies (**Fig. 7.4**) showed that **6**@TiO_2 fibers showed high stability and reusability.

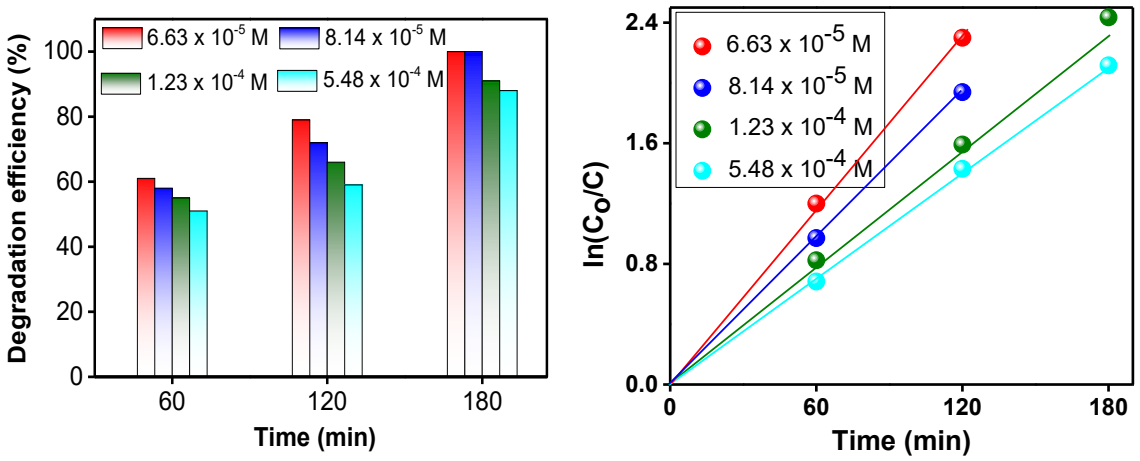

Fig 7.6. Percentage degradations and kinetics plots at various Rhodamine 6G concentrations for photosono-catalytic process using functionalized **6**@TiO_2 fibers in the presence of PMS at pH 9.

Table 7.7: Degradation efficiencies, rate constant (K_{obs}) and half-life of photosono-catalytic degradation processes in various concentrations of Rhodamine 6G.

[Rhodamine 6G]	efficiency (%)	k_{obs} (min^{-1}) x10^{-4}	$\tau_{1/2}$ (min)
6@TiO_2 fibers + PMS			
6.63 × 10^{-5} M	100	133	52
8.14 × 10^{-5} M	100	128	59
1.23 × 10^{-4} M	91	74	73
5.48 × 10^{-4} M	88	69	97
6@g-C_3N_4 NS-TiO_2 fibers			
6.63 x 10^{-5} M	100	91	76
8.72 x 10^{-5} M	97	73	94
1.23 x 10^{-4} M	92	69	100
1.93 x 10^{-4} M	89	66	105

7.2.3. Reaction mechanism of Rhodamine 6G using

Based on the results obtained from EPR, quenching experiments and photophysics, the reaction mechanism for degradation of Rhodamine 6G was proposed. The mechanism of sonocatalysis (**Fig. 7.7A**) involves the formation and collapse of bubbles upon irradiation of the aqueous solution by ultrasound. The collapse of bubbles generates high temperature and pressure conditions (cavitation effect), which subsequently generate hydroxide radicals ($^{\bullet}OH$) and emit hot light called sonoluminescence [16].

In both photo and sono-catalytic processes, **Pc**-TiO_2 fibers become excited from the ground state ($\mathbf{S_o}$) to the first excited state ($\mathbf{S_1}$) to generate electron (e^-)-hole (h^+) pairs (**Eq. 7.6**) upon being irradiated with visible light and sonoluminescence (**Fig. 7.7B**). Some electrons recombine with holes to produce fluorescence and whereas some undergo intersystem crossing (**ISC**) to a forbidden triplet ($\mathbf{T_1}$) state and subsequently generate singlet oxygen ($\mathbf{^1O_2}$) by type II and other ROS by type I mechanisms.

Some electrons are transferred to TiO_2 fibers. The electrons in TiO_2 fibers interact with O_2 to generate $O_2^{\bullet-}$ (**Fig. 7.7B**). In another process, the PMS is activated by visible light (photo) and ultrasound in the form of sonoluminescence to generate $SO_4^{\bullet-}$ and $^{\bullet}OH$ (**Eq. 7.7**). The photosono-generated electrons also activate PMS to $^{\bullet}OH$, SO_4^{2-} and $SO_4^{\bullet-}$ through (**Eq. 7.8**) and (**Eq. 7.9**), respectively [230].

The electrons also interact with molecular O_2 to generate superoxide radical ($O_2^{\bullet-}$) (**Eq. 7.10**). The titanium oxide undergoes a redox reaction to generate $SO_5^{\bullet-}$ and $SO_4^{\bullet-}$ (**Eq. 7.11**) and (**Eq. 7.12**). The $^1O_2$ is also generated from $O_2^{\bullet-}$ and $SO_5^{\bullet-}$ through (**Eq. 7.13**)

and (**Eq. 7.14**), respectively [231]. The $SO_4^{\bullet-}$, $^{\bullet}OH$, $O_2^{\bullet-}$ and $^1O_2$ participate in the degradation of Rhodamine 6G (**Eq. 7.15**) [232].

$$Pc\text{-}TiO_2 \text{ fibers} + \text{visible light} + \text{sonoluminescence} \rightarrow Pc\text{-}TiO_2 \text{ fibers } (e^-/h^+) \quad \textbf{(7.6)}$$

$$HSO_5^- + \text{visible light} + \text{sonoluminescence} \rightarrow SO_4^{\bullet-} + {}^{\bullet}OH \quad \textbf{(7.7)}$$

$$HSO_5^- + e^- \rightarrow SO_4^{2-} + {}^{\bullet}OH \quad \textbf{(7.8)}$$

$$HSO_5^- + e^- \rightarrow SO_4^{\bullet-} + {}^{-}OH \quad \textbf{(7.9)}$$

$$O_2 + e^- \rightarrow O_2^{\bullet-} \quad \textbf{(7.10)}$$

$$HSO_5^- + Ti^{4+} \rightarrow Ti^{3+} + H^+ + SO_5^{\bullet-} \quad \textbf{(7.11)}$$

$$HSO_5^- + Ti^{3+} \rightarrow Ti^{4+} + {}^{-}OH + SO_4^{\bullet-} \quad \textbf{(7.12)}$$

$$O_2^{\bullet-} + 2H_2O \rightarrow {}^1O_2 + H_2O_2 + 2HO^- \quad \textbf{(7.13)}$$

$$2SO_5^{\bullet-} + H_2O \rightarrow 3{}^1O_2 + 2SO_4^{2-} + 2H^- \quad \textbf{(7.14)}$$

$$SO_4^{\bullet-} + {}^{\bullet}OH + O_2^{\bullet-} + {}^1O_2 + \text{Rhodamine 6G} \rightarrow \text{degraded products} \quad \textbf{(7.15)}$$

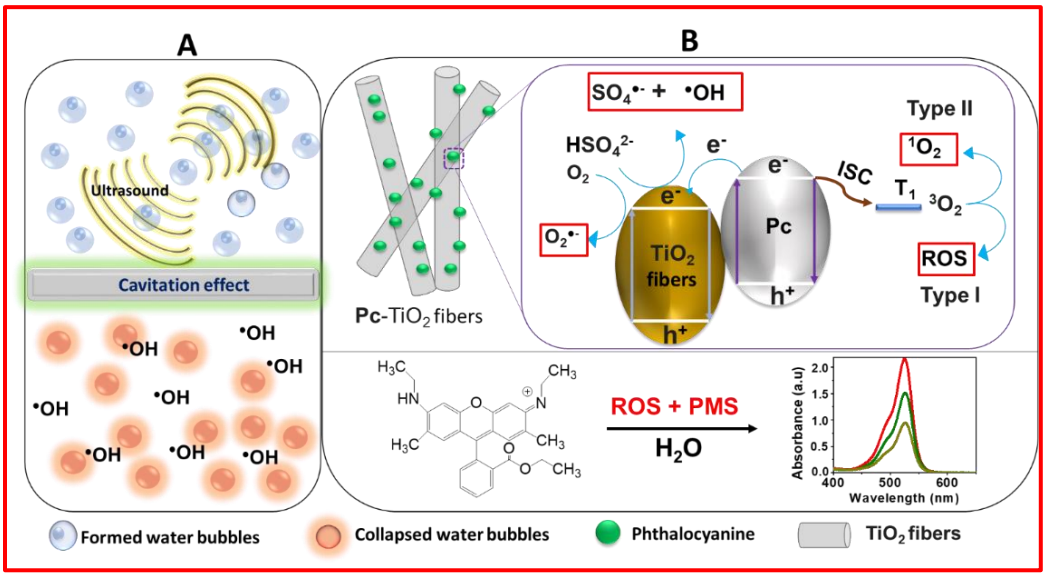

Fig 7.7. Acoustic cavitation of water molecules by ultrasound resulting in formation and collapse of the water bubbles and production of $^{\bullet}OH$ species by cavitation effect **A,** excitation of **3**@TiO_2 fibers, **4**@TiO_2 fibers, **5**@TiO_2 fibers and **6**@TiO_2 fibers by visible light and sonoluminescence **B**, in Photosono-degradation mechanism of Rhodamine 6G in the presence of PMS.

7.2.4. The effect of the initial Rhodamine 6G concentration in 6@g-C_3N_4 NS-TiO_2 fibers catalysed photosono-catalytic processes

The initial concentration of the organic pollutant also plays an important role in degradation efficacy. Hence, the effect of the initial concentration: 6.63 x 10^{-5}, 8.72 x 10^{-5}, 1.23 x 10^{-4} and 1.93 x 10^{-4} M of Rhodamine 6G were studied in photosono-catalytic degradation process using **6**@g-C_3N_4 NS-TiO_2 fibers. The degradation efficacies and kinetics plots are shown in **Fig. 7.8** and **Table 7.7**. The degradation efficiencies obtained using 6.63 x 10^{-5}, 8.72 x 10^{-5}, 1.23 x 10^{-4} and 1.93 x 10^{-4} M were 100, 97, 92 and 89%, respectively. Hence the efficiencies are high at low concentrations. The kinetic plots showed linear relationship suggesting that all the reactions followed first order kinetics with respect to the initial Rhodamine 6G concentration. The kinetics plot for 6.63 x 10^{-5} M ends at 180 min because complete degradation was achieved at 240 min, which means C_o was equals to zero which make $\ln(C_o/C)$ to be not defined.

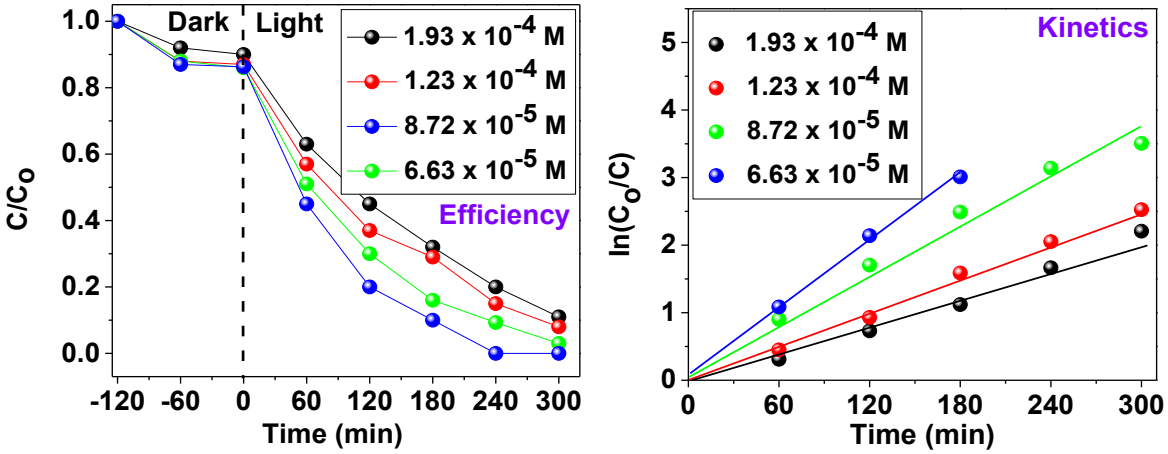

Fig. 7.8. Degradation efficiencies and kinetics for photosono-catalytic degradation process using **6**@g-C_3N_4 NS-TiO_2 fibers at various Rhodamine 6G concentrations.

7.2.5. The effect of the initial concentration of Rhodamine 6G and 2,4-DCP in 7@g-C_3N_4 NS -TiO_2 fibers catalysed photosono-catalytic processes

In order to evaluate the effect of the initial concentration of Rhodamine 6G and 2,4-DCP, the photocatalytic degradation studies were performed using 1.23×10^{-4}, 8.14×10^{-5}, 6.63×10^{-5}, 3.62×10^{-5} and 1.98×10^{-5} M concentrations of Rhodamine 6 G and 2,4-dichlorophenol. The kinetic data plots for **7**@g-C_3N_4 QDs-TiO_2 fibers photocatalyzed reactions at different concentrations are presented in **Fig. 7.9**. The k_{obs} values decreased (and rate and half-life increased) with an increase in concentrations of both Rhodamine 6 G and 2,4-dichlorophenol, **Tables 7.8** and **7.9**. The decrease in k_{obs} implies that the relative quantity of the Rhodamine 6 G and 2,4-dichlorophenol degraded for the same reaction time is less in concentrated solutions. The high catalytic activities (higher k_{obs}) were obtained using **7**@g-C_3N_4 QDs-TiO_2 fibers for both Rhodamine 6 G and 2,4-dichlorophenol.

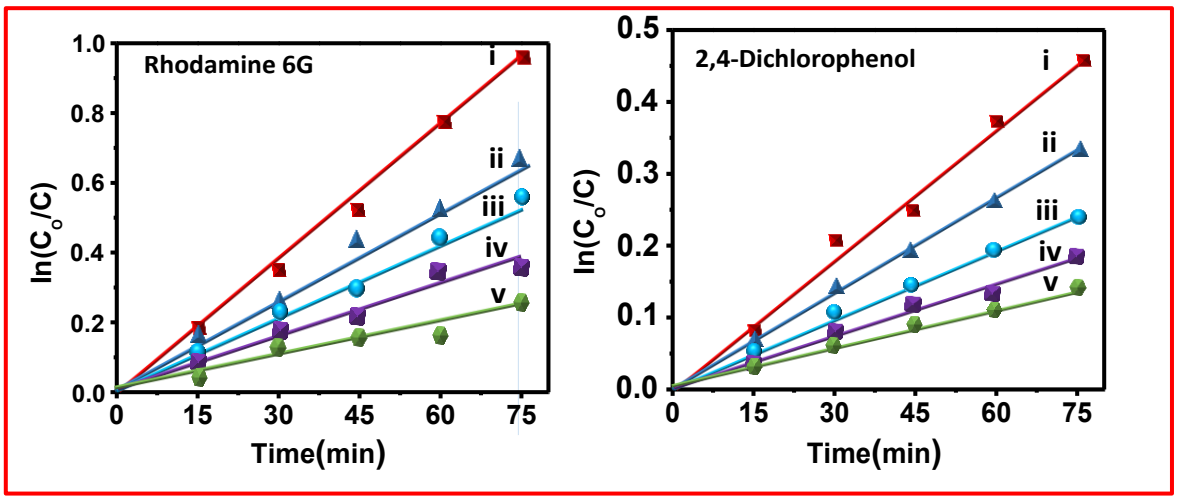

Fig. 7.9. Pseudo first order kinetics plots for the degradation of 1.98 X 10^{-5}, 3.62 X 10^{-5}, 6.63 X 10^{-5}, 8.14 X 10^{-5} and 1.23 X 10^{-4} M of Rhodamine 6G and 2,4-dichlorophenol.

Table 7.8: Kinetic data for the degradation of Rhodamine 6G using **7**@g-C_3N_4 QDs - TiO_2 fibers hybrid.

[Rhodamine 6G] (M)	K_{obs} (min^{-1})	Rate (mol $L^{-1}min^{-1}$)	$t_{1/2}$ (min)
	7@g-C_3N_4 QDs-TiO_2 fibers	**7**@g-C_3N_4 QDs-TiO_2 fibers	**7**@g-C_3N_4 QDs-TiO_2 fibers
1.98×10^{-5}	0.0178	3.52×10^{-7}	39
3.62×10^{-5}	0.0084	4.97×10^{-7}	82
6.63×10^{-5}	0.0067	6.14×10^{-7}	103
8.14×10^{-5}	0.0061	6.48×10^{-7}	114
1.23×10^{-4}	0.0056	6.89×10^{-7}	123

Table 7.9: Kinetic data for the degradation of 2,4-dichlorophenol using **7**@g-C_3N_4 QDs -TiO_2 fibers hybrid.

[2,4-dichlorophenol] (M)	K_{obs} (min^{-1})	Rate (mol $L^{-1}min^{-1}$)	$t_{1/2}$ (min)
	7@g-C_3N_4 QD -TiO_2 fibers	**7**@g-C_3N_4 QDs-TiO_2 fibers	**7**@g-C_3N_4 QDs-TiO_2 fibers
1.98×10^{-5}	0.0073	1.45×10^{-7}	95
3.62×10^{-5}	0.0054	1.93×10^{-7}	128
6.63×10^{-5}	0.0036	2.39×10^{-7}	192
8.14×10^{-5}	0.0032	2.57×10^{-7}	216
1.23×10^{-4}	0.0024	2.95×10^{-7}	288

7.3. The effect of the pH of the solution

7.3.1. 6@TiO_2 fibers catalysed photo-catalytic degradation of Rhodamine 6G

The effect of the pH of the solution on the degradation efficiency in the presence of PMS is shown in **Fig 7.10** and **Table 7.10**. The effect of the pH on degradation

efficiency is complex and is affected by various factors, such as the nature of the catalyst. To investigate the effect of the pH of the solution, Rhodamine 6G degradation was degraded at pHs 3, 6, 9 and 12 using the photosono-catalytic process in the presence of **6**@TiO_2 fibers (as an example). The studies were limited to 180 min since 100% was obtained after 180 min. The results are shown in **Fig. 7.10** and **Table 7.10**. The degradation efficiencies obtained at pH 3, 6, 9 and 12 were 28%, 57%, 100% and 100%, respectively.

The lowest degradation was obtained at pH 3 and the highest degradation was obtained at pHs 9 and 12. The higher degradation efficiency obtained at pHs 9 and 12 can be envisaged from the charge density at the surface of the catalyst at various pH values. At pHs 3 and 6 the surface of the **6**@TiO_2 fibers is covered by positive charges. Since Rhodamine 6G is also positively charged, repulsion between **6**@TiO_2 fibers and Rhodamine 6G occurs at pH 3 and 6 which subsequently reduces surface adsorption and degradation. Inversely, as the pH is increased to 9 and 12 the surface of the **6**@TiO_2 fibers are covered by negative charges and there is attraction between **6**@TiO_2 fibers and Rhodamine 6G, which enhances surface adsorption of Rhodamine 6G to **6**@TiO_2 fibers [233]. Nonetheless, it can be seen that as the pH increases above pH 9, a slight decline in degradation efficiency could be observed, **Table 7.10**. This could be caused by the fact that at pH greater than 9, HSO_5^- converts to SO_5^{2-}, which subsequently obstructs ROS generation [234]. The degradation kinetic studies followed pseudo-first-order kinetics with linear fits.

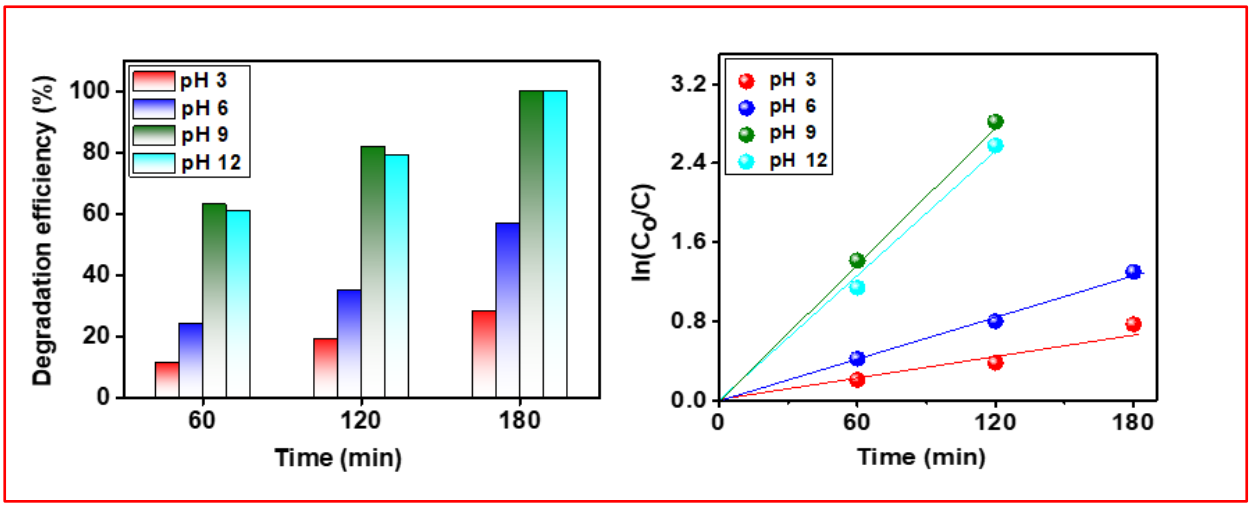

Fig 7.10. Rhodamine 6G (6.63×10^{-5} M) percentage degradations and kinetics plots for the photosono-catalytic process at various pH values using **6**@TiO_2 fibers in the presence of PMS.

Table 7.10: Degradation efficiencies, rate constant (Kobs) and half-life of photosono-catalytic degradation processes in various pH solutions using **6**@TiO_2 fibers in the presence of PMS

pH	Degradation efficiency (%)	k_{obs} (min^{-1}) x10^{-4}	$\tau_{1/2}$
6@TiO_2 fibers + PMS			
pH 3	28	18	366
pH 6	57	36	128
pH 9	100	133	52
pH 12	100	130	53
6@g-C_3N_4 NS-TiO_2 fibers			
pH 3	55	37	198
pH 6	83	59	117
pH 9	100	91	76
pH 12	100	85	81

7.3.2. 6@g-C_3N_4 NS-TiO_2 fibers catalysed photosono-catalytic degradation of Rhodamine 6G

The effect of the initial pH of the solution in **6**@g-C_3N_4 NS-TiO_2 fibers catalysed Rhodamine 6G was investigated. Rhodamine 6G degradations were studied at pH 3, 6, 9 and 12 using 6.63 x 10^{-5} M in the presence of **6**@g-C_3N_4 NS-TiO_2 fibers. The degradation efficacies and kinetics plots are shown in **Fig. 7.11** and **Table 7.10**. The degradation efficacies obtained at pH 3, 6, 9 and 12 were 55, 83, 100 and 100% at pH 3, 6, 9 and 12, respectively. At pH 3 and 6 the degradation efficacy was low. This is due to the fact that the surface of the catalyst is covered by positive charges and since Rhodamine 6G is also positively charged, an electrostatic repulsion transpires between the catalyst and Rhodamine 6G, as stated above. This phenomenon reduces the efficiency of the process. At pH 9 and 12, maximum degradations were achieved. This is a result of an electrostatic attraction between the surface of the catalyst and Rhodamine 6G [232]. The kinetic studies revealed that the reactions follow the first-order kinetics with respect to the initial pH of the solution. The highest k_{obs} and the shortest $\tau_{1/2}$ were obtained at pH 9.

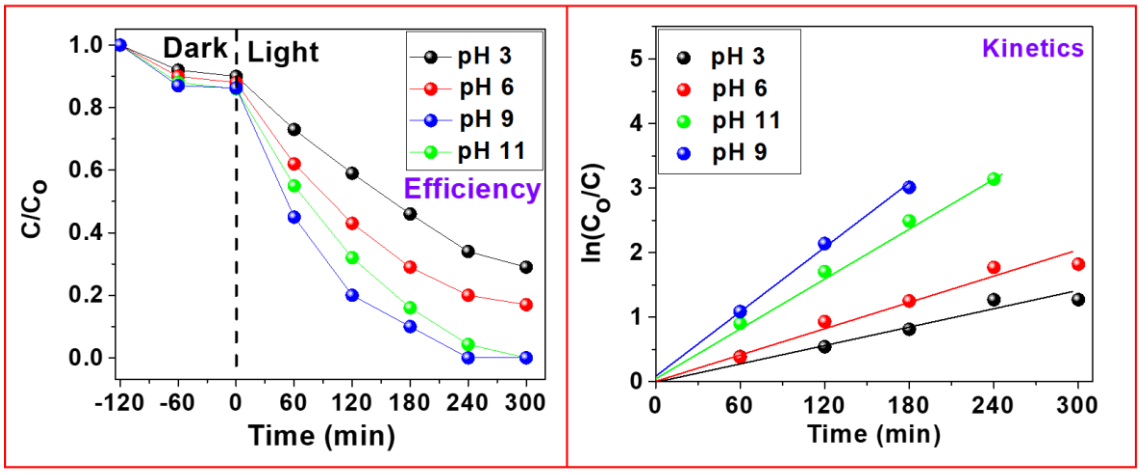

Fig. 7.11. Degradation efficiencies and kinetics for photosono degradation process using **6**@g-C_3N_4-TiO_2 fibers at various pH values.

7.4. Summary for the Chapter

Various parameters such radical initiators, initial concentration and pH were investigated. The addition of radical initiators enhanced degradation efficiency. An increase in initial concentration resulted to a decrease in degradation efficiencies for both Rhodamine 6G and 2,4-dichlorophenol. The degradation of Rhodamine 6G was more effective at pH 9 than at pH 3, 7 and 12, suggesting that the pH of the solution is important in degradation efficiency.

Chapter eight

This chapter discusses the conclusion and future prospects of this work.

8.1. Conclusion and future work

This work reports for the first time the synthesis of wide range of zinc phthalocyanines and porphyrin. The phthalocyanines were conjugated to g-C_3N_4 nanosheets (g-C_3N_4 NS), g-C_3N_4 quantum dots (g-C_3N_4 QDs) and $MnFe_2O_4$ nanoparticles. The porphyrin was conjugated to g-C_3N_4 quantum dots. The conjugates of the phthalocyanine and porphyrin with nanoparticles (g-C_3N_4 NS, g-C_3N_4 QDs and $MnFe_2O_4$ NPs) were supported with TiO_2 fibers and ZnO fibers to form the hybrids. The hybrids were used for photo-, sono- and photosono-catalytic degradation of organic pollutants in water. The conjugates and hybrids were characterized with various microscopic and spectroscopic techniques such as scanning electron microscopy-dispersive X-ray Spectroscopy (SEM-EDX), transmission electron microscopy (TEM), UV-Vis spectroscopy, solid-state UV-Vis spectroscopy, Fourier-transform infrared spectroscopy (FT-IR), X-ray photoelectron spectroscopy (XPS), thermogravimetric analysis (TGA), X-ray diffraction spectroscopy (XRD) and electron paramagnetic resonance (EPR).

The singlet oxygen quantum yield of the conjugate was improved compared to that of the phthalocyanines and porphyrin alone. The singlet oxygen quantum yield of the functionalized fibers were lower than those obtained from the respectively conjugates. This was due to the fact that the singlet oxygen quantum yield studies of functionalized fibers were performed in water whereas the singlet oxygen quantum yield of the conjugates were performed in DMF. Water quenches singlet oxygen.

The photo-, sono- and photosono-catalytic degradation studied were performed using functionalized fibers. The organic pollutants that were degraded were Rhodamine 6G and 2,4-dichlorophenol. Rhodamine 6G was degraded using photo-, sono- and

photosono-catalytic processes whereas 2,4-dichlorophenol was degraded using photo-catalytic process only. The effects of the radical initiators including *tert*-butyl hydrogen peroxide, azo-bis-isobutyronitrile and hydrogen peroxymonosulfate were studied in the in photo-, sono- and photosono-catalytic degradation processes. In the presence of radical initiators, complete degradation of Rhodamine 6G was achieved using photosono-catalytic processes. The reactive oxygen species quenching experiments and EPR results revealed the photocatalytic studies were dominated by singlet oxygen only, whereas sono- and photosono-catalytic degradation process were dominated by singlet oxygen and hydroxide radicals reactive species.

Looking ahead, the conjugates and their respective functionalized fibers hybrid will be studied inactivation of bacteria in water using photosonodynamic antimicrobial chemitherapy, since industrial wastewater is often polluted by bacteria. Furthermore, the study will be extended by studying the degradation efficiencies of the same catalysts in wastewaters containing mixtures of organic pollutants and mixtures of organic pollutants with bacteria.

References

1. T. Yu, Y. Chen, T. Hu, J. Feng, W. Xing, L. Tang, W. Tang, Recent advances in the applications of encapsulated transition-metal nanoparticles in advanced oxidation processes for degradation of organic pollutants: A critical review, Appl. Catal., 342 (2024) 123401.
2. K.K. Sodhi, M. Kumar, D.K. Singh, Insight into the amoxicillin resistance, ecotoxicity, and remediation strategies, J. Water Process Eng., 39 (2021) 101858.
3. E. Fosso-Kankeu, H. Mittal, S. Marx, S.S. Ray, Hydrogel-Based Bioflocculants for the Removal of Organic Pollutants from Biodiesel Wastewater, J. Polym. Environ., 25 (2017) 844–853
4. L.W. Perelo, Review: In situ and bioremediation of organic pollutants in aquatic sediments, J. Hazard. Mat., 177 (2010) 81-89
5. Y. Wang, T. Pan, Y. Yu, Y. Wu, Y. Pan, X. Yang, A novel peroxymonosulfate (PMS)-enhanced iron coagulation process for simultaneous removal of trace organic pollutants in water, Water Res.,185 (2020) 116136
6. X. Li, A. Li, Z. Li, H. Sun, P. Shi, Q. Zhou, C. Shuang, Organic micropollutants and disinfection byproducts removal from drinking water using concurrent anion exchange and chlorination process, Sci. Total Environ., 752 (2021) 141470.
7. P.E. Stackelberg, E.T. Furlong, M.T. Meyer, S.D. Zaugg, A.K. Henderson, D.B. Reissman, Persistence of pharmaceutical compounds and other organic wastewater contaminants in a conventional drinking-water-treatment plant, Sci. Total Environ., 329 (2004) 99–113.
8. E. Domingues, E. Fernandes, J. Gomes, R.C. Martins, Advanced oxidation processes perspective regarding swine wastewater treatment, Sci. Total Environ., 776 (2021) 145958.

9. B. Riano, M. Coca, M.C. García-Gonzalez, Evaluation of Fenton method and ozone-based processes for colour and organic matter removal from biologically pre-treated swine manure, Chemosphere, 117 (2014) 193–199.
10. M. Zhang, H. Dong, L. Zhao, D. Wang, D. Meng, A review on Fenton process for organic wastewater treatment based on optimization perspective, Sci. Total Environ., 670 (2019) 110-121.
11. M. Dastborhan, A. Khataee, S. Arefi-Oskoui, Y. Yoon, Synthesis of flower-like MoS_2/CNTs nanocomposite as an efficient catalyst for the sonocatalytic degradation of hydroxychloroquine, Ultrason. Sonochem., 87 (2022) 106058
12. H. Barndok, D. Hermosilla, C. Han, D.D. Dionysiou, C. Negro, A. Blanco, Degradation of 1,4-dioxane from industrial wastewater by solar photocatalysis using immobilized NF-TiO2 composite with monodisperse TiO2 nanoparticles, Appl. Catal. B: Environ., 180 (2016) 44–52.
13. T.K. Ghorai, N. Biswas, Photodegradation of rhodamine 6G in aqueous solution via $SrCrO_4$ and TiO_2 nano-sphere mixed oxides, J. Mater. Technol., 2 (2013) 10-17.
14. M. Czaplicka, Sources and transformations of chlorophenols in the natural environment, Sci. Total Environ., **322** (2004) 21–39.
15. S. Zhu, D. Wang, Photocatalysis: Basic Principles, Diverse Forms of Implementations and Emerging Scientific Opportunities, Adv. Energy Mater., 7 (2017) 1700841.
16. M. Samanta, M. Mukherjee, U.K. Ghorai, C. Bose, K.K. Chattopadhyay, Room temperature processed copper phthalocyanine nanorods: A potential sonophotocatalyst for textile dye removal, Mater. Res. Bull., 123 (2020) 110725.
17. S. Farhadi, F. Siadatnasab, Synthesis and structural characterization of magnetic cadmium sulfide-cobalt ferrite nanocomposite, and study of its activity for dye degradation under ultrasound, J. Mol. Struct., 1123 (2016) 171-179.
18. S. Supriya, V.S. Shetti, G. Hegde, Conjugated systems of porphyrin–carbon nanoallotropes: a review, New J. Chem., 42 (2018) 12328.
19. R.J.P. Williams, The Properties Of Metalloporphyrins, Chem. Rev., 56 (1956) 299.

20. Z. Valicsek, O. Horváth, Application of the electronic spectra of porphyrins for analytical purposes: The effects of metal ions and structural distortions, J. Microchem., 107 (2013) 47-62.
21. A.G. Dandridge, H.A.E. Drescher, S.H. Dunworth, J. Thomas, Scottish Dyes Limited GB Patent, (1929) 322.
22. P. Erk, H. Hengelsberg, Phthalocyanine dyes and pigments. In the porphyrin handbook, applications of phthalocyanines, Kadish, K.M. Smith, K.M. Guilard, R. Eds. Elsevier Science: New York, Chapter 119, Volume 19, (2003) 105-147.
23. W. Ji, T.X. Wang, X. Ding, S. Lei, B.H. Han, Porphyrin and phthalocyanine-based porous organic polymers: From synthesis to application, Coord. Chem. Rev., 439 (2021) 213875.
24. D.A. Gkika, K. Ladomenou, M. Bououdina, A.C. Mitropoulos, G.Z. Kyzas, Adsorption and photocatalytic applications of porphyrin-based materials for environmental separation processes: A review, Sci. Total Environ., 908 (2024) 168293
25. M. Tian, T. Wada, H. Kimura-Suda, H. Sasabe, Novel non-aggregated unsymmetrical metallophthalocyanines for second-order non-linear optics, J. Mater. Chem., 7 (1997) 861-863.
26. M.O. Senge, M. Fezekas, E.G.A. Notaras, W.J. Blau, M. Zawadzaka, O.B. Locos, E.M. Mhuircheartaigh, Nonlinear optical properties of porphyrins, Adv. Mat., 19 (2007) 2737-2774.
27. D. Kessel, Relocalization of cationic porphyrins during photodynamic therapy. Photochem Photobiol Sci., **1** (2002) 837–840
28. J.D. Spikes, Phthalocyanines as photosensitizers in biological systems and for the photodynamic therapy of tumors, Photochem. Photobiol., 43 (1986) 691-699.
29. V. Crowl, Consumer Demands in the Paint Industry, J. Soc. Dyer. Colour., 81 (1965) 545-552.
30. S.Q. Lomex, Phthalocyanine and quinacridone pigments: their history,properties and use, Stud. Conserv., 50 (2013) 19-29

31. S. Mori, M. Nagata, Y. Nakahata, K. Yasuta, R. Goto, M. Kimura, M. Taya, Enhancement of incident photon-to-current conversion efficiency for phthalocyanine-sensitized solar cells by 3D molecular structurization, J. Am. Chem. Soc., 132 (2010) 4054-4055
32. L.L. Li, E.W.G. Diau, Porphyrin-sensitized solar cells, Chem. Soc. Rev., 42 (2013) 291-304.
33. X. Zhang, Z. Wu, X. Zhang, L. Li, Y. Li, H. Xu, X. Li, X. Yu, Z. Zhang, Y. Liang, Highly selective and active CO_2 reduction electrocatalysts based on cobalt phthalocyanine/carbon nanotube hybrid structures, Nat. Commun., 8 (2017) 14675-14682.
34. C.X. Zhao, B.Q. Li, J.N. Liu, J.Q. Huang, Q. Zhang, Transition metal coordinated framework porphyrin for electrocatalytic oxygen reduction, Chin. Chem. Lett., 30 (2019) 911-914
35. K.P. Priyanka, S. Sankararaman, K.M. Balakrishna, T. Varghese, Enhanced visible light photocatalysis using TiO_2/phthalocyanine nanocomposites for the degradation of selected industrial dyes, J. Alloys Compd., 720 (2017) 541-549.
36. S. Silvestri, A.R. Fajardo, B.A. Iglesias, Supported porphyrins for the photocatalytic degradation of organic contaminants in water: a review, Environ. Chem. Lett., 20 (2022) 731–771.
37. C.C. Leznoff, S.M. Marcuccio, S. Greenberg, A. Lever, K.B. Tomer, Metallophthalocyanine dimers incorporating five-atom covalent bridges, Can. J. Chem., 63 (1985) 623-631.
38. V.N. Nemykin, E.A. Lukyanets, Synthesis of substituted phthalocyanines, *Arkivoc, i (2010)* 136-208.
39. N.B. McKeown, Phthalocyanine materials: synthesis, structure and function, Cambridge University Press, New York, Chapter 2, Volume 6 (1998) 12-30.
40. J. Chen, N. Chen, J. Huang, J. Wang, M. Huang, Derivatizable phthalocyanine with single carboxyl group: synthesis and purification, Inorg. Chem. Commun., 9 (2006) 313-315.
41. A. Naumov, E. Kudrik, G. Shaposhnikov, Synthesis and properties of symmetrical and asymmetrical phthalocyanines with D, L-leucine fragments, Chem. Heterocycl. Compd., 40 (2004) 469-474

42. Y. Liu, D. Zhu, T. Wada, A. Yamada, H. Sasabe, Synthesis and characterization of a novel unsymmetrical metal-free phthalocyanine with donor-acceptor substituents, Heterocyclic Chem., 31 (1994) 1017
43. C.F. van Nostrum, R.J.M. Nolte, Functional supramolecular materials: self-assembly of phthalocyanines and porphyrazines, Chem. Comm., (1996) 2385
44. N. Kobayashi, R. Kondo, S.I. Nakajima, T. Osa, New route to unsymmetrical phthalocyanine analogs by the use of structurally distorted subphthalocyanines, J. Am. Chem. Soc., 112 (1990) 9640.
45. J. Vacus, G. Memetzidis, P. Doppelt, J. Simon, The synthesis of unsymmetrically functionalized platinum and zinc phthalocyanine complexes, J. Chem. Soc. Chem. Commun., 37 (1994) 697-698
46. G. de la Torre, C.G. Claessens, T. Torres, Phthalocyanines: The need for selective synthetic approaches, Eur. J. Org. Chem., 2000 (2000) 2821-2830.
47. P. Rothemund, A.R. Menotti, Porphyrin Studies. IV.1 The Synthesis of α,β,γ,δ-Tetraphenylporphine, J. Am.Chem. Soc., 63 (1941) 267.
48. J.S. Lindsey, Synthesis of meso-substituted porphyrins. In The Porphyrin Handbook; M. Kadish, K. M. Smith, R. Guilard, Eds; Academic Press: San Diego, CA, USA, 2000.
49. P. Faugeras, J. Vergnaud, R. Lucas, B. Boe, K. Teste, R. Zerrouki, Iodine-catalyzed one-pot synthesis of unsymmetrical mesosubstituted porphyrins, Tetrahedron, 66 (2010) 1994
50. R. Naik, P. Joshi, S.P. Kaiwar, R.K. Deshpande, Facile synthesis of meso-substituted dipyrromethanes and porphyrins using cation exchange resins, Tetrahedron, 59 (2003) 2207.
51. S. Nia, X. Gong, C. Michael, M. Jurow, Solvent-free synthesis of meso-tetraarylporphyrins in air : product diversity and yield optimization, J. Porphyr. Phthalocya., 14 (2010) 621
52. A.D. Adler, F.R. Longo, J.D. Finarelli, J. Goldmacher, J. Assour, L.A. Korsakoff, A simplified synthesis for meso-tetraphenylporphin, J. Org. Chem., 32 (1967) 476.
53. M.G.H. Vicente, K.M. Smith, Porphyrins and Derivatives : Synthetic Strategies and Reactivity Profiles, Curr. Org. Chem., 4 (2000) 139.

54. H. Isago, Optical spectra of phthalocyanines and related compounds a Guide for beginners, Springer, Japan, (2015) 21-40.
55. M.J. Stillman, T. Nyokong, Absorption and magnetic circular dichroismspectral properties of dianion, Pc(-2). In Phthalocyanines, Properties and Applications, C.C. Leznoff, A.B.P. Lever, Eds. VCH Publishers, Inc. New York, Volume 1, Chapter 3, (1989) 133.
56. M. S. Gouterman, Spectra of porphyrins J. Mol. Spectrosc., 6 (1961) 138.
57. R. Chandra, M. Tiwari, P. Kaur, M. Sharma, R. Jain, S. Dass, J. Indian, Metalloporphyrins-Applications and clinical significance, Clin. Biochem., 15 (2000) 183.
58. N.A. Kuznetsova, O.L. Kaliya, Oxidative photobleaching of phthalocyanines in solution, J. Porphyr. Phthalocya., 16 (2012) 705–712.
59. K. Palewska, M. Sujka, B.U. Wójcik, J. Sworakowski, J. Lipiński, S. Nešpůrek, J. Rakušan, M. Karásková, Light-induced effects in sulfonated aluminum phthalocyanines-potential photosensitizers in the photodynamic therapy: Spectroscopic and kinetic study, J. Photochem. Photobiol., A,197 (2008) 1-12
60. C. Würth, M. Grabolle, J. Pauli, M. Spieles, U. Resch-Genger, Relative and absolute determination of fluorescence quantum yields of transparent samples**,** Nat. Protoc., 8 (2013) 1535.
61. D. Magde, R. Wong, Fluorescence quantum yields and their relation to lifetimes of Rhodamine 6G and fluorescein in nine solvents: Improved absolute standards for quantum yields, Photochem. Photobiol., 75 (2002) 327–334.
62. S. M. Bachilo, R. B. Weisman, Determination of Triplet Quantum Yields from Triplet−Triplet Annihilation Fluorescence, J. Phys. Chem. A, 104 (2000) 7711.
63. Z. Wang, A. Toffoletti, Y. Hou, J. Zhao, A. Barbon, B. Dick, Insight into the drastically different triplet lifetimes of BODIPY obtained by optical/magnetic spectroscopy and theoretical computations, Chem. Sci., 12 (2021) 2829.
64. A. Wang, X. Chen, L. Zhang, G. Zhang, L. Zhou, S. Lu, J. Zhou, S. Wei, Effects of pH on aggregation and photodynamic activities of cationic zinc phthalocyanines substituted with amides, J. Photochem, Photobiol. A, 288 (2014) 1-12.

65. T. Nyokong, Effects of substituents on the photochemical and photophysical properties of main group metal phthalocyanines, Coord. Chem. Rev., 251 (2007) 1707–1722.
66. E.A. Kuzmina, T.V. Dubinina, L.G. Tomilova, Recent advances in chemistry of phthalocyanines bearing electron-withdrawing halogen, nitro and *N*-substituted imide functional groups and prospects for their practical application, New J. Chem., 43 (2019) 9314-9327.
67. G. Dilber, A. Nas, M. Pişkin, M. Durmus, Asymmetrically tetra-substituted phthalocyanine derivatives: synthesis, photophysical and photochemical properties, Transit. Met. Chem., 47 (2022) 157–168.
68. S.A. Majeed, K.E. Sekhosana, A. Tuhl, Progress on phthalocyanine-conjugated Ag and Au nanoparticles: Synthesis, characterization, and photo-physicochemical properties, Arab. J. Chem., 13 (2020) 8848-8887.
69. J. Yang, C. Zhang, R. He, J. Yao, J. Wang, Insight into impacts of π–π assembly on phthalocyanine based heterogeneous molecular electrocatalysis, J. Phys. Chem. Lett., 15 (2024) 4705-4710.
70. Y.I. Openda, S. Mgidlana, T. Nyokong, In vitro photoinactivation of S. aureus and photocatalytic degradation of tetracycline by novel phthalocyanine-graphene quantum dots nano-assemblies, J. Lumin., 246 (2022) 118863.
71. S. Srivishnu, D. Banerjee, R.A. Ramnagar, J. Rathod, L. Giribabu, V.R. Soma, Optical, Electrochemical, Third-Order Nonlinear Optical Investigations of 3,4,5-Trimethoxy Phenyl Substituted Non-Aqueous Phthalocyanines, Front. Chem., 9 (2021) 713939
72. R. Zugle, E. Antunes, S. Khene, T. Nyokong, Photooxidation of 4-chlorophenol sensitized by lutetium tetraphenoxy phthalocyanine anchored on electrospun polystyrene polymer fiber, Polyhedron, 33 (2012) 74-81
73. P. Khoza, T. Nyokong, Visible light transformation of Rhodamine 6G using tetracarbazole zinc phthalocyanine when embedded in electrospun fibers and in the presence of ZnO and Ag particles, J. Coord. Chem., 68 (2015) 1117–1131
74. S. Mapukata, N. Kobayashi, M. Kimura, T. Nyokong, Asymmetrical and symmetrical zinc phthalocyanine-cobalt ferrite conjugates embedded in electrospun fibers for dual

photocatalytic degradation of azo dyes: Methyl Orange and Orange G, J. Photochem. Photobiol. A, 379 (2019) 112-122

75. S. Mapukata, T. Nyokong, Development of phthalocyanine functionalised TiO_2 and ZnO nanofibers for photodegradation of methyl orange, New J. Chem. 44 (2020) 16340-16350
76. B. Jones, D. Mafukidze, T. Nyokong, Fabrication of electrospun fibers from a porphyrin linked to polyacrylonitrile polymer for photocatalytic transformation of phenols, J. Mol. Struct., 213 (2020) 128191
77. S.H. El-Khalafy, M.M. Azaam, E.M. El-nshar, E.A. Kamoun, E.R. Kenawy, Catalytic activity of Co (II)-porphyrin anchored onto polymeric support of electrospun polyacrylonitrile nanofber: synthesis and efcient green oxidation of crystal violet dye with hydrogen peroxide, Biomass Convers. Bior., (2023) 1-12
78. I. Khan, K. Saeed, I. Khan, Nanoparticles: Properties, applications and toxicities, Arab. J. Chem., 12 (2019) 908-931.
79. B.H. Alshammari, M.M.A. Lashin, M.A. Mahmood, F.S. Al-Mubaddel, N. Ilyas, N. Rahman, M. Sohail, A. Khan, S.S. Abdullaev, R. Khan, Organic and inorganic nanomaterilas: Fabrication properties and applications, RSC Adv., 33 (2023) 13735-13785.
80. M. Srinivasan, M. Rajabi, Multifunctional nanomaterials and their applications in drug delivery and cancer therapy, Nanomaterials, 5 (2015) 1690-1703.
81. Z.P. Xu, Q.H. Zeng, G.Q. Lu, A.B. Yu, Inorganic nanoparticles as carriers for efficient cellular delivery, Chem. Eng. Sci., 61 (2006) 1027–1040.
82. K. Yang, F. Zhang, Y. Chen, H. Zhang, B. Xiong, H. Chen, Recent progress on carbon-based composites in multidimensional applications, Compos. A: Appl. Sci. Manuf., 157 (2022) 106906.
83. J.L Dormann, D Fiorani, E Tronc, I. Prigogine, Magnetic relaxation in fine-particle systems. In Advances in Chemical Physics, I. Prigogine, S.A Rice, Volume 98, Chapter 4, Wiley, New York, (1997) 283-494.

84. D.A. Vinnik, S.A. Gudkova, V.E. Zhivulin, E.A. Trofimov, Ferrite-Based Solid Solutions: Structure Types, Preparation, Properties, and Potential Applications, Inorg. Mater., 57 (2021) 1109–1118.
85. D. H. K. Reddy and Y.S. Yun, Spinel ferrite magnetic adsorbents: alternative future materials for water purification?, Coord. Chem. Rev., 315 (2016) 90–111.
86. B. Yalcin, S. Ozcelik, K. Icin, K. Senturk B. Ozcelik, L. Arda, Structural, optical, magnetic, photocatalytic activity and related biological effects of $CoFe_2O_4$ ferrite nanoparticles, J. Mater Sci: Mater Electron., 32 (2021) 13068–13080
87. P.A. Vinosha, A. Manikandan, A.S.J. Ceicilia, A. Dinesh, G.F. Nirmala, A.C. Preetha, Y. Slimani, M.A. Almessiere, A. Baykal, B. Xavier, Review on recent advances of zinc substituted cobalt ferrite nanoparticles: Synthesis characterization and diverse applications, Ceram. Int., 47 (2021) 10512-10535
88. B. Issa, I.M. Obaidat, B.A. Albiss, Y. Haik, Magnetic nanoparticles: surface effects and properties related to biomedicine applications, Int. J. Mol. Sci., *14 (2013)* 21266-21305.
89. S. Jauhar, J. Kaur, A. Goyal, and S. Singhal, Tuning the properties of cobalt ferrite: a road towards diverse applications, RSC Adv., 6 (2016) 97694-97719.
90. Z. Gao, J. Zhu, Q. Zhu, C. Wang, Y. Cao, Spinel ferrites materials for sulfate radical-based advanced oxidation process: A review, Sci. Total Environ., 847 (2022) 157405.
91. P.A. Vinosha, L.A. Mely, J.E. Jeronsia, S. Krishnan, S.J. Das, Synthesis and properties of spinel ZnFe2O4 nanoparticles by facile co-precipitation route, Optik, 134 (2017) 99-108.
92. T. Tatarchuk, M. Bououdina, J.J. Vijaya, L.J. Kennedy, Spinel ferrite nanoparticles: synthesis, crystal structure, properties, and perspective applications, Nanophys. Nanomater. Interface Stud. Appl., 195 (2017) 305-325.
93. H. Khan, Effective heterogeneous photocatalytic degradation of crystal violet dye using manganese ferrite nanoparticles, Pakistan J. Anal. Environ. Chem., 20 (2019) 32-38
94. N. Kaur, M. Kaur, Comparative studies on impact of synthesis methods on structural and magnetic properties of magnesium ferrite nanoparticles, Process. Appl. Ceram., (2014) 2015.

95. P.A. Vinosha, S.J. Das, Investigation on the role of pH for the structural, optical and magnetic properties of cobalt ferrite nanoparticles and its effect on the photo-fenton activity, Mater. Today Proc., 5 (2018) 8662-8671.
96. R. Wu, J. Qu, H. He, Y. Yu, Removal of azo-dye Acid Red B (ARB) by adsorption and catalytic combustion using magnetic $CuFe_2O_4$ powder, Appl. Catal. B Environ., 48 (2004) 49-56,
97. S.B. Somvanshi, M.V. Khedkar, P.B. Kharat, K.M. Jadhav, Influential diamagnetic magnesium (Mg^{2+}) ion substitution in nano-spinel zinc ferrite ($ZnFe_2O_4$): thermal, structural, spectral, optical and physisorption analysis, Ceram. Int., 46 (2020) 8640-8650.
98. S.E. Shirsath, D. Wang, S.S. Jadhav, M.L. Mane, S. Li, Ferrites obtained by sol–gel method, Handbook of Sol-Gel Science and Technology, Cham, Springer, (2017) 1-41.
99. A. Sutka, G. Mezinskis, Sol–gel auto-combustion synthesis of spinel-type ferrite nanomaterials, Front. Mater. Sci., 6 (2012) 128-141.
100. A.A.R. Rodríguez, M.B.M. Trejo, M.J.M. Zaragoza, V.C. Martínez, A.L. Ortiz, E.M. Guerra, M.S. Domínguez, Spinel-type ferrite nanoparticles: synthesis by the oil-in-water microemulsion reaction method and photocatalytic water-splitting evaluation, Int. J. Hydrog. Energy**,** 44 (2018) 1-9.
101. M. Kaur, N. Kaur, Ferrites: synthesis and applications for environmental remediation. In ferrites and ferrates: Chemistry and applications in sustainable energy and environmental remediation. Editors: V.K. Sharma, R. Doong, H. Kim, R.S. Varma, D.D. Dionysiou, Volume 1238, Chapter 4, (2016) 113-136.
102. J. Kurian, M.J. Mathew, Structural, optical and magnetic studies of $CuFe_2O_4$, $MgFe_2O_4$ and $ZnFe_2O_4$ nanoparticles prepared by hydrothermal /solvothermal method, Magn. Magn. Mater., 451 (2017) 121-130.
103. K.K. Kefeni, T.A.M. Msagati, B.B. Mamba, Ferrite nanoparticles: synthesis, characterisation and applications in electronic device, Mater. Sci. Eng. B, 215 (2017) 37-55.

104. M.P. Reddy, A.M.A. Mohamed, One-pot solvothermal synthesis and performance of mesoporous magnetic ferrite MFe_2O_4 nanospheres, Micropor. Mesopor. Mater., 215 (2015) 37-45

105. S.M. El-sheikh, F.A. Harraz, M.M. Hessien, Magnetic behavior of cobalt ferrite nanowires prepared by template-assisted technique, Mater. Chem. Phys., 123 (2010) 254-259.

106. K. Yan, X. Wu, X. An, X. Xie, Facile synthesis and catalytic property of spinel ferrites by a template method, J. Alloys Compd., 552 (2013) 405-408.

107. J. Yan, B. Chai, Y. Liu, G. Fan, G. Song, Construction of 3D/2D $ZnFe_2O_4$/g-C_3N_4 S-scheme heterojunction for efficient photo-Fenton degradation of tetracycline hydrochloride, Appl. Surf. Sci., 607 (2023) 155088.

108. K.K. Kefeni, B.B. Mamba, Photocatalytic application of spinel ferrite nanoparticles and nanocomposites in wastewater treatment: Review, Sustain. Mater. Technol., 23 (2020) e00140.

109. E. Alves Jr, F.C. Bezerra, R.A. Guerra, N. Zufelato, C.S. Martins, J.C. Desordi, A.R.L. Caires, A.F. Bakuzis, P.J. Gonçalves, Coupling of cationic porphyrins on manganese ferrite nanoparticles: A potential multifunctional nanostructure for theranostics applications, J. Photochem. Photobiol. A, 438 (2023) 114551.

110. R. Dillert, D.H. Taffa, M. Wark, T. Bredow, D.W. Bahnemann, research update: photoelectrochemical water splitting and photocatalytic hydrogen production using ferrites (MFe2O4) under visible light irradiation, Appl. Mater., 3 (2015) 3510-3519.

111. S. Sun, S. Gu, J. Sun, F. Xia, G. Chen, First principles investigation of the electronic properties of graphitic carbon nitride with different building block and sheet staggered arrangement, J. Alloys Compd., 735 (2018) 131–139.

112. S. Zhang, P. Gu, R. Ma, L. Luo, T. Wen, G. Zhao, W. Cheng, X. Wang, Recent developments in fabrication and structure regulation of visible-light-driven g-C_3N_4-based photocatalysts towards water purification: A critical review, Catal. Today, 335 (2019) 65–77.

113. Z. Gu , M. Jin, X. Wang, R. Zhi, Z. Hou, J. Yang, H. Hao, S. Zhang, X. Wang, E. Zhou, S. Yin, Recent Advances in g-C3N4-Based Photocatalysts for NOx Removal, Catalysts, 13 (2023) 192.

114. G. Liu, P. Niu, C. Sun, S.C. Smith, Z. Chen, G.Q. Lu, H.M. Cheng, Unique electronic structure induced high photoreactivity of sulfur-doped graphitic C_3N_4, J. Am. Chem. Soc., 132 (2010) 11642–11648.

115. N. Rono, J.K. Kibet, B.S. Martincigh, V.N. Nyomori, A review of the current state of graphitic carbon nitride, Crit. Rev. Solid State Mater. Sci., 46 (2021) 189-217.

116. Z. Mao, J. Chen, Y. Yang, D. Wang, L. Bie, B.D. Fahlman, Novel g-C_3N_4/CoO nanocomposites with significantly enhanced visible-light photocatalytic activity for H_2 evolution, ACS Appl. Mater. Interfaces, 9 (2017) 12427–12435.

117. Y. Deng, L. Tang, G. Zeng, Z. Zhu, M. Yan, Y. Zhou, J. Wang, Y. Liu, J. Wang, Insight into highly efficient simultaneous photocatalytic removal of Cr(VI) and 2,4-Diclorophenol under visible light irradiation by phosphorus doped porous ultrathin g-C_3N_4 nanosheets from aqueous media: performance and reaction mechanism, Appl. Catal. B: Environ., 203 (2017) 343–354.

118. Z. Mo, H. Xu, Z. Chen, X. She, Y. Song, J. Wu, P. Yan, L. Xu, Y. Lei, S. Yuan, H. Li, Self-assembled synthesis of defect-engineered graphitic carbon nitride nanotubes for efficient conversion of solar energy, Appl. Catal. B: Environ., 225 (2018) 154–161.

119. S. Zhang, C. An, R. Zhang, D. Kong, D. Xu, S. Zhang, Template-free synthesis of boron-doped graphitic carbon nitride porous nanotubes for enhanced photocatalytic hydrogen evolution, Langmuir, 40 (2024) 6453-6462.

120. Y.L.T. Ngo, W.M. Choi, J.S. Chung, S.H. Hur, Highly biocompatible phenylboronic acid-functionalized graphitic carbon nitride quantum dots for the selective glucose sensor, Sens. Actuat. B: Chem., 282 (2019) 36–44.

121. H. Liu, X. Wang, H. Wang, R. Nie, Synthesis and biomedical applications of graphitic carbon nitride quantum dots, J. Mat. Chem. B, 7 (2019) 5432-5448.

122. X. Du, G. Zou, Z. Wang, X.A. Wang, Scalable Chemical Route to Soluble Acidified Graphitic Carbon Nitride: An Ideal Precursor for Isolated Ultrathin g-C_3N_4 Nanosheets, Nanoscale*, 7* (2015) 8701–8706.

123. A. Mandal, M. Mukherjee, R. Mandal, B. Mukherjee, Immobilization of Iron Phthalocyanine on carbon nitride support for visible light driven dye degradation: Experimental investigation integrated with DFT study, Surfaces and Interfaces, 42 (2023) 103507.

124. Ö. Görmez, E. Yakar, B. Gözmen, B. Kayan, A. Khataee, CoFe2O4 nanoparticles decorated onto graphene oxide and graphitic carbon nitride layers as a separable catalyst for ultrasound-assisted photocatalytic degradation of Bisphenol-A, Chemosphere, 288 (2022) 132663.

125. B. Chai, T. Y. Peng, J. Mao, K. Li and L. Zan, Graphitic carbon nitride (g-C_3N_4)–Pt-TiO_2 nanocomposite as an efficient photocatalyst for hydrogen production under visible light irradiation, Phys. Chem. Chem. Phys., 14 (2012) 16745–16752.

126. S. Kamal, G.T. Pan, S. Chong, T.C.K. Yang, Ultrasonically induced sulfur-doped carbon nitride/cobalt ferrite nanocomposite for efficient sonocatalytic removal of organic dyes, *Processes, 8 (*2020) 104.

127. B. Chai, J. Yan, C. Wang, Z. Ren, Y. Zhu, Enhanced visible light photocatalytic degradation of Rhodamine B over phosphorus doped graphitic carbon nitride, Appl. Surf. Sci., 391 (2017) 376-383.

128. Z. Ma, C. Zeng, L. Hu, Q. Zhao, Q. Yang, J. Niu, B. Yao, Y. He, A high-performance photocatalyst of ZnTCPP sensitized porous graphitic carbon nitride for antibiotic degradation under visible light irradiation, Appl. Surf. Sci., 484 (2019) 489-500.

129. M. Malika, S.S. Sonawane, Low-frequency ultrasound assisted synthesis of an aqueous aluminium hydroxide decorated graphitic carbon nitride nanowires-based hybrid nanofluid for the photocatalytic H_2 production from Methylene blue dye, Sustain. Energy Technol. Assess., 44 (2021) 100979.

130. S. Liu, S. Zhou, C. Hu, M. Duan, M. Song, F. Huang, J. Cai, Coupling graphitic carbon nitrides with tetracarboxyphenyl porphyrin molecules through π–π stacking for efficient photocatalysis. J Mater Sci: Mater Electron., 31 (2020). 10677–10688

131. T.T. Nguyen, H.T. Bui, G.T. Nguyen, T.N. Hoang, C.V. Tran, P.H. Ho, P.T. Hoai Nguyen, J.Y. Kim, S.W. Chang, W.J. Chung, D.D. Nguyen, D.D. La, Facile preparation of porphyrin@g-C_3N_4/Ag nanocomposite for improved photocatalytic degradation of organic dyes in aqueous solution, Environ. Res., 231 (2023) 115984.

132. T. Xu, D. Wang, L. Dong, H. Shen, W. Lu, W. Chen, Graphitic carbon nitride co-modified by zinc phthalocyanine and graphene quantum dots for the efficient photocatalytic degradation of refractory contaminants, Appl. Catal. B: Environ., 244 (2019) 96-106

133. T.S. Rad, Z. Ansarian, A. Khataee, B. Vahid, E. Doustkhah, N-doped graphitic carbon as a nanoporous MOF-derived nanoarchitecture for the efficient sonocatalytic degradation process, Sep. Purif. Technol., 256 (2021) 117811.

134. M. Preeyanghaa, V. Vinesh, P. Sabarikirishwaran, A. Rajkamal, M. Ashokkumar, B. Neppolian, Investigating the role of ultrasound in improving the photocatalytic ability of CQD decorated boron-doped g-C_3N_4 for tetracycline degradation and first-principles study of nitrogen-vacancy formation, Carbon, 192 (2022) 405-417.

135. M. Fendrich, O.P. Bajpai, R. Edla, A. Molinari, P. Ragonese, C. Maurizio, M. Orlandi, A. Miotello, Towards the Development of a Z-Scheme FeOx/g-C_3N_4 Thin Film and Perspectives for Ciprofloxacin Visible Light-Driven Photocatalytic Degradation, Appl. Sci., 13 (2023) 10591.

136. Y. Yea, S.S.D. Elanchezhiyan, R. Saravanakumar, G. Jagan, J.U. Choi, K. Saravanakumar, C.M. Park, All-solid-state Z-scheme ZnFe–LDH/rGO/g-C_3N_5 heterojunction for enhanced sonophotocatalytic degradation of ciprofloxacin: Performance and mechanistic insights, Environ. Res., 247 (2024) 118209.

137. Zhang, C. Shao, X. Li, Y. Sun, M. Zhang, J. Mu, P. Zhang, Z. Guo, Y. Liu, Hierarchical assembly of ultrathin hexagonal SnS_2 nanosheets onto electrospun

TiO_2 nanofibers: enhanced photocatalytic activity based on photoinduced interfacial charge transfer, Nanoscale, 5 (2013) 606–618.

138. J. Zhang, J. Xin, C. Shao, X. Li, X. Li, S. Liu, Y. Liu, Direct Z-scheme heterostructure of p-$CuAl_2O_4$/n-Bi_2WO_6 composite nanofibers for efficient overall water splitting and photodegradation, J. Colloid Interface Sci., 550 (2019) 170–179.
139. J. Xue, T. Wu, Y. Dai, Y. Xia, Electrospinning and electrospun nanofibers: Methods, materials, and applications, Chem. Rev., 2019, 119, 5298−5415.
140. D. Li, Y. Xia, Electrospinning of nanofibers: Reinventing the wheel?. Adv. Mater., 16 (2004) 1151– 1170.
141. J. Xue, T. Wu, Y. Dai, Y. Xia, Electrospinning and electrospun nanofibers: Methods, materials and applications, Chem. Rev., 119 (2019) 5298−5415.
142. S. Jian, J. Zhu, S. Jiang, S. Chen, H. Fang, Y. Song, G. Duan, Y. Zhang, H. Hou, Nanofibers with diameter below one nanometer from electrospinning, RSC Adv., 8 (2018) 4794−4802.
143. S. Kang, J. Hwang, Fabrication of hollow activated carbon nanofibers (HACNFs) containing manganese oxide catalyst for toluene removal via two-step process of electrospinning and thermal treatment, J. Chem. Eng., 379 (2020) 122315.
144. N.N. Maslakci, S. Ulusoy, E. Uygun, H. Cevikbas, L. Oksuz, H.K. Can, A.U. Oksuz, Ibuprofen and acetylsalicylic acid loaded electrospun PVP-dextran nanofiber mats for biomedical applications, Polym. Bull., 74 (2017) 3283–3299.
145. K. H. Lee, R. Farheen, Z. Arshad, M. Ali, H. Hassan, Mubark Alshareef, A. Dahshan, U. Khalid, Optimized Cu-doping in ZnO electro-spun nanofibers for enhanced photovoltaic performance in perovskite solar cells and photocatalytic dye degradation, RSC Adv., 14 (2024) 15391–15407.
146. M.D. Calisir, M. Gungor, A. Demir, A. Kilic, M.M. Khan, Nitrogen-doped TiO_2 fibers for visible-light-induced photocatalytic activities, Ceram. Int., 46 (2020) 16743-16753.

147. B. Jones, D. Mafukidze, T. Nyokong, Fabrication of electrospun fibers from a porphyrin linked to polyacrylonitrile polymer for photocatalytic transformation of phenols, J. Mol. Struct., 1213 (2020) 128191.

148. X. Zheng, Y. Liu, X. Liu, Q. Li, Y. Zheng, A novel PVDF-TiO_2@g-C_3N_4 composite electrospun fiber for efficient photocatalytic degradation of tetracycline under visible light irradiation, Ecotoxicol. Environ. Saf., 210 (2021) 111866.

149. Y. Li, Z. Ren, M. Gu, Y. Duan, W. Zhang, K. Lv, Synergistic effect of interstitial C doping and oxygen vacancies on the photoreactivity of TiO_2 nanofibers towards CO_2 reduction, Appl. Catal. B, 317 (2022) 121773.

150. N. Singh, J. Prakash, M. Misra, A. Sharma, R.K. Gupta, Dual Functional Ta-Doped Electrospun TiO_2 Nanofibers with Enhanced Photocatalysis and SERS Detection for Organic Compounds, ACS Appl. Mater. Interfaces, 9 (2017) 28495−28507.

151. S.M. Boyer, J. Liu, S. Zhang, M.I. Ehrlich, D.L. McCarthy, L. Tong, J.B. DeCoste, W.E. Bernier, W.E. Jones, The role of ruthenium photosensitizers in the degradation of phenazopyridine with TiO_2 electrospun fibers, *J. Photochem. Photobiol. A Chem.,* 329 (2016) 46-53.

152. N. Bao, Y. Li, Z. Wei, G. Yin, J. Niu, Adsorption of dyes on hierarchical mesoporous TiO_2 fibers and its enhanced photocatalytic properties, J. Phys. Chem. C, 115 (2011) 5708-5719

153. L.J. Antila, P. Myllyperkiö, S. Mustalahti, H. Lehtivuori, J.K. Tommola, Injection and ultrafast regeneration in dye-sensitized solar cells, J. Phys. Chem. C, 118 (2014) 7772-7780.

154. L. Liu, Y. Li, Dual strategies to construct electrospun $NiCo_2O_4$/boron-doped $LaCoO_3$ heterojunction catalysts to activate peroxymonosulfate for organic pollutant degradation, J. Alloys Compd., 968 (2023) 172184.

155. A. Naseri, M. Samadi, N.M. Mahmoodi, A. Pourjavadi, H. Mehdipour, A.Z. Moshfegh, Tuning Composition of Electrospun ZnO/CuO Nanofibers: Toward Controllable and

Efficient Solar Photocatalytic Degradation of Organic Pollutants, J. Phys. Chem. C, 121 (2017) 3327-3338.

156. B. Wulayimujiang, F. Guo, Q. Ma, Y. Wen, Y. Yang, H. Huang, Q. Xie, M. Shen, J. Liu, S. Cheng, An all-in-one a PAN/MXene@Ag–Ag_2S nanofibrous aerogel for efficient oil/water separation, solar interfacial evaporation and photocatalytic degradation of high-concentration dyes, J. Mater. Chem. A, 12 (2024) 19187–19200
157. J. Abdi, G. Mazloom, B. Hayati, Sonocatalytic degradation of tetracycline hydrochloride using SnO_2 hollow-nanofiber decorated with UiO-66-NH_2. J. Environ. Manage., 370 (2024) 122572
158. B.L. Wang, Y. Li, P. Han, Electrospinning preparation of g-C_3N_4/Nb_2O_5 nanofibers heterojunction for enhanced photocatalytic degradation of organic pollutants in water, Sci. Rep., 11 (2021) 22950
159. J. Zhang, W. Zhao, J. Pan, R. Tang, The Sono-Photocatalytic Performance of PAN/g-C_3N_4/CdS Nanofibers Heterojunction, Materials, 14 (2021) 5959
160. P. Singh, K. Mondal, A. Sharma, Reusable electrospun mesoporous ZnO nanofiber mats for photocatalytic degradation of polycyclic aromatic hydrocarbon dyes in wastewater, J. Colloid Interface Sci. 394 (2013) 208–215.
161. C. Zhang, N. Li, D. Chen, Q. Xu, H. Li, J. He, J. Lu, The ultrasonic-induced-piezoelectric enhanced photocatalytic performance of ZnO/CdS nanofibers for degradation of bisphenol A. J. Alloy Compd., 885 (2021) 160987.
162. X. Li, S. Raza, C. Liu, Directly electrospinning synthesized Z-scheme heterojunction TiO2@Ag@Cu2O nanofibers with enhanced photocatalytic degradation activity under solar light irradiation, J. Environ. Chem. Eng., 9 (2021) 106133
163. R. Zhang, Y. Ma, W. Lana, D. E. Sameen, S. Ahmed, J. Dai, W. Qin, S. Li, Y. Liu, Enhanced photocatalytic degradation of organic dyes by ultrasonic-assisted electrospray TiO_2/graphene oxide on polyacrylonitrile/β-cyclodextrin nanofibrous membranes, Ultrason. Sonochem. 70 (2021) 1053

164. B. Fu, J. Li, H. Jiang, X. He, Y. Ma, J. Wang, C. Hu, Modulation of electric dipoles inside electrospun $BaTiO_3$@TiO_2 core-shell nanofibers for enhanced piezo-photocatalytic degradation of organic pollutants, Nano energy, 93 (2022) 106841.

165. E. Erzunov, A. Rassolova, A. Batnar, S. Tonkova, R. Rumyantsev, V. Maizlish, V. Aleks andriskii, A. Vashurin, The influence of methoxy- group position on thermal stability and properties of novel isomeric 4-[(methoxy)phenoxy] phthalonitriles and phthalocyanine complexes based on them, Dyes Pigments, 219 (2023) 111600

166. Z. Huang, L. Huang, Y. Huang, Y. He, X. Sun, X. Fu, X. Xu, G. Wei, D. Chen, C. Zhao, Phthalocyanine-based coordination polymer nanoparticles for enhanced photodynamic therapy, Nanoscale, 9 (2017) 15883

167. N. Ndebele, S. Mgidlana, T. Nyokong, Electrochemical detection of nitrite using an asymmetrically substituted cobalt phthalocyanine conjugated to metal tungstate nanoparticles, Electroanalysis, 34 (2022) 1348-1362

168. Y. Köysal, S. Isik, N. Akdemir, E. Agar, C. Kantar, 4-(3,5-Dimethoxyphenoxy) phthalo-nitrile, Acta Cryst. E, 60 (2004) 930-931

169. L. C. Makola, M. Managa, T. Nyokong, Enhancement of photodynamic antimicrobialtherapy through the use of cationic indium porphyrin conjugated to Ag/$CuFe_2O_4$ nanoparticles, Photodiagn. Photodyn., 30 (2020) 101736

170. O.J. Achadu, T. Nyokong. *In situ* one-pot synthesis of graphitic carbon nitride quantum dots and its 2,2,6,6-tetramethyl(piperidin-1-yl) oxyl derivatives as fluorescent nanosensors for ascorbic acid, *Anal. Chim. Acta*, 991 (2017) 113.

171. S. Cao, H. Chen, F. Jiang, X. Wang, Nitrogen photofixation by ultrathin aminefunctionalized graphitic carbon nitride nanosheets as a gaseous product from thermal polymerization of urea, Applied Catal., 224 (2018) 222–229.

172. M.S. Nunes, M.A. Morales, A. Paesano, J.H. de Araújo, Synthesis and characterization of monophasic $MnFe_2O_4$ nanoparticles for potential application in magnetic hyperthermia, Ceram. Int., 50 (2024) 25333-25341

173. S. Mapukata, T. Nyokong, Development of phthalocyanine functionalised TiO_2 and ZnO nanofibers for photodegradation of methyl orange, New J. Chem., 44 (2020) 16340–16350
174. D. Li and Y. Xia, Fabrication of titania nanofibers by electrospinning, Nano Lett., 3 (2003) 555–560.
175. N. Akhlaghi, G. Najafpour-Darzi, M. Mohammadi, Surface modification of magnetic $MnFe_2O_4$@SiO_2 core-shell nanoparticles with deposited layer of 3- aminopropyl triethoxysilane, Iran. J. Mater. Sci. Eng., 17 (2020) 77–86
176. P. Rokicka-Konieczna, A. Wanag, A. Sienkiewicz, E.K. Nejman, A.W. Morawski, Antimacrobial effect of TiO_2 nanoparticles modified with APTES, Cat. Comm., 134 (2020) 105862.
177. B. Röder, M. Büchner, I. Rückmann, M.O. Senge, Correlation of photophysical parameters with macrocycle distortion in porphyrins with graded degree of saddle distortion, Photochem. Photobiol. Sci., 9 (2010) 1152- 1158.
178. A. Ogunsipe, J. Chen, T. Nyokong, T, Photophysical and photochemical studies of zinc(II) phthalocyanine derivatives-effects of substituents and solvents. New J. Chem., 28 (2004), 822.
179. T.H. Thi, C. Desforge, C. Thiec, S. Gaspard, Singlet-singlet and triplet-triplet intramolecular transfer processes in a covalently linked porphyrin-phthalocyanine heterodimer, J. PhysChem., 93 (1989) 1226–1233.
180. A.M. Brouwer. Standards for photoluminescence quantum yield measurements in solution, Pure Appl. Chem., 83 (2011) 2213.
181. R.W. Redmond, J.N. Gamlin, A compilation of singlet oxygen yields from biologically relevant molecules, Photochem. Photobio., 70 (1999) 391-475.
182. W. Spiller, H. Kliesch, D. Wöhrle, S. Hackbarth, B. Röder, G. Schnurpfeil, Singlet oxygen quantum yields of different photosensitizers in polar solvents and micellar solutions, J. Porphyr. Phthalocyanines, 2 (1998), 145–158.

183. A. Ogunsipe, T. Nyokong, Photophysical and photochemical studies of sulphonated non-transition metal phthalocyanines in aqueous and non-aqueous media, J. Photochem. Photobiol. A Chem., 173 (2005) 211.

184. L.C. Nene, A. Sindelo, J. Britton, T. Nyokong, Effect of ultrasonic frequency and power on the sonodynamic therapy activity of cationic Zn(II) phthalocyanines, J. Inorg. Biochem., 217 (2021) 111397

185. P. Shengyen, Z. Rongxin, M. Hui, D. Daili, P. Xiangjun, Q. Fei, C. Wei, Facile in-situ design strategy to disperse TiO2 nanoparticles on graphene for enhanced photocatlytic degradation of Rhodamine 6G, Appl. Catal., 218 (2017) 208–219.

186. A.J. Barrik, P.R. Gogate. Degradation of 2,4-dichlorophenol using combined approach based on ultrasound, ozone and catalyst, Ultrason. Sonochem., 36 (2017) 517.

187. Han, J. Sun, G. K. Chuah, S. Jaenicke, Enhanced *p*-cresol photodegradation over BiOBr/Bi_2O_3 in the presence of rhodamine B, RSC Adv., 7 (2017) 145-152.

188. E.D. Sherly, J.J. Vijaya, L.J. Kennedy, Visible-light-induced photocatalytic performances of ZnO–CuO nanocomposites for degradation of 2,4-dichlorophenol, Chinese J. Catal., 36 (2015) 1263–1272.

189. T. Nyokong, Structure and Bonding: functional phthalocyanine molecular materials, Vol. 2252, Editors: J. Jiang. Series Ed. D.M.P. Mingos, Springer, 135 (2010) 45-87.

190. M. Uttamlal, A.S. Holmes-Smith. The excitation wavelength dependent fluorescence of porphyrins, *Chem. Phys. Lett.*, 454 (2008) 223.

191. Z.D. Liu, H.X. Zhao, C.Z. Huang, Obstruction of photoinduced electron transfer from excited porphyrin to graphene oxide: a fluorescence turn-on sensing platform for iron (III) ions, PLoS One, 7 (2012) 50367.

192. J. Wang, Y. Zheng, T. Peng, J. Zhang, R. Li. *ACS Sustain.* Asymmetric Zinc Porphyrin Derivative-Sensitized Graphitic Carbon Nitride for Efficient Visible-Light-Driven H_2 Production, *Chem. Eng.*, 5 (2017) 7549.

193. S. Sadjadpour, S. Safarian, S.J. Zargar, N. Sheibani. Antiproliferative effects of ZnO, ZnO-MTCP, and ZnO-CuMTCP nanoparticles with safe intensity UV and X-ray irradiation, *Biotechnol. Appl. Biochem.*, 63 (2015) 113.

194. V. Giegold, L. Lange, R. Ciesielski, A. Hartschuh, Non-linear Raman scattering intensities in graphene, Nanoscale, 12 (2020) 5612–5617

195. Z. Li, C. He, Z. Wang, Y. Gao, Y. Dong, C. Zhao, Z. Cheng, Y. Wu, W. Song, An ethylenediamine-modified graphene oxide covalently functionalized with tetracarboxylic Zn(II) phthalocyanine hybrid for enhanced nonlinear optical properties, Photochem. Photobiol. Sci., 16 (2016) 910-919

196. F. Wen, Y. Li, X. Huang, L. Peng, T. Zhang, Y. Xu, Utilizing three-dimensional ordered microporous $NiFe_2O_4$ loaded with g-C3N4 as a heterogeneous photo-fenton catalyst for tetracycline degradation, J. Alloys Comp., 958 (2023) 170403.

197. S. Barman, M. Sadhukhan, Facile bulk production of highly blue fluorescent graphitic carbon nitride quantum dots and their application as highly selective and sensitive sensors for the detection of mercuric and iodide ions in aqueous media, J. Mater. Chem., 22 (2012), 21832-21837.

198. X. Ma, M. Luo, L. Yan, N. Tang, J. Li, Preparation of a magnetically recyclable visible-light driven photocatalyst based on phthalocyanine and visible lightcatalytic degradation of methyl orange and p-nitrophenol, New. J. Chem., 43 (2019) 9589-9795

199. D. Guo, J. Zhang, G. Liu, X. Luo, F. Wu, Cobalt phthalocyanine-based nanorods as efficient catalysts for chemical conversion of CO2 under ambient conditions, J. Mater. Sci. 56 (2021) 10990-10999.

200. J. Deng, S.F. Feng, X. Ma, C. Tan, H. Wang, S. Zhou, T. Zhang, J. Li, Heterogeneous degradation of Orange II with peroxymonosulfate activated by ordered mesoporous $MnFe_2O_4$, Sep. Purif. Technol., 167 (2016) 181-189

201. R. Prabakaran, R. Kesavamoorthy, G. Reddy, F.P. Xavier, Structural investigation of copper phthalocyanine thin films using X-Ray diffraction, raman scattering and optical absorption measurements, Phys. Status Solidi B, 229 (2002) 1175-1186

202. X. Zhou, W. Xu, G. Liu, D. Panda, P. Chen, Size-dependent catalytic activity and dynamics of gold nanaoprticles at the single molecule level, J. Am. Chem. Soc., 123 (2009) 138-146

203. L. Alagna, A. Capobianchi, M.P. Casaletto, G. Mattogno, M. Paoletti, G. Pennesi, G. Ro ssi, C. Nazional, A.M. Paoletti, Effect of molecular packing on the solid-state spectra of ruthenium phthalocyanine: anomalous behavior of a monodimensional stacked assembly, J. Mater. Chem., 11 (2001) 1928-1935.

204. G. Fan, C. Cai, S. Yang, B. Du, J. Luo, Y. Chen, X. Lin, X. Li, Y. Wang, Sonophotocatalytic degradation of ciprofloxacin by $Bi_2MoO_6/FeVO_4$ heterojunction: Insights into performance, mechanism and pathway, Sep. Purif. Technol., 303 (2022) 122251

205. K. Shen, K. Wu, D. Wang, Band alignment of ultra-thin hetero-structure ZnO/TiO2 junction, Mater. Res. Bull., 51 (2014) 141-144.

206. F. Cheng, S.M. Sajedin. S.M, S.M. Kelly, A.F. Lee, A. Kornherr, UV-stable paper coated with APTES-modified P25 TiO_2 nanoparticles, Carbohydr. Polym., 114 (2014) 246-252

207. G. Dai, S. Liu, Y. Liang, H. Liu, Z. Zhong, A simple preparation of carbon and nitrogen co-doped nanoscaled TiO2 with exposed {001} facets for enhanced visible-light photocatalytic activity, J. Mol. Catal. A. Chem., 368 (2013) 38-42

208. E.O. Oseghe, S.M. Maddila, P.G. Ndungu, S.B. Jonnaladda, Effect of surfactant concentration on active species generation and photocatalytic properties of TiO_2, Appl. Catal., 176 (2015) 288-297

209. A.K. Zak, R. Razali, W.H.A. Majid, M. Darroudi, Synthesis and characterization of a narrow size distribution of zinc oxide nanoparticles, Int. J. of Nanomed., 6 (2011) 1399-1403

210. Z.B. Zhang, C.C. Wang, R. Zakaria, J.Y. Ying, Role of particle size in nano-crystalline TiO_2-based photo-catalysts, J. Phys. Chem. B, 102 (1998), 1087

211. M. Pandey, M. Singh, K. Wasnik, Targeted and enhanced antimicrobial inhibition of mesoporous ZnO-Ag_2O/ Ag, ZnO-CuO, and ZnO-SnO_2 composite nanoparticles, ACS Omega, 34 (2021) 1276-1279

212. X.F. Zhang, W. Guo, Indole substituted zinc phthalocyanine: Improved photosensitizing ability and modified photooxidation mechanism, J. Photochem. Photobiol. A, 221 (2011) 117-124.

213. N. Kuznetsova, N. Gretsova, E. Kalmykova, E. Makarova, S. Dashkevich, V. Negrimovskii, O. Kaliya, O. Lukyanets, Relationship between the photo-chemical properties and structure of porphyrins and related compounds. Russ. J. Gen. Chem., 70 (2000) 133-140

214. S.M. Bachilo, R.B. Weisman, Determination of triplet quantum yields from triplet-triplet annilation fluorescence, J. Phys. Chem. A, 104 (2000) 7711-7714

215. T. G. B. De Souza, M. G. Vivas, C. R. Mendonça, S. Plunkett, M. A. Filatov, M. O. Senge, L. J. De Boni, Studying the intersystem crossing rate and triplet quantum yield of meso-substituted porphyrins by means of pulse train fluorescence technique, J. Porphyr. Phthalocya., 20 (2016) 282 -291.

216. J.R. Darwent, P. Douglas, A. Harriman, G. Porter, M.C. Richoux, Metal phthalocyanines and porphyrins as photosensitizers for reduction of water to hydrogen, Coord. Chem. Rev., 44 (1982), 83–126.

217. N.A. Kuznetsova, N.S. Gretsova, V.M. Derkacheva, S.A. Mikhalenko, L.I. Solov'eva, O.A. Yuzhakova, O.L. Kaliya, E.A. Luk'yanets, Russ. J. Gen. Chem., 72 (2002) 300

218. M.L. Bechec, T. Pigot, S. Lacombe, Chemical quenching of singlet oxygen and other reactive oxygen species in water: a reliable method for the determination of quantum yields in photochemical process, ChemPhotoChem., 2 (2018) 622-631.

219. P. Khoza, T. Nyokong, Photocatalytic behaviour of zinc tetraamino phthalocyanine-silver nanoparticles immobilized on chitosan beads, J. Mol. Cat. A: Chem., 399 (2015) 25-32.

220. L. C. Nene, A. Magadla, T. Nyokong, Enhanced Mitochondria Destruction on MCF-7 and HeLa Cell Lines In Vitro Using Triphenyl-phosphonium-Labelled Phthalocyanines in

Ultrasound-Assisted Photodynamic Therapy Activity, J. Photochem. Photobiol. B: Biol., 235 (2022) 112553

221. K.V. Kumar, K. Porkodi, F. Rocha, Langmuir-Hinshelwood kinetics – a theoretical study, Catal. Commun., 9 (2008) 82–84.

222. R. Tang, H. Zeng, C. Feng, S. Xiong, L. Li, Z. Zhou, D. Gong, L. Tang, Y. Deng, Twisty C-TiO_2/PCN S-Scheme Heterojunction with Enhanced n→π* Electronic Excitation for Promoted Piezo-Photocatalytic Effect, Small, 19 (2023) 2207636.

223. V.M. Gowri, S.A. John, Fabrication of bulk, nanosheets and quantum dots of graphitic carbon nitride on electrodes: Morphology dependent electrocatalytic activity, J. Electroanalytical Chem., 895 (2021) 115474.

224. K.K. Childress, K. Kim, D.J. Glugla, C.B. Musgrave, C.N. Bowman, J.W. Stansbury, Independent Control of Singlet Oxygen and Radical Generation via Irradiation of a Two-Color Photosensitive Molecule, Macromolecules, 52 (**2019)** 4968-4978

225. P. Kumari, A. Meena, Green synthesis of gold nanoparticles from *Lawsoniainermis* and its catalytic activities following the Langmuir-Hinshelwood mechanism, Colloids Surf. A: Physicochem. Eng., 606 (2020) 125447.

226. J. Pan, Y. Yang. W. Fang, W. Liu, K. Le, D. Xu. X. Li, Fluorescent phthalocyanine-graphene conjugate with enhanced NIR absorbance for imaging and multi-modality therapy, ACS App. Nano. Mat., 1 (2018) 2785-2795

227. M. Conte, Y. Ma, C. Loyns, P. Price, D. Rippon, V. Chechik, Mechanistic insight into TEMPO-inhibited polymerisation: simultaneous determination of oxygen and inhibitor concentrations by EPR, Org. Biomol. Chem., 7 (2009) 2685–2687.

228. C. Walling, L. Heaton, Radical Formation in the Reactions of t-Butyl Hydroperoxide with Styrene. J. Am. Chem. Soc., 87 (1965) 38–47.

229. L. Peng, Y. Shang, B. Gao, X. Xu, Co3O4 anchored in N, S heteroatom co-doped porous carbons for degradation of organic contaminant: role of pyridinic N-Co binding and high tolerance of chloride, Appl. Catal. B., 282 (2021) 119484

230. C.Y. Jin, J. Kang, Z.L. Li, M. Wang, Z.M. Wu, Y.H. Xie, Enhanced visible light photocatalytic degradation of tetracycline by MoS2/Ag/g-C3N4 Z-scheme composites with peroxymonosulfate. Appl. Surf. Sci., 514 (2020) 146076

231. S. Wang, Y. Liu, J. Wang, Peroxymonosulfate activation by Fe-Co-codoped graphite carbon nitride for degradation of sulfamethoxazole. Environ. Sci. Tech., 54 (2020) 10361-10369.

232. H. Fang, Y. Han, X. Feng, W. Ji, C.T. Au, S-scheme heterojunction g-C_3N_4/Ag/AgNCO for efficient tetracycline removal in a photo-assisted peroxymonosulfate system. Sep. Purif. Technol., 296 (2022) 121210.

233. T.A. Kurniawan, Z. Mengting, D. Fu, S.K. Yeap, M.H.D. Othman, R. Avtar, T. Ouyang, Functionalizing TiO_2 with graphene oxide for enhancing photocatalytic degradation of methylene blue (MB) in contaminated wastewater. J. Environ. Manage., 270 (2020) 110871

234. J. Wei, K. Rong, Y. Wang, L. Liu, Y. Fang, S. Dong, Hierarchical porous nanosheets of Co-Mn bimetallic oxide from deep eutectic solvent for highly efficient peroxymonosulfate activation, Nano. Res., 7 (2023) 10381-1091.

APPENDIX

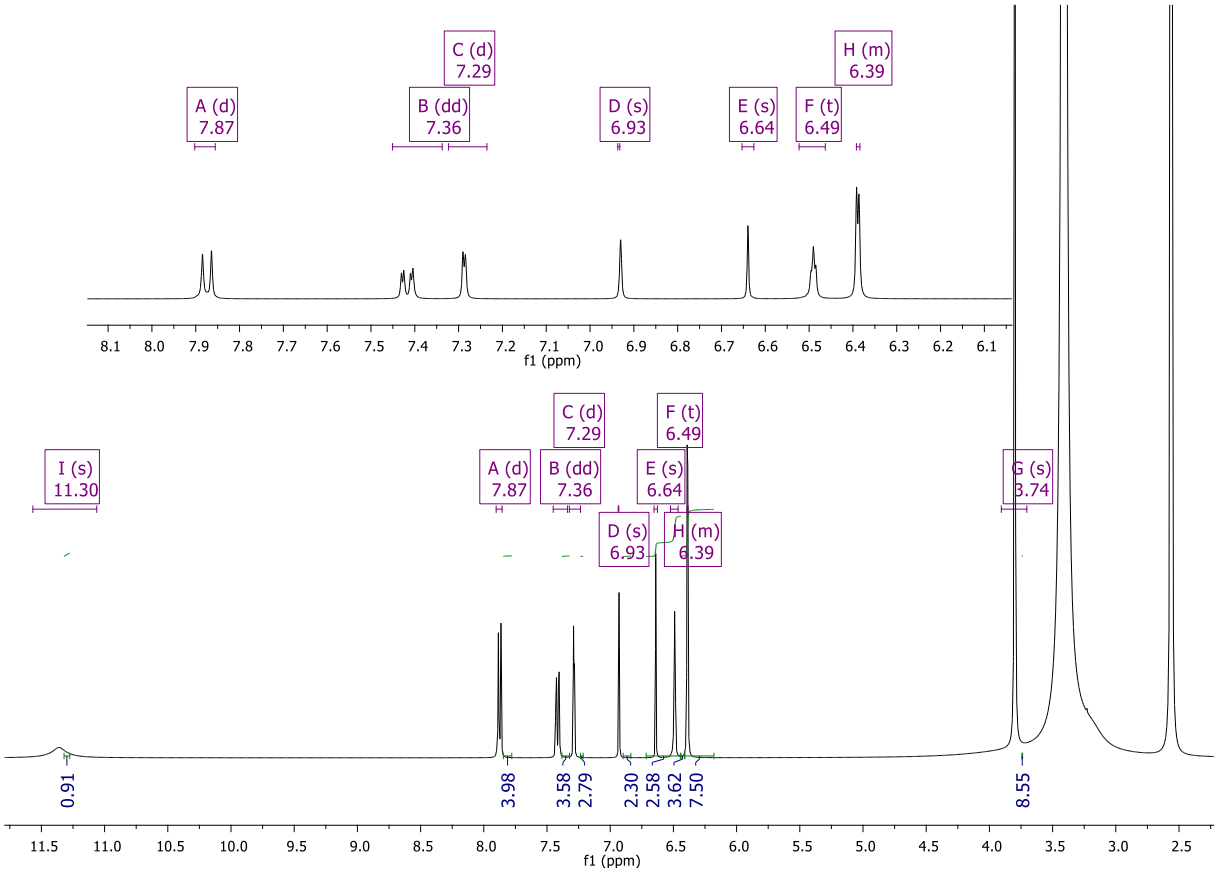

Appendix 1. NMR spectrum of the complex **3** (insert spectrum is expanded aromatic region).

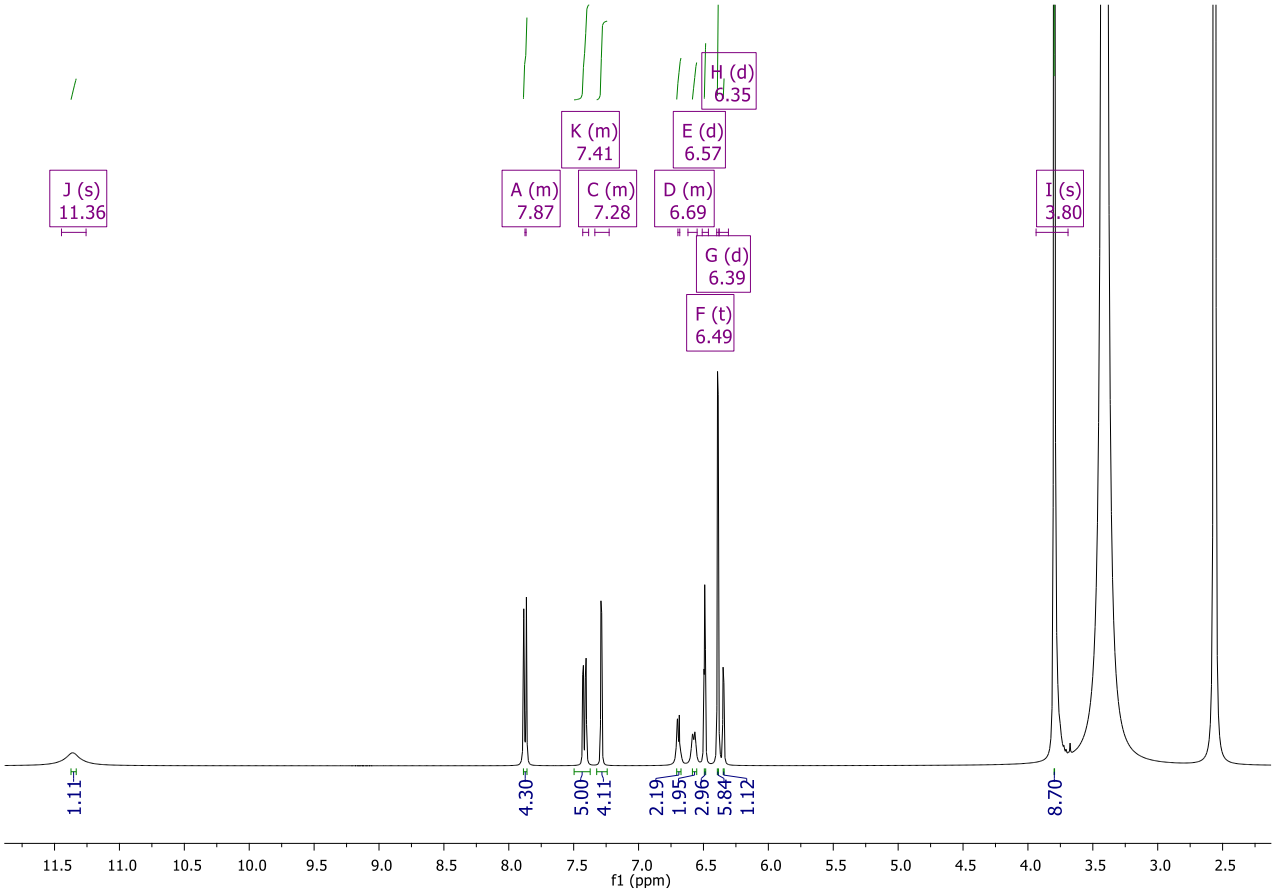

Appendix 2. NMR spectrum of the complex **4.**

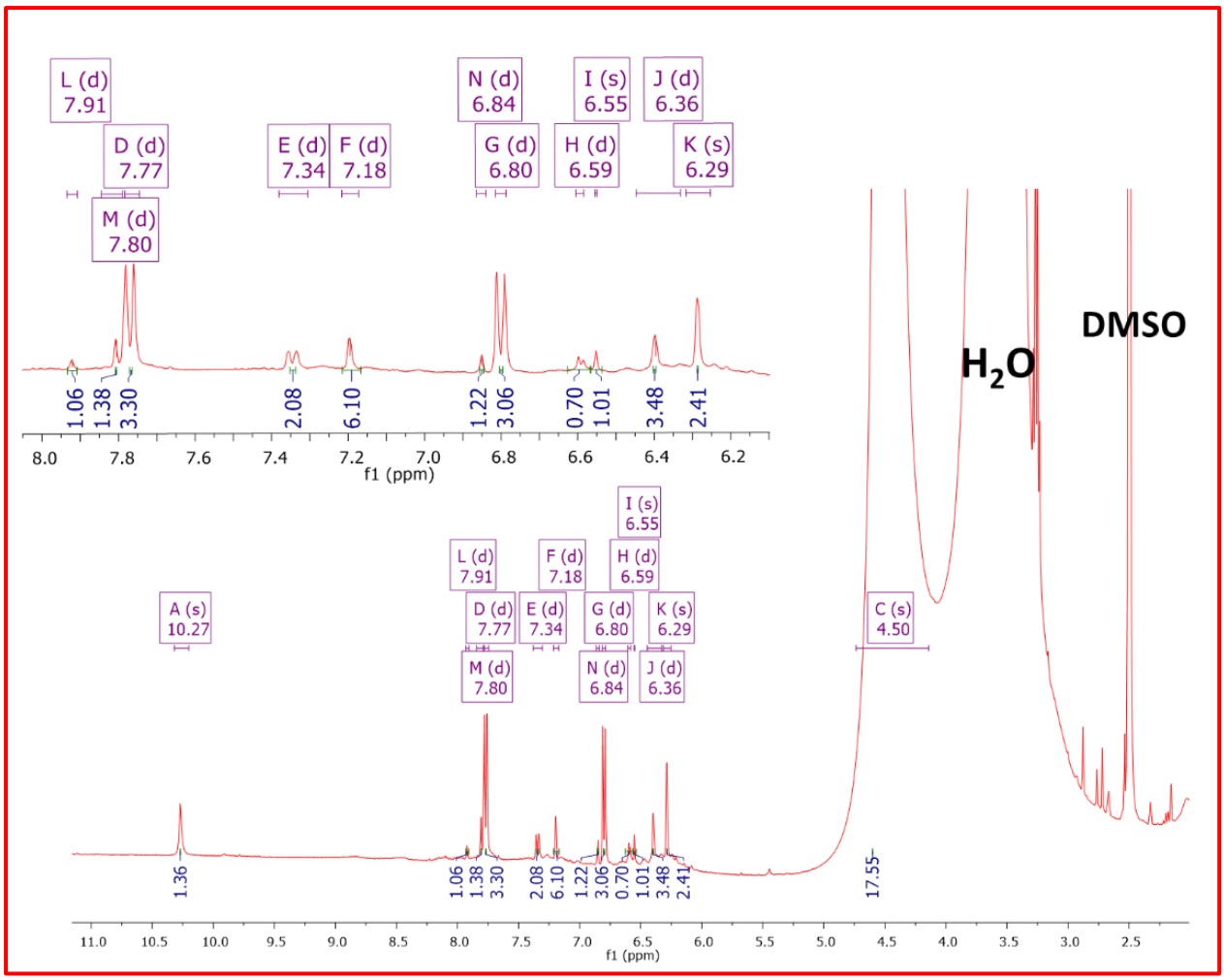

Appendix 3. NMR spectrum of the complex **6.**

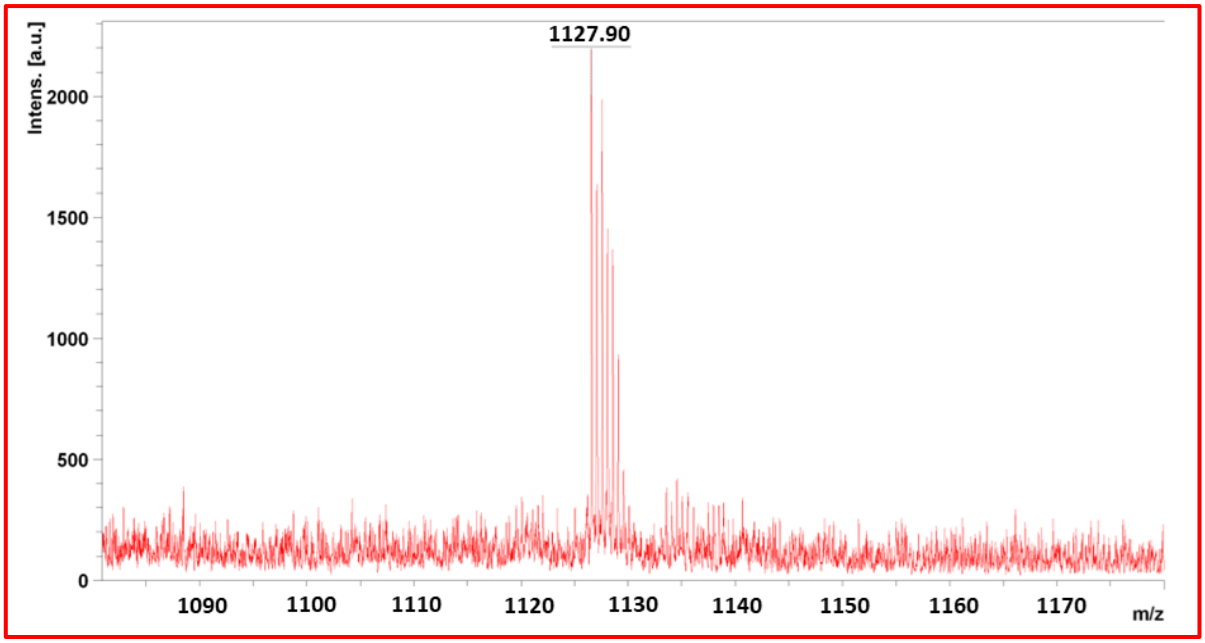

Appendix 4. Mass spectrum of the complex **3**.

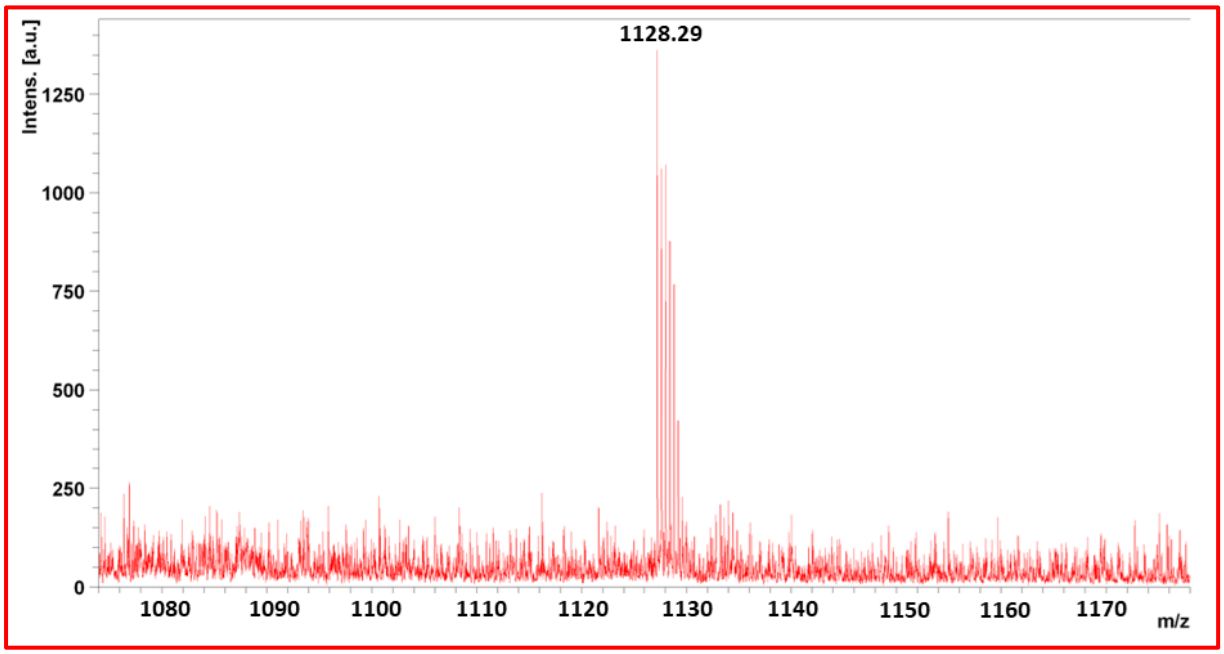

Appendix 5. Mass spectrum of the complex **4**.

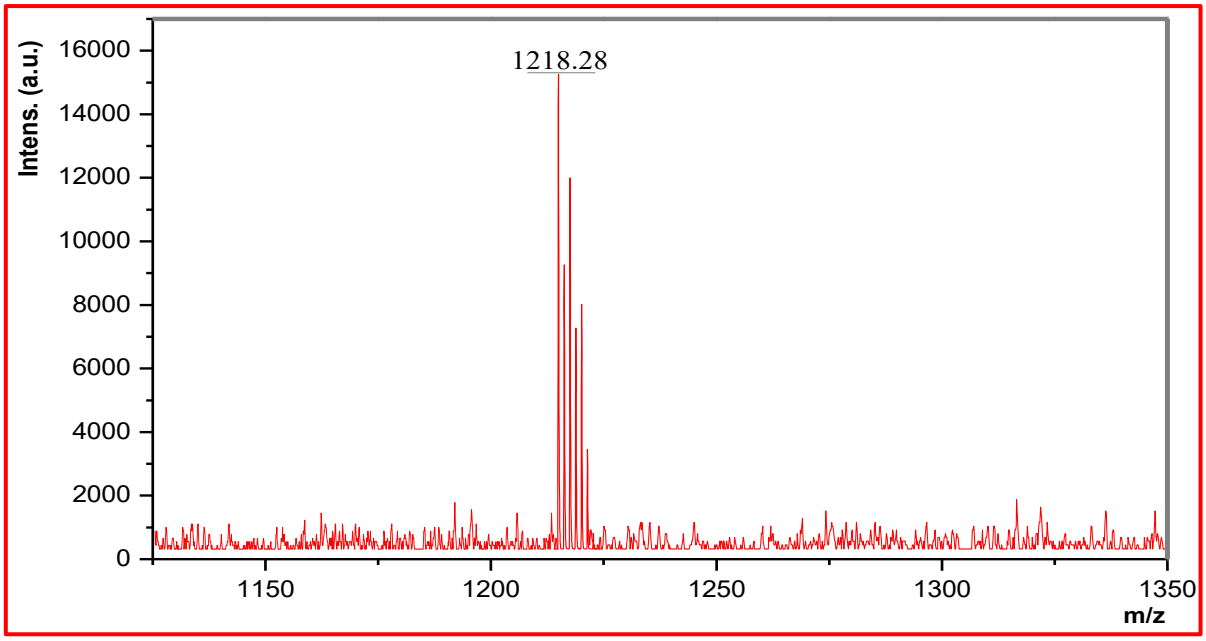

Appendix 6. Mass spectrum of the complex **6**.

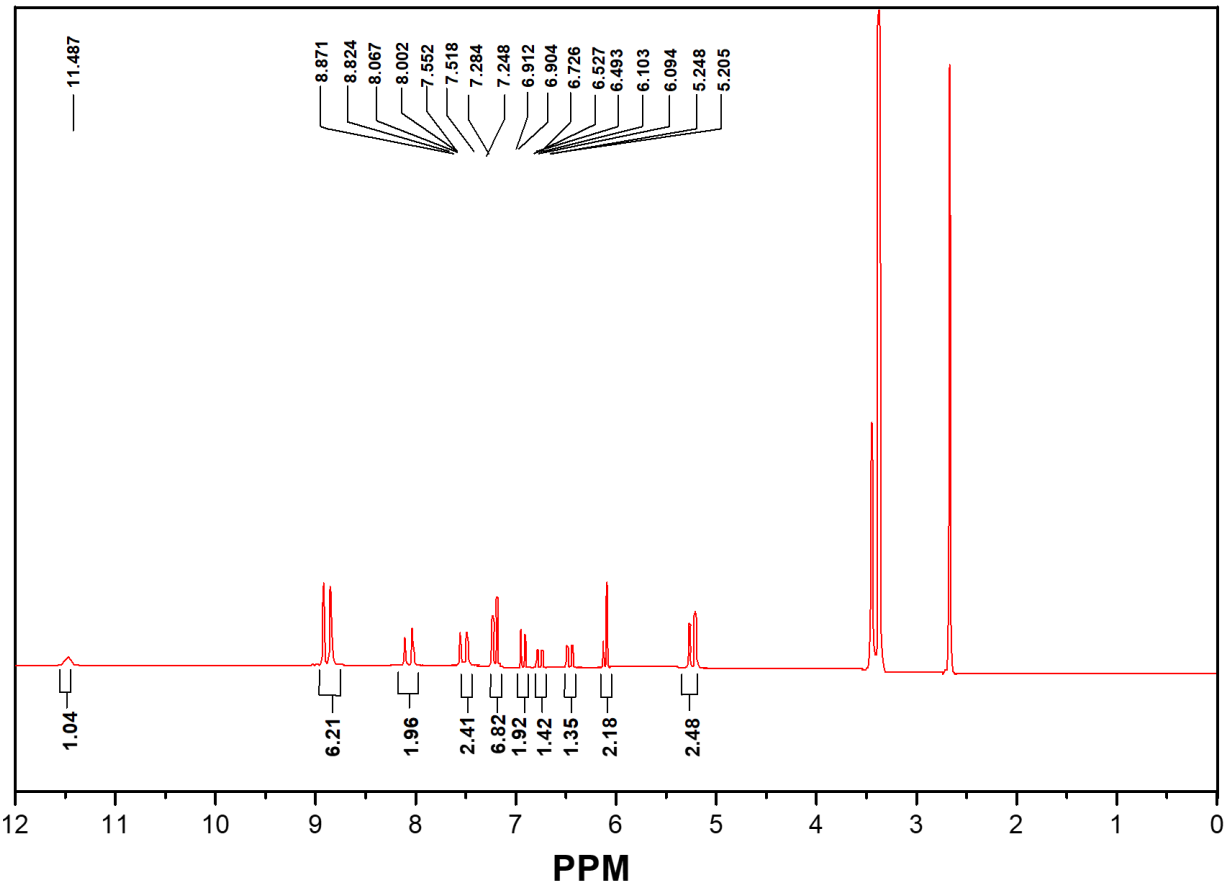

Appendix 7. NMR spectrum of the complex **7.**

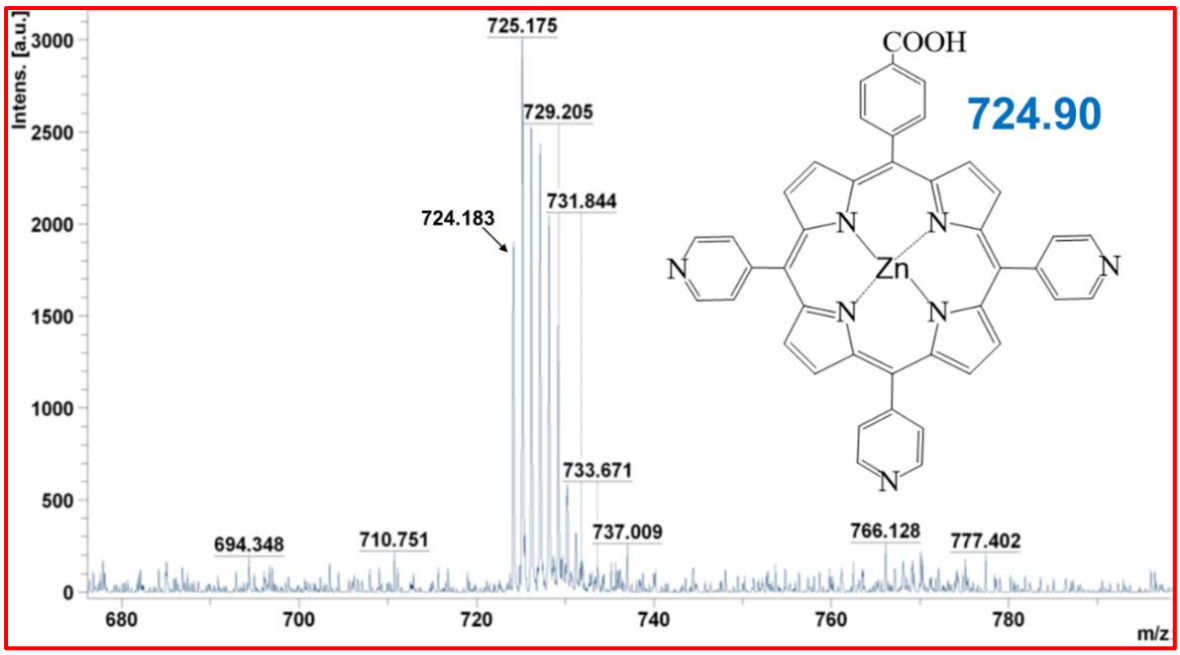

Appendix 8. Mass spectrum of the complex **7**.

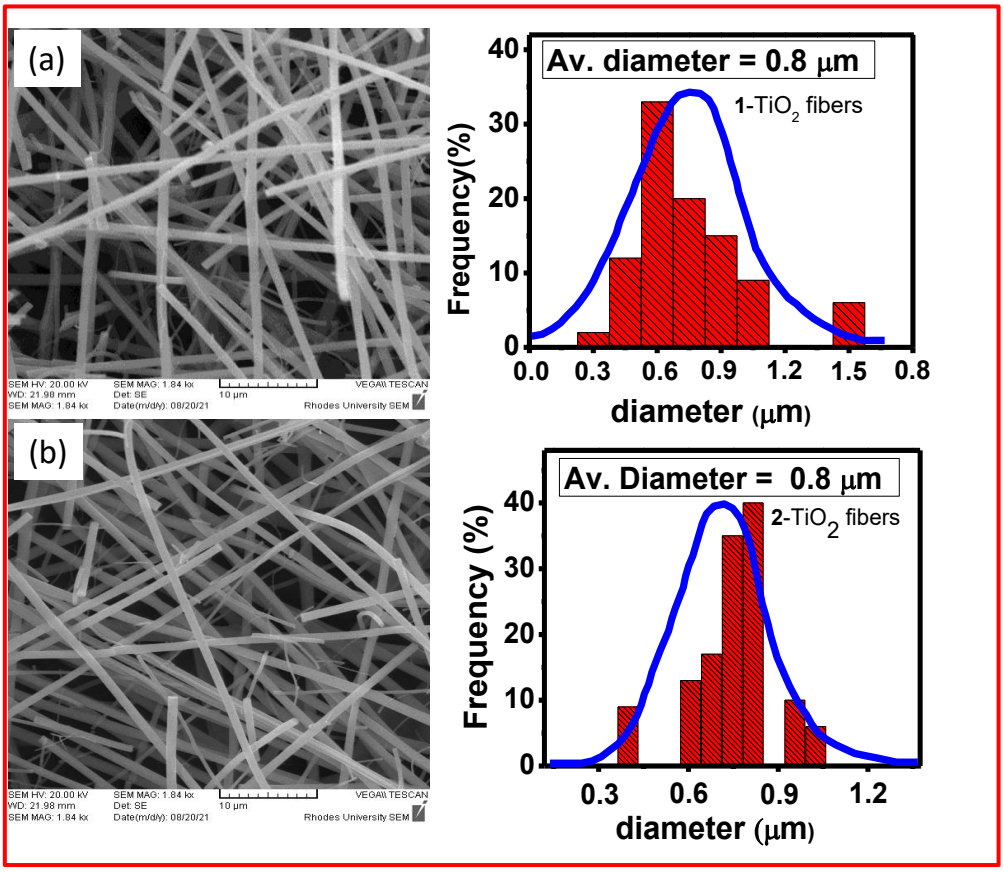

Appendix 9. SEM images and diameter histograms of **1**-TiO_2 fibers **(a)** and **2**-TiO_2 fibers **(b)**.

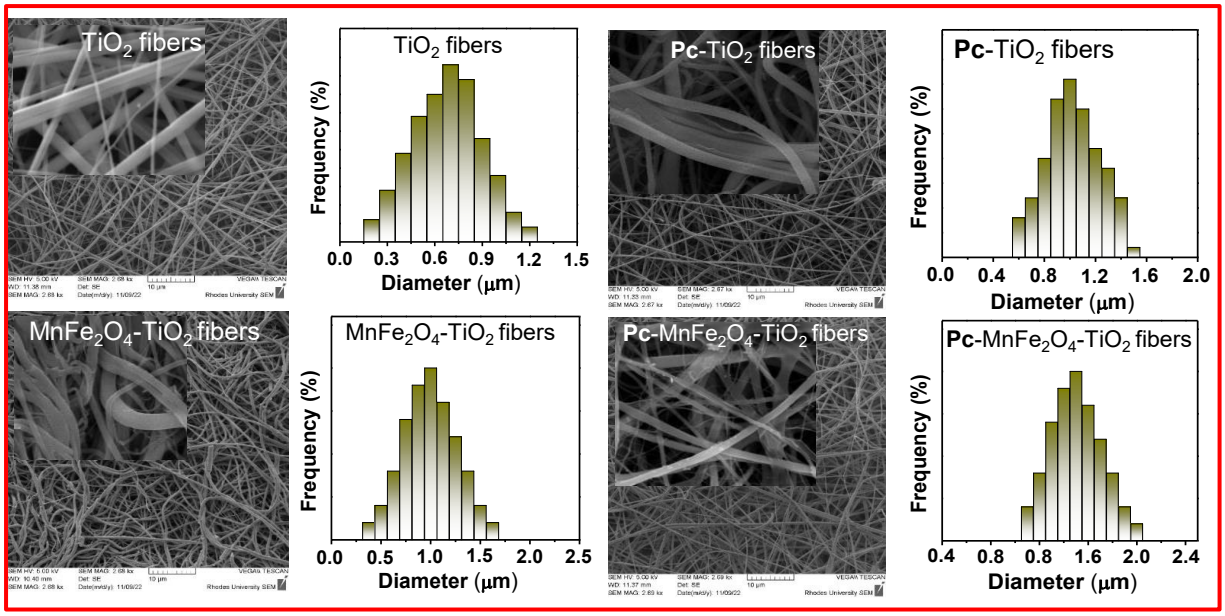

Appendix 10. SEM images, EDX and diameter histograms of TiO_2 fibers and **5**-TiO_2 fibers, $MnFe_2O_4$-TiO_2 fibers and **5**@$MnFe_2O_4$-TiO_2 fibers.

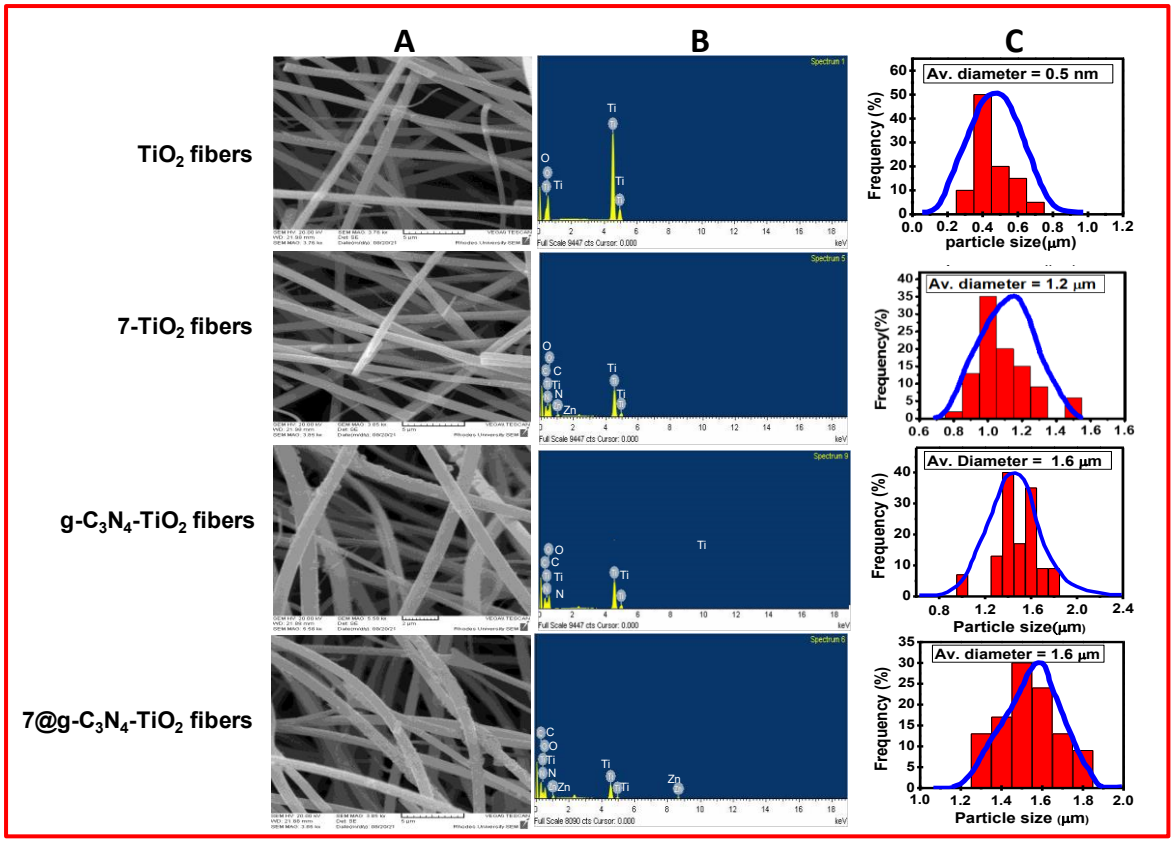

Appendix 11. SEM images **A**, EDX **B** and diameter histograms **C** of TiO_2 fibers, **7**-TiO_2 fibers, g-C_3N_4 QDs-TiO_2 fibers and **7**@g-C_3N_4 QDs-TiO_2 fibers.

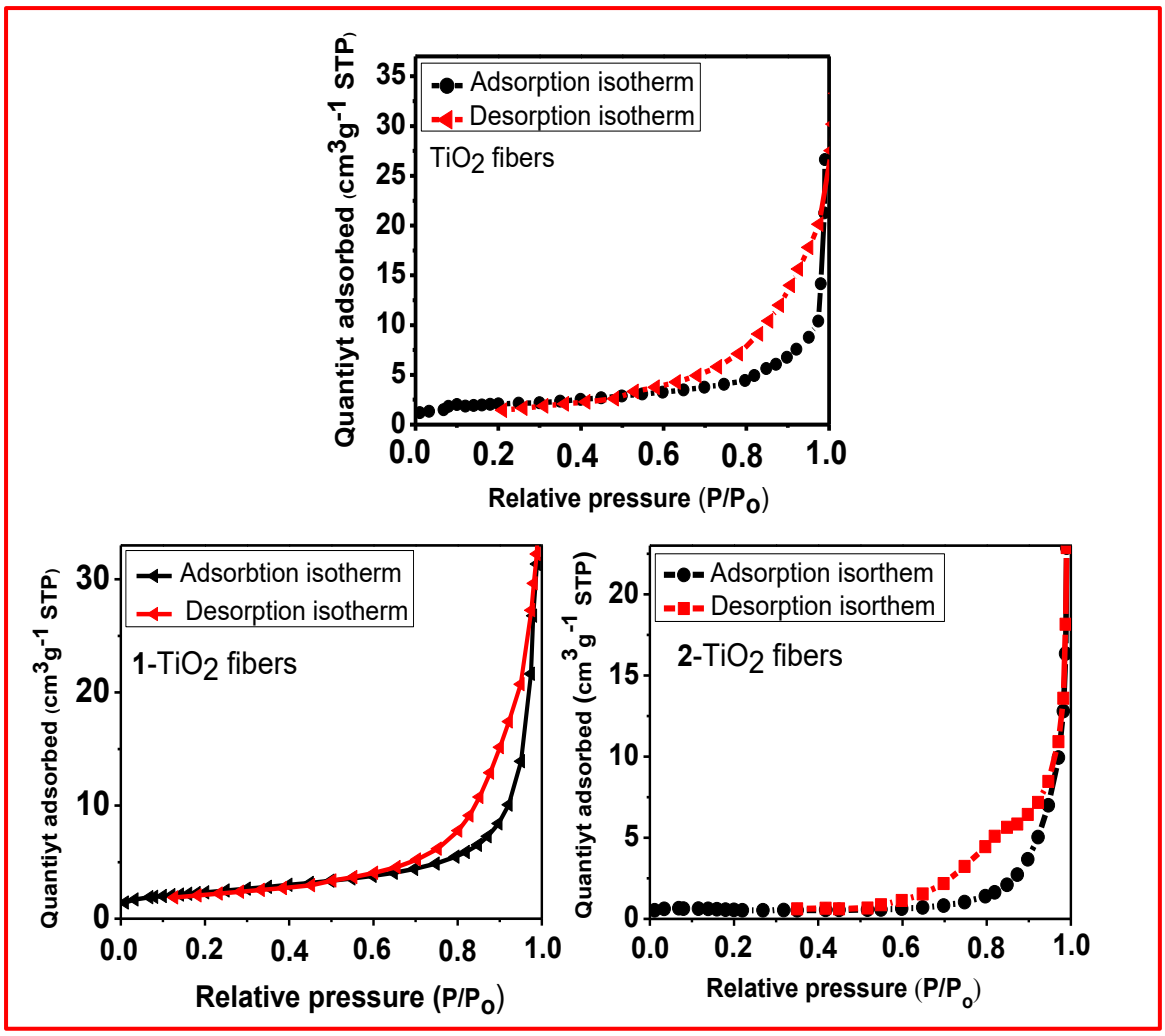

Appendix 12 BET isotherms of TiO_2 fibers, **1**-TiO_2 fibers and **2**-TiO_2 fibers

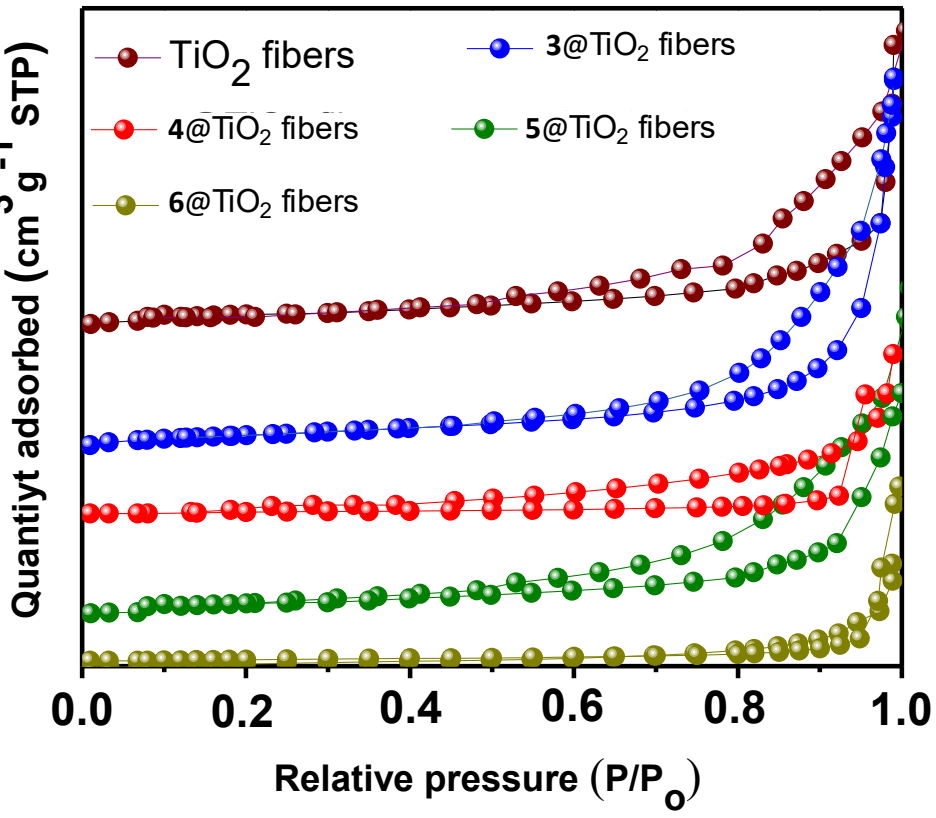

Appendix 13. BET isotherms of TiO_2 fibers, **3**@TiO_2 fibers, **4**@TiO_2 fibers,**5**@TiO_2 fibers and **6**@TiO_2 fibers.

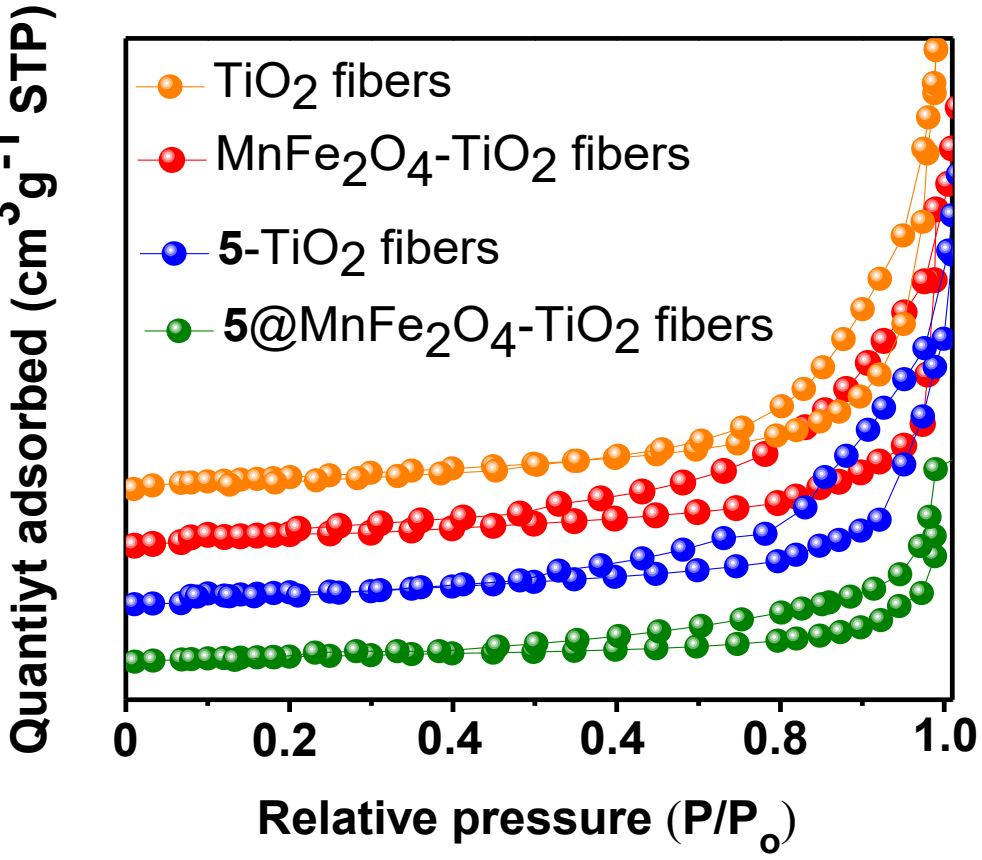

Appendix 14. BET isotherms of TiO_2 fibers, $MnFe_2O_4$-TiO_2 fibers, **5**@TiO_2 fibers and **5**@$MnFe_2O_4$-TiO_2 fibers.

Appendix 15

Methods used in density functional theory (DFT)

DFT geometry optimizations were carried out for complexes **1**, **2**, **3** and **4** at the B3LYP/6-31G(d) level of theory with the Gaussian 09 software package [1]. Electrostatic potential (ESP) surfaces were mapped onto total electron density isosurfaces at 0.0004 a.u. with Gaussview at the B3LYP/6-31G(d) level of theory to visualize the predicted charge distribution across complexes **1**, **2**, **3** and **4**.

References

1. M. J. Frisch, G. W. Trucks, H. B. Schlegel, G. E. Scuseria, M. A. Robb, J. R. Cheeseman, G. Scalmani, V. Barone, B. Mennucci, G. A. Petersson, H. Nakatsuji, M. Caricato, X. Li, H. P. Hratchian, A. F. Izmaylov, J. Bloino, G. Zheng, J. L. Sonnenberg, M. Hada, M. Ehara, K. Toyota, R. Fukuda, J. Hasegawa, M. Ishida, T. Nakajima, Y. Honda, O. Kitao, H. Nakai, T. Vreven, J. A. Montgomery, Jr., J. E. Peralta, F. Ogliaro, M. Bearpark, J. J. Heyd, E. Brothers, K. N. Kudin, V. N. Staroverov, T. Keith, R. Kobayashi, J. Normand, K. Raghavachari, A. Rendell, J. C. Burant, S. S. Iyengar, J. Tomasi, M. Cossi, N. Rega, J. M. Millam, M. Klene, J. E. Knox, J. B. Cross, V. Bakken, C. Adamo, J. Jaramillo, R. Gomperts, R. E. Stratmann, O. Yazyev, A. J. Austin, R. Cammi, C. Pomelli, J. W. Ochterski, R. L. Martin, K. Morokuma, V. G. Zakrzewski, G. A. Voth, P. Salvador, J. J. Dannenberg, S. Dapprich, A. D. Daniels, O. Farkas, J. B. Foresman, J. V. Ortiz, J. Cioslowski, and D. J. Fox, *Gaussian, Inc., Wallingford CT* (2016).

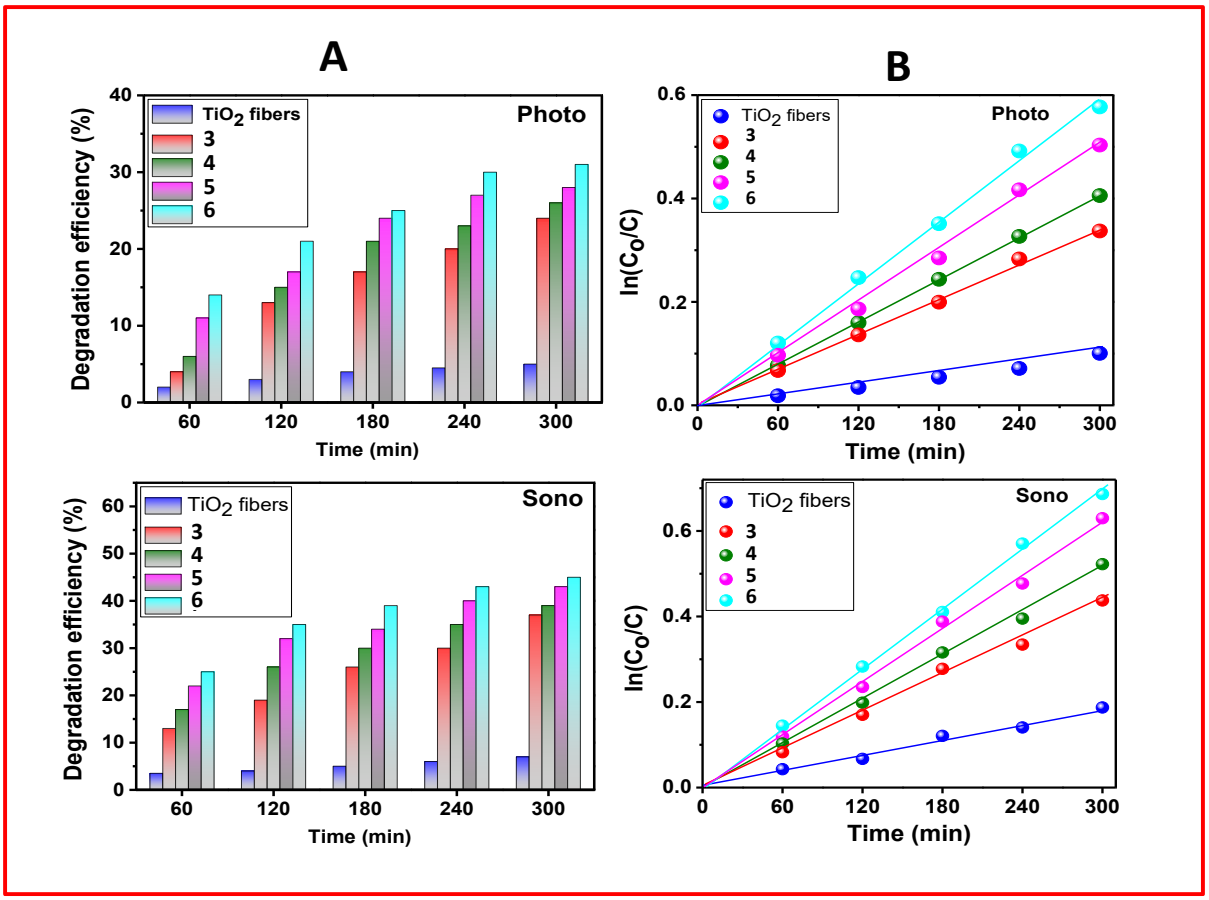

Appendix 16. Degradation efficiency **A**, and kinetics plots **B**, of photo, and sono-catalytic degradation of Rhodamine 6G using pristine TiO_2 fibers and **3**, **4**, **5** and **6** complexes.

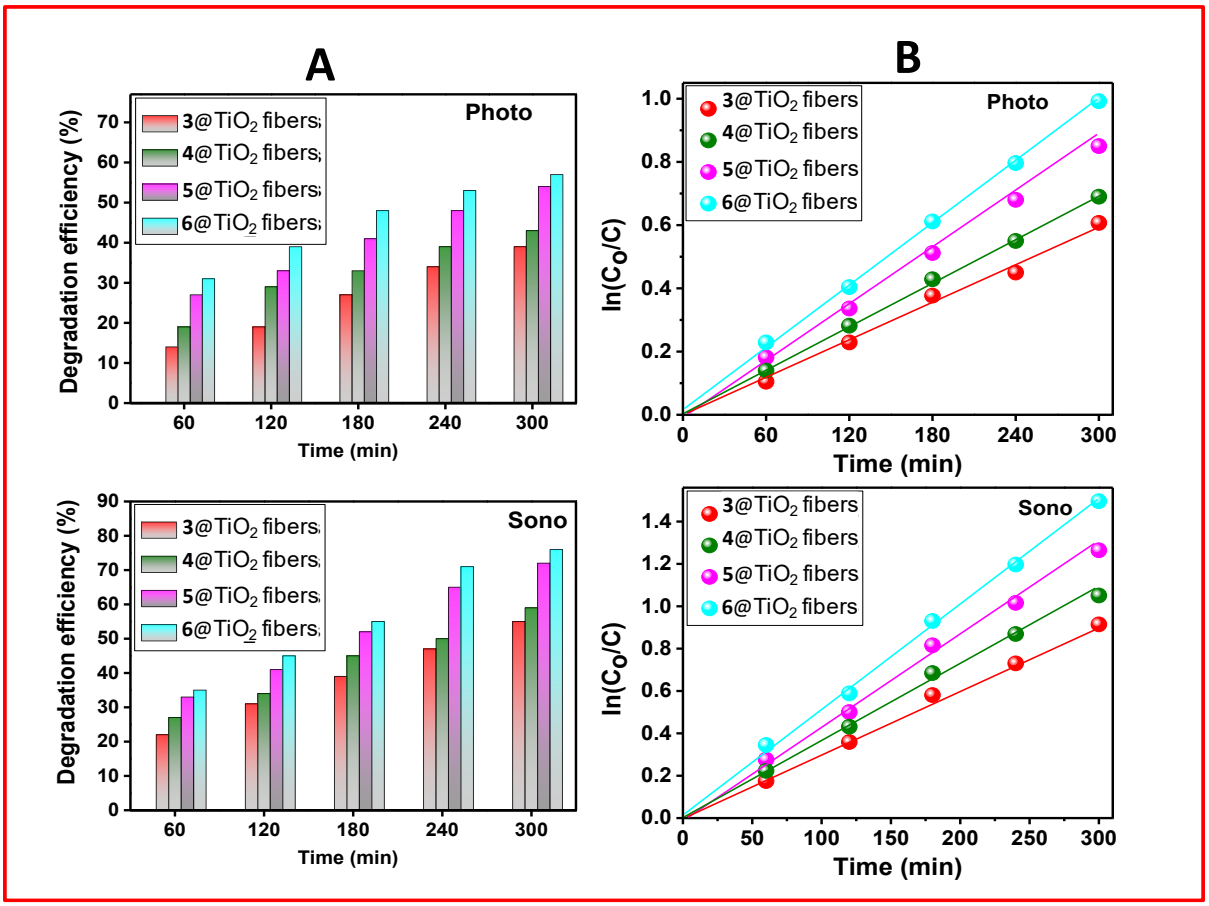

Appendix 17. Degradation efficiency **A**, and kinetics plots **B**, of photo, and sono-catalytic degradation process using pristine **3**@TiO_2 fibers, **4**@TiO_2 fibers, **5**@TiO_2 fibers and **6**@TiO_2 fibers.

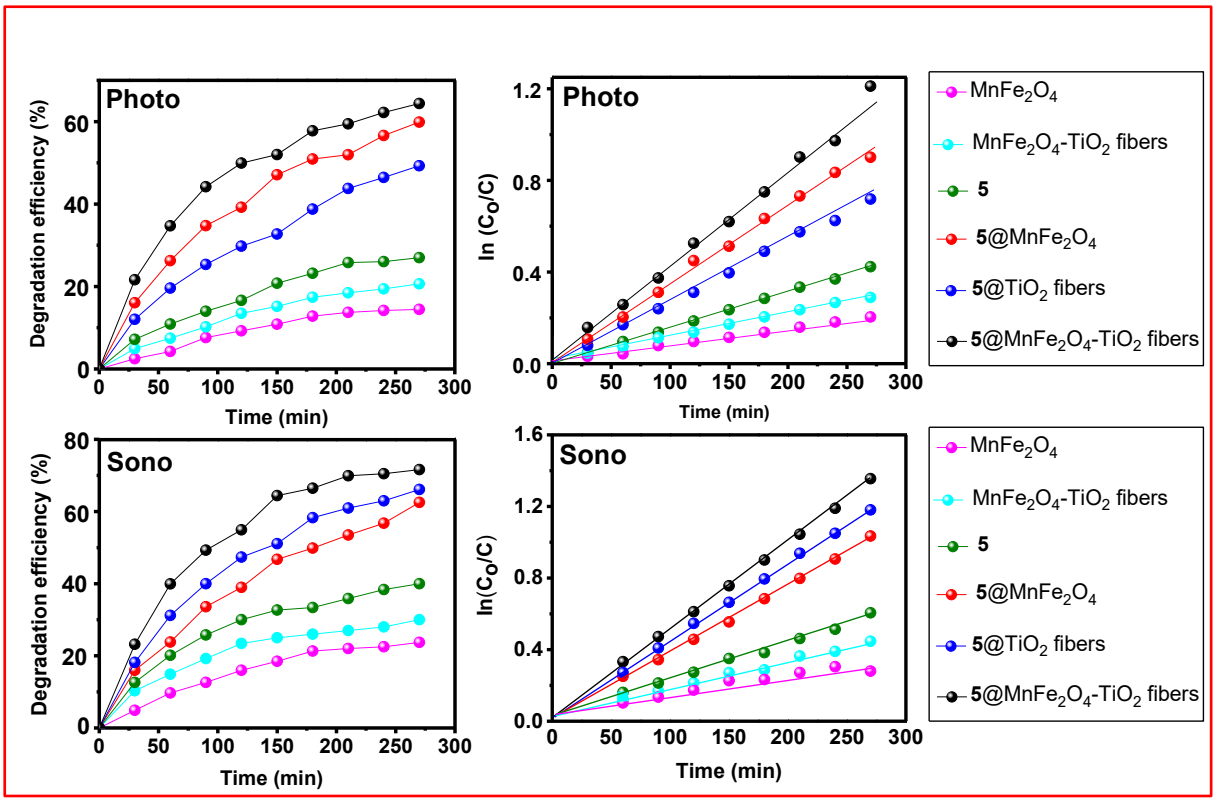

Appendix 18. Degradation efficiency and reaction kinetics properties for degradation of Rhodamine (6.63×10^{-5} M) 6 G at pH 9 using various catalysts.

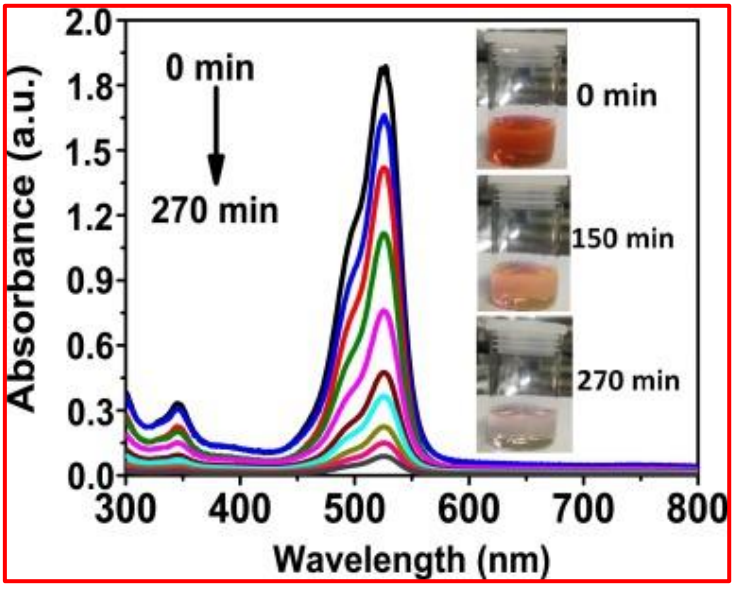

Appendix 19. Rhodamine 6G (6.63×10^{-5} M) spectral changes using 6@g-C3N4 NS-ZnO fibers.

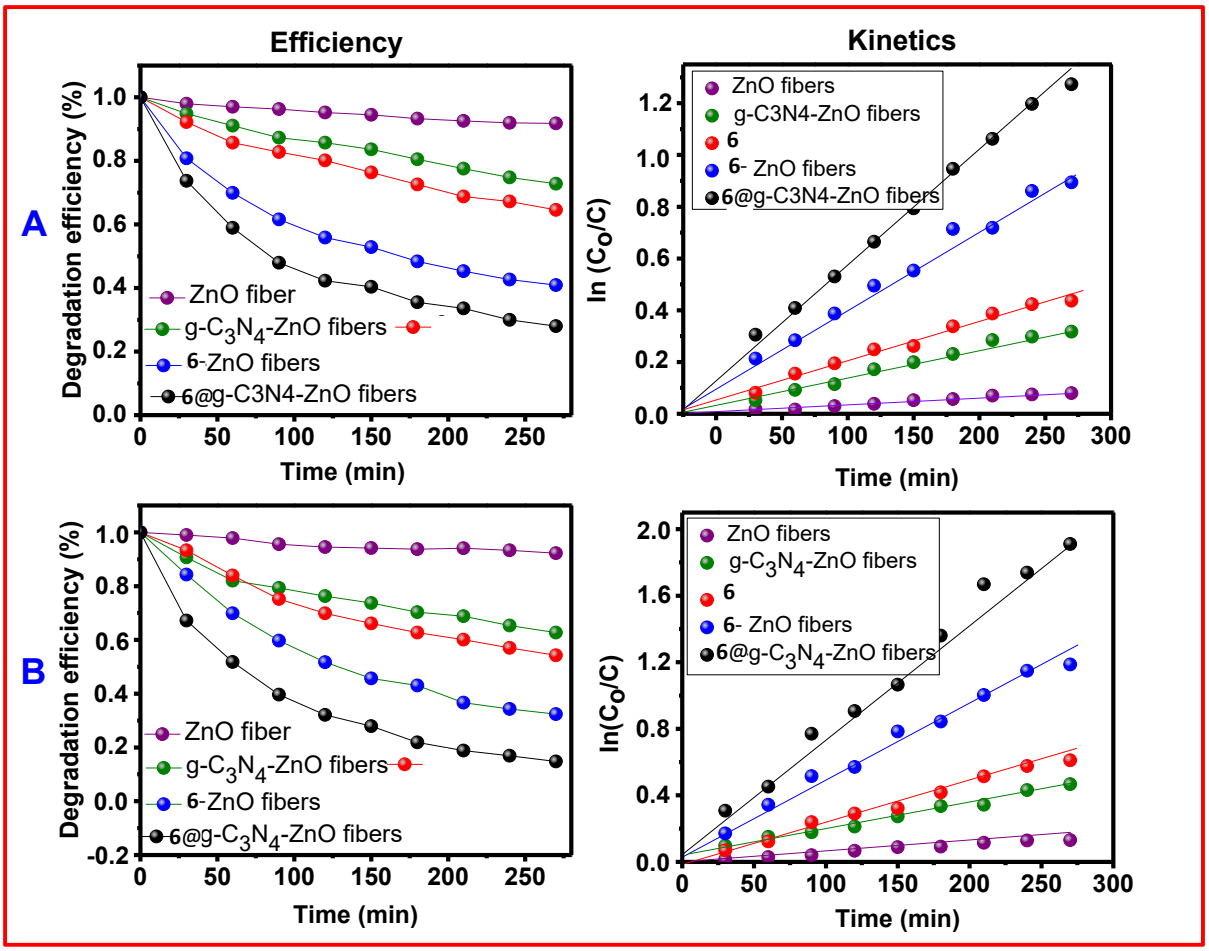

Appendix 20. Degradation efficiencies and kinetic plots of the photo- **A**, and sono- **B** catalytic degradation of Rhodamine 6G (6.63×10^{-5} M) using various catalysts.

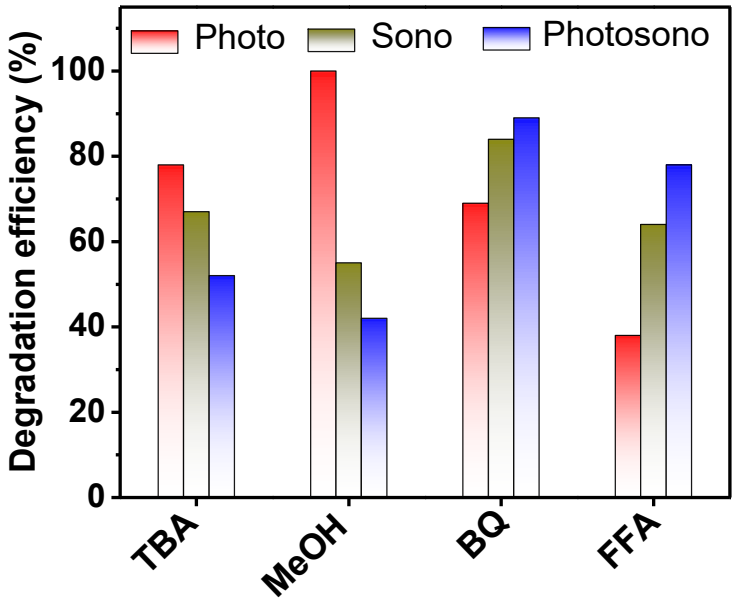

Appendix 21. Degradation efficiencies of photo, sono and photosono-catalytic degradation processes (at 180 min) using **6**@TiO_2 fibers in the presence of PMS and reactive oxygen species scavenging agents.